TECHNICAL DIGEST
1 9 9 6

HOLOGRAPHY

April 29–30, 1996
BOSTON, MASSACHUSETTS

1996 TECHNICAL DIGEST SERIES
VOLUME 4

19961025 041

O
SA
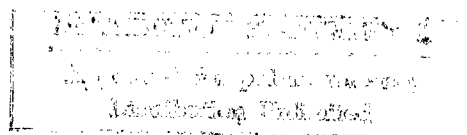
REPORT DOCUMENTATION PAGE

Form Approved
OMB NO. 0704-0188

1. AGENCY USE ONLY *(Leave blank)*	2. REPORT DATE September 13, 1996	3. REPORT TYPE AND DATES COVERED Final Aug. 19, 1996 – Aug. 18, 1997

4. TITLE AND SUBTITLE
Organization of the 1996 Holography Topical Meeting

5. FUNDING NUMBERS

6. AUTHOR(S)
David W. Hennage

DAAH04-96-1-0434

7. PERFORMING ORGANIZATION NAMES(S) AND ADDRESS(ES)
Optical Society of America
2010 Massachusetts Ave. NW
Washington, DC 20036

8. PERFORMING ORGANIZATION REPORT NUMBER

9. SPONSORING / MONITORING AGENCY NAME(S) AND ADDRESS(ES)

U.S. Army Research Office
P.O. Box 12211
Research Triangle Park, NC 27709-2211

10. SPONSORING / MONITORING AGENCY REPORT NUMBER

ARO 35469.1-PH-CF

11. SUPPLEMENTARY NOTES
The views, opinions and/or findings contained in this report are those of the author(s) and should not be construed as an official Department of the Army position, policy or decision, unless so designated by other documentation.

12a. DISTRIBUTION / AVAILABILITY STATEMENT

Approved for public release; distribution unlimited.

12 b. DISTRIBUTION CODE

13. ABSTRACT *(Maximum 200 words)*

The main purpose of the Holography Topical Meetings was to convene researchers to discuss new applications and fundamental developments in the field of holography.

Holographic devices and techniques are important to many advanced optical systems. These systems often employ holography to record information on spatial carrier frequencies. In addition, the principles of holography have been used to solve difficult imaging problems.

14. SUBJECT TERMS

15. NUMBER IF PAGES

16. PRICE CODE

17. SECURITY CLASSIFICATION OR REPORT UNCLASSIFIED	18. SECURITY CLASSIFICATION OF THIS PAGE UNCLASSIFIED	19. SECURITY CLASSIFICATION OF ABSTRACT UNCLASSIFIED	20. LIMITATION OF ABSTRACT UL

Summaries of the papers

presented at the topical meeting

HOLOGRAPHY

April 29–30, 1996
Boston, Massachusetts

1996 Technical Digest Series
Volume 4

SPONSORED AND MANAGED BY
Optical Society of America

DTIC QUALITY INSPECTED 3

Articles in this publication may be cited in other publications. To facilitate access to the original publication source, the following form for the citation is suggested:

Name of Author(s), "Title of Paper," in *Holography*, Vol. 4, 1996 OSA Technical Digest Series (Optical Society of America, Washington DC, 1996), pp. xx-xx.

Optical Society of America

Printed in the U.S.A.

Contents

HOLOGRAPHY
TECHNICAL PROGRAM COMMITTEE

3rd FLOOR REGISTRATION AREA
7:00am–5:30pm
Registration

HAMPTON A/B

8:30–10:00am
HMA • Imaging and Sensing
Joseph C. Marron, ERIM, Presider

8:30am (Invited)
HMA1 • Holographic methods for imaging through scattering media, P. Naulleau, E. Arons, J. Lopez, D. Dilworth, E. Leith, Univ. Michigan. Various new optical coherence techniques have been developed for imaging through highly scattering media, such as biological tissue. These are described, analyzed, and experimentally demonstrated. **(p. 2)**

9:00am (Invited)
HMA2 • Interferometric imaging through atmospheric turbulence, David G. Voelz, USAF Phillips Laboratory. Theory and experiment results are presented for imaging techniques that utilize coherent illumination, exploit wave front sensing receiver principles, and are relatively insensitive to receiver plane phase aberrations. **(p. 5)**

9:30am
HMA3 • Synthetic aperture holography for three-dimensional incoherent imaging, Joseph Rosen, Amnon Yariv, California Institute of Technology. Three-dimensional imaging of incoherent optics sources by a Michelson stellar interferometer is considered. A general three-dimensional paraxial theorem of the spatial coherence is presented and applied for generation of a synthetic aperture hologram. **(p. 9)**

9:45am
HMA4 • In-line acousto-optic architectures for holographic interferometry and sensing, Nabeel A. Riza, Univ. Central Florida. Novel Bragg cell-based in-line scanning optical systems are introduced for holographic interferometry and sensing applications with use of both heterodyne and almost-baseband signal detection techniques. **(p. 13)**

INDEPENDENCE BALLROOM
10:00–10:30am
Coffee Break

HAMPTON A/B

10:30am–12:00m
HMB • Holographic Memories
Yeshayahu Fainman, University of California, San Diego, Presider

10:30am (Invited)
HMB1 • Holographic memories, Demetri Psaltis, California Institute of Technology. Abstract not available. **(p. 18)**

11:00am
HMB2 • High-speed holographic recording of 500 images in hole burning rare-earth-doped crystals, R. Kachru, X. A. Shen, SRI International. Five hundred images are recorded and retrieved holographically at 30 Hz in Eu3+: Y2SiO5 crystal with use of the hybrid time frequency technique. This frame rate is one of the highest demonstrated frame rates for any optical technique. **(p. 19)**

11:15am
HMB3 • A technique for control of crosstalk noise in volume holography, Mark McDonald, Mark A. Neifeld, Univ. Arizona. We simulate crosstalk noise in holographic memory and estimate storage limits. We examine reduced density and apodized storage. Simple apodizers reduce crosstalk by 99%. **(p. 22)**

11:30am
HMB4 • Characterization of volume holographic associative searching, Keith G. Richling, Pericles A. Mitkas, Colorado State Univ. We present experimental work that characterizes the reconstruction of reference beams when a volume holographic memory is used for associative searching of database records. **(p. 26)**

11:45am
HMB5 • Some peculiarities of joint angular-spectral selectivity function of reflection holograms, Vladimir B. Markov, Anatolii I. Khizhnyak, Institute of Applied Optics, Ukraine, Colombia. The selective properties of reflection holographic gratings in the case of a strong deviation from Bragg conditions of both wavelength and angle of incident beam are discussed. **(p. 29)**

12:00m-1:30pm
Lunch on Own

GARDNER A&B

1:30–3:00pm
JMC • Joint Session on Diffractive and Micro-Optics and Holography I
Raymond Kostuk, University of Arizona, Presider

1:30pm (Invited)
JMC1 • Fabrication of micro-optics and diffractive lenses using analogue methods, M. C. Hutley, National Physical Laboratory, UK. We review mechanical and optical techniques for generating blazed diffracting components and consider how the lessons learned may be applied to current technological developments. **(p. 34)**

2:00pm
JMC2 • Laser-written diffraction gratings in quantum dot and island metal films, Yu. Kaganovskii, M. Rosenbluh, Bar-Ilan Univ., Israel. Pulsed laser interference diffraction gratings are written in thin films composed of quantum dots in glass and in thin metal island films. **(p. 38)**

2:15pm
JMC3 • High-efficiency transmission gratings fabricated in bulk fused silica, H. T. Nguyen, B. W. Shore, J. A. Britten, S. J. Bryan, S. Falabella, R. D. Boyd, M. D. Perry, Lawrence Livermore National Laboratory. We present the design and performance of high-efficiency transmission gratings fabricated in bulk fused silica for use in ultraviolet high-power laser systems. **(p. 42)**

2:30pm
JMC4 • Ultrahigh spatial-frequency, high-contrast periodic structures produced by interference lithography, H. T. Nguyen, J. A. Britten, R. D. Boyd, B. W. Shore, M. D. Perry, *Lawrence Livermore National Laboratory.* We develop a process to produce high-aspect ratio, high-frequency periodic profiles recorded in a photoresist layer by interference lithography. **(p. 45)**

2:45pm
JMC5 • Diffractive diffusers at the fabrication limit, Hans Peter Herzig, Wolfgang Singer, *Institute of Microtechnology, Switzerland;* Eckhard Piper, Johannes Wangler, *Carl Zeiss, Germany.* The design and fabrication of diffractive elements, generating flat-top intensity distributions for partial coherent lasers at short wavelengths, is presented. **(p. 49)**

INDEPENDENCE BALLROOM
3:00pm-3:30pm
Coffee Break

HAMPTON A/B

3:30–5:15pm
HMC • Applications
James R. Leger, *University of Minnesota, Presider*

3:30pm (Invited)
HMC1 • Progress in holographic 3-D video displays, S. Benton, *Massachusetts Institute of Technology.* Abstract not available. **(p. 54)**

4:00pm
HMC2 • Construction of a holographic three-dimensional printer using silver-halide film plates, O. Birkeland, T. E. Grahl-Nielsen, *EPM Consultants a.s, Norway;* K. E. Olsen, I. Singstad, *Univ. Bergen, Norway;* R. Andreassen, *Norway.* We present construction of a holographic printer using a multistereographic technique. The end product is a reflection hologram from computer-processed AutoCad images. **(p. 55)**

4:15pm (Invited)
HMC3 • Applications of holography for femtosecond time-domain processing, Andrew M. Weiner, *Purdue Univ.* We discuss storage and processing of femtosecond time-domain signals based on extensions of traditional Fourier optics and holography methods. **(p. 59)**

4:45pm
HMC4 • Temporal phase conjugation with space-time processors, Dan M. Marom, Pang-chen Sun, Yeshayahu Fainman, *Univ. California-San Diego.* Space-time processors are shown to posses temporal phase conjugation and self-referencing properties essential for distortionless optical communication via spatial-temporal encoding-decoding. **(p. 62)**

5:00pm
HMC5 • Two-dimensional phase unwrapping of a noise-contaminated optical interferogram, Ching-Wei Liao, M. A. Fiddy, *Univ. Massachusetts-Lowell.* Phase unwrapping of interference patterns is considered with use of an approach that exploits a priori knowledge of real point zero locations in the wave front.
(p. 66)

3rd FLOOR REGISTRATION AREA

7:30am–5:30pm
Registration

COMMONWEALTH ROOM

8:30–10:00am
HTuA • Materials
Willis S. Colburn, *Kaiser Optical Systems Inc., Presider*

8:30am (Invited)
HTuA1 • Photopolymer materials for holographic optical elements, Kirk W. Steijn, William J. Gambogi, T. John Trout, *DuPont Holographic Materials.* Photopolymer materials for recording volume holographic gratings have been developed. Film performance and applications in holographic optical elements are discussed. **(p. 70)**

9:00am
HTuA2 • Fast photorefractive multiple quantum well working at 1.55 mm, A. Le Corre, H. L'haridon, S. Salaun, R. Lever, M. Baudet, M. Gauneau, J. C. Keromnes, J. Pleumeekers, S. Mottet, B. Lambert, G. Moisan, C. Vaudry, C. De Matos, S. Gosselin, *France Telecom CNET/LAB.* We present multiple quantum well photorefractive InGaAs(P)-InP devices working at 1.55 um. First results on diffraction efficiency and lateral diffusion are reported on. **(p. 74)**

9:15am
HTuA3 • Polymer-based volume hologram for a surface-normal 3 X 3 nonblocking wavelength-selective crossbar, Charles Zhou, Ray T. Chen, *Univ. Texas-Austin.* A 3 X 3 non-blocking wave-length-selective crossbar is demonstrated by use of a polymer-based wavelength-dispersive phase volume hologram and GRIN lenses. **(p. 78)**

9:30am
HTuA4 • Holographic recording kinetics in photopolymer media, E. Kovalenko, S. Sharangovich, T. Zelenskya, *Tomsk State Academy of Control Systems and Radio Electronics, Russia.* The analytical model of hologram recording kinetics in polymer materials is offered. The model takes into account the changes of refractive index connected with the processes of photopolymerization and displacement of inert components on account of monomer diffusion. This model is in the qualitative agreement with the known experimental results and can be useful for destination and optimization of the parameters of the photopolymer materials. **(p. 84)**

9:45am
HTuA5 • Dynamical model of reconstruction and amplification of holograms in photopolymer materials, Eugene S. Kovalenko, Sergey N. Sharangovich, *Tomsk State Academy of Control Systems and Radio Electronics, Russia.* The theoretical model describing the dynamical process of holograms reconstruction and their optical amplification in amorphous photopolymer material is developed, taking into account the photopolymerization kinetics and components diffusion. The peculiarities of kinetics of the hologram amplification, space-time transformation of the holographic gratings field, and time evolution of the spectral-angle sensitivity of the amplification process are discussed. **(p. 86)**

INDEPENDENCE BALLROOM

10:00am-10:30am
Coffee Break/Exhibits

COMMONWEALTH ROOM

10:30am–12:00m
JTuB • Poster Previews
G. Michael Morris, *University of Rochester and Rochester Photonics Corp., Presider*

10:30am
JTuB1a • Fabrication and experiment of a diffractive phase element that implements wavelength demultiplexing and focusing, Bizhen Dong, Guoqing Zhang, Guozhen Yang, Benyuan Gu, Shihai Zheng, Dehua Li, Yansong Chen, *Academia Sinica, China.* The design and fabrication of diffractive phase elements for wavelength demultiplexing and focusing are presented. Experimental results are in good coincidence with numerical simulations. **(p. 92)**

10:30am
JTuB1b • A new kind of diffractive phase element applied to wavelength demultiplexing and annular focusing, Benyuan Gu, Guoqing Zhang, Bizhen Dong, Guozhen Yang, *Academia Sinica, China.* A design of diffractive phase elements first applied to wavelength demultiplexing and annular focusing is presented. Numerical simulations are in good agreement with the desired performances. **(p. 96)**

10:32am
JTuB2 • Off-axis Talbot effect and array generation in planar optics, Markus Testorf, Jurgen Jahns, *Fern Univ. Hagen, Germany;* Nikolay A. Khilo, Andrey M. Goncharenko, *Belarussian Academy of Sciences.* The Talbot effect for oblique angles of light propagation is investigated. Experimental verifications and considerations on a planar integration of Talbot array illuminators are included. **(p. 100)**

10:34am
JTuB3 • Diffractive elements developed for uniform illumination in inertial confinement fusion, Qiu Yue, Fan Dianyuan, Deng Ximing, *Chinese Academy of Sciences;* Deng Xuegong, Li Yongpin, *China Univ. Science and Technology.* A type of diffractive element is designed and fabricated for uniform illumination in inertial confinement fusion. Experiment results are given. **(p. 104)**

10:36am
JTuB4 • Achromatization for multiple narrowband sources using hybrid multi-order diffractive lenses, Kevin J. McIntyre, G. Michael Morris, *Univ. Rochester.* Multiple refractive and diffractive lenses can be combined to form hybrid lenses suitable for systems with multiple narrowband sources. **(p. 107)**

10:38am
JTuB5 • Array generator design for an optical analog-to-digital converter, Joseph N. Mait, *U.S. Army Research Laboratory;* Barry L. Shoop, *U.S. Military Academy.* We present the design of an eight-level phase-only diffractive element that generates a 7 x 7 nonuniform array of spots. The array generator is used to implement error diffusion within an optical analog-to-digital converter. **(p. 111)**

10:40am
JTuB6 • Electric fields and Poynting vectors in dielectric gratings, Bruce W. Shore, Michael D. Feit, *Lawrence Livermore National Laboratory;* Lifeng Li, *Univ. Arizona.* We discuss and illustrate the use of electric field magnitudes, energy density, and Poynting vectors as tools for understanding phenomena associated with dielectric gratings. **(p. 114)**

10:42am
JTuB7 • Diffractive-refractive achromatic optical processor for white-light spatial filtering, P. Andres, *Univ. Valencia, Spain;* E. Tajahuerce, J. Lancis, V. Climent, M. Fernandez-Alonso, *Univ. Jaume I, Spain.* We present a novel diffractive-refractive achromatic optical processor, with very low residual chromatic aberrations, to perform white-light spatial-frequency filtering of color inputs. **(p. 116)**

10:44am
JTuB8 • Diffractive optical elements for tracking and receiving in optical space communication systems, P. Blattner, H. P. Herzig, K. J. Weible, *Univ. Neuchatel, Switzerland.* Different designs of a diffractive optical element used for tracking and receiving in laser communication terminal are presented. Elements based on these designs are realized and compared. **(p. 120)**

10:46am
JTuB9 • Scalar design of diffractive elements using direct and indirect optimization, Joseph N. Mait, *U.S. Army Research Laboratory.* We present a general procedure for the design of diffractive optical elements and use scalar diffraction theory to apply it to the design of three common diffractive elements. The procedure reveals that most common design techniques can be classified as either direct or indirect optimizations. **(p. 124)**

10:48am
JTuB10 • High efficiency dielectric reflection gratings, B. W. Shore, M. D. Perry, J. A. Britten, R. D. Boyd, M. D. Feit, H. Nguyen, R. Chow, G. Loomis, *Lawrence Livermore National Laboratory;* Lifeng Li, *Univ. Arizona.* We discuss the design and fabrication of all-dielectric reflection gratings that place theoretically 99% of the incident light into a single diffraction order. **(p. 128)**

10:50am
JTuB11 • Design of phase-shifting masks for enhanced-resolution optical lithography, Guo-Zhen Yang, Zhi-Yuan Li, Bi-Zhen Dong, Ben-Yuan Gu, Guo-Qing Zhang, *Academia Sinica, China.* An approach based on the general theory of amplitude-phase retrieval in optics is presented for the design of phase-shifting masks for enhanced-resolution optical lithography. **(p. 132)**

10:52am
JTuB12 • Flat-top beam generation using an iteratively designed binary phase grating, Jun Amako, Tomio Sonehara, *Seiko Epson Corp., Japan.* The grating phase, optimized by the simulated-annealing algorithm, produces in-phase diffracted waves that interfere constructively to form a uniform amplitude and phase profile in a Fourier domain. **(p. 136)**

10:54am
JTuB13 Surface-relief gratings with sharp edges: Improvement of the convergence of the coordinate transformation method, Lifeng Li, *Univ. Arizona.* The convergence of the coordinate transformation method of Chandezon et al. for surface-relief gratings with sharp edges is improved substantially with use of the correct Fourier factorization procedure. **(p. 139)**

10:56am
JTuB14 Liquid crystal phase modulation technique to reduce the spatial frequency of interferometric fringes, P. Douglas Knight Jr., *Univ. North Carolina-Charlotte.* A technique to reduce the spatial frequency of interferometric fringes is proposed with use of a spatial light modulator to perform phase modulation. **(p. 143)**

10:58am
JTuB15 Synthesis of fully continuous phase screens for tailoring the focal plane irradiance profiles, Sham Dixit, Mike Feit, *Lawrence Livermore National Laboratory.* We present an iterative procedure for constructing fully continuous phase screens for tailoring the focal plane intensity distributions. **(p. 147)**

11:00am
JTuB16 Fabrication of large aperture kinoform phase plates in fused silica for smoothing focal plane intensity profiles, Mike Rushford, Sham Dixit, Ian Thomas, Mike Perry, *Lawrence Livermore National Laboratory.* We have fabricated large aperture (40-cm) kinoform phase plates for producing super-Gaussian focal plane intensity profiles. **(p. 151)**

11:02am
JTuB17 Speckle-free phase Fresnel holograms and beam-shaping elements, Luiz Goncalves Neto, Yunlong Sheng, *Univ. Laval, Canada.* We describe optical speckle-free phase Fresnel holograms. We choose the constant initial phase for iterations, which can avoid the speckles caused by isolated point zeros in the reconstruction plane. **(p. 154)**

11:04am
JTuB18 High-efficiency fast diffractive lens for beam coupling, Yunlong Sheng, Dazeng Feng, *Univ. Laval, Canada.* Iterative simulated annealing is implemented in the design of a high-efficiency fast lens for focusing and shaping elliptical beams. The aberrations introduced in the design are evaluated. **(p. 158)**

11:06am
JTuB19 Effective medium theory of symmetric two-dimensional subwavelength periodic structures, Philippe Lalanne, *France.* We present the effective medium theory of two-dimen-

sional symmetric periodic structures. Predictions are verified with rigorous computation. **(p. 162)**

11:08am
JTuB20 • Z-scan measurement in amorphous As2S3 thin film, Yeung Joon Sohn, Chong Hoon Kwak, Ok Shik Choe, *Yeungnam Univ., Korea.* The complex nonlinear refractive index is measured and analyzed in an amorphous As2S3 thin film by adaptation of the sensitive cw z-scan technique. *(p. 166)*

11:10am
JTuB21 • Simplified processing method of dichromated gelatin derived from Agfa 8E75HD plates, Yong Seok Im, Young Lak Lee, Chong Hoon Kwak, Ok Shik Choe, *Yeungnam Univ., Korea;* Sang Cheol Kim, *Samsung Aerospace Industries Ltd, Korea.* A simplified method to make dichromated gelatin hologram is presented. If one starts with Agfa 8E75HD plates, the complete processing time is just two hours and high diffraction efficiency of 81.5% is obtained. **(p. 170)**

11:12am
JTuB22 • Analysis of focal tolerance and fine pattern resolutions formed by phase conjugation in dichromated gelatin hologram, Yong Seok Im, Young Lak Lee, Chong Hoon Kwak, Ok Shik Choe, *Yeungnam Univ., Korea.* An image of 1 um line width formed by holographic phase conjugation is measured clearly within the focal tolerance of about 40 um and is analyzed theoretically.
(p. 174)

11:14am
JTuB23 • Wavelength-agile fluorescence microscopy filter using photorefractive barium titanate, Robert Kersten, Salvador Fernandez, Ciencia Inc.; George Fischer, Robert Boyd, *Univ. Rochester.* Holograms in photorefractive materials are used as passive wavelength-agile notch filters in fluorescence spectroscopy applications, thus filtering out coherent light while transmitting incoherent light. **(p. 178)**

11:16am
JTuB24 • Holographic interferometry methods for conducting stress analysis on quartz crystal components, Jill A. Brosig, *Motorola.* Holographic interferometry is used to study mechanical loading on quartz blanks resulting from mount structure. After identifying the magnitude and location of real-time-induced stresses, the design is optimized by change of such parameters as geometry and materials. **(p. 181)**

11:18am
JTuB25 • A computational model for holographic sensing, Ben Bakker, Val Bykovski, *Univ. Massachusetts-Lowell.* A novel analytical concept based on holographic recognition of light patterns from a sample is proposed and demonstrated computationally. **(p. 184)**

11:20am
JTuB26 • Computer-generated hologram for reconstruction of unusual mode image, Gao Wenqi, Tan Suqing, Zhou Jin, *Nanjing Univ., China.* Three kinds of computer-generated holograms of unusual reconstruction mode are reported.

Theoretic analysis and corresponding experimental results are given. **(p. 187)**

11:22am
JTuB27 • Measurement and analysis of compound amplitude and phase holographic gratings, Y. J. Wang, M. A. Fiddy, Y. Y. Teng, D. A. Pommet, L. Malley, *Univ. Massachusetts-Lowell.* We describe the effect on the reconstruction of a bleached hologram of the inevitable presence of a residual amplitude hologram that is usually neglected. The modeling of this offers insights into its possible exploitation for some applications. **(p. 191)**

INDEPENDENCE BALLROOM

11:30am–1:30pm
Poster Session

GARDNER A&B

1:30–3:00pm
JTuC • Joint Session on Diffractive and Micro-Optics and Holography II
Michael Gale, *Paul Scherrer Institute, Presider*

1:30pm (Invited)
JTuC1 • Diffraction optics—a century from basic studies to mass production, Erwin G. Loewen, *Spectronic Instruments, Inc.* It has taken 100 years to combine basic concepts for diffraction optics with a series of enabling technologies to arrive at commercially useful products. **(p. 196)**

2:00pm
JTuC2 • Liquid crystal grating based on modulation of circularly polarized light, Jay E. Stockley, Kristina M. Johnson, *Univ. Colorado-Boulder;* Gary D. Sharp, Steven A. Serati, Ping Wang, *Boulder Nonlinear Systems Inc.* We present theoretical and experimental results for analog phase modulators and gratings using chiral smectic liquid crystals as rotative wave plates acting on circular polarization. **(p. 199)**

2:15pm
JTuC3 • Diffractive optical elements for three-dimensional displays based on the partial pixel 3-D display architecture, G. P. Nordin, M. W. Jones, R. G. Lindquist, J. H. Kulick, S. T. Kowel, *Univ. Alabama-Huntsville.* We examine the use of diffractive optical elements to realize three-dimensional, holographic-like displays based on the partial pixel 3-D display architecture, and we describe our current implementations of real-time displays. **(p. 203)**

2:30pm
JTuC4 • Beam-pointing stabilization and increased ladar heterodyne mixing efficiency using a liquid crystal phased array device, Mark J. Missey, *Vincent Dominic, Univ.;* Edward A. Watson, *Wright Laboratory.* Active beam-pointing stabilization and increased coherent laser radar mixing efficiency applications for an addressable liquid crystal phased array are investigated. **(p. 207)**

2:45pm
JTuC5 • Programmable wave-front generation with two binary phase spatial light modulators, Guoguang Yang, Seth Broomfield, *Univ. Oxford, UK*. A programmable wave-front generation system that uses two binary phase SLMs is a space-variant system with high diffraction efficiency. It is implemented experimentally with two ferroelectric liquid crystal SLMs. **(p. 211)**

INDEPENDENCE BALLROOM

3:00–3:30pm
Coffee Break/Exhibits

COMMONWEALTH ROOM

3:30pm-5:15pm
HTuD • Holographic Optical Elements
Dean Faklis, *PSC, Inc., Presider*

3:30pm (Invited)
HTuD1 • Modeling issues for the design of volume holographic and surface relief grating structures, Raymond K. Kostuk, Charles W. Haggans, Eugene Campbell, Tae-Jin Kim, *Univ. Arizona*. Important fabrication factors that influence grating design are summarized and modeled. Examples of polarization control and multiplexed diffractive elements are discussed. **(p. 216)**

4:00pm (Invited)
HTuD2 • Highly selective optical elements, Nadia Rheinhand, *Russian Academy of Sciences*. Abstract not available. **(p. 220)**

4:30pm
HTuD3 • A geometrical derivation of WRITE beam criteria for multiplexed color hologram readout using wave-vector triads, Monish R. Chatterjee, Shih-Tun Chen, *SUNY-Binghamton*. A wave-vector triad approach developed recently for studying misaligned reconstructed beams is used to establish necessary WRITE beam criteria for the readout of multiplexed color holograms. **(p. 221)**

4:45pm
HTuD4 • Computer-generated holographic photonic band gap structures designed using inverse scattering techniques, S-M. Chang, D. A. Pommet, L. Malley, M. A. Fiddy, *Univ. Massachusetts-Lowell*. New modeling techniques based on inverse scattering procedures are used to design a photonic band gap structure that is realized by a computer-generated hologram. Numerical algorithm issues are discussed and experimental results are presented. **(p. 225)**

5:00pm
HTuD5 • Ray-tracing approach to computer-generated holography with detour phase coding for precision three-dimensional beam patterns, Shih-Ming Chang, Drew A. Pommet, Michael A. Fiddy, Freeman C. Lin, *Univ. Massachusetts-Lowell*. A ray-tracing method incorporating a detour phase coding scheme is used to encode computer-generated holograms that allow for very precise three-dimensional reconstructions. **(p. 227)**

5:15pm
Closing Remarks

Imaging and Sensing

HMA 8:30 am-10:00 am
Hampton A/B

Joseph C. Marron, *Presider*
ERIM

Holographic methods for imaging through scattering media

P. Naulleau, E. Arons, J. Lopez, D. Dilworth, and E. Leith
University of Michigan, Ann Arbor, MI 48109-2122

Light entering highly diffusing material is scattered severely in all directions. However, the component that has scattered the least will best form a shadow image of any absorbing objects encountered in the medium. In the case of a short pulse of light entering the diffusing medium, the emerging pulse can be many orders of magnitude longer than the incident pulse, because of multiple scattering. The light at the beginning of this long pulse (the first arriving light) is the least scattered component and must be temporally isolated from the remainder of the pulse in order to use it for imaging. This is accomplished through the use of a very fast gate.

Holography has been used successfully to gate the first arriving light. Here, the reference beam is adjusted so that it interferes only with the first arriving light, and the later arriving light is thus excluded from the reconstructed wave. The major advantage of the holographic method is that short pulse illumination is not required; continuous-wave light of short coherence length is equally effective and easier to generate.

We employ electronic holography. Here, a hologram is formed on the surface of a detector, such as a CCD camera. The hologram is read into a computer, which then computes the image in a manner analogous to the conventional optical reconstruction process; the resulting image is displayed on a monitor. The advantages of electronic holography over conventional holography have been found to be considerable. We have worked in this area for several years and have demonstrated a number of interesting and effective ideas. Here we describe some additional ideas.

a. Combined speckle differencing and first arriving light
Speckle differencing is an established technique for distinguishing between stationary and moving scatterers. We have combined this technique with that of the first arriving light. Experiments shown this combination to be powerful.

The speckle differencing method, as we apply it, has two modes: one where the embedded objects move, and one where the embedded objects are relatively stationary and the scattering medium

moves. Let the objects of interest be moving, and the scattering medium in which the objects are embedded be stationary, or comparatively stationary. In the biological area, this situation would arise if blood flow through tissue is to be measured. One thus takes two successive speckle images on a CCD camera, in an interval sufficiently short that the blood has moved, while the other biological tissue has not. The difference speckle pattern is thus produced from light that has interacted with the flowing blood. Experiments show that when this technique is combined with the first arriving light technique, the combination is far more effective than either by itself.

A more sophisticated form of speckle differencing becomes possible in holography, where the phase, as well as the amplitude, of the speckles is retained; here we take the difference of the holograms, not just of the speckle pattern intensity reconstructed from the holograms. When this is done, a method called fringe differencing results, in which the complex amplitude of the speckles are subtracted, not just the intensity differences. This technique is well adapted to the situation where the embedded objects are completely stationary and the scattering medium is non stationary. This is the typical situation where the scattering medium is living biological tissue and the object is absorbing material.

b. Ensemble-averaged imaging

We describe a process called ensemble-averaged imaging. We ask: Can we carry out an averaging process that preserves the phase? We consider a random medium, such as uniform scatterers in a fluid. A ray starting at a point A reaches point B by many paths. The paths taken are a random process. The phase delay ϕ of the light arriving at B is therefore a random process. We consider an ensemble of such random media, such as a medium with fluid-suspended particles that are constantly moving. With the progression of time, many different realizations of the ensemble occur. We average the arriving field $a\exp(j\phi)$ over the ensemble, obtaining an ensemble-averaged field $|a|\exp(j\phi)$. In the ensemble average, the phase delay ϕ should be a deterministic function of the distance r between the points A and B. Setting $\phi(r)$ = constant defines a phase contour, which can be viewed as an ensemble-averaged wavefront. Can this averaged wavefront be treated like a deterministic wavefront in a uniform medium? Can it be focused by a lens? Can the ensemble-averaged collection of wavefronts, i.e., the ensemble-averaged wavefront, be treated like conventional wavefields to form images, Fourier transforms, etc.? If this can be done, the ensemble-averaged field in a random scattering medium can be treated like the deterministic field in a clear medium. It would then be possible to image into scattering media without the use of broad source or broad spectrum light, although the use of multiple wavelength or source elements might hasten the convergence process. To record the phase requires holography, and thus a reference

beam. The ensemble averaged field would exist only within the computer memory, unless the stored data were read out to form a hologram of the ensemble-averaged wave field.

c. Chirp-Stretch

We suggest an alternative to the conventional short-pulse gating techniques. The method exchanges the generation of a time gate with the generation of a frequency gate. The technique consists of radiating a chirp pulse of a controlled length having a duration equal to, or somewhat longer than, the stretch factor for the scattering medium. If an impulse of light emerges from a scattering medium as a stretched pulsed of duration, for example 5 picoseconds, then a chirp pulse of about this same length or somewhat longer should be radiated.

In this technique we radiate a pulse $\exp j(2\pi f_0 t + \pi \gamma t^2)$. The delayed pulse, for a specific delay time t', is $\exp j[2\pi f_0(t-t') + \pi \gamma(t-t')^2]$. We mix this with a reference pulse $\exp j[2\pi f_0(t-t_r) + \pi \gamma(t-t')^2]$, producing $[\exp j 2 f_0(t_r-t') + \pi \gamma(t'^2-t_r^2)] \exp[j2\pi \gamma(t_r-t')t]$, a constant frequency. There is a one-to-one correspondence between delay and frequency. To separate the first arriving light from the reminder requires a narrow band filter instead of a gate. The techology of filter synthesis is different from gate synthesis; thus it may in some cases be advantageous to use this chirp technique instead of the conventional pulse. This technique has been employed in mircrowave radars, and its distinct advantages in that field are have been established. Its advantages for the photon migration application are being explorsed.

Interferometric Imaging Through Atmospheric Turbulence

David G. Voelz
USAF Phillips Laboratory, Unconventional Imaging Branch
Kirtland Air Force Base, NM 87117-5776
Telephone: 505/846-5162, Fax: 505/846-2045, email: voelz@plk.af.mil

1. INTRODUCTION

A variety of unconventional techniques for imaging targets using coherent (laser) illumination have recently been proposed and analyzed.[1,2] These techniques were primarily derived and developed for the observation of objects, such as spacecraft, at long distances through atmospheric turbulence. Several of the techniques exploit the idea of making 2-D spatial measurements of the coherent optical wave front at the receiver plane. In this paper we briefly review two laser imaging techniques that utilize wave front measurements and we discuss some of the merits, limitations and application of the techniques. References are provided for further investigation.

Figure 1 is a schematic that shows the principle components of a laser imaging system that employs a spatially sampled receiving aperture array. Consider an object that is flood-illuminated by a coherent laser beam. The optical field at the receiver pupil-plane can be written

$$E_r(x,y,t) = A_r(x,y)\exp\{j(2\pi\nu t + \phi_r(x,y) + \phi_{atm}(x,y))\} \tag{1}$$

where ν is the optical frequency and A_r and ϕ_r are the signal amplitude and phase at time t and position (x,y). $\phi_{atm}(x,y)$ is an aberration phase, due to the atmosphere for example, that is picked up upon propagation to the receiver plane. If one could measure or obtain estimates of A_r and ϕ_r, then the optical field at the object plane could be calculated. For example, if the object is in the far-field of the receiver then the object plane field is given by

$$E_o(x',y',t) = K\mathcal{F}_{xy}[A_r(x,y)\exp\{j\phi_r(x,y)\}]\exp\{j2\pi\nu t\} \tag{2}$$

where $\mathcal{F}_{xy}$ is a 2-dimensional Fourier transform, (x',y') are object plane coordinates and K is an appropriate constant. An intensity image of the object is then given by $|E_o(x',y',t)|^2$.

As with conventional imaging using a lens, the receiving aperture diameter classically limits the imaging resolution that can be attained. However, other attributes associated with laser imaging do not have straight-forward counterparts with conventional incoherent imaging:

- The illumination of diffuse objects with coherent light results in a speckle pattern at the receiver array. The speckles contain object information but are also considered a noise source that contaminates recovered single snapshot images. This problem is usually handled by collecting, recovering and averaging a set of independent speckled images.

- Techniques that rely on coherent wavefront measurement require that the coherence length of the laser light must be greater than twice the depth of the object so that light

backscattered from "deep" parts of the object interferes coherently with light scattered from "near" parts of the object.

- A speckle sampling criterion exists for the receiver array. Typically, the detector sample rate must be on the order of two samples per smallest intensity speckle for a recovery to be possible.

- To first order, rotation of an object with respect to the receiver plane causes the backscattered speckle pattern to scan across the receiving array. Excessive smearing associated with the scanning can be detrimental, but the effect also affords the implementation of synthetic aperture receiving schemes.[3]

2. HETERODYNE ARRAY IMAGING

To measure the received field phase ϕ_r in the optical regime, one must resort to some type of interferometric technique. Heterodyne array imaging is one possible approach.[4-7] Figure 2 shows a schematic of a coherent heterodyne imaging system. A local oscillator beam (shown in the figure as being derived from the illumination source) is combined with the backscattered signal light before detection on a two-dimensional array. If the local oscillator beam is given by

$$E_{lo}(t) = A_{lo}\exp\{j2\pi(\nu-\Delta\nu)t + \phi_{lo}\} \qquad (3)$$

where it is assumed that the amplitude A_{lo} and phase ϕ_{lo} are constant over all (x,y), then the intensity signal observed is

$$\begin{aligned} I(x,y,t) &= \mid E_r(x,y,t) + E_{lo}(t)\mid^2 \\ &= A_r(x,y)^2 + A_{lo}{}^2 + 2A_r(x,y)A_{lo}\cos(2\pi\Delta\nu t + \phi_r(x,y) + \phi_{atm}(x,y) - \phi_{lo}) \qquad (4) \end{aligned}$$

By examining the component of the signal associated with the beat frequency $\Delta\nu$, the signal amplitude A_r can be found (multiplied by the constant A_{lo}) and the phase function $\phi_r(x,y) + \phi_{atm}(x,y) + \phi_{lo}$ can be obtained. With regard to the phase function, ϕ_{lo} can be assumed to be zero without loss of generality. However, removing the $\phi_{atm}(x,y)$ term from the sum is more difficult. Cederquist et al.[8] have suggested one approach based on a digital shearing idea for estimating and removing phase error terms.

A key aspect of a heterodyne receiving system is its sensitivity to Doppler shifting of the returning light. Doppler shifts, due to radial (line-of-sight) velocity of the object, cause the beat frequency $\Delta\nu$ to shift and in fact $\Delta\nu$ can be a function of (x,y). Clark et al.[4] provide a short discussion of the incorporation of Doppler signatures into 2-dimensional spatial heterodyne imaging. For a closely related application of heterodyne imaging, Marron and Schroeder[8] present a technique based on frequency sweeping the illumination laser to produce object depth profiles as well as 2-dimensional spatial imagery.

3. SHEARED COHERENT IMAGING PHOTOGRAPHY

A second interferometric imaging technique is shown in Fig 3. This technique is known as Sheared Coherent Imaging Photometry (SCIP) or sometimes Sheared-Beam Imaging.[9,10] SCIP is based on an implementation of an amplitude shearing interferometer. Consider three illumination laser beams with optical frequencies of ν, ν-$\Delta\nu_x$ and ν-$\Delta\nu_y$ and apertures positioned at the corners of a right triangle with spacings Δx and Δy between beams. The three fields returned from the object are then given by

$$E_r(x,y,t) = A_r(x,y)\exp\{j(2\pi\nu t + \phi_r(x,y) + \phi_{atm}(x,y))\}$$

$$E_{rx}(x,y,t) = A_r(x+\Delta x,y)\exp\{j(2\pi(\nu-\Delta\nu_x)t+ \phi_r(x+\Delta x,y) + \phi_{atm}(x,y))\}$$

$$E_{ry}(x,y,t) = A_r(x,y+\Delta y)\exp\{j(2\pi(\nu-\Delta\nu_y)t + \phi_r(x,y+\Delta y) + \phi_{atm}(x,y))\} \tag{5}$$

where E_{rx} is the field that is shifted in the x direction and E_{ry} is the field shifted in the y direction. Note that each field carries the same aberration phase term since the phase aberration is assumed to be located at the receiver plane. Detecting the combined fields yields

$$I(x,y,t) = |E_r(x,y,t)+E_{rx}(x,y,t)+E_{ry}(x,y,t)|^2$$

$$
\begin{aligned}
= \; & A_r(x,y)^2 + A_r(x+\Delta x,y)^2 + A_r(x,y+\Delta y)^2 \\
& + 2A_r(x,y)A_r(x+\Delta x,y) \cos(2\pi\Delta\nu_x t + \phi_r(x,y) - \phi_r(x+\Delta x,y)) \\
& + 2A_r(x,y)A_r(x,y+\Delta y) \cos(2\pi\Delta\nu_y t + \phi_r(x,y) - \phi_r(x,y+\Delta y)) \\
& + 2A_r(x+\Delta x,y)A_r(x,y+\Delta y) \cos(2\pi(\Delta\nu_y-\Delta\nu_x)t + \phi_r(x+\Delta x,y) - \phi_r(x,y+\Delta y))
\end{aligned} \tag{6}
$$

By demodulating the intensity signal at the beat frequencies $\Delta\nu_x$, $\Delta\nu_y$ and $\Delta\nu_y$-$\Delta\nu_x$, estimates of the field amplitude $A_r(x,y)$ and spatial phase differences $\phi_r(x,y) - \phi_r(x+\Delta x,y)$, $\phi_r(x,y) - \phi_r(x,y+\Delta y)$ and $\phi_r(x+\Delta x,y) - \phi_r(x,y+\Delta y)$ can be made. Because of the common path nature of the beams, the phase aberration term is canceled from the phase difference quantities. However, to finally reconstruct the field phase $\phi_r(x,y)$ the phase differences must be effectively integrated. Appropriate phase reconstructors are discussed by Hutchin[9] and Idell and Gonglewski[2].

The clear advantage of the SCIP technique is the cancellation of near-field phase aberrations. The drawbacks are the complicated transmit scheme and the requirement for a phase reconstructor. Several aspects of this technique including the effects of photon noise, finite detector size and varying shear lengths have been examined to determine the performance limitations of the concept.[9-11] Laboratory experiments have also been done to verify the practicalities of the technique.[10]

4. REFERENCES

1. P.S. Idell and D.G. Voelz, "Non conventional Laser Imaging using Sampled-Aperture Receivers," *Optics and Photonics News*, 8-15, April 1992.

2. P.S. Idell and J.D. Gonglewski, "Image synthesis from wavefront sensor measurements of a coherent diffraction field," Opt. Lett. **15**, 1309-1311, 1990.

3. D.B. Rider, D.G. Voelz, J.D. Gonglewski and K.A. Bush, "Imaging correlography using an inverse synthetic aperture," Signal Recovery and Synthesis IV, Optical Society of America, 1992 Technical Digest Series Vol. 11, 58-60, 1992.

4. S.E. Clark, L.R. Jones, and L.F. DeSandre, "Coherent array optical imaging," Appl. Opt. **30**, 1804-1810, 1991.

5. J.K Boger, J.D. Gonglewski and D.G. Voelz, "Experimental techniques in heterodyne laser speckle imaging," Proc. Lasers '91, Soc. for Opt. and Quantm. Elec., STS Press, McLean, VA, 1992.

6. D.G. Voelz, K. Bush, D.B. Rider, and J.D. Gonglewski, "Detection analysis for a heterodyne array imaging system," Proc. 1992 Meeting of the IRIS Specialty Group on Active Systems, Vol. I, 59-66, 1993.

7. J.C. Marron and K.S. Schroeder, "Three-dimensional lensless imaging using laser frequency diversity," Appl. Opt. **31**, 255-262, 1992.

8. J.N. Cederquist, J.R. Fienup, J.C. Marron, T.J. Schulz and J.H. Seldin, "Digital shearing laser interferometry for heterodyne array phasing," Proc. SPIE **1416**, 1991.

9. R.A. Hutchin, "Sheared Coherent Interferometric Photography: A technique for lensless imaging," Proc. SPIE **2029**, 1993.

10. D.G. Voelz, J.D. Gonglewski, and P.S. Idell, "SCIP computer simulation and laboratory verification," Proc. SPIE **2029**, 1993.

11. L. Sica, "Sheared beam imaging: an evaluation of its optical compensation of thick atmospheric turbulence," submitted to App. Opt., 1995.
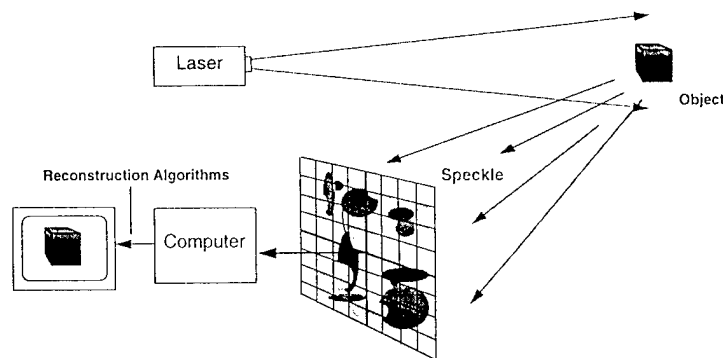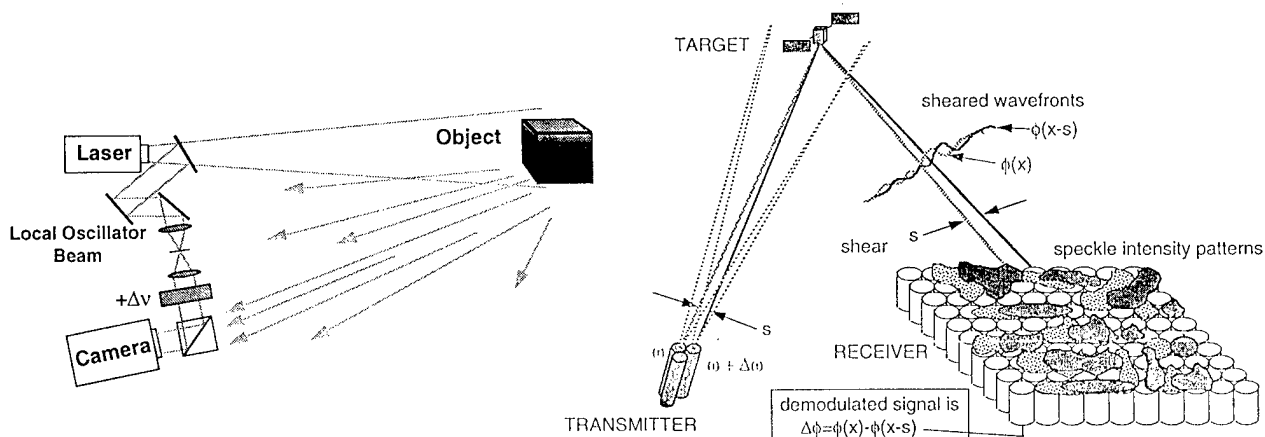
Fig. 1. Sampled-aperture laser imaging system.

Fig. 2 Heterodyne laser imaging system.　　Fig. 3 Sheared Coherent Imaging Photography.

Synthetic Aperture Holography for Three Dimensional Incoherent Imaging

Joseph Rosen and Amnon Yariv
California Institute of Technology, m/s 128-95
Pasadena, CA 91125
Tel: 818-395 4823   Fax: 818-405 0928   Email: Rosen@seqaxp.caltech.edu

The Michelson stellar interferometer (MSI)[1] is used for measuring the shape of planar objects which emit quasi-monochromatic, spatially incoherent light. Its principle of operation is based on measuring interference patterns obtained by two pinholes of the Young experiment. The fringes' visibility, and phase, versus the gap between the pinholes is equal to the complex degree of coherence. According to Van Cittert-Zernike theorem, the complex degree of coherence is proportional to the Fourier transform of the source's intensity distribution[1]. Thus, measuring the complex degree of coherence versus pinholes separation and performing inverse Fourier transform yield the image distribution of the source.

In this Letter we examine the problem of three dimensional (3-D) imaging by the MSI. Based on the general 3-D paraxial theorem of the spatial coherence we propose a method to measure the 3-D information of source objects, and discuss the measurement limitations. We show that the MSI output result is equivalent to a Fourier hologram containing the information on the object's 3-D intensity distribution.

A schematic diagram of the proposed MSI is shown in Fig. 1. We assume that the object is a quasimonochromatic spatially incoherent light source. This light source $I_s(x_s,y_s,z_s)$ illuminates from the far field two pinholes located in the coordinates system (x,y,z). Without loss of generality, we assume that the axis connecting the pinholes passes through the origin and z, z_s are on the same line. A point source, located a distance R_1 from one pinhole, and R_2 from the other pinhole, illuminates them by a spherical wave with a complex amplitude proportional to[1] $\exp(jkR_i)/R_i$, where $i = 1,2$, $k = 2\pi/\lambda$, and λ is the average wave length. From the pinholes, the light propagates through two equal paths to a lens. The upper and the lower pinholes illuminate the lens with spherical waves, resulting in two plane waves at the back focal plane at angles φ and $-\varphi$ to the lens's axis. When the contributions of all the incoherent source points are taken into account, the intensity distribution on the back focal plane is

$$I(y_o) = A^2 \iiint I_s(x_s,y_s,z_s)\left|\frac{1}{R_1}\exp[jk(R_1 + y_o\sin\varphi)] + \frac{1}{R_2}\exp[jk(R_2 - y_o\sin\varphi)]\right|^2 dx_s dy_s dz_s$$

$$\cong 2(A/R)^2 I_o\left[1 + |C(\bar{r}_1,\bar{r}_2)|\cos(ky_o\sin\varphi + \arg\{C\})\right], \tag{1}$$

where

$$C(\bar{r}_1,\bar{r}_2) = I_o^{-1}\iiint I_s(x_s,y_s,z_s)\exp[jk(R_1 - R_2)]dx_s dy_s dz_s , \tag{1a}$$

$I_o = \iiint I_s(x_s,y_s,z_s)dx_s dy_s dz_s$, $\bar{r}_i = (x_i,y_i,z_i)$ are the coordinates of the i-th pinhole, R is the distance between the origins of the coordinate systems (x,y,z) and (x_s,y_s,z_s), A is a complex constant and y_o is the coordinate of the back focal plane. we neglect the effect of the finite pinholes' aperture, assuming for simplicity that each of them is a mathematical point. Note that the angle φ is not necessarily dependent on the distance between the pinholes.

If R is much larger than any other distance in the system the difference (R_1-R_2) is approximated as

$$R_1 - R_2 = \left[(R+z_1 - z_s)^2 + (x_1 - x_s)^2 + (y_1 - y_s)^2\right]^{\frac{1}{2}} - \left[(R+z_2 - z_s)^2 + (x_2 - x_s)^2 + (y_2 - y_s)^2\right]^{\frac{1}{2}}$$

$$\cong \Psi + \alpha z_s - \bar{\beta} \cdot \bar{r}_{T,s} + \gamma |\bar{r}_{T,s}|^2 \ , \tag{2}$$

where

$$\alpha = \frac{|\Delta \bar{r}| \sin^2 \theta}{2R^2} \left(|\bar{r}_1 + \bar{r}_2| + \frac{2|\bar{r}_1||\bar{r}_2|\cos\theta}{R} \right), \quad \bar{\beta} = \frac{|\Delta \bar{r}| \sin\theta}{R}(\cos\phi, \sin\phi),$$

$$\gamma = \frac{|\Delta \bar{r}| \cos\theta}{2R^2}, \quad \bar{r}_{T,s} = (x_s, y_s), \quad \Delta \bar{r} = \bar{r}_1 - \bar{r}_2 \ ,$$

θ and ϕ are the polar and the azimutal angles of the coordinate systems (x,y,z) and Ψ is equal to all the terms in Eq. (2) which cannot be neglected, but are not dependent on x_s, y_s or z_s. Substituting Eq. (2) into Eq. (1a) yields

$$C(\bar{r}_1, \bar{r}_2) = I_o^{-1} \exp(jk\Psi)\iiint I_s(x_s, y_s, z_s) \exp\left[jk\left(\alpha z_s - \bar{\beta}\cdot\bar{r}_{T,s} + \gamma |\bar{r}_{T,s}|^2\right)\right] dx_s dy_s dz_s \ . \tag{3}$$

C is the complex visibility function of the interference grating $I(y_o)$, and the complex degree of coherence between the two pinholes. Eq. (3) is the generalization of the Van Cittert-Zernike theorem to the case of correlation between any two points at the paraxial zone illuminated by a 3-D source from the far field. We refer to it as the general 3-D paraxial theorem of the spatial coherence. Unlike a previous generalization[2] ours is valid only for the paraxial regime, and we consider the phase terms α and γ in Eq. (3) which were neglected in Ref. [2].

At this point we can analyze a MSI geometry which leads to a simplification of Eq. (3). If we take the pinholes' axis to be orthogonal to the z axis, and fix one pinhole at the origin, C becomes a function of the coordinates (x,y) of the other pinhole. In this case

$$C(x,y) = C_o \iiint I_s(x_s, y_s, z_s) \exp\left[\frac{j2\pi(x^2 + y^2)z_s}{2\lambda R^2} - \frac{j2\pi}{\lambda R}(xx_s + yy_s) \right] dx_s dy_s dz_s \ . \tag{4}$$

This complex degree of coherence is analogous to that describing a coherent diffraction in a spherical lens system[3]. Suppose a 3-D object with a shape equal to $I_s(x_s, y_s, z_s)$, located around the front focal plane of a lens with a focal length R. When this object is illuminated by a plane wave propagating along z, the complex amplitude diffracted from this object toward the back focal plane has a distribution proportional to $C(x,y)$ given by Eq. (4). Note that the physics is different in this case since this time both $I_s(x_s, y_s, z_s)$ and $C(x,y)$ indicate coherent field distributions. The complex field $C(x,y)$ in this case can be recorded in a 2-D hologram by interfering it with a second, coherent, plane wave at the recording plane. In our, incoherent, case the complex function $C(x,y)$ is recorded without any reference. The experimental recording of the complex function $C(x,y)$ can be accomplished as follows: The pinholes' plane of the MSI shown in Fig. 1 is arranged to be perpendicular to the z axis. One pinhole is fixed at the origin, while the other is moved in a Cartesian grid. At each pinhole position (x,y) a diffraction grating is generated in the MSI output. Only two parameters the visibility and phase are extracted from each grating, for each location of the moving pinhole. Completing the process along the full grid yields a sampled version of $C(x,y)$.

As mentioned above $C(x,y)$ is analogous to a coherent Fourier hologram, and based on this analogy we know that the incoherent source distribution can be reconstructed. Having $C(x,y)$ the reconstruction of the incoherent 3-D source is done by computing u_r given by

$$u_r(x_o, y_o, z_o) = \iint C(x,y) \exp\left[\frac{j2\pi(x^2+y^2)z_o}{2\lambda L_2^2}\right] \exp\left[\frac{j2\pi}{\lambda L_1}(xx_o + yy_o)\right] dxdy, \qquad (5)$$

where L_1, L_2 are the digital reconstruction constants. In case of an optical reconstruction $C(x,y)$ is displayed in the front focal plane of a lens with a focal length of f. It is straightforward to show that Eq. (5) describes the complex field distribution around the back focal plane ($z_o=0$) if $L_1=L_2=-f$, and u_r is multiplied by a linear phase factor of z_o which eliminated by any intensity detector.

The magnification of this imaging process is L_1/R in the transverse dimension and $(L_2/R)^2$ along the z axis. The minimum depth distance which can be resolved in this case is $\Delta z_{s,min} = 2\lambda R^2/r_{max}^2$, where $r_{max} = (x_{max}^2 + y_{max}^2)^{1/2}$ and (x_{max}, y_{max}) are the maximum distances in which the moving pinhole riches. On the other hand, the minimum planar distance which can be resolved in the target is $(\Delta x_{s,min}, \Delta y_{s,min}) = \lambda R(1/x_{max}, 1/y_{max})$. Assume the observed object is limited by a box with sides length of (X_S, Y_S, Z_S), the step size of the pinhole should be no large than $(\delta x_{max}, \delta y_{max}) = \lambda R^2 \left[(x_{max} Z_s + RX_s)^{-1}, (y_{max} Z_s + RY_s)^{-1}\right]$, in order to enter the whole object into the MSI's field of view.

As an example we take three words as our qusimonochromatic incoherent homogeneous light source. Each of the three words is positioned at a different location along the z axis. Each word is a collection of points source of spherical waves. Our simulation is completely based on Eq. (1), without any further approximation, and therefore the results are also used as a verification of Eq. (4).

We simulated the MSI operation with the parameters $R=10^5 m$, $\lambda = 10\,\mu m$, $(x_{max}, y_{max}) = (128,128)m$, $(X_s, Y_s, Z_s) = (0.6,0.2,14)m$, $(\delta x_{max}, \delta y_{max}) = (2,2)m$. The results are shown in Fig. 2. A partial collection of the output gratings from the MSI is shown in Fig. 2a . In our simulated MSI we assume that the gratings are all one dimensional, with the same frequency and orientation. The only important information contained in this collection of gratings is their visibility and phase. These two parameters are measured from each grating, and the resulting two dimensional visibility and phase distribution are shown in Fig. 2b and 2c, respectively. Each value (i,j) in this matrices indicates the visibility (phase) of the grating obtained when the moving pinhole is in the (i,j) location. Finally the reconstruction results in three planes along the z_o axis are shown in Figs. 2d,e,f. These results are obtained by calculating Eq. (5) for three different values of z_o. At each plane a different set of letters is focused, thus reconstruction of the object in the 3-D space is strictly possible.

In conclusion we have proposed and simulated a new method of synthetic aperture incoherent holography. By this method, we are able to measure the complex visibility function containing 3-D information of the incoherent source. This 3-D distribution can be reconstructed in the same sense of coherently recorded hologram. The system has synthetic aperture width equal to the double of the maximum separation between the pinholes, while the actual aperture is only the aperture of the two pinholes. This property gives to the proposed system an advantage over other methods of incoherently recorded holograms[4].

REFERENCES

1. M. Born and E. Wolf, Principles of Optics, 4th ed. (Pergamon Press) Chap. 10, p. 491 (1970).
2. W. H. Carter and E. Wolf, Optica Acta, 28, 227 (1981).
3. A. Yariv, Optical Electronics, 4th ed. (Saunders College Publishing) Appen. E, p. 705 (1991).
4. A. W. Lohmann, J. Opt. Soc. Am. 55, 1555 (1965). G. Sirat and D. Psaltis, Opt. Lett. 10, 4 (1985).
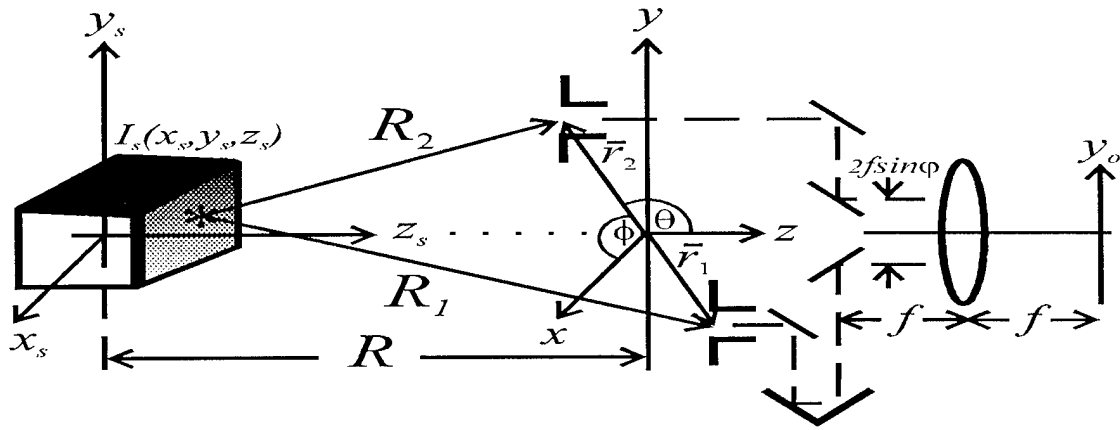
Figure 1.   Schematic system of the MSI for 3-D imaging.

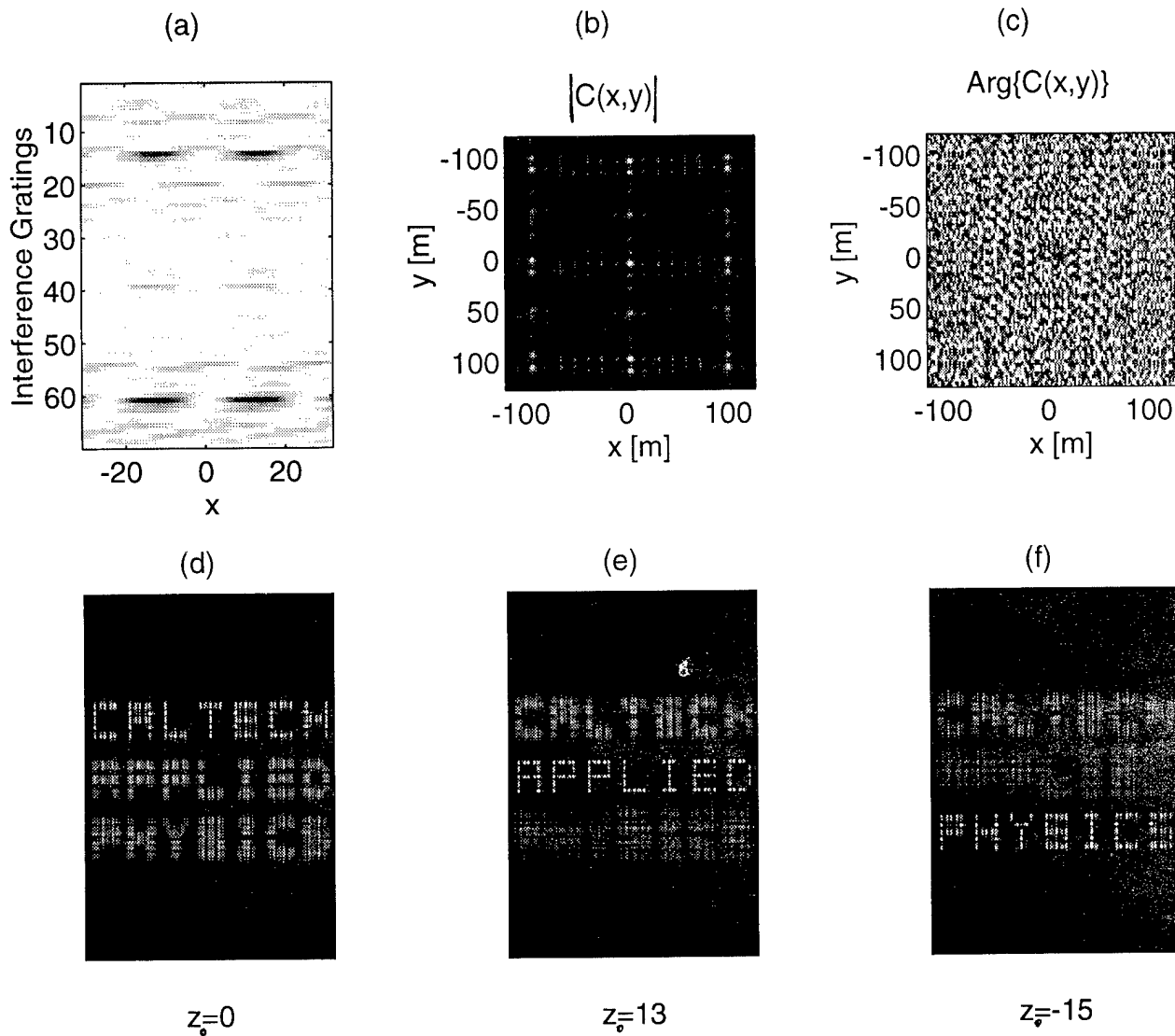Figure 2.   (a) Computer-simulation of the partial collection (64) of the MSI output interference gratings. (b-c) The two dimensional visibility function, magnitude (b) and phase (c), calculated from all the interference gratings of 2.a. (d-f) The reconstruction of the hologram shown in 2.b.c at three different planes along the z axis. In each plane only one word is in focus, indicating its original location in the object space.

In-Line Acousto-Optic Architectures for Holographic Interferometry and Sensing

Nabeel A. Riza
Center for Research & Education in Optics and Lasers (CREOL)
and the Department of Electrical & Computer Engineering
University of Central Florida
4000 Central Florida Boulevard, P. O. Box 162700, Rm 280, Orlando, FL 32816-2700
email: riza@creol.ucf.edu; Tel: 407-823-6829, Fax: 407-823-6880

1. Introduction

Novel two Bragg cell and one Bragg cell acousto-optic (AO) interferometers are introduced in this paper. These interferometers can be used as a variety of optical instruments such as holographic interferometers, interferometric sensors, material characterization tools, and diagnostic measurement systems such as turbulence and flow/temperature assessment. To this date, to the best of the author's knowledge, no such optical systems have been proposed for interferometric sensing and measurement tools that offer high optical power (e.g., 1 W CW), high speed scanning (e.g., < 50 μs per scan spot) interferometer systems with both heterodyning and almost baseband options for accurate diagnostic measurements. The bulk optics nature of our optical system design allows for high optical power interferometric applications.
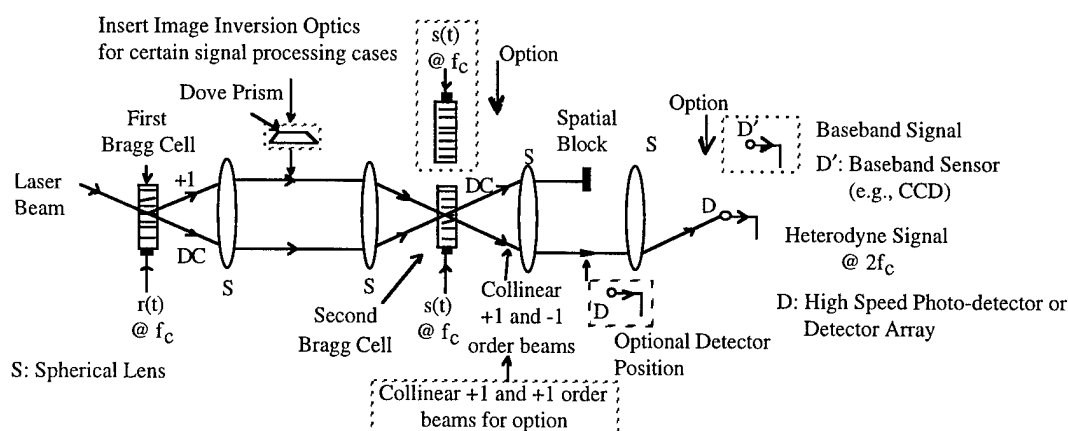
Previously, two significant Bragg cell-based optical interferometers have been developed mainly for optical signal processing applications. These are the Mach-Zehnder AO interferometer [1], and the in-line Koester prism AO interferometer [2]. Although the in-line Koester prism design offers much improved mechanical and vibrational stability than the Mach-Zehnder AO interferometer design, there still remain key sources of optical phase instabilities due to the use of independent Koester prism components for the optical beam splitting and beam combining operations. Over the last several years, the author has developed and experimentally demonstrated a compact, heterodyne and baseband type, optical interferometer architecture for a host of photonic information processing applications such as phased array antenna/radar control [3-9] and radio frequency (rf) signal correlation [10,11], convolution [12], notch filtering [13], and spectrum analysis operations [14]. This interferometric architecture is shown in Fig.1 above, and consists of two AO devices or Bragg cells in an in-line configuration, where the first Bragg cell acts as an optical beam splitter and the second Bragg cell acts as an optical beam combiner. Thus, using only four optical components (two Bragg cells and two lenses), all in the path of the interfering optical beams, one is able to realize a compact, low component count interferometer. Compared to the Mach-Zehnder and Koester prism AO interferometers, no separate optical beam splitters and beam combiners are required; the AO cells inherently take care of these operations. Thus, the basic interferometer shown in Fig.1 has an important property that is desirable for all optical interferometers; namely, excellent mechanical stability and tolerance to optical phase instabilities via the almost common-path in-line design. Notice that the system is perfectly collinear, except between the two Bragg cells where the two interfering beams are physically separated, although, still in-line and in close proximity (e.g., 1 cm). Thus, any thermal, mechanical, or air turbulence effects impinging on this instrument are suffered almost exactly by both interfering beams on the photo-detector. In fact, the heterodyne detection operation via optical mixing at the photodiode results in the cancellation of this phase noise. Furthermore, our AO interferometer makes efficient use of the undiffracted light, making a higher power efficiency instrument. Thus, the basic "Riza interferometer" architecture (see Fig.1), as coined by fellow researchers in the field, has recently been used by both industry

(Photonic Systems Inc., Melbourne, FL, [15]) and government (USAF Rome Labs, [16-19]) optical engineers to build advanced signal processing systems requiring high phase stability optical interferometric processing. In this paper, we show how the basic interferometer architecture in Fig.1 can be modified and used to form useful interferometric diagnostic and measurement tools [20].

2. Proposed In-line Scanning AO Interferometers

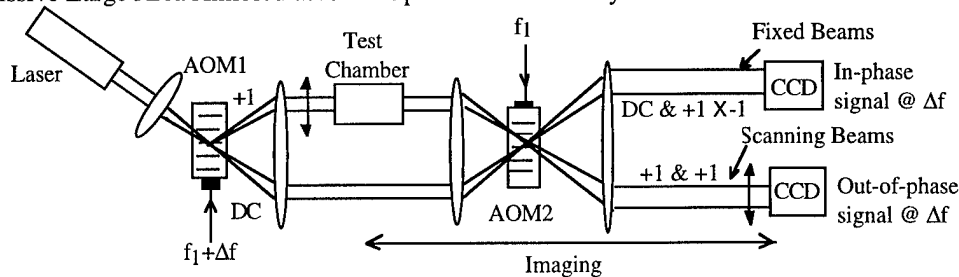### 2.1 Transmissive Large Area Almost Baseband Optical Interferometry

Fig.2 above shows an interferometer set-up for transmissive almost baseband optical interferometry using a slow speed photosensor such as a charge coupled device (CCD). Note the large circular cross-section probe/test beam area. This system generates an interferogram that is on a slowly varying (e.g., $\Delta f=1$ Hz) temporal carrier that is required for gathering complete test medium phase data. This system uses AO modulators (AOMs) versus AO deflectors (AODs) to generate the large test area for placing the test medium. The output sensors can also be holographic storage mediums such as photorefractive crystals and thin-films or any other sensing medium. Note that, if required, fast spatial carriers in these interferometers can be generated using beam deflection optics such as tilt prisms or nematic liquid crystal (NLC) deflectors [21] in one of the optical beam paths between the AOMs.

2.2 Reflective Almost Baseband Optical Interferometry

HWP: Half-Wave Plate
QWP: Quarter-Wave Plate
P: Polarizer at 45 deg. to s and p directions
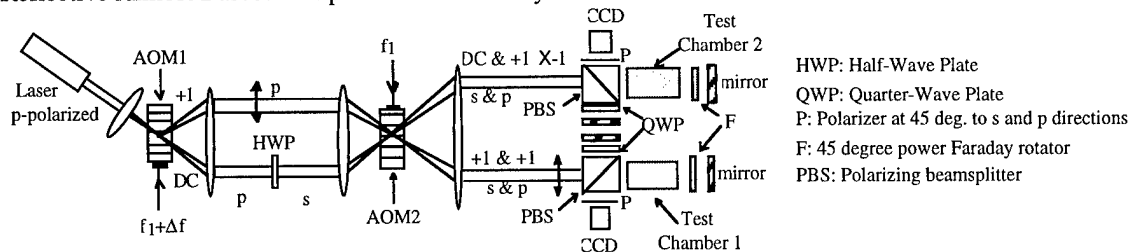F: 45 degree power Faraday rotator
PBS: Polarizing beamsplitter

Fig.3 above shows the interferometer set-up for reflective almost baseband optical interferometry with large circular cross-section probe/test beams. Note the use of polarization optics to separate the signal and reference beams. The detailed workings of this and other interferometers to follow are quite similar to the basic one in Fig.1, and so are self explanatory, and will not be dealt with in detail in this paper.

2.3 Reflective Heterodyne Optical Interferometry on a High Frequency Intermediate Frequency (IF)

HWP: Half-Wave Plate
QWP: Quarter-Wave Plate
P: Polarizer at 45 deg. to s and p directions
F: 45 degree power Faraday rotator
PBS: Polarizing beamsplitter

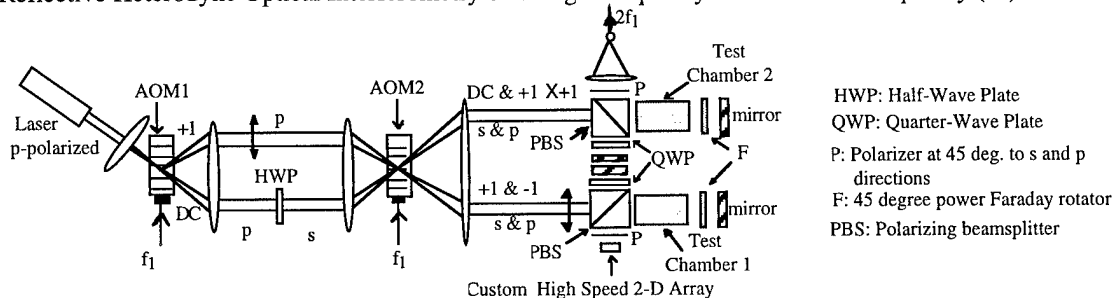Fig.4 above shows an interferometer set-up for reflective optical interferometry with high frequency (e.g., 120 MHz) IF outputs and large circular cross-section probe/test beams. One output setup is using the scanned beams with a high speed large area 2-D detector array, while the other output set-up is using a fixed high speed point detector with beams that stay stationary even when the AOM frequency is changed to do scanning.

2.4 High Speed Line/Point Scanning (x-direction) Transmissive Heterodyne Optical Interferometry on Large IFs
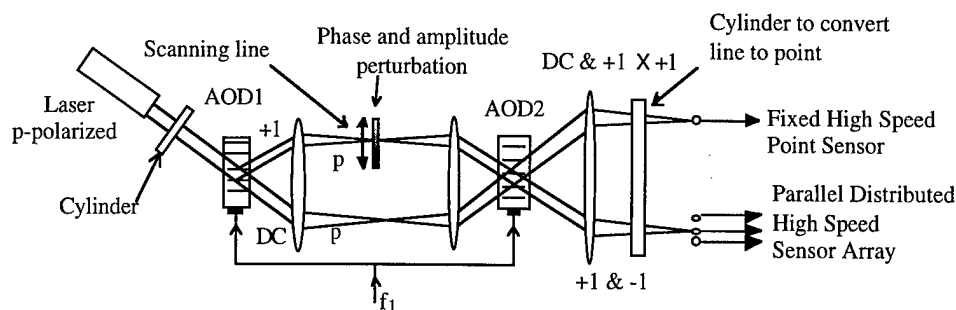

Fig.5 above shows the interferometer set-up for transmissive optical interferometry with high frequency IF outputs and a point/line scanning probe/test beam. The output set-up is using a fixed high speed point detector with beams that stay stationary even when the AOD frequency is changed to do scanning. Without the two cylinders, the collimated input laser beam gives a scanning point beam on the sampling zone. Complex optical information can be read using the line scanned system if the fixed high speed point sensor is replaced by a vertical (in paper) linear array of high speed point sensors. In this case, the last cylinder must be removed.

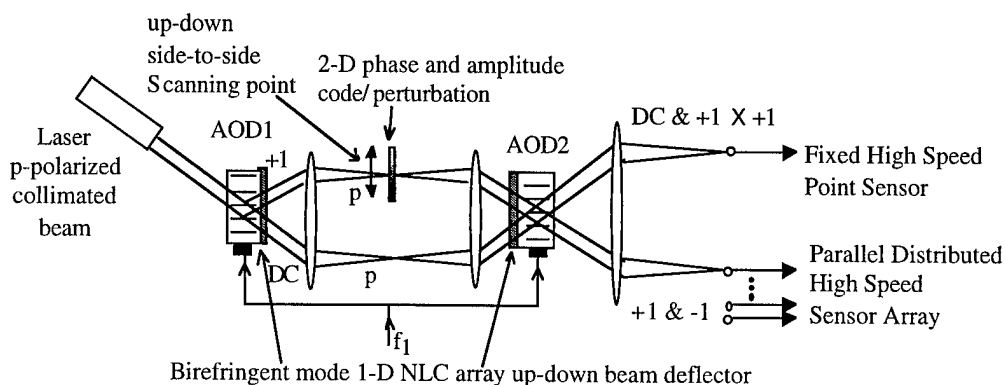2.5 High Speed x-y Point Scanning Transmissive Heterodyne Optical Interferometry on Large IFs

Fig.6 above shows the interferometer set-up for transmissive optical interferometry with IF outputs and a point scanning probe/test beam. The output set-up is using a fixed high speed point detector with beams that stay stationary even when the AOD frequency is changed to do scanning. The collimated input laser beam gives a scanning point beam on the 2-D test zone. 2-D amplitude/phase information can be read using the point scanned system using AODs and NLC deflectors.

2.6 Reflective Heterodyne Optical Interferometry using a Single Bragg Cell
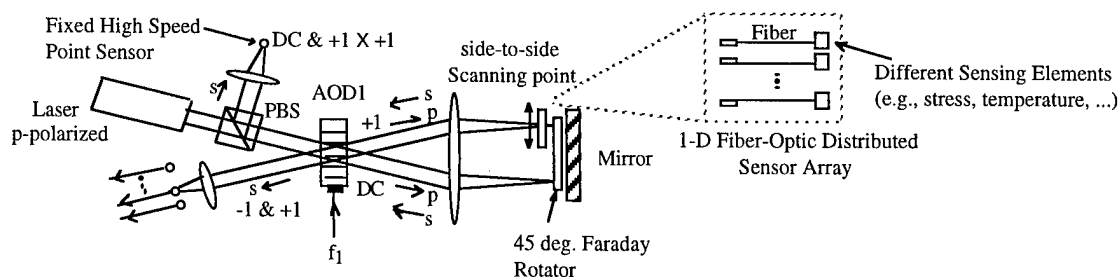
Fig.7 above shows how a single Bragg cell can be used to form a reflection-type interferometer. In this case, a point scans in 1-D, so a 1-D phase/amplitude test medium can be read. The scanning ability via Bragg cells and NLC devices allows these systems to act as spatially distributed optical point sensors via the use of fiber-optic probes, where the instrument can monitor any of the desired fiber-optic probes in a time-multiplexed fashion using just one

point detector. If simultaneous sensor detection is required, the same system can do it using an array of point detectors, as shown in Fig.7.

3. Conclusion

Advantages of our proposed interferometers include high mechanical stability, high speed optical scanning, low system noise via the IF heterodyne detection option, and both reflective and transmissive system options. These interferometers can be used for several applications such as holographic recording and retrieval, shock wave and turbulence flow measurements, thin film/surface characterization, material optical birefringence measurements, free-space optical and fiber-optic remote sensing. Furthermore, these interferometers have high optical power (> 100 mW) tolerance, and both CW and high peak power pulsed sources can be used as the light input. Future work relates to the experimental demonstration of these systems, and a discussion on system limitations such as scan area size, scan speed, overall system size, etc.

4. References

[1] A. Vander Lugt, "Interferometric spectrum analyzer," Applied Optics, Vol.20, No.16, pp.2770-2779, 1981.

[2] M. D. Koontz, "Miniature interferometric spectrum analyzer," in Optical Information Processing II, Proc. Soc. Photo-Opt. Instrum. Eng. 639, pp.126-130, 1986.

[3] N. A. Riza, "Novel acousto-optic systems for spectrum analysis and phased array radar signal processing," Ph.D dissertation, (California Institute of Technology, Pasadena, Calif., 1989) in *University Micofilms*, Ann Arbor, MI.

[4] N. A. Riza, "Acousto-optic architectures for multi-dimensional phased array antenna processing," *Opt. Technol. Microwave Appl. Conference SPIE Proceedings*, Vol. 1476, pp.144-156, 1991.

[5] N. A. Riza and D. Psaltis, "Acousto-optic signal processors for transmission and reception of phased array antenna signals," *Applied Optics*, vol.30, no.23, pp.3294-3303, 1991.

[6] N. A. Riza, "A compact high performance optical control system for phased array radars," *IEEE Photonics Tech. Lett.*, Vol.4, No.9, pp.1073-1076, Sept., 1992.

[7] N. A. Riza, "An acousto-optic phased array antenna beamformer for multiple simultaneous beam generation," *IEEE Photonics Tech. Lett.*, Vol.4, No.7, pp.807-809, July, 1992.

[8] N. A. Riza, "Liquid crystal-based optical control of phased array antennas," *IEEE /OSA Journal of Lightwave Tech.*, Vol.10, No.12, pp. 1974-1984, Dec., 1992.

[9] N. A. Riza, "Acousto-optic liquid crystal analog beamfomer for phased array antennas,"*Applied Optics*, Vol. 33, No.17, pp.3712-3724, June 10, 1994.

[10] N.A. Riza, "The in-line acoustooptic interferometer as a correlator and spectrum analyzer," *SPIE Conf. on Optical Implementation of Information Processing*, Vol. 2026, pp.130-141, 1993.

[11] N. A. Riza, "In-line interferometric time integrating acoustooptic correlator,"*Applied Optics*, Vol.33, No.14, pp.3060-3069, May 10, 1994.

[12] N. A. Riza, "Space Integrating Interferometric Acousto-optic Convolver," *IEEE Photonic Technology Letters*, Vol.7, No.3, pp. 339-341, 1995.

[13] N. A. Riza, "Novel space/time integrating acoustooptic architectures for radar signal processing," SPIE Proc. Vol. 2155, Jan., 1994.

[14] N. A. Riza, "Optically efficient interferometric acousto-optic architecture for spectrum analysis," *Applied Optics*, Vol.31, No.17, pp.3194-3196, June 10, 1992.

[15] P. A. Wasilousky, D. R. Pape, J. A. Carter III, T. A. Sunderlin, "Optoelectronic radar receiver for real-time radar imaging," SPIE Proc. Vol. 2562, No.05, July, 1995.

[16] C. W. Keefer and M. J. Ward, "Modified interferometric in-line time integrating correlator," SPIE Proc. Vol. 2026, pp., July, 1993.

[17] C. W. Keefer, M. E. Turbyfill, and H. G. Andrews II, "Multichannel acousto-optic correlator for time delay computation," SPIE Proc. Vol. 2240, pp.64-74, April, 1994.

[18] H. G. Andrews II, M. E. Turbyfill, and C. W. Keefer, "Anti-jamming optical beamforming systems," SPIE Proc. Vol. 2216, pp.58-66, April, 1994.

[19] J. M. Lutsko, M. E. Turbyfill, E. K. Walge, and H. G. Andrews II, "Multichannel in-line time integrating correlator and its applications," SPIE Proc. Vol. 2481, pp.153-159, April, 1995.

[20] N. A. Riza, Patent Disclosure.

[21] N. A. Riza and M. C. DeJule, "Novel three terminal adaptive nematic liquid crystal lens device," *Optics Letters*, Vol. 19, No. 14, pp. 1013-1015, July 15, 1994.

Holographic Memories

HMB 10:30 am-12:00 m
Hampton A/B

Yeshayahu Fainman, *Presider*
University of California, San Diego

Holographic Memories

Demetri Psaltis
California Institute of Technology

Summary not available.

High-Speed Holographic Recording of 500 Images in Hole Burning Rare-Earth Doped Crystals

R. Kachru and X. A. Shen
Molecular Physics Laboratory
SRI International
333 Ravenswood Avenue
Menlo Park, CA 94025
Phone: (415) 859-3727 / Fax: (415) 859-6196

One of the unique and perhaps the most attractive features of an optical memory is its ability to store and retrieve information in a bit-parallel format.[1-3] Recently, we have proposed a new scheme for parallel data storage in TDOM.[4,5] This scheme was proven to be practical and can be implemented with existing technologies. In a proof-of-principle experiment, four wavelength-multiplexed single-page volume spectral holograms, generated with black-and-white transparencies, were successfully stored in a single spatial location at a speed of approximately 23 μs/frame. The experimental results project system's input/output bandwidth to exceed 40 Gbps, two orders of magnitude faster than a semiconductor cache memory.

Here, we report on the use of the proposed scheme to demonstrate the storage of a large number of spectral holograms. A schematic of the experimental setup for demonstrating the storage and retrieval of volume spectral holograms is shown in Fig. 1. The experiments were performed on the $^7F_0$-$^5D_0$ transition (site 1 at 579.88 nm) of Eu^{3+}:Y_2SiO_5. This transition has an inhomogeneous linewidth of ~4 GHz and a dephasing time of ~1 ms. Recording and playback were controlled entirely by a computer. During the recording, the computer first tuned the laser to a desired wavelength (or data channel) within the inhomogeneously broaden absorption line, downloaded a pre-selected frame to an SLM through a frame grabber for information encoding, and then illuminated the sample with the reference (also known as the write pulse) and data pulses. This procedure was repeated a different channel until all 500 images were stored. The data were later retrieved by illuminating each channel with a read pulse, and the reconstructed images were detected by a gated intensified CCD camera and digitized by the frame grabber.
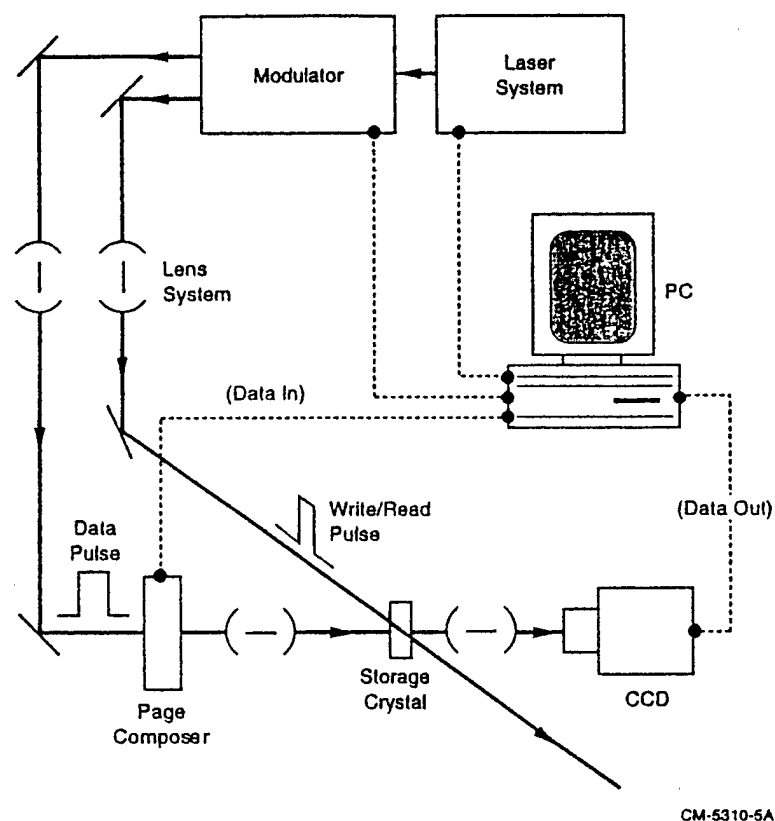
CM-5310-5A

Figure 1. A schematic of experimental setup for demonstrating the storage of 500 wavelength-multiplexed spectral holograms.

Five minutes after the completion of the recording, we retrieved the data by illuminating each spectral grating with a read pulse that was identical to the reference pulse used in the recording. All 500 stored images were retrieved faithfully and 6 sample echo images are shown in Fig. 2. We have used three retrieval schemes, forward, reverse and random retrievals at a speed of 30 fps, and found no noticeable cross talk between adjacent images. The experiments also show that the echo efficiency, which was measured to be $\sim 10^{-3}$, remained unchanged from channel to channel, independent of the retrieval methods used. In the case of random retrieval, we found that each data channel can be read more than 10 times with a good signal-to-noise ratio, consistent with the experimental results obtained with slides.[5] The achieved frame rate, although slower than 13.5 Kfps estimated from the single page recording time, is to our knowledge the fastest recording speed demonstrated for any optical storage technique.
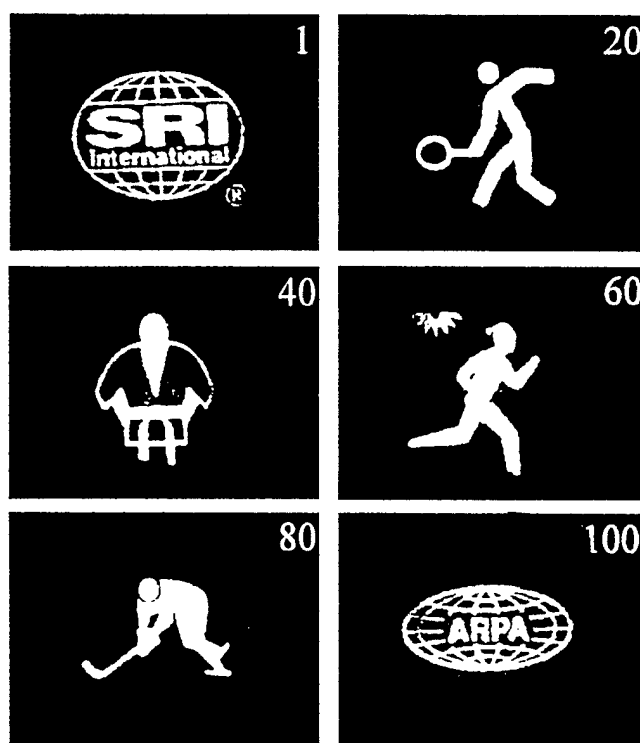
Figure 2. Experimental results showing 6 sample images retrieved from TDOM.

Our results, suggest a minimum storage capacity of 10,000 frames per spatial spot (or 5,000 frames per optical site) for $Eu^{3+}:Y_2SiO_5$. For a frame containing 500×500 bits (obtained, for example, by using 2×2 pixels to represent an information bit in an array of 1000×1000 pixels), the projected storage capacity would be approximately 2.5 Gbits per spot, or ~360 Gb/cm^3 (Take into account the spot size of ~1.0 mm $\times$ 1.0 mm $\times$ 7.0mm used in the experiment.[5]).

ACKNOWLEDGMENTS

REFERENCES

1. F. H. Mok, M.C. Tackitt, and H. M. Stoll, Opt. Lett. **16**, 605 (1991); F. H. Mok, Opt. Lett. **18**, 951 (1993).

2. B. Kohler, S. Bernet, A. Renn, and U. P. Wild, Opt. Lett. **18**, 2144 (1993).

3. J. F. Heanue, M. C. Bashaw, and L. Hesselink, Science **265**, 749 (1994).

4. Y. S. Bai and R. Kachru, Opt. Lett. **18**, 1189 (1993).

5. X. A. Shen, E. Chiang, and R. Kachru, Opt. Lett. **19**, 1246 (1994).

A technique for control of crosstalk noise in volume holography

Mark McDonald and Mark A. Neifeld

Electrical and Computer Engineering Department
Optical Sciences Center
University of Arizona
Tucson, AZ 85721
(V) (520) 621-3317
(F) (520) 621-8076

Volume holographic data storage offers many potential advantages over conventional magnetic mass storage including high parallelism, fast access, and high storage capacity. The high capacity of volume holography is partially attributable to the Bragg selectivity of thick media. For angularly multiplexed uniform gratings in media of finite thickness the Bragg diffraction efficiency has a well known $\text{sinc}^2(\vartheta)$ dependence $vs.$ dephasing ($i.e.$, dephasing $\vartheta \propto \Delta\theta$ reconstruction angle for angular multiplexing). When a desired hologram is read out at a particular reconstruction angle, holograms stored at other angles will also be reconstructed, albeit with much lower efficiency. The superposition of the undesired reconstructions is known as crosstalk and this phenomenon has been investigated by several authors[1,2]. Such crosstalk will result in noise on the data detected from the desired hologram and can be diminished by reducing the density of the angular multiplexing[2]. Thus, crosstalk forms an upper bound on volume holographic memory density and capacity in the limit of small fixed noise sources. In this paper, we will consider the storage capacity limit imposed by crosstalk for a grating that is uniform throughout the finite medium and compare this with the limit obtained when the grating is apodized to reduce crosstalk. We will also show experimental verification of the apodization effect.

The properties of a volume grating with finite extent can be examined by decomposing the grating into its Fourier components. When the grating modulation depth is uniform over its finite length we find the traditional $\text{sinc}^2(\gamma\Delta\theta)$ behavior in diffraction efficiency $vs.$ reconstruction angle, where γ is a system dependant proportionality constant. Such behavior is commonly seen in practice and in figure 1 we show diffraction efficiency η $vs.$ Bragg mismatch for an experimentally stored uniform grating (dotted curve). This figure displays the expected $\text{sinc}^2(\gamma\Delta\theta)$ form; however, in the experiment small errors with respect to uniform grating strength ($e.g.$ absorption) result in the imperfect nulls. The square root of the diffraction efficiency corresponding to the electric field diffraction efficiency, is more relevant to crosstalk and a significant feature of such a $\text{sinc}(\gamma\Delta\theta)$ distribution is its slow decay envelope and infinite variance. As a result, electric field crosstalk from widely spaced holograms can contribute. A second significant feature of the $\text{sinc}(\gamma\Delta\theta)$ function is its nulls. Neighboring holograms placed exactly on these angular nulls produce no crosstalk. Unfortunately, this ideal can be achieved only with storage of plane wave objects. When an object contains an angular range of plane waves ($e.g.$, an extended object in Fourier plane storage) all but one of these plane wave components will fail to be stored on a null and thus produce crosstalk.

Previous analysis has used a Crosstalk to Signal ratio (XSR) metric introduced by Gu, $et\ al.$, and Heanue, $et\ al.$ [1,2]

$$XSR = \frac{\left| \left\langle \left| \sum_j X_{cj} a_j \right|^2 \right\rangle - \left\langle |a_c|^2 \right\rangle \right|}{\left\langle |a_c|^2 \right\rangle}, \quad (1)$$

where the a_j are the stored data on the jth page and the electric field diffraction efficiency from page j to the desired page c is X_{cj}. This metric gauges the mean increase in power delivered to on and off levels. Gu, et. al. observed that XSR increases toward the edge of any object and reaches a peak for the object stored near the maximum reference angle ($\sim$0.9$\times$Mmax) and studied crosstalk under these worst case assumptions. This XSR finds the average impact of crosstalk but overlooks the variance in crosstalk power which must be known in order to evaluate the crosstalk noise to signal ratio (NSR)

$$NSR = \frac{\sqrt{\sigma_1^2 + \sigma_0^2}}{\mu_1 - \mu_0}, \quad (2)$$

where μ_i and σ_i^2 are the means and variances of the on (i = 1) and off (i = 0) levels. An exact determination of crosstalk is in principle possible; however, we choose to regard the data stored in the memory as random. Analysis of the sum of the many small crosstalk contributions parallels the analysis of speckle and can be found in standard texts[3]. We find from the probability density functions for the 0 level and the 1 level that expressions for the means and the standard deviations are monotonic functions of the Gu XSR. Thus, we observe that the NSR will be a maximum when XSR is a maximum; however, the NSR rises more sharply with Mmax than the XSR. In this paper we simulate the performance of a volume holographic memory containing random data pages and form estimates for the relevant means, variances, and corresponding NSR. Since we retain all terms in the crosstalk noise, we can extend the analysis of crosstalk to include modifications to the finite, uniform grating such as those arising from absorption and/or apodization.

In the simulation model we store data pages of 2.5° extent as Fourier transform holograms in a 50 mm length medium which suffers an 18% intensity absorption. The solid line with open squares in figure 2 shows the result for XSR vs. Mmax where the number of stored patterns is N=2$\times$Mmax+1 and the holograms are stored on adjacent diffraction efficiency minima. The worst case XSR (Mmax=10,000) shows values of less than 1%. This would seem to indicate an acceptable level of performance in most data storage applications; however, the NSR curve (filled □, dashed line) exhibits 50 to 100 times higher values when variance is included, reaching potentially unacceptable values of nearly 10%. A traditional remedy for reducing crosstalk is to space the data pages (i.e., holograms) farther apart on integer multiples of the first minima of the η vs. $\Delta\theta$ curves[2]. The impact of this diminished angular density is shown in figure 2 with holograms stored on the second nulls (◇) and third nulls (○) for both XSR (solid lines) and NSR (dashed lines). Reducing the angular storage density does reduce crosstalk; however, the NSR still remains at levels of 0.05 even when spaced on every third null. Given the marginal improvement in reducing the angular density from 1/2 to 1/3, further reduction in NSR appears limited with this method.

Altering the spatial modulation depth envelope of the hologram can result in improvements in system performance. This principle of apodization is exploited in optical disk memory and is common in signal

processing[4]. A variant of grating apodization for a single, limiting case was recently proposed and examined in simulation for its impact on XSR[5]. The choice of apodization is itself a broad subject and we confine our discussion to a particular form having merit in the consideration of crosstalk. The apodization should vanish smoothly at the edge of the crystal to minimize ringing in its Bragg selectivity (*i.e.*, the square of the Fourier transform of the modulation depth envelope). A simple function satisfying this goal is an apodization of the grating strength which decreases linearly in the crystal from a central peak to zero at its edges. The electric field Bragg selectivity of such a triangular grating envelope function is given by its Fourier spectrum as $\text{sinc}^2(\gamma\Delta\theta)$ and its intensity diffraction efficiency would therefore be $\eta \propto \text{sinc}^4(\gamma\Delta\theta)$. Figure 1 depicts an experimental reconstruction showing the $\sim\text{sinc}^4(\gamma\Delta\theta)$ dependence (solid curve). The value of $\text{sinc}^4(\gamma\Delta\theta)$ is far lower than that of $\text{sinc}^2(\gamma\Delta\theta)$ in the vicinity of a null thus decreasing crosstalk when finite tolerances are allowed. There exists a storage density cost associated with this triangular apodization. The triangular grating envelope can be regarded mathematically as the convolution of two rectangular grating envelopes each 1/2 the length of the crystal. Thus the Fourier spectrum of the triangular envelope is broadened 2× with respect to the Fourier spectrum of a rectangular grating strength envelope of width equal to the entire crystal length. This broadening in Bragg sensitivity is evident in figure 1 as the central peak of the $\text{sinc}^4(\gamma\Delta\theta)$ is broadened in angle by $\sim$2× with respect to that of the $\text{sinc}^2(\gamma\Delta\theta)$ shown. While this appears to halve the memory capacity the actual result is an increase in storage density when a target crosstalk NSR must be achieved. The lines with filled triangles in figure 2 display the simulation results for NSR *vs.* Mmax for the $\text{sinc}^4(\gamma\Delta\theta)$ distribution. Both the XSR (open $\triangle$) and the NSR (filled $\triangle$) are substantially reduced with a $\text{sinc}^4(\gamma\Delta\theta)$ distribution; however, as the XSR underestimates the crosstalk noise, it also overestimates the performance improvement due to apodization. Still, the NSR is reduced to nearly 10^{-4}. From these results we may conclude that apodization can strongly suppress crosstalk noise permitting storage of a larger number of data pages and a higher memory capacity than is the case if uniform gratings are used.

We have experimentally produced volume holograms with programmable apodizations and Bragg selectivities. These experimental results support simulations that indicate significant increase in volume holographic storage capacity when intra-page crosstalk is the limiting noise source of the optical memory. In future work we will consider the apodization inherent in the supporting optical system, the crosstalk performance of more general apodizing functions, and the cost in peak diffraction efficiency associated with apodization.

References

1. C. Gu, J. Hong, I. McMichael, R. Saxena and F. Mok, "Cross-talk-limited storage capacity of volume holographic memory," JOSA A, 9, 1978-1983 (1992).

2. J. Heanue, M. Bashaw, and L. Hesselink, "Sparse selection of reference beams for wavelength- and angular-multiplexed volume holography," JOSA A, 12, 1671-6 (1995).

3. J. Goodman, Statistical Optics (Wiley, New York, 1985), chap. 2, p. 50-4.

4. J. Proakis, Digital Communications, 3rd ed., (McGraw-Hill, New York, 1995), chap. 9, p. 534-75.

5. C. Gu and F. Dai, "Cross-talk noise reduction in volume holographic storage with an extended recording reference," Optics Letters, **20**, 2336-8 (1995).

Figure 1
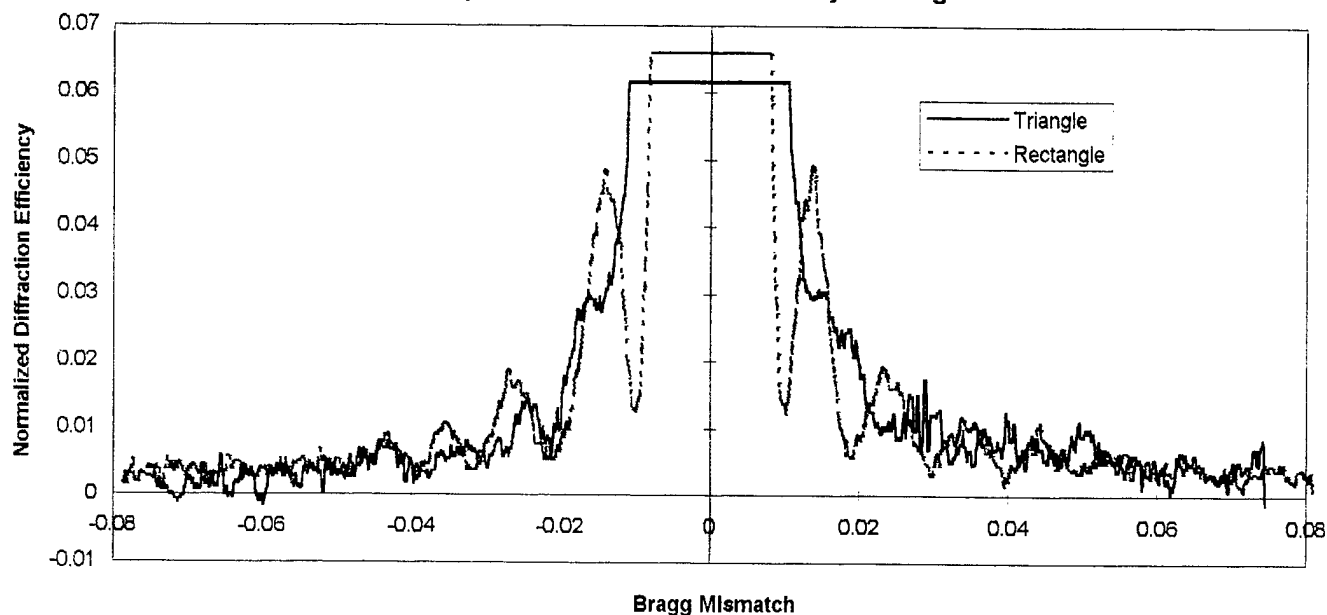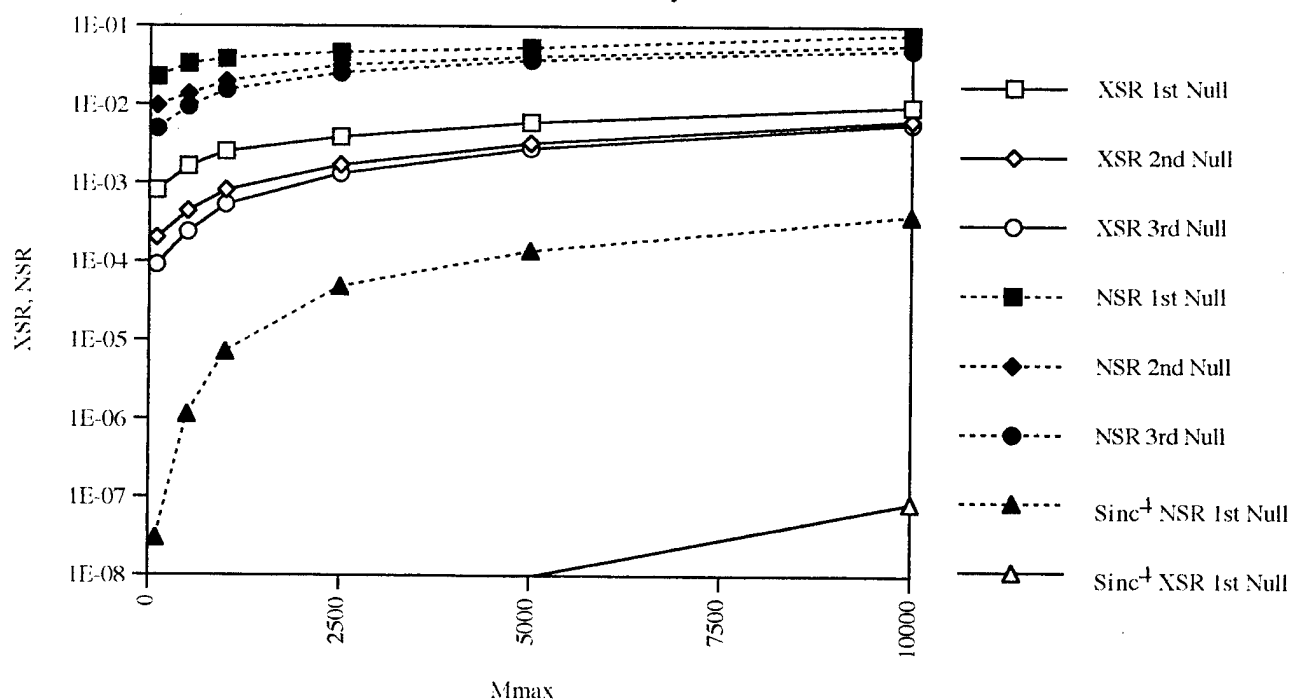### Apodized Diffraction Efficiency vs. Angle

Figure 2
Crosstalk Noise vs. Memory Size

Characterization of Volume Holographic Associative Searching

Keith G. Richling and Pericles A. Mitkas
*Optoelectronic Computing Systems Center and the
Department of Electrical Engineering
Colorado State University
Fort Collins, CO 80523
Phone: (970) 491-7481
Fax: (970) 491-2249*

1   Introduction

Volume holographic memories are a prime candidate for the storage of large relational databases because of their large storage capacities[1] and their associative nature[2,3]. We have successfully used a computer-controlled angular-multiplexing photorefractive-based volume holographic memory to store database records, search through the records, and recall the information stored in the memory. In this paper we present and discuss experimental results where the memory is accessed in its associative mode.

The associative mode gives us the ability to search the entire contents of the memory by presenting a search argument and receiving the location of the matching elements. As an example, if we assume that the records of Table 1 are stored in the memory with each row corresponding to a memory location and each column being a field, then we can search all the records by applying a search argument. In this example the first field contains the name of a state and the second contains a telephone area code for that state. If we applied the search argument given in Table 2, then we would receive an indication that memory element 5 contains the desired data, which is given in Table 3. Moreover, if we applied a search argument of Colorado, then we would receive information telling us that locations 3, 4, and 5 contain the information of interest, which are 303, 719, and 970.

State Name	Telephone Area Code
Arizona	520
Arizona	602
Colorado	303
Colorado	719
Colorado	970
Nebraska	308
Nebraska	402
Wyoming	307

Table 1. Example of Associative Searching: Database Records Stored in a Memory

	970

Table 2. Example of Associative Searching: The Search Argument

Colorado	970

Table 3. Example of Associative Searching: The Output

2 System

Figure 1 depicts the volume holographic database system (VHDS) that we use in our experiments. To record information we load the data into the spatial light modulator (SLM), create a unique reference angle through the reference beam generation arm, and then open shutters SH_1 and SH_2. After a predetermined time the shutters are closed, at which point the interference pattern of the two beams has been successfully recorded in the photorefractive crystal. This process is repeated until all the information has been stored. To recall this information we generate a unique reference angle, open shutter SH_1, and then capture the data on the camera CCD_1. This process can be repeated as needed. The most important aspect of this system, though, is its ability to search every record stored in the memory in a single step. To perform searching, we must first have multiple pages of data stored within the memory. With the data in place, we load the SLM with a search argument, open shutter SH_2, and capture an image of the reference beam that was used to record the data on the camera CCD_2. Using this image we can determine the angular "address" of the desired information. The search argument

that is presented to the VHDS can range in size from an entire page of data to just a small section of a page. This gives us the ability to search for a very specific record, or to search for multiple records that contain similar information.
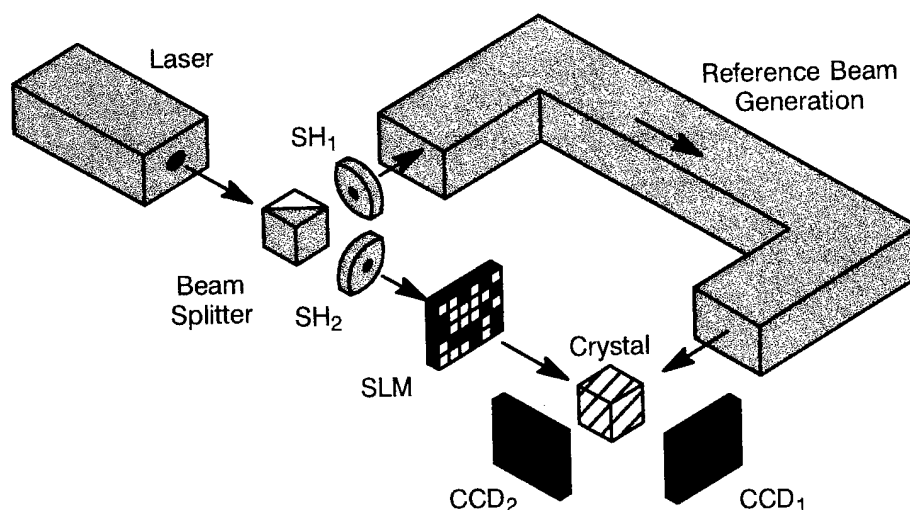

Figure 1. Volume Holographic Database System

3 Experimental Results

Experimental observation of the reconstruction of reference beams has given us insight into several properties of associative searching of a volume holographic memory. First is that reference beams can be reconstructed when even small search arguments are used. Second, multiple reference spots can be seen when the same information is contained within several different pages. Lastly, we observed how the size and position of the search argument affects reconstruction.

4 References

1. J. R. Wullert II and Y. Lu, "Limits of the Capacity and Density of Holographic Storage," *Applied Optics*, Vol. 33, No. 11, Apr. 10, 1994, pp. 2192–2196.

2. Y. Owechko, "Nonlinear Holographic Associative Memories," *IEEE Journal of Quantum Electronics*, Vol. 25, No. 3, Mar. 1989, pp. 619–634.

3. P. A. Mitkas and L. J. Iraklitos, "Three-Dimensional Optical Storage for Database Processing," *Optical Memory and Neural Networks*, Vol. 3, No. 2, 1994, pp. 217–229.

Some peculiarities of joint angular-spectral selectivity function of reflection holograms

Vladimir B. Markov, Anatolii I. Khizhnyak
Institute of Applied Optics
National Academy of Sciences - Centro Internacional de Fisica
10-G, Kudryavskaya St., Kiev, Ukraine - A.A. 49490, Bogota, Colombia
tel.(380-44) 212-21-58 - tel.(57-1) 368-15-17
fax.(380-44) 212-48-12 - tel.(57-1) 368-13-35

Introduction

Selective properties of 3D holograms have been the subject of investigation since early beginning of holography. It is mainly through the understanding of the information capacity of volume holograms and possibility to create high density storage systems [1-3]. No less of importance this feature of 3D holograms has for holographic displays, where the viewing zone of the image observation should be relatively wide [4].

It is well-known fact, that variations of the reconstructing wave vector value, affect not only the efficiency of the diffraction process [5], but also, due to selective properties of thick holographic grating, leads to the deterioration in the reconstructed image quality [6,7]. The problem of angular selectivity of thick holograms has been studied by several authors, but mainly for relatively small deviation of the incident wave vector from the Bragg conditions [5,8]. However, this is not true for the holographic displays, in particular, for reflection holography with white light reconstruction and very wide zone of observation (more then 120°).

In this report some results of the theoretical analysis and experimental study of joint function of angular-spectral selectivity of thick reflection gratings are presented. This function was first introduced by [9], in connection with analysis of selective properties of single layer full color holograms.

Theoretical analysis

The amplitude of the signal wave $S(z) = S_o \exp(-i\vec{\sigma}\vec{r})$, generated due to diffraction of the plane wave $R(r) = R_o \exp(-i\vec{\rho}\vec{r})$ on thick reflection grating can be found from standard coupled-wave approximation [5], since conditions of reconstruction allow to neglect by highest diffraction orders [8]. Here $\vec{\sigma}$ and $\vec{}$ are propagation vectors of the waves R and S, respectively. For correct analysis some restrictions should be imposed on the value of the angles of the incident Θ_R and reconstructed Θ_S beams. For these beams to be observed outside of the grating, their value should not exceed the value of the total internal reflection angle of the recording medium, i.e.: $\sin(\Theta_R)$; $\sin(\Theta_S) < 1/n_0$, where n_0 is refraction index of the recording medium.

If the standard procedure of the coupled-wave equations analysis is applied, the expression that describes the behavior of the diffracted wave has the form:

$$\frac{d^2 S}{dz^2} + i\bar{\Delta}\frac{dS}{dz} - \left(\frac{\pi v}{\lambda_R}\right)^2 \frac{S}{\beta_S \beta_R} = 0, \tag{1}$$

where $\overline{\Delta} = \dfrac{2\pi}{\lambda_R}(\dfrac{\lambda_R}{\Lambda}\beta_K - \beta_R - \beta_S)$, $\beta_R = \cos(\Theta_R)$, $\beta_S = \cos(\Theta_S)$, $\beta_K = \cos(\Theta_K)$ Λ is grating spacing; $|\overline{K}| = 2\pi/\Lambda$; $\nu = (^{2\pi}\!/_\lambda)\Delta n$, Δn is the amplitude of the refraction index n_0 modulation.

From Eq.(1) the expression for the diffraction efficiency η can be obtained in the form:

$$\eta(\lambda_R, \Theta_R) = \frac{|S|^2}{|R|^2} = \frac{\beta_R}{\beta_S} \cdot \frac{\left|\tanh\left[\sqrt{g}\,\xi\right]\right|^2}{\left|\,|g| + \Delta^2\right|\left|\tanh\left[\sqrt{g}\,\xi\right]\right|^2}, \tag{2}$$

here $\Delta = \dfrac{\lambda_R}{2\pi}\overline{\Delta}$, $g = 1 - \dfrac{\Delta^2\,\beta_S\,\beta_R}{\gamma^2}$, $\xi = \dfrac{\pi\,\gamma\,T}{\lambda_R\,\sqrt{\beta_S\,\beta_R}}$.

The expression (2) differs from traditionally referred for reflection grating [8]:

$$\eta(\delta\Theta,\ \delta\lambda) = \left\{ 1 - \frac{\left(1 - \xi^2\,/\,\nu^2\right)}{\sinh^2\!\left(\nu^2 - \xi^2\right)^{1/2}} \right\}^{-2}, \tag{3}$$

where $\xi_k = \dfrac{\delta\lambda}{\lambda}\left(\dfrac{2\pi n_0}{\lambda}\right)T\sin\Theta_R$ $\xi = f(\delta\Theta,\ \delta\lambda)$ is de-phasing factor, that depends upon angular $\delta\Theta$ or spectral $\delta\lambda$ deviation from the Bragg's conditions. The difference between Eq.(2) and Eq.(3) is because the arbitrary deviation of λ_R and Θ_R from Bragg conditions has been assumed in the first case.
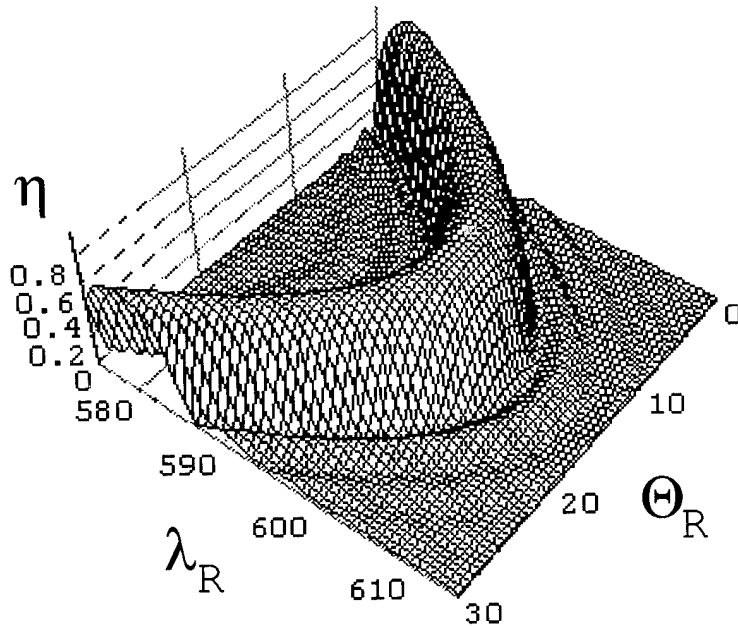

Fig. 1. Joint function of angular-spectral selectivity of phase reflection hologram (as calculated from Eq. 2)

Fig.1 demonstrates, calculated from Eq.1, typical behavior of the diffraction efficiency of thick phase reflection grating, when conditions of reconstruction strongly differs from those of Bragg. In this particular case, the assumed grating was identical to one, recorded at asymmetric geometry ($\Theta_R = 15°$ and $\Theta_S = 5°$, respectively) with wavelength $\lambda = 633$ nm. Its reconstruction is calculated for the case of wide-band ("white-light) illumination, which is the most common for reflection holographic displays. It follows from Fig.1 that through the combination of an angular tilt (in frame of angular selectivity) and spectral shift one can keep almost permanent value of the reconstructed signal in comparably wide diapason of the reconstructing angles.

Experimental technique, results and discussions

The PFG-03 and PFG-03c fine-grain silver-halide emulsions were used to record high efficiency phase gratings. The emission of the single frequency He-Ne laser (P=50 mW) has been used to record test gratings. The recording and processing techniques were similar to those described in [9,10], and allowed one to get phase reflection gratings with diffraction efficiency up to $\eta \approx 60\%$ at exposure ~ 2 mJ/cm^2.

The effects connected with angular and spectral selectivity of the phase reflection grating have been studied experimentally using specially modified SF-6 spectrophotometer. The angular divergence of the illuminating beam used to reconstruct the hologram was about $\delta\Theta_R \leq 1°$ and spectral resolution $\delta\lambda_R \approx 0.4$ nm. This level of $\delta\lambda_R$ is good enough, taking into account expected level of the spectral selectivity $\delta\lambda_\eta \leq 20$ nm of the holographic grating for used experimental geometry and layer thickness T = 8 mkm. The angular accuracy of holographic grating positioning in the measuring system was about $\Delta\theta \approx 20$ ang. min.

For experimental study of selective properties of 3D reflection gratings, the hologram was placed in the holder and tilted on angle that corresponds to recording geometry. The diffracted beam was fed into photocalorimeter to measure diffracted beam intensity I_S. The measured data, normalized against corresponding wavelength intensities in the reference channel, were used as the value of diffraction efficiency. By tuning reconstructing wave length λ_R and adjusting (turning out) the angular position Θ_R of the hologram the maximum value of diffracted signal $I_S(\lambda_R, \Theta_R)$ was measured.

Typical dependence of the diffraction efficiency behavior upon wavelength tuning and/or variations of the incident angle of the reconstructing beam is presented on Fig.2. It shows clearly that optimal level of the diffracted signal can be observed not only at the conditions, that correspond to those of the recording geometry, i.e. when $\delta\Theta_R = 0$ and $\lambda_R \approx 630$ nm (small shift toward the shortest wavelengths is due to emulsion shrinkage), but also for the shifted wavelengths. However, in this case the spatial position of the hologram and reconstructing source has to be changed.

It is also clear that whenever the hologram is reconstructed at the angle different from used at the recording geometry, the color of the holographic image will be tuned arbitrary in the directions of the shorter wavelengths. This comes from the requirement to satisfy the conditions of conservation between the wave vectors of interacting beams and that of grating, i.e. $\bar{p} + \bar{K} = \bar{\sigma}$. All these effects have to be taken into account when color image is reconstructed with reflection

holographic display. In fact, the above described effects can affect the reconstructed image quality, when such type of holographic display is observed (or illuminated) from the direction deviated from Bragg's conditions.
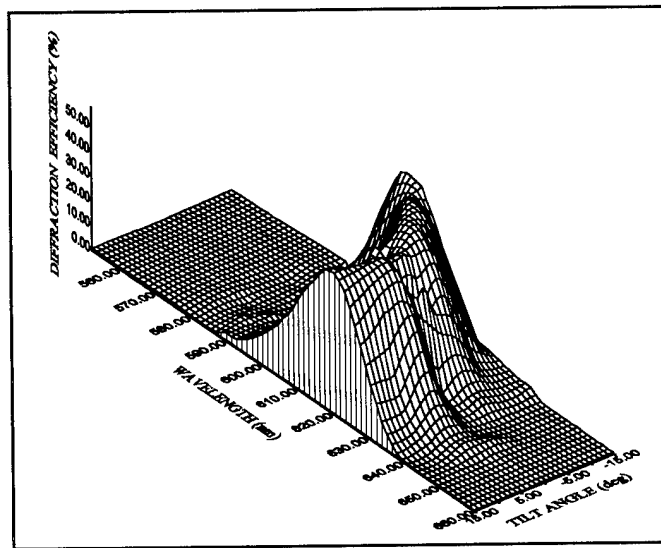

Fig. 2. Experimentally observed function of spectral/angular selectivity for reflection hologram

Conclusions

In this report the results of the theoretical analysis and experimental study of selective properties of thick reflection gratings are presented. It is shown that the character of joint function for angular-spectral selectivity, besides traditional for 3D grating parameters, like its period and thickness, also depends upon recording geometry and spectral bandwidth of the reconstructing light source. The obtained data are interesting for proper color reflection hologram recording and reconstruction.

Reference

1. P.J. van Heerden, *Appl. Opt.*, **2**, p.393, 1963.
2. F.S.Chen, J.T.La Machia, D.B.Fraser, *Appl. Phys.Lett.*, **13**, p.232, 1968.
3. R.J.Collier, C.B.Burkhardt, L.H.Lin, *Optical holography*, Ch.16, Academic Press, N. Y., 1971
4. V. B. Markov, I. G. Yavtuschenko, *Bild und Ton*, n°2, 37-42, 1982.
5. H. Kogelnik, *Bell Syst. Techn. J.*, **48**, p.2909, 1969.
6. A.A. Ward, J.C.W.Newell, L.Solimar, *Proc. SPIE*, v.**600**, p.57, 1985.
7. S.P.Vorobjev, Opt.&Spectroscopy, **65**, p.656, 1988
8 L.Solimar and D.J.Cook, Wolume Holography and Wolume Gratings, Ch. 4, Academic Press, 1981.
9. V. B. Markov, *Proc. SPIE*, **2406**, 1995.
10.H. Bjelkhagen, D. Vukicevic, *Proc.SPIE*, *2333*, 1995.

Joint Session on Diffractive and Micro-Optics and Holography I

JMC 1:30 pm-3:00 pm
Gardner A&B

Raymond Kostuk, *Presider*
University of Arizona

Fabrication of micro-optics and diffractive lenses using analogue methods

M C Hutley
National Physical Laboratory
Teddington
TW11 0LW, UK
Tel (44) 181 943 6122 Fax (44)181 943 2945

Introduction

The most important aspect of producing a diffracting optical component that will compare well with its refracting or reflecting counterpart is to achieve an adequate level of diffraction efficiency. Binary diffracting structures in amplitude and phase forms have been available for about a century but since their efficiency is limited to 10% and 40% respectively they have not found significant application. In order to achieve high efficiency it is necessary to exercise some control over the form of the grooves and for most practical cases it is necessary to generate a saw-tooth "blazed" profile. A blazed profile is one in which the individual facets behave, to a first approximation, like tiny prisms which send the light by reflection or refraction in the same direction that the spacing of the grooves sends it by diffraction.

Much of the current development in diffracting optics is based on producing a digitised approximation to the ideal profile by the superposition of a series of binary steps using the technology of photolithography. The purpose of the present paper is to review other attempts to achieve diffracting components with the ideal groove profile, to summarise the lessons that have been learned from this experience, and to consider the extent to which they are appropriate to the new generation of technology.

2. Mechanical methods.

Until recently the only diffracting component that had any widespread application was the diffraction grating. The production of gratings was the supreme challenge to mechanical and machine control engineering. It is interesting to note that the justification for the effort of making a grating was that the chromatic dispersion was far greater than that of a prism. In many modern applications for diffracting optics, dispersion is a disadvantage. It is also interesting to note that the much of the machine control technology developed for ruling engines has been carried over to photomask writers on which the current diffracting optics boom is based.

The production of blazed plane gratings was first achieved by Strong in 1935 (1). For a plane grating of constant pitch the appropriate facet angle may be achieved by the correct orientation of the diamond ruling tool. This no longer holds for a concave grating and severely limits the numerical aperture over which a concave grating will work. This led to the development of "multi-partite" gratings in which different sections were ruled at different angles (2) or to complex toolholders in which the diamond rotated as ruling progressed.

More complex structures such as Fresnel-zone plates can be generated mechanically by single point diamond turning.(3) In this case the facet angle and the width of the groove both vary across the aperture so a far higher degree of control is required. The current best quality machines are capable of producing good quality diffracting components, particularly if they are to be used in the infrared where mechanical tolerances are comparatively relaxed. The only question that arises is "why bother?". If one has the capability to produce a surface that will control the optical phase

across the aperture, why introduce a phase step of π every time one crosses the Fresnel zone boundary ? The sharp edges of the groove are likely to produce scattering and one needs a sharper tool than is required to turn a lens. The savings in weight and material are negligible, even for germanium. Why not simply make an aspheric lens ? In most practical cases the answer lies in hybrid designs in which aberrations (particularly chromatic) of the diffracting component are balanced against those of refracting components. As stand-alone devices they have little to offer optically, but the thinner structure may be easier to replicate or may absorb less energy.

3. Interference techniques

Standing waves

The recording of interference fringes to produce diffracting structures has been used for over a century. In 1875 Cornu photographed Newton's rings to generate a zone plate and in 1901 Cotton (4) recorded standing waves and proposed the holographic reconstruction of arbitrary wavefronts. Sheridan in 1968 recorded standing waves in photoresist to generate blazed holograms and Hutley refined the technique for the production of spectroscopic quality gratings (5). During exposure the photoresist is aligned obliquely to the fringe pattern so there are within the bulk of the resist, layers which are alternately soluble and insoluble. After development the shape of the profile is determined by the shape of the oblique insoluble layers near the surface.

The shortcoming of this approach is that the separation of the standing waves is equal to half the wavelength of light in the photoresist. This defines the separations of the planes of the facets of the grooves (which in turn is half the Littrow blaze wavelength). In theory the blaze wavelength should be equal to the recording wavelength divided by the refractive index of the resist. In practice it less than that so that with an argon laser at 458 nm the blaze wavelength is about 220 nm. This is ideal for ultraviolet and visible spectroscopy but is too shallow by a factor of about ten for transmission diffracting optics.

The technique can readily be applied to zone plates by placing a point source at the centre of curvature of a concave mirror. A longer blaze wavelength is achieved if light is incident through the substrate and it can be increased still further by selective reactive ion etching of the structure into the substrate so that it is possible to achieve high efficiency in transmission.

The great advantage of this approach is that it is possible to produce in a few minutes, components which combine large area (>100 mm), high numerical aperture and spectroscopic quality.

Fourier Synthesis

The fringes in a two beam interferometer possess a sinusoidal variation of intensity. It is possible to build up any desired intensity profile by superimposing a Fourier series of sinusoidal patterns of appropriate amplitude and phase. This approach has been adopted (6,7) for plane gratings and good results obtained for two Fourier components. However, the best results were obtained for gratings in which a single sinusoid would have been quite efficient and the technological difficulties were significant. It is difficult to see how the technique could practically be applied to any component other than plane gratings. The author has attempted to obtain the second Fourier component by frequency doubling the output of an argon laser but with limited success.

Multiple beam interferometry

With multiple beam interferometers it is possible to obtain an intensity profile that is other than sinusoidal. For example, by carefully selecting the reflectance and phase change on reflection of the mirrors in a Fabry Perot interferometer it is possible to produce asymmetric fringes which are a good approximation to a saw-tooth.(8) These may then be recorded directly in photoresist or photographic plates which are bleached and swollen to yield blazed zone plates.(9)

An alternative approach is to use the symmetrical transmission fringes of a Fabry-Perot interferometer of high finesse. The fringes can be considered as delta functions and have approximately the same spatial distribution as the Fresnel zone boundaries. If the fringes are recorded in photoresist and the plates are scanned in such a way that the fringes expand by one period, it is possible to control the exposure so as to build up a saw-tooth profile (10,11). By this means good saw tooth profiles and efficiencies of the order of 80% were obtained for transmission zone plates in the visible.

General Photosculpture Techniques

The term "photosculpture" applies when the shape of a photosensitive surface is determined by the intensity distribution to which it is exposed. The simplest manifestation of this is to scan the area with a focussed laser beam and vary the intensity to achieve the correct exposure. This can be achieved either on an optical lathe (12) or on a rectangular raster (13). Both are capable of producing items with both rectangular and circular symmetry. This approach gives a far greater flexibility of design than is available from interferometry, but the price that one pays is that it is slow and therefore requires extreme mechanical stability. In some cases the writing time is so great that the latent image recorded at the beginning of the process begins to fade before it can be developed. A very detailed knowledge of the properties of the resist is therefore required in order to compensate for this.

For items which have circular symmetry a simpler system may be used in which blazed circular grooves are generated by rotating the photosensitive material under an image of a triangular light source (14, 15). After exposing one groove, the projection system is translated radially, the width of the image is adjusted and the next zone is exposed. This has the advantage that the optical projection system is working on axis with a relatively small field but has the disadvantage that as the zones become narrower, the energy from the source is reduced and exposure times become longer. The production of items of large aperture and high numerical aperture is therefore difficult.

Finally, it is possible to generate a desired exposure pattern by producing a variable density mask.(12,16,17) Strictly this is not an "analogue" technique because the variable density is usually produced as a half-tone dot pattern. However, if this is then reduced photographically the detail of the dots is lost.

General Summary of Results

All of the techniques described above have been able to produce blazed diffracting structures with reasonable efficiencies . For very coarse structures the efficiency can be very high (90% or so) but for the finer structures needed for high numerical apertures the efficiency is lower. The reason is that the efficiency depends upon the spatial resolution of the recording system. In order to

achieve 90% of the maximum theoretical efficiency it is necessary that the steep facet of the saw-tooth should occupy no more than 5% of the width of the groove. The finest groove width d for which one might expect 90% efficiency is twenty times the spatial resolution δ. For an optical recording system $\delta = 1.22 \lambda_0 / NA_{(system)}$ If d is the width of the outermost zone on a zone plate, we have from the grating equation that $d = m\lambda / NA_{(zone\ plate)}$. If $d = 20\delta$ we may now write:

$$NA_{(zone\ plate)} = m\lambda \ \frac{NA_{(system)}}{\lambda_0 25}$$

This means that **whatever** optical system is used to generate a diffracting structure the maximum numerical aperture (for 90% of theoretical efficiency, used at the same wavelength in first order) is one twenty fifth of the numerical aperture of the system used to record the structure. Thus, if the recording system has f/1 optics, the best that can be achieved is f/25. Given that $NA_{(system)}$ is limited, the only possibilities to improve on the factor of 25 are:

Increase **m** and work at higher orders of diffraction. This approach has been adopted by Gale and colleagues (13). The consequences are that the modulation depth is greater. The chromatic behaviour is changed in that the free spectral range is reduced and the efficiency performance is that of an echelle. In the limit, when the order number is equal to the Fresnel number, one has re-invented the lens!

Increase λ. This is not usually an option but it does mean that one can use visible light to generate devices for use in the infrared at around 10 μm (18)

Decrease λ_0. One can gain some improvement (perhaps a factor of 4) by using UV to record optics for use in the visible, but if one really needs to combine high efficiency in first order with high numerical aperture one is forced to use higher resolution lithography such as e-beam. If one also requires a large physical aperture, this is likely to be very expensive.

Happily, there are applications for components of low NA and for those with small apertures. So diffracting optics does have a rôle but there remain some severe technological challenges.

References

1. Strong. J (1935) Phys Rev **48**,480
2. Hutley M C (1982)" Diffraction Gratings" Academic Press. London (and references therein)
3. Goto K, Mori K, Hatakoshi G,Takahashi S. (1987) Jpn Jnl App Phys. **26** supp 26-4. 135-140
4. Cotton A. (1901) Seances Soc Français Phys 70-73
5. Hutley M C (1975) Opica Acta **22**,1-13
6. Schmahl G (1974) Proc 4th Int Conf Vac UV Radiation Phys. Hamburg.
7. Breidne M, Johansson S, Nilson L-E and Åhlen H. Optica Acta **26**. 1427-1441
8. Aebischer N. Nouv Rev d'Opt App (1971)**2**,351-366
9. Ferrière R, Andres P, Illueca C. (1984) J Opt(Paris) **15**,213-218
10. Claire J J, Françon M and Laude J-P. (1970) C R Acad Sc Paris **270**,1600-1603.
11. Hutley M C, Stevens R F, Wilson S J. (1988) J Mod Opt**2**,265-280.
12. Koronkovich V P et al. (1984) Optik **67** ,257-266
13. Gale M T, Rossi M, Schütz (1994) Proc SPIE **2045**
14. Schwider J, Grzanna J, Spolaczyk R and Burov R, (1980) Optica Acta **27**,683-698
15.Emerton N, Smith R W,and Cañas R G. (1987) IERE **76** 99-103 (Holographic systems components and applications. Cambridge.)
16.Moreno V,Hutley M C, Tyrer J R. (1989)IEE**311**,76-79(Holographic systems components and applications, Bath)

17. Purdy D.(1994) Pure Appl Opt.**3**,167-175.
18. Hutley M C, Stevens R F, Wilson S J. (1991) Opt Engg **30** 1005-1010

LASER WRITTEN DIFFRACTION GRATINGS IN QUANTUM DOT AND ISLAND METAL FILMS

Yu. Kaganovskii and M. Rosenbluh

Department of Physics, Bar-Ilan University, Ramat-Gan 52900, Israel

Phone: 972-3-531-8296; fax: 972-3-535-3298

We demonstrate a new direct method of recording of interference patterns which are stable under high light intensities. The patterns are written on thin glass films containing quantum dots or on metal island films by the interference of two pulsed laser beams. A pulsed dye laser at 584 nm, with a 7 nsec pulse, and pulse intensities of 2-5 MW/cm^2 produced gratings with a period l depending on the angle, α, between the two beams according to $l = \lambda/2\sin(\alpha/2)$.

The quantum dot films were obtained by the simultaneous vacuum condensation, onto a glass substrate, of SiO and Cu from two separate sources. The Cu concentration was varied from 1 to 10 at%, and the overall film thickness varied from 20 to 300 nm (the thinnest films were prepared for TEM examination of the Cu distribution). The average size of the Cu particles in the films, after condensation, was about 10 nm.

Electron microscope micrographs reveal that the gratings form as a result of two processes: SEM shows a local buildup of the film on the substrate along lines of high light intensity (Fig. 1). A similar but random buildup, seen as separate round hillocks, is also observed after heat treatment of the films at ~500°C temperature.
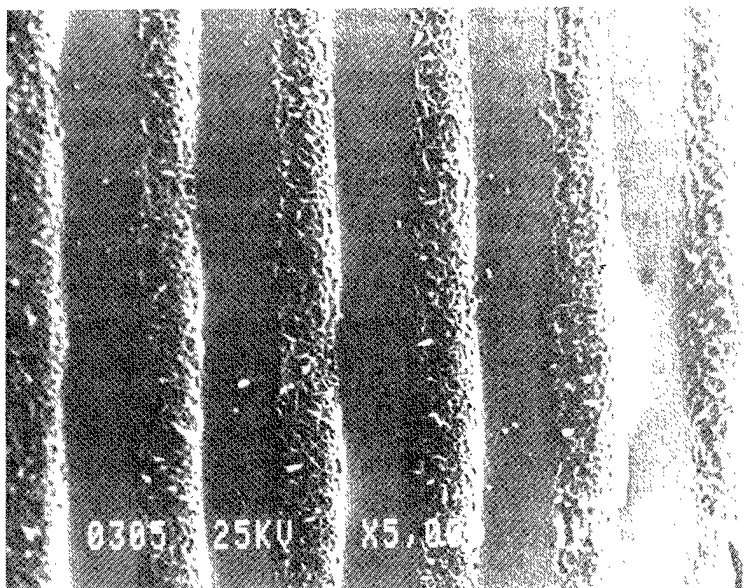

Figure 1. SEM micrograph of 6.2 μm grating in a SiO glass film containing quantum dots of Cu.

The second mechanism responsible for the grating formation is revealed in a TEM micrograph, (Fig. 2), which shows an increase of Cu particle size in the high light intensity regions. The average growth rate of the Cu particle radius is very high, about 10^{-9} cm per laser pulse, so that the average radius grows by a factor of 2 after 10^3 pulses. In regions with low light intensity the Cu particles do not change their size and the film remains stable.
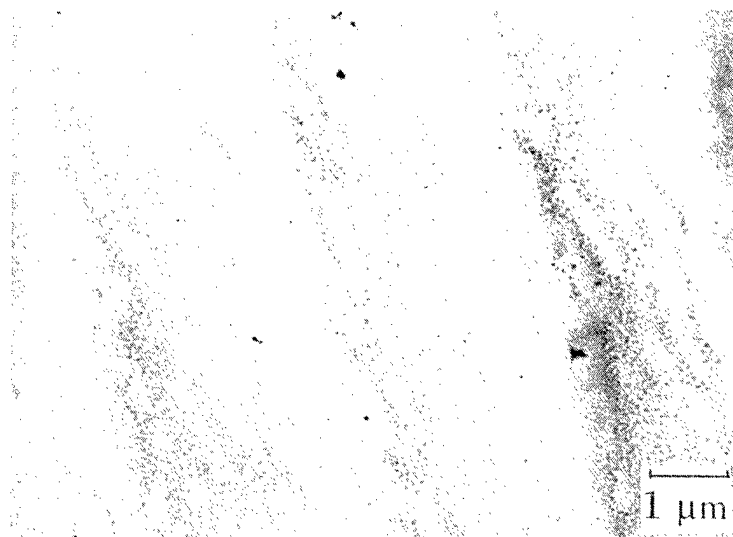

Figure 2. TEM picture of 3 μm grating written in a SiO glass film containing quantum dots of Cu.

In separate experiments island films of Cu, Au and In with a thickness of 10-20 nm, were vacuum condensed on a heated glass or NaCl substrate. TEM studies, (Fig. 3), of the island film morphology after laser irradiation show gratings which are made up of lines containing metal
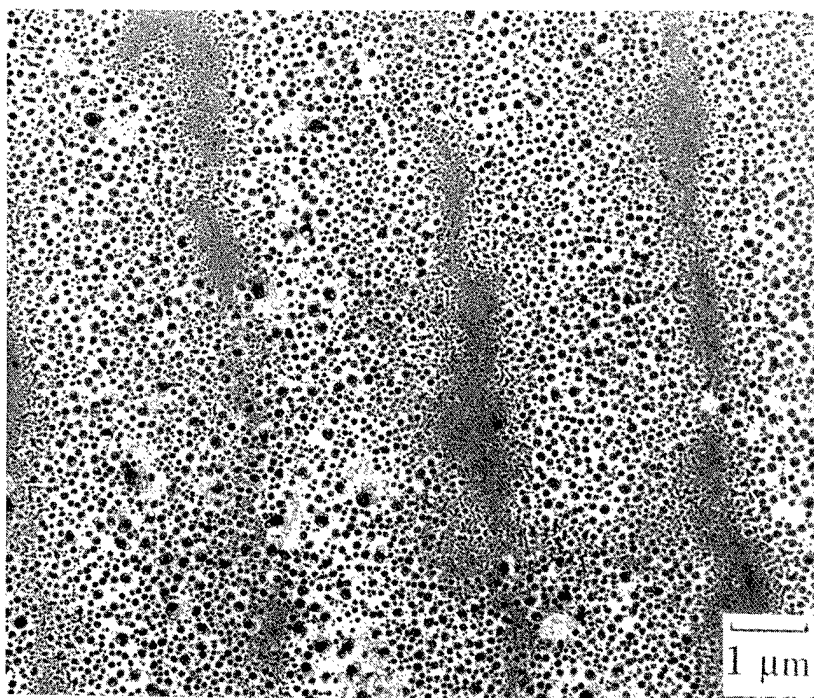

Figure 3. 3 μm period grating written in a Cu island film of 20 nm thickness.

islands of an average size which are bigger than islands in surrounding areas. The average island size in regions of high intensity illumination as well as the width of the line, grows with exposure time, indicating a very fast surface coalescence of the islands, while the island size in the low intensity regions (interference minima) does not change with time.

To determine the mechanism of grating formation for both types of sample we consider the heat distribution near the absorbing particle, of radius R, in a transparent matrix during the laser pulse with duration τ. The particle's temperature changes as a result of a balance between the absorbed energy and the conductive heat loss to the glass matrix. The time dependent particle temperature, $T_1(t)$, is determined by the equation:

$$\frac{dT_1}{dt} = \frac{\Delta q}{\tau c_1 v} + 4\pi R^2 \kappa c_2 \frac{\partial T_2}{\partial r}\bigg|_{r=R}, \qquad (1)$$

where $\Delta q/\tau = \alpha I v$ is the energy absorbed by particle per unit time; α is the absorption index, κ is the heat conductivity of the glass, I is the pulse intensity, $v = 4\pi R^3/3$ is the volume of the particle, c_1 and c_2 are the heat capacities per unit volume of the particle and glass matrix, and $T_2(r,t)$ is the temperature distribution near the particle. Considering the problem for a 7 nanosecond pulse, we may suppose $\partial T_2/\partial t \approx 0$ and look for a steady state solution, because the characteristic time, $t_{ch} \approx l^2/6\kappa$, for heat spreading over the average distance l between particles, is much less than τ. Thus, with $l \approx 5\times10^{-6}$ cm and $\kappa \approx 10^{-2}$ cm²/s we obtain $t_{ch} \approx 5\times10^{-10}$s, which is at least an order of magnitude less than τ. Thus except for a short time of order t_{ch} at the start and end of the pulse we may consider the particle's temperature as a constant.

In this case the temperature distribution around the particle is determined by the expression

$$T_2(r) = T_m + \frac{(T_R - T_m)R}{r} \qquad (2)$$

where T_m is the temperature of the matrix and T_R is the temperature of a particle with the radius R. It follows from (2), that $(\partial T_2/\partial r)_{r=R} = -(T_R - T_m)/R$. Substituting this into (1) with $\partial T_1/\partial t = 0$, we obtain

$$T_R = T_m + \frac{\alpha I}{3c_1\kappa}R^2, \qquad (3)$$

i.e. the temperature of a particle is proportional to the square of its radius. With $\alpha = 10^7$ cm⁻¹, $c_1 \approx 4\times10^6$ J/Km³, $\kappa \approx 10^{-2}$ cm²/s, $I \approx 6\times10^6$ W/cm², $R \approx 10$ nm, we obtain $T_R - T_m \approx 500$ K, and for a particle with $R \approx 20$ nm the difference is $T_R - T_m \approx 2500$ K.

The atom flux directed towards the Cu particle from the glass matrix, is $J = -D(dC/dr)_{r=R} \approx D\Delta C/R$, where D is the Cu atomic diffusion coefficient in glass around the particle, C is the Cu concentration in SiO glass and ΔC is the difference between concentration of Cu in the glass matrix the equilibrium concentration at the particle temperature. This flux leads to a growth of the Cu particles with a rate

$$dR/dt = J\,\Omega = D\Omega\Delta C/R, \qquad (4)$$

where Ω is the atom volume. With $D=10^{-6}$ cm^2/s (the glass surrounding the Cu particle becomes liquid during the laser pulse); $\Omega\Delta C = 10^{-1}$; $R= 10^{-6}$ cm we obtain $dR/dt= 10^{-1}$ cm/s, which is in a good agreement with the experimental value.

The theoretical analysis of the heat distribution on the glass surface surrounding a metal island is similar to what was presented above for the metal particle inside the transparent matrix. This indicates that the island temperature during the 7 nanosecond laser pulse can be as high as 2500°C (for an $R \approx 20$ nm island size) and increases with size proportional to R^2. Thus two-dimensional diffusional coalescence[1] cannot explain the observed results. We propose a new mechanism for the coalescence of the metal particles which is connected with the overall random surface motion of liquid islands in a local temperature gradient, and collisions during this motion. The temperature distribution around each metal particle on the substrate is described by an expression similar to Eq. 2. Small random drifts of a liquid drop in a temperature gradient must lead to an overall directed average motion to colder regions. During this motion, the biggest (and therefore hottest) liquid drops coalesce with the smaller solid particles. In the Figure 3 the tracks of such motion and coalescence can be discerned as areas besides the larger coalesced particles that were left empty of metal particles.

1. I. M. Lifshits and V. V. Slyozov, J. Phys. Chem. Solids, **19**, 35 (1961).

High-Efficiency Transmission Gratings Fabricated in Bulk Fused Silica

H.T. Nguyen, B.W. Shore, J.A. Britten, R.D. Boyd, S.J. Bryan, S. Falabella, and M. D. Perry

Lawrence Livermore National Laboratory, P.O. Box 808, L-443, Livermore, CA 94550

Tel. (510) 423-2111, FAX (510) 422-9294

I. Introduction

High power ultraviolet lasers are now widely used in the semiconductor industry and inertial confinement fusion research, and are finding increased application in medical therapy. Whether based on excimers or frequency converted solid-state, high power ultraviolet lasers continue to be plagued by issues of optical damage and a limited choice of optical components for beam manipulation. In particular, system performance is often limited by the damage threshold of cavity and transport mirrors. Beam transport and steering based on refractive optics are limited not by surface damage as is the case with reflective systems but instead by bulk damage induced by two photon absorption, color center formation and self-focusing. These limitations can, in principle, be overcome in many applications by the use of transmission gratings fabricated in high damage threshold, transparent materials.

We present the design and performance of high-efficiency transmission gratings fabricated in bulk fused silica for use in ultraviolet high-power laser systems. By controlling the shape, depth, and duty cycle of the grooves we have achieved a diffraction efficiency exceeding 95% in the $m = -1$ order. By directly etching the grating profile in bulk fused silica we have achieved damage threshold greater than 13 J/cm^2 for 1 nsec pulses at 351 nm.

II. Theory

The efficiency of a grating depends, for given wavelength λ, polarization and angle of incidence α, on groove period d, groove depth h, and the shape of the grating profile. For suitable choice of these parameters the transmission efficiency can approach 100%. The most efficient gratings are obtained when only two orders can propagate, namely the zero order (specular reflection) and the -1 order, and when the incident radiation impinges

close to the Littrow angle, arcsin($\lambda/2d$) (autocollimation). By suitably choosing the groove spacing d for given wavelength λ we can exclude all other orders. This possibility follows from the basic grating equation relating angle of incidence α to angle of diffraction β_m for order m,

$$\sin \beta_m = \sin \alpha + (m\lambda/ d). \tag{1}$$

Our goal for permitting only two orders can be assured by fixing the grating period to be smaller than the wavelength. For light of wavelength 351 nm this implies a groove period of 351 nm or less.

The geometry of diffraction is entirely set by the grating equation, and is independent of groove depth or profile. With period = 350 nm the Littrow angle, at which reflective diffraction into order -1 coincides with incident radiation, is 30°. With this incident angle the transmitted light into order -1 emerges into air at an angle of 30°. Thus there will be a 60° angle between the two transmitted orders as they emerge into air.

Taking the groove spacing to be 350 nm, we found that there was a range of parameters at which the efficiency was 97% or better. Our target design is for a period of 350 nm, a depth of around 600 nm, and with duty cycle of 0.5 (i.e. the grooves have width 175 nm) to be used with TE polarized light. Figure 1 illustrates the profile and efficiency for this design. This design has a theoretical efficiency of 98% into $m = -1$ order.
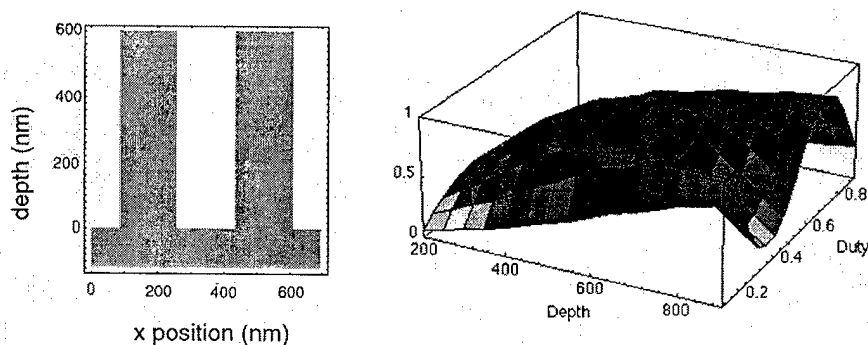

Figure 1. Right: Theoretical transmission efficiency, $\lambda = 351$ nm, order -1 and TE polarization, as a function of groove depth (nm) and duty cycle for a rectangular-profile grating etched into silica (left frame). Incident angle is Littrow angle, groove spacing is d = 350 nm. The peak efficiency (97.6%) occurs for depth of 600 nm and duty cycle 0.5.

III. GRATING FABRICATION

Our fabrication of gratings proceeds through several steps. We first prepare, on suitably flat and polished substrates, carefully controlled thickness of photoresist. We next use laser interference lithography to pattern the photoresist with the desired profiles. We develop the resultant latent image to form a corrugated photoresist grating, which we transfer etch into the substrate. A typical photoresist grating and a grating etched into bulk fused silica is shown in Figure 2.
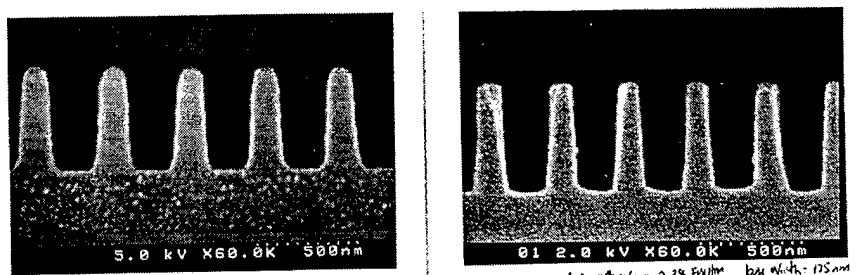
Figure 2A. Grating profile patterned in photoresist, 2B) Grating profile etched into bulk fused silica.

IV. EXPERIMENTAL RESULTS

We have fabricated a grating that exhibits a diffraction efficiency in excess of 95% in the $m = -1$ order and 2% in the transmitted 0 order at the Littrow angle of the grating. The light that is not present in these two orders appears to be diffusely scattered. This can be seen from the hazy appearance of the sample. We attribute this to the defects in the bulk fused silica substrate that was used. This can be corrected by using super polished fused silica substrates (fused silica substrates that have been etched/polished to minimize substrate polishing damage). It is expected that with these substrates a diffraction efficiency of greater than 97% can be obtained. Experimental results are in good agreement with our theoretical computations.

In addition, we have conducted damage test of these transmission grating using a 3 ns pulse from a frequency-tripled Q-switched Nd:YAG laser. The grating was situated to the TE-polarized laser beam at the use angle of 30°. Both front and back surfaces had a damage threshold of 13.2 J/cm^2. These values are typical for standard bulk fused silica.

Ultrahigh Spatial-Frequency, High-Contrast Periodic Structures Produced by Interference Lithography

H.T. Nguyen, J.A. Britten, R.D. Boyd, B.W. Shore, and M. D. Perry

Lawrence Livermore National Laboratory, P.O. Box 808, L-443, Livermore, CA 94550

Tel. (510) 423-2111, FAX (510) 422-9294

I. Introduction

During efforts to produce multilayer high efficiency dielectric reflection gratings in oxides, 351nm high efficiency transmission gratings, and other development work, we required very high-contrast grating profiles in photoresist. High-contrast profiles are profiles with very steep sidewalls, greater than 80 degrees. It is quite difficult to achieve high-contrast profiles using interference lithography. The electric field distribution is sinusoidal. Therefore, one would conclude that the profile would resemble a sinusoid, as shown in Figure 1a. Early work with interference lithography produced grating profiles similar to the ones shown in Figure 1a.[1-3] We have learned that if great care is taken in the processing steps, very different profiles can be achieved. Figure 1b shows a very high-contrast, high-aspect ratio grating profile in photoresist. The difference between Figure 1a and Figure 1b is that 1) the photoresist profile in Figure 1b has completely developed through to the substrate, and 2) the contrast characteristics of the photoresist used in Figure 1b are superior over the photoresist used in Figure 1a.
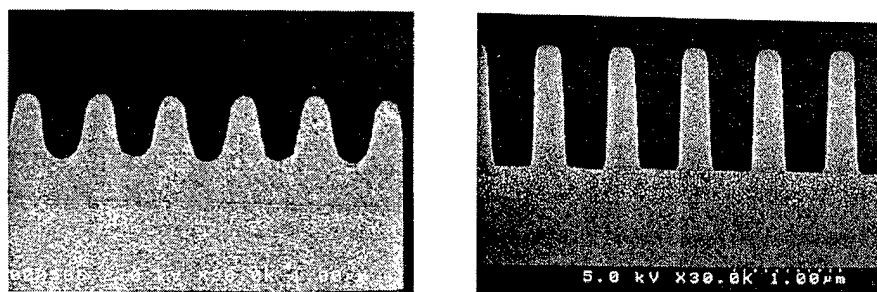

Figure 1a) Scanning electron micrograph of sinusoidal profile in photoresist, 1b) Scanning electron micrograph of high-contrast profile photoresist.

In addition to high-contrast photoresist and the complete dissolution of the grating troughs to the substrate, the exposure laser must operate single-frequency. This is essential for the production of high-aspect ratio, high-contrast grating profiles since the contrast of the exposure laser is transferred to the photoresist during exposure.

Etched structures such as grating profiles etched into a SiO_2 layer atop a multilayer dielectric stack, and a ultraviolet transmission grating etched into bulk fused silica, require high-contrast for high-efficiency. These are more easily made with a high-contrast mask.

It is also important to mention that a high-contrast profile is not always desired or needed for all applications. In fact, a distorted sinusoidal profile is used for all of our metallic overcoated gratings.[4] Additionally, we have developed a process to control the duty cycle, the full-width-at-half-maximum of the structure divided by its period, of the structures from 0.6 to 0.17.

II. Vertical Sidewalls

The use of different types of photoresist has become very important to our processing technique. We have discovered that each of the different photoresists used have individual advantages and disadvantages. By choosing a particular photoresist we can now control the photoresist profiles, from a distorted sinusoid to a rectangular profile, from a duty cycle of greater than 0.6 to less than 0.17. For instance, Photoresist A used to produce very steep side walls has excellent contrast characteristics but low sensitivity, requiring exposure fluence $>120mJ/cm^2$. On the other hand, Photoresist B has very high sensitivity, requiring an exposure fluence of about $20mJ/cm^2$, but its contrast characteristics are lower. Figures 2a and 2b show grating profiles of these photoresist exposed under similar conditions.
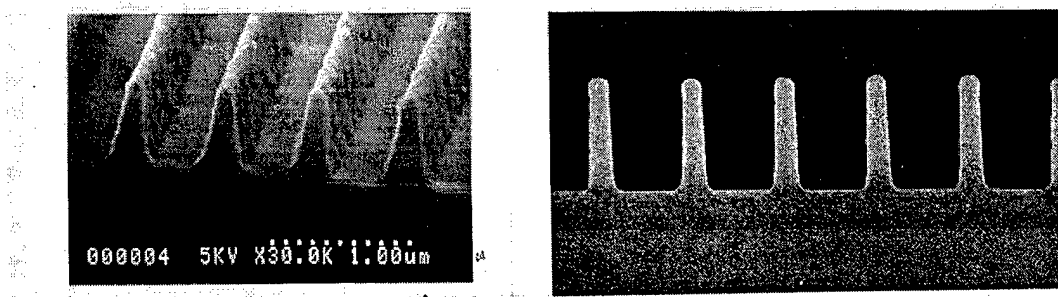

Figure 2a) Typical profiles produced with Photoresist A, 2b) Typical high-contrast profile produced with Photoresist B

The difference in the grating profiles shown is a function of the photoresist used. Even though all of the resist are diazonapthoquinone-based (DNQ), they exhibit different contrast characteristics. The basic differences between these resist are the transparency of the resin, synthesizer, and concentration of the photoactive compound. Photoresist B uses a more transparent resin which results in less UV light being absorbed, and lateral scattering yielding steeper side walls.

Diffractive diffusers at the fabrication limit

Hans Peter Herzig, Wolfgang Singer

Institute of Microtechnology, Rue A.-L. Breguet 2, CH-2000 Neuchâtel, Switzerland
Phone +41 38 234 251, Fax +41 38 254 276

Eckhard Piper, Johannes Wangler

Carl Zeiss, Postfach 1369/1380, D-73446 Oberkochen, Germany
Phone +49 7364 20 3823, Fax +49 7364 20 4509

1 Introduction

Diffractive micro-optical elements gained increasing interest for beam-shaping, e.g., the laser treatment of materials,[1] and for illumination systems. The fabrication technologies for diffractive micro-optical elements bring in advance high accuracy and reproducibility, especially of the periodicity of the elements. In monochromatic applications, diffractive micro-optical elements are only restricted by the limits of the fabrication technology.

In this paper we discuss the design and fabrication of optical diffusers for deep UV lithography. The diffusers generate a flat-top intensity distribution,[2] for a partially coherent excimer-laser at 248nm. We investigated far-field distributions with a uniform intensity over a rectangular shape. High efficiency and a space-invariant response of the diffractive elements are required. In detail, the diffusers have to be almost independent of the size, the shape, and the homogeneity of the illumination.

The fabrication limits due to the restricted resolution of the fabrication technology are a severe restriction for the design of diffractive elements for short wavelengths applications. Therefore, a conventional design was preferred to the IFTA-algorithm.[3] In this case, the utilization of arrays of binary micro Fresnel lenses[4] with adapted geometry is straight forward. The lenses generate the desired angular spectrum, while the array property warrants the space invariance of the element. However, binary Fresnel lenses suffer usually from binarization noise and a large zeroth diffraction order, which violates the homogeneity condition of flat-top distributions. The small oscillations in the far-field due to the binarization noise can be smoothed out with partially coherent or, in the limit, incoherent illumination. Furthermore, we show that the zeroth order is reduced by the addition of a constant phase offset to the transmission phase function of the lens array.

Binary diffractive elements with two phase levels usually have low diffraction efficiency (40.5 %).[5] For the generation of symmetrical intensity distributions, however, both the plus and the minus first diffraction order contribute to the desired intensity distribution, increasing the diffraction efficiency (~ 80 %). In order to improve the efficiency, multi-level elements have to be employed. We investigated also elements with varying numbers of phase levels, where the number of levels is chosen according to the resolution limit of the fabrication technology. As will be shown, these elements have a locally varying diffraction efficiency.

2 Design considerations

The basic set-up is shown in Fig. 1. A diffractive element is illuminated by a multi-mode excimer-laser with given beam divergence in x- and y-direction at a wavelength of 248nm. The required intensity distribution is then obtained in the Fourier-plane of the second lens system.
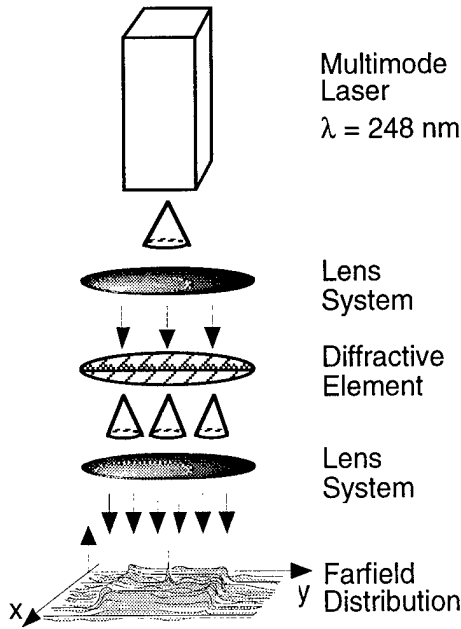
Fig. 1. Set-up for the generation of flat-top distributions (simplified).

The phase grating to generate the flat-top intensity distribution is designed as an array of micro-Fresnel lenses of rectangular shape. For a given focal length, the shape of a single diffractive lens defines the shape and the diameter of the far-field distribution. Due to the divergent illumination with a partially incoherent source, the far-field of the lenses is added incoherently and with small displacements. In the following, we assume that the source is ideally incoherent. The modal distribution of the laser is approximated roughly by a rect-function. The intensity distribution in the far-field is therefore given by a convolution of the square of the amplitudes with a rect-function. As will be shown in detail, the incoherent source has a smoothing effect to the fine oscillations of the coherent intensity distribution.

3 Calculation methods for the far-field distribution

Phase gratings or Fresnel zone lenses are conventionally fabricated as a binary or multilevel phase grating. In that case the direct computation of the far-field according to the Fresnel series by a sum of Bessel-functions can be applied.[6] For this reason, first the transition points tp_n of the m-level Fresnel lens with focal length f for the wavelength λ have to be calculated. The phase values φ_n of the transmission function are given by

$$\varphi_n = n\frac{2\pi}{m} = \frac{2\pi}{\lambda}\left(\sqrt{f^2 + tp_n^2} - f\right) + \varphi_{off} \, , \tag{1}$$

where we have introduced a constant offset-phase φ_{off}. The offset-phase defines the interference between the first few contributions to the Fresnel series. The first and second contribution, e.g., can be adjusted that they are destructively interfering in the center of the far-field distribution. The influence of the offset-phase to the high-frequencies is negligible.
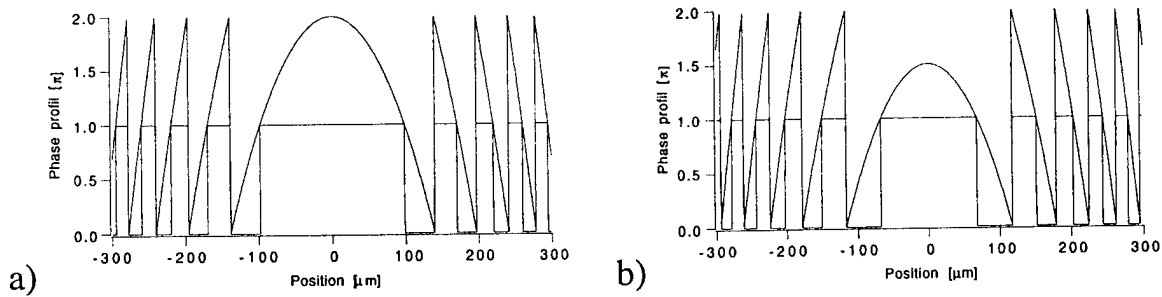

Fig. 2. Continuous phase function and binary approximation (a) without offset-phase, (b) with offset-phase of 0.45 π.

4 Effect of offset-phase and incoherent illumination

Due to the approximation of the continuous phase profile by a binary or staircase grating (Fig. 2), the far-field shows rapid oscillations or binarization noise (Fig. 3). This noise is smoothed out by the incoherent illumination (Fig. 4). In the center of the zone plate, the approximation of the phase function by a binary phase grating is poor (Fig. 2). With a constant offset-phase of 0.45 π, the large central part of the zone plate, which is not diffracting at all, is decreased (Fig. 2b). The large unmodulated region in the spectrum of a zone plate (Fig. 3a) without phase offset is modulated (Fig. 3b). After convolution of the power spectrum with the spectrum of the incoherent source, the large zero order vanishes almost completely (Fig. 4b) :
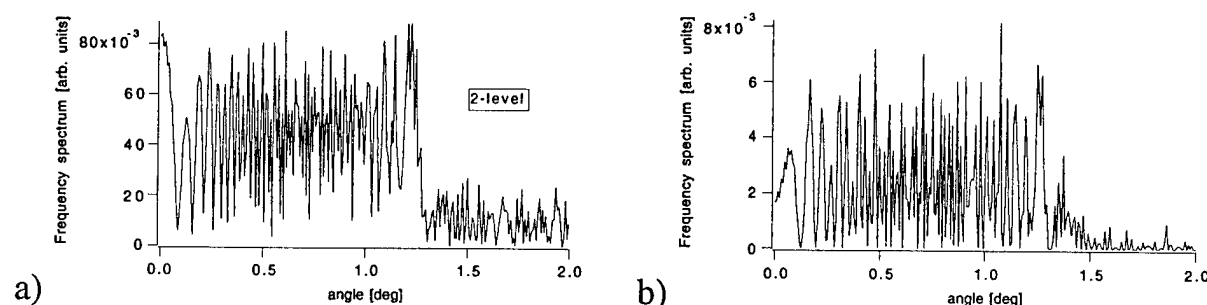

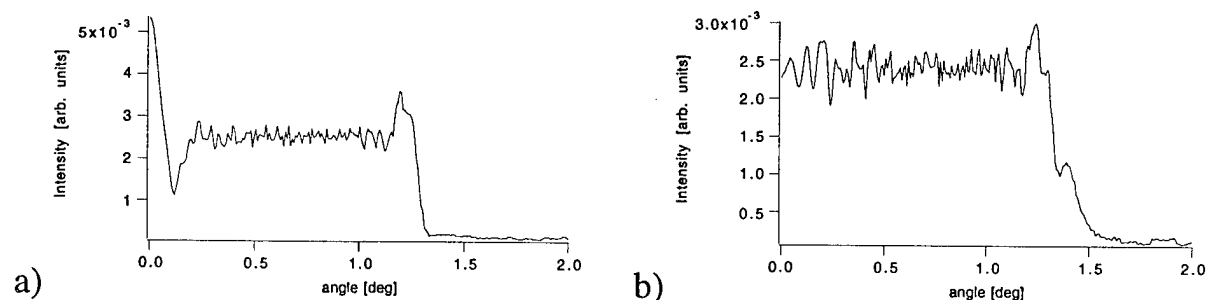**Fig. 3.** Spectrum of the binary elements given in Fig. 3.

Fig. 4. Far-field distribution after incoherent illumination (divergence 1 mrad).

A further comparison is concerned with diffusers of different size, but constant numerical aperture. The number of Fresnel zones and thus the number of contributions to the Fresnel sum increases with the size of the Fresnel zone plate. The frequency spectra exhibit an increasing modulation with increasing element size. Therefore, the homogeneity of the intensity distribution after convolution improves reasonably with increasing element size. However, with increasing element size of the micro-Fresnel lenses the space invariance of the diffuser is reduced. The optimum is a trade-off between homogeneity of the intensity distribution and space-invariance of the element.

A first design of a rectangular far-field distribution was performed with an array of rectangular binary Fresnel lenses without offset-phase. The design angles were 4 and 5.5 degrees in x and y, respectively. Figure 5 shows the results for the x-direction. In a second design, a Fresnel zone plate was fabricated with a constant offset phase. The results for the simulation and for the measurement are compared in Figs. 5 and 6. Both measurements show a significant deviation from the simulation result in the zero[th] order due to fabrication errors, while the design angles (4 degree and 5.5 degree) are obeyed. The elements were fabricated in quartz by RIE and they have a smallest feature size in the order of 1 μm.
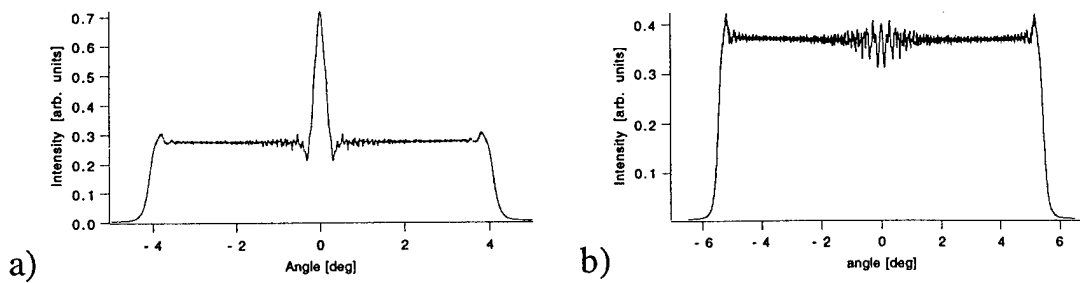
Fig. 5. Simulation result for a binary phase element (a) without offset-phase (design angle 4 degrees) and (b) with offset-phase (design angle 5.5 degrees).
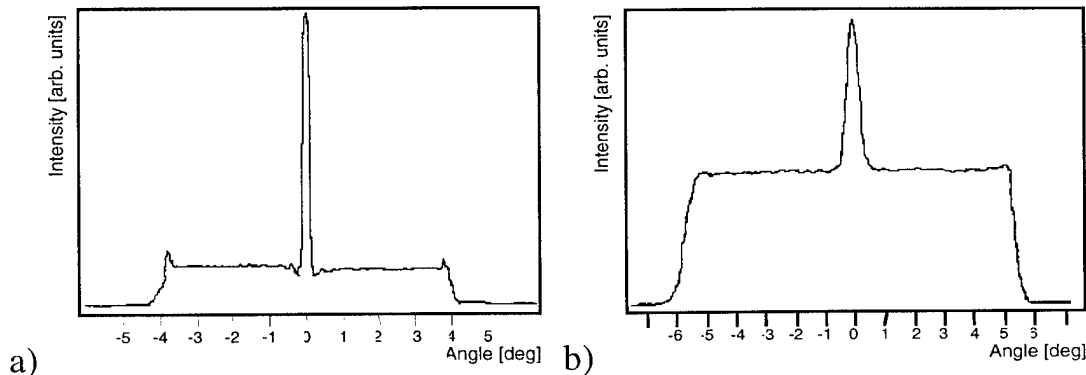

Fig. 6. Measurement result for the elements given in Fig. 5.

In summary, we have shown that by a simple addition of a constant offset-phase to the continuous phase profile, the spectrum of the binary or multilevel phase grating can be modified. The offset-phase design can especially be applied to improve the homogeneity of the far-field distribution.

However, etch depth errors induce an enlargement of the zero[th] order. Therefore we found a large zero[th] order from the measurements even for the optimized micro Fresnel lens. However, the total amount of energy in the central peak remains very small and it is therefore advantageous to defocus or to block the zero[th] order.

References

[1] Ch. Budzinski, H.J. Tiziani, "Radiation resistant diffractive optics generated by micro electroforming", Laser und Optoelektronik **27** (1), 54 - 61 (1995)

[2] T.H. Bett, et al., "A binary phase zone plate array for laser beam spatial intensity distribution conversion", in *Holographic Systems, Components and Applications*, Conference Publication 379, Neuchâtel 1993, pp. 249 - 254 (1993)

[3] Joseph N. Mait, "Understanding diffractive optic design in the scalar domain", J. Opt. Soc. Am. A **12**, pp. 2145 - 2158 (1995)

[4] H. Nishihara and T. Suhara, "Micro Fresnel Lenses", in *Progress in Optics* Vol. **24**, Elsevier 1987, p. 4 (1987)

[5] E. Hasman, N. Davidson and A.A. Friesem, "Efficient multilevel phase holograms for CO_2-Lasers", Optics Letters **16**, pp. 423 - 425 (1991)

[6] I.N. Ross, D.A. Pepler, C.N. Danson, "Binary phase zone plate design using calculations of far-field distributions", Opt. Commun. **116**, 55 - 61, (1995)

Applications

HMC 3:30 pm-5:15 pm
Hampton A/B

James R. Leger, *Presider*
University of Minnesota

Progress in Holographic 3-D Video Displays

S. Benton
Massachusetts Institute of Technology

Summary not available.

Construction of a Holographic 3D Printer

using Silver-Halide Filmplates

R. Andreassen, O.Birkeland, T.E.Grahl-Nielsen,
K.E.Olsen and I.Singstad

Dept. of Physics University of Bergen,
Allegt.55 N-5007 Bergen, Norway
Phone: +4755582750 Fax:+4755589440
EPM Consultants a.s,
Grenseveien 107, N-0663 Oslo, Norway
Phone: +4722649065 Fax:+4722649305

Introduction

This paper reports on the production of multi stereo hologram from a series of computer images with different camera views which are copied onto a LCD panel, one image view at a time. The LCD images serves as an object in a conventional holographic set up, and two production methods are considered, two-step reflection hologram, produced from a master hologram and one-step reflection hologram.

This project is a cooperation between Department of Physics, University of Bergen and the Oslo located company EPM Consultants a.s., which is looking for a practical application for holographic multi stereograms produced from CAD systems.

Production of holographic multi sterogram from two-dimensional photographs is a well established technique. The technology of transferring objects produced in CAD systems via computer images to reflection holograms is being developed by many research groups during the last years, and there has been an increasing interest in the industry for these types of holograms. The product designers and people in the boarding rooms in the industry are looking for a fast and a not too expensive way to visualize models of planed products. Holographic multi sterograms produced from two-dimensional computer models may be a good solution.

The aim of the present project is to develop a kind of automatic hardcopy printer, and we are emphasizing the study of the mechanical and optical systems for the production of a composite hologram on a movable silver-halide filmplate which is multiple exposed through a narrow fixed vertical slit.

In particular, in the vertical strip method there is no vertical parallax, so the reconstructed hologram image is generally somewhat distorted, however there is little needs for this lost parallax since the viewer is scanning the image in the horizontal direction

Description of the technique

The starting point in the experiment is an image library of 70 2D images, with 70 different camera views produced by AutoCAD. The producing of the photorealism and rendering were performed with the computer program AutoVision. In fact there is one file for each of the 70 two dimensional images. As a object we used a machine tool part. For efficient controlling of the hologram production a Windows software program was made up, Automatic Real Image Printer (ARIP). This menu driven program dumps bitmapped images to the computer screen, and it is easy to observe what camera view is on the LCD screen during the exposure of a hologram.

The LCD panel is a projection device that can be connected to most computers. The LCD panel in the present experiment, was model Impact 256 from ASK Co. Norway, having these specifications: color resolution 256 K, VGA display 640x480 (RGB) pixel mode for precise imaging, response time 130 msec, and contrast ratio 18:1
The bitmapped images from the computer are projected onto the LCD screen, having a resolution of 256 colors. LCD panels are equipped with a polarizer which has to be taken into consideration in the holographic set up using polarized laser beams.
The collimated object beams illuminate the LCD screen and the image on the LCD panel is then transferred to a diffuser screen. The photographic emulsion will experience the images from the diffuser in a similar manner as spherical waves from a real object in a conventional holographic set up.
The final hologram is composed of 70 sub hologram, each of 1-2 mm width and having the different camera views of the original 2D computer images. The figure shows the set up for the one-step process.
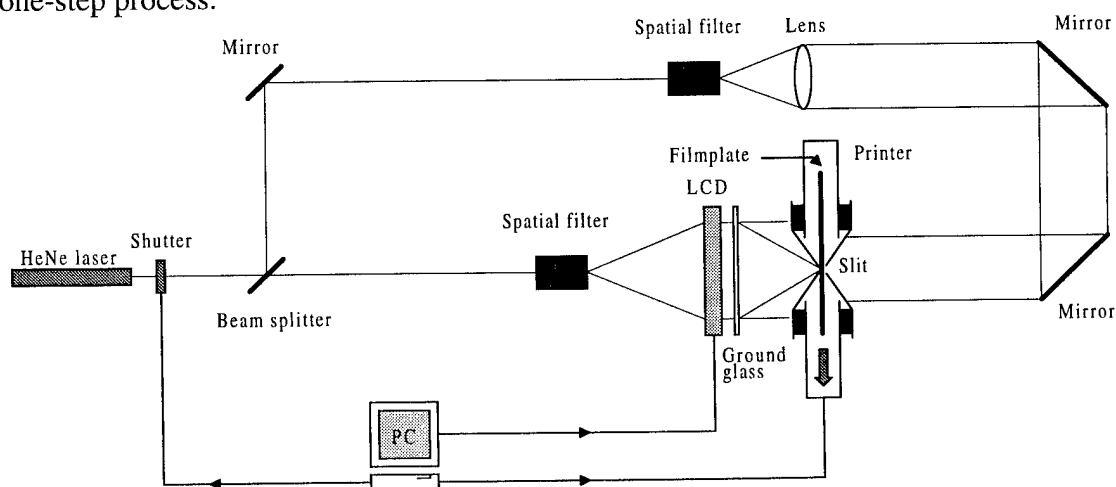
The laser system consists of a Melles Griot, 24 mW He-Ne laser, 632.8 nm wavelength and a linearly polarized beam. The laser provides sufficient power for production of reflection hologram by the two-step process, using a transmission hologram as a master hologram, but the laser power is not so adequate for the one-step process.
A mechanical system was built, in aluminum, applying a stepping motor, (24 V, 0.3 A) to transport the filmplate in 70 steps past a fixed slit of nominally width of 1 mm. Filmplates of sizes 4x5

inches were applied, even though provisions were made for the larger filmplates, 8x10 inches. The drive system incorporates a fixed nut and a moving lead screw, 1 step = 10 μm, to move the filmplates passed the metal slit so the entire film surface is exposed. The travel range for the filmplate was 300 mm in minimum 30 sec.

The metal slits have to be placed very close to the emulsion surface to avoid light scattering into the region next to the physical width of a slit, into unexposed areas and the previously exposed area of the emulsion, the metal slits were therefor set almost in contact with the emulsion surface.

Furthermore, the plane of incidence of the reference beam on the filmplate was parallel to that of the image-bearing object beam, thus avoiding the shadows due to the edges of the slit which else would produce sharp boundaries between the 70 separate sub holograms in the emulsion.

To obtain this an optical breadboard mounted on top of the optical table, and the slit widths were adjustable by micrometer screws.

In the set up for the one-step reflection hologram the object beam and the reference beam illuminated the photographic plate from opposite sides, therefore two collinear adjustable slits are applied in this case. Even then it was difficult to get rid of the visible boundaries on the hologram due to the multiple exposures, they were clearly visible on the master hologram, however in the two-step process the final reflection hologram was without any sign of these multiple exposures, and a clear 3D image was seen.

Care was taken in avoiding unnecessary vibrations during the movement and exposure of the filmplate.

The stability of the integrated system was examined by using a kind of a Michelson interferometric setup, and we found that the system needed about 15 sec between the stop of the motor to a reliable, noise free exposure could take place. To reduce noise from extern sources, as the draft from fans, a plastic cage was mounted on the optical table.

Conclusion

Holographic technique is still a largely unexplored area and holography offers solutions to diverse questions in imaging science. The experiments with production of holographic multi stereograms from computer produced 2D pictures are promising, and we find that high quality holograms can be produced fairly easily in the two-step process, applying a transparent LCD panel in a conventional holographic set up. The last step is a rather conventional holographic production of a reflection hologram.

The loss of light intensity in the LCD screen was mush less severe to the final result than expected, so these kind of LCD screens is sure to become a valuable component in a future 3D printer construction.

Reflection holograms were produced in the two-step and one-step method on small filmplates, 4in. x 5in. The two-step method still gives the best results, even if this technique may be not practical in an automatic printer construction. The question is how automatic this type of equipment need to be. The one-step method is more demanding as to the quality of the mechanical components, and even though a chose of the right lens system may make it possible to use low power (mW) laser, however, there is a cost/benefit tradeoffs here.

The two-step method produced nice looking holograms, so called image plane hologram, and interested costumes seamed to appreciates these holograms. The disturbing visible lines between the sub-holograms in the master hologram were completely gone in the final result.

The mechanical configuration including the stepping motor, worked satisfactory, even if at this early stage, the developments of the films were done manually.

As to the silver-halide materials there is now in the industry an increasing demands for environmentally-friendly materials and processes, however the new photopolymer materials are much less light sensitive than conventional emulsions, and would therefore require new high power laser systems.

In the percent experiment a medium power helium-neon laser was used, but laser diodes with coherence lengths of a few cm might be a future chose.

References

1. Masahiro Yamaguchi, Nagaaki Ohyama, Tossio Honda. SPIE Vol. 1212 Practical Holography IV (1990)
2. Tosiho Honda, D.K. Kang, K. Shimura, H. Enomoto, M. Yamaguchi and N. Ohyama. SPIE Vol. 1461 Practical Holography V, (1991).
3. Masahiro Yamaguchi, Nagaaki Ohyama, and Toshio Honda. Appl. Opt. Vol 31, 217 (1992).
4. Thor Erling Grahl-Nielsen. Thesis work , NTH , Trondheim, Norway, (1992).
5. Olav Birkeland. Thesis work, Dept. of Physics, University of Bergen, Norway, (1994).

Applications of Holography for Femtosecond Time-Domain Processing

Andrew M. Weiner
Purdue University
School of Electrical and Computer Engineering
West Lafayette, IN 47907-1285
phone (317)494-5574
FAX (317)494-6951
email: amw@ecn.purdue.edu

In this talk we discuss Fourier optics methods for signal processing in the femtosecond time domain [1]. Applications include pulse shaping and waveform synthesis, storage, recall, and matched filtering of ultrafast optical signals, time-to-space and space-to-time conversion, and ultrafast transmultiplexing for data format conversion.

Our first work in this area, which we refer to as pulse shaping, utilizes powerful Fourier synthesis methods for generating arbitrarily shaped femtosecond optical waveforms [2]. In pulse shaping an incident femtosecond pulse is spread into its constituent spectral components by a grating and lens. A spatially patterned mask then modulates the phase and amplitude of the spatially dispersed spectral components. After the spectral components are recombined by a second lens and grating, a shaped output pulse is obtained, with the pulse shape given by the Fourier transform of the pattern transferred by the mask onto the spectrum. The setup for femtosecond pulse shaping is sketched in Fig. 1, and one example of a resulting ultrafast pulse ("bit") sequence at a 2.5 THz rate is shown in Fig. 2 [3]. This pulse shaping method clearly has much in common with well known Fourier optics methods for filtering of spatial images. Pulse shaping masks have been implemented in a number of ways, including microlithographic patterning techniques, programmable spatial light modulators, holographic masks, and deformable mirrors. Sufficient precision is available that pulse shaping has been successfully applied for several experiments involving ultrahigh-speed communications, soliton propagation and all-optical switching in fibers, ultrafast spectroscopy, and frequency-domain data storage. A review of pulse shaping methods and applications is given in [1].
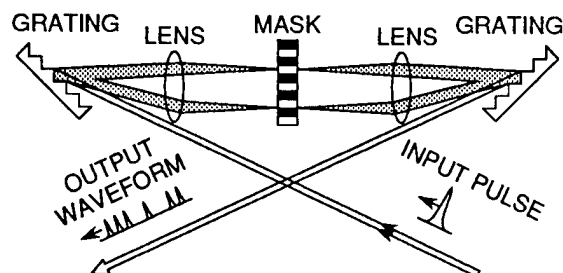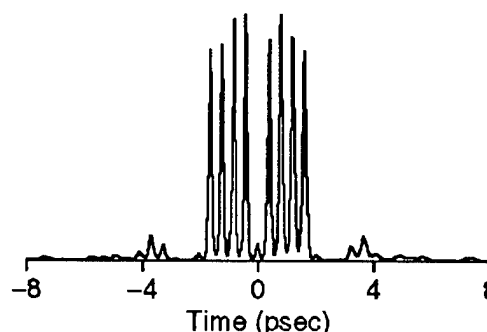
Fig. 1 Femtosecond pulse shaping apparatus.

Fig. 2 Ultrafast optical pulse ("bit") sequence, generated through femtosecond pulse shaping.

Our time-domain holographic processing experiments constitute a temporal analog of off-axis, Fourier transform, spatial holography, in which information on a patterned signal beam is recorded as a set of fringes arising due to interference with a spatially uniform reference beam. In our temporal work, the reference is a short pulse with a broad and regular spectrum. The signal is a shaped pulse with a patterned spectrum. The reference and signal beams are directed into the grating and lens apparatus previously used for pulse shaping. Now the prepatterned mask (or

spatial light modulator, etc.) is replaced by a holographic recording material. Spectral holograms are written by recording the interference between matching frequency components from signal and reference beams. Different frequency components are recorded at different spatial locations of the hologram. Illumination of the spectral hologram with a short test pulse produces either a real or a time-reversed reconstruction of the initial signal waveform, depending on the experimental geometry, just as reconstruction of off-axis spatial holograms can yield either real or conjugate images. Similarly, illumination of the spectral hologram with a temporally shaped test pulse yields either the convolution or correlation of the test and signal waveforms, again depending on the geometry.

This spectral holography approach was first analyzed by Mazurenko [4] and demonstrated in the ultrafast time domain by Weiner et al [5]. The experiments were performed using visible femtosecond pulses from a CPM dye laser and using a thermoplastic plate as the holographic medium. One example of our results, which illustrates matched filtering of femtosecond pulses, is shown in Fig. 3. The short output pulse shown in Fig. 3(a) results when all three pulses (signal, reference, and test) are ultrashort pulses with no distortion. Figure 3(b) shows the result obtained when pulse shaping is used to encode the signal pulse only into a low intensity pseudonoise burst suitable for use in code-division multiple-access (CDMA) data networks [6]. Finally in Fig. 3(c), both signal and test pulses are encoded in the same way; the identical distortions cancel, and an intense bandwidth-limited output pulse is restored. In a similar way, matched filtering and spectral holography can be used to remove dispersive pulse broadening and timing jitter. A key point is that since holographic matched filters are self-aligning, one can decode or process incoming signals without having to precisely specify those signals beforehand.
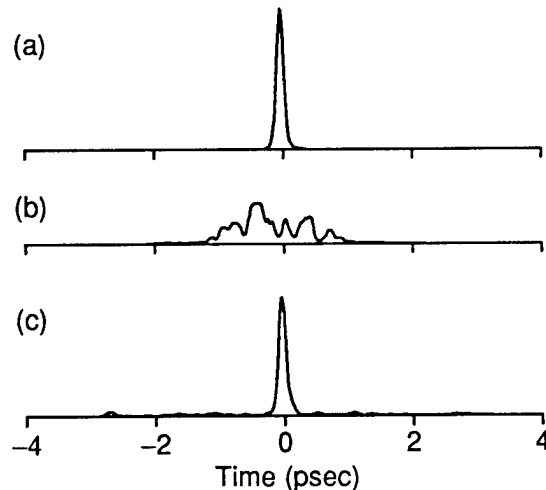

Fig. 3   Holographic matched filtering of coded ultrafast waveforms. (a) None of pulses are coded. (b) The signal is coded using pulse shaping. (c) Both signal and test pulses are coded, resulting in matched filtering operation and a restored output pulse.

In addition to pure time-domain processing, holography can also be applied to implement time-to-space conversion operations, which in principle could make possible demultiplexing of ultrahigh-speed data packets. In time-to-space conversion experiments [7], spectral holograms are first recorded as above but are then read-out using a CW laser diode in place of a femtosecond test pulse. The laser diode "interprets" the spectral hologram as containing spatial information; therefore, reconstruction of the hologram provides a spatial version of the original time-domain signal waveform. Experiments demonstrating time-to-space conversion were performed using a femtosecond Ti:sapphire laser source and a photorefractive thin film of GaAs/GaAlAs multiple quantum wells operating as the holographic material. The use of a dynamic photorefractive film

allows the spectral hologram to adaptively track variations in the incoming signal, and read-out at the exciton peak improves sensitivity and diffraction efficiency.

One objective of our current research is to expand on the relationship between time and space in pulse shaping and spectral holography to convert (transmultiplex) between high-speed optical signals coded in different representations. In addition to time-to-space (serial-to-parallel) conversion as above, we also aim to demonstrate all-optical methods for converting from space to time (parallel to serial), from time to wavelength, and from wavelength to time. Furthermore, by processing the space domain signals using smart pixel arrays, more sophisticated operations (e.g., time slot or wavelength slot interchanging) may be implemented. An generic view of signal processing via time-space-wavelength transformations is shown in Fig. 4.
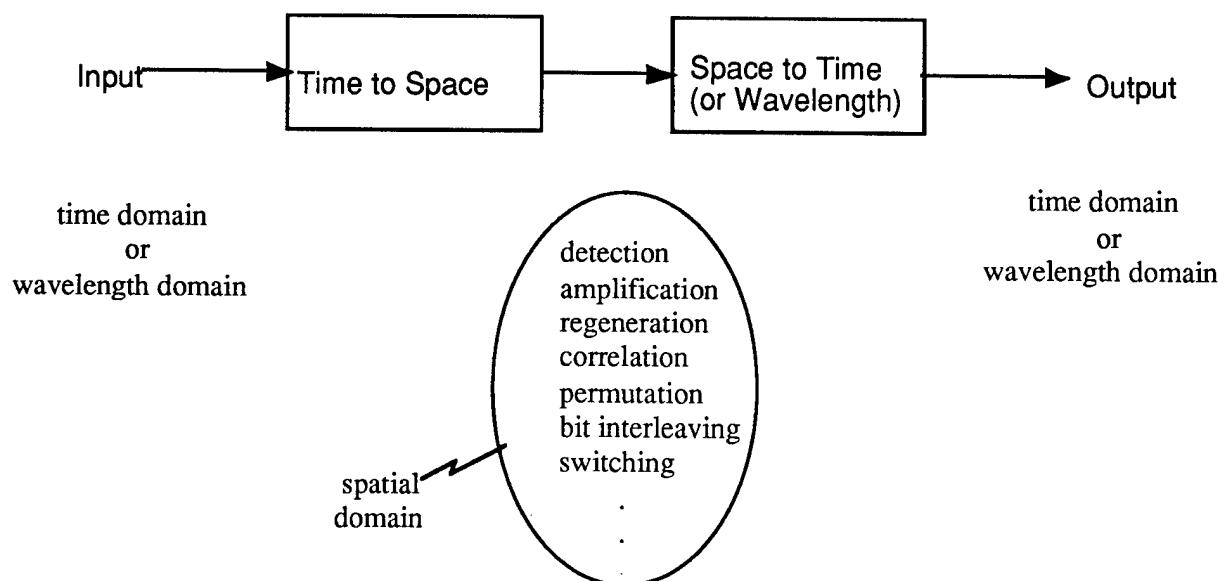

Fig. 4. Generalized holographic pulse processing. By converting interchangeably between time, space, and wavelength domains, sophisticated transmultiplexing applications may be possible.

In summary, we describe a variety of femtosecond optical signal processing techniques based on extensions of the well known methods of Fourier optics and holography.

References

1. A. M. Weiner, "Femtosecond optical pulse shaping and processing," Prog. Quantum Electron. **19**, 161-238 (1995).
2. A. M. Weiner, J. P. Heritage, and E. M. Kirschner, "High-resolution femtosecond pulse shaping," J. Opt. Soc. Amer. B **5**, 1563-1572 (1988).
3. A. M. Weiner and D. E. Leaird, "Generation of Terahertz-Rate Trains of Femtosecond Pulses by Phase-only Filtering," Optics Letters **15**, 51-53 (1990).
4. Y. T. Mazurenko, "Holography of Wave Packets," Appl. Phys. B **50**, 101-114 (1990).
5. A. M. Weiner, D. E. Leaird, D. H. Reitze, and E. G. Paek, "Femtosecond Spectral Holography," IEEE J. Quantum Electron. **28**, 2251-2261 (1992).
6. A. M. Weiner and J. A. Salehi, "Optical Code-Division Multiple-Access," in *Photonics in Switching,* J. Midwinter, ed. (Academic Press, San Diego, 1993), vol. II, pp. 73-118.
7. M. C. Nuss, M. Li, T. H. Chiu, A. M. Weiner, and A. Partovi, "Time-to-Space Mapping of Femtosecond Pulses," Opt. Lett. **19**, 664-666 (1994).

TEMPORAL PHASE-CONJUGATION WITH SPACE-TIME PROCESSORS

Dan M. Marom, Pang-chen Sun, and Yeshayahu Fainman

University of California at San Diego
Department of Electrical and Computer Engineering
La Jolla, CA 92093-0407

An all-optical parallel-to-serial and serial-to-parallel conversion by holographic spatial-to-temporal and temporal-to-spatial frequency encoding aimed at applications in high-speed optical communications have recently been demonstrated[1]. In this manuscript we analyze the performance of the system with ultra-short pulses.

The spatial-to-temporal frequency encoding processor (Fig. 1a) consists of two independent optical channels for carrying temporal and spatial signals. The temporal information carrying channel consists of a pair of gratings and a 4-F lens arrangement. The incident pulses are transformed by the input reflecting grating and the first lens into a temporal frequency spectrum distributed on the focal plane, in spatial domain, while the second lens and the output reflecting grating perform the inverse transformation of the temporal spectrum distribution back to the time domain. The spatial information carrying channel utilized with a CW laser source is a simple optical spatial Fourier transform arrangement consisting of the input image and the reference waves introduced via a beamsplitter to share the second lens of the temporal channel in the backward direction. To achieve interaction between the temporal and spatial frequencies information, a real time holographic material in a four-wave mixing arrangement is used.

When characterizing the all-optical processor, an assumption is being made concerning the bandwidth $\Delta\omega$ of the pulses, to simplify the calculations. Specifically, $\Delta\omega/\omega_c \approx 1\%$, justifying an estimation of ω by ω_c, where ω_c is the central optical frequency. While this assumption is valid for pulses of duration in the hundreds of femtoseconds, it does not hold for shorter pulses. By substituting a first-order approximation for ω of the form $\omega \equiv \omega_c + \delta\omega$, we gain a better understanding of the system performance and its unique advantages.

The output of the system, in space-time coordinates $(x'';t)$, as given by Eq. 8 of Ref. 1

$$s_0(x'';t) = F_\omega^{-1}[\{P(\omega - \omega_c)\exp[-j(\omega - \omega_c)t_0]\}$$
$$\times \left\{ \sum_n A_n w''\left[-x'' + n(\frac{\omega_w}{\omega}\Delta)\alpha\right]\exp\left[-j\frac{n(\omega - \omega_c)\omega_w\Delta}{c\omega}\alpha\right]\right\}], \tag{1}$$

where the term in the first wiggled parenthesis represents the spectrum of the pulse, the term in the second wiggled parenthesis is the frequency response of the system, F_ω^{-1} denotes the inverse Fourier transform (FT), $P(\omega)$ is the temporal FT of the envelope of the pulse, ω_w is the frequency of the CW source used to record the hologram, Δ is the spatial separation between channels in the spatial domain, $\alpha = \sin(\theta)$ with θ being the inclination angle between the incident wave and the reflection grating, n is the integer corresponding to the n-th spatial channel, A_n is the bit information in the n-th channel, t_0 is the temporal delay between the signal and the reference waves (see Fig. 1a), and c is the speed of light. The frequency ω is replaced by $\omega_c + \delta\omega$, and $\frac{1}{\omega} = \frac{1}{\omega_c + \delta\omega} \cong \frac{1}{\omega_c} - \frac{\delta\omega}{\omega_c^2}$, as $\delta\omega \ll \omega_c$. This assumption will be valid for bandwidths as large as 10% of the optical carrier. Thus, the output assumes the form

$$s_0(x'';t) = \sum_n A_n \exp[j\omega_c t] \int\limits_{-\infty}^{\infty} P(\delta\omega)w''\left[-x'' - n\Delta'' - n\Delta''\frac{\delta\omega}{\omega_c}\right]$$

$$\times \exp\left[j\frac{n\Delta''}{c\omega_c}\delta\omega^2\right]\exp\left[j\delta\omega(t - t_0 - n\frac{\Delta''}{c})\right]d\delta\omega \ , \tag{2}$$

where $\Delta'' \equiv \dfrac{\alpha\omega_w\Delta}{\omega_c}$. The additional shift term, $n\Delta''\dfrac{\delta\omega}{\omega_c}$, and the quadratic phase, $\exp\left[j\dfrac{n\Delta''}{c\omega_c}\delta\omega^2\right]$ of Eq. 2, represent the change from derivation in the original paper [1].

For simplicity, a Gaussian pulse of duration τ in the time domain is assumed. Temporal and spectral forms of the pulse are related by the Fourier transform pair

$$p(t) = \exp\left[-\frac{t^2}{2\tau^2}\right] \overset{FT}{\Longleftrightarrow} P(\omega) = \tau\exp\left[-\frac{\tau^2\omega^2}{2}\right]. \tag{3}$$

The output of the processor for an incident, transform limited, Gaussian pulse is given by

$$s_0(x'';t) = \sum_n A_n \exp[j\omega_c t] \int\limits_{-\infty}^{\infty} \tau\exp\left[-\frac{\tau^2\delta\omega^2}{2}\right]\exp\left[j\frac{n\Delta''}{c\omega_c}\delta\omega^2\right]$$

$$\times w''\left[-x'' - n\Delta'' - n\Delta''\frac{\delta\omega}{\omega_c}\right]\exp[j\delta\omega t_n]d\delta\omega, \tag{4}$$

where $t_n \equiv t - t_0 - n\dfrac{\Delta''}{c}$ is the time delay of the n-th pulse or bit encoded. The first term in the integral of Eq. 4 is a Gaussian pulse spectrum (therefore band-limited), the second term is a quadratic phase term and the third term is the input aperture, of duration much longer than the Gaussian pulse. Assuming $\delta\omega/\omega_c = 10\%$, the effect of the aperture can be neglected. A similar justification does not apply to the quadratic phase term. The quadratic phase results in a frequency chirp imposed on the pulse spectrum. After solving Eq. 4, the output becomes

$$s_0(x'';t) = \sum_n A_n \exp[j\omega_c t]w''[-x'' - n\Delta'']\frac{1}{\sqrt[4]{1 + \xi^2 n^2}}\exp\left[j\frac{n\xi}{2}\right]\exp\left[-\frac{t_n^2}{2\tau^2}\frac{1 + j\xi n}{1 + \xi^2 n^2}\right], \tag{5}$$

where we used the definition $\xi \equiv \dfrac{2\Delta''}{c\omega_c\tau^2}$. Eq. 5 describes a sequence of temporal pulses, each with a slightly shifted aperture position (as in Ref. 1), but with a different relative phase and a broadened pulse-width since these pulses are no longer transform limited. A simulated output for the amplitude sequence of such pulses is represented in Fig. 2. The information carrying pulses broaden on the expense of lowering their peak amplitude as their number in a sequence increases.

To determine the effect of the quadratic phase during the decoding process, we analyze the temporal-to-spatial frequency decoding processor [2] (Fig. 1b). The temporal pulses, corresponding to the encoded data bits, are interfered with a reference pulse. It is assumed that the intensity of the reference pulse is much higher than the intensity of each of the signal pulses, to neglect intersignal interference terms. Therefore, each signal pulse interferes with the reference pulse independently. The pulses are incident on a reflecting grating and Fourier transformed by a lens. The pulses' temporal frequency spectrum interfere with the spectrum of the reference pulse in space, at the focal plane of the system. A real time volume hologram is recorded by the interference pattern and read out with a CW laser source. The CW diffracted field is FT to the spatial domain to represent, back in space, the original data of the encoded bits.

The interference of the reference pulse envelope, $r(t) = \exp\left[-\dfrac{t^2}{2\tau^2}\right]$, which is identical to that

of $p(t)$, and $s_n(t) = \dfrac{1}{\sqrt[4]{1+\xi^2 n^2}}\exp\left[j\dfrac{n\Delta''}{2}\right]\exp\left[-\dfrac{t_n^2}{2\tau^2}\dfrac{1+j\xi n}{1+\xi^2 n^2}\right]$ for the n-th signal pulse

envelope, as obtained from Eq. 5, is analyzed (t_n is the pulse separation, given by

$t_n = t_0 + \dfrac{n\Delta''}{c}$). The effect of the aperture of the encoder, $w''[-x'' - n\Delta'']$, is canceled after

coupling the pulses into a fiber for transmission. The temporal spectrum of the signal, $S_n(\omega)$, and that of the reference pulse, $R(\omega)$, are both affected the system's frequency response, $W(\omega)$, determined by the FT of the grating aperture. These two spectra are superimposed in the holographic material that responds to the intensity distribution, $|S_n(\omega)W(\omega) + R(\omega)W(\omega)|^2$. The holographic signal $S_n^*(\omega)R(\omega)|W(\omega)|^2$ corresponds to the desired diffraction term. Integrating over all frequencies to obtain the average fringe pattern, results in

$$H(x) \equiv \int_{-\infty}^{\infty} S_n^*(\omega)R(\omega)|W(\omega)|^2 d\omega \propto \int_{-\infty}^{\infty} \exp\left[-(\omega - \omega_c)^2 \tau^2\right]$$
$$\times \exp\left[j(\omega - \omega_c)^2 \dfrac{n\Delta''}{c\omega_c}\right]\exp\left[-j(\omega - \omega_c)t_n\right]\left|W(x + \dfrac{\omega - \omega_c}{\omega}\alpha F)\right|^2 d\omega. \tag{6}$$

Recalling the earlier assumption $\omega \equiv \omega_c + \delta\omega$, we use $\dfrac{\omega - \omega_c}{\omega} = \dfrac{\delta\omega}{\omega_c + \delta\omega} \cong \dfrac{\delta\omega}{\omega_c} - \left(\dfrac{\delta\omega}{\omega_c}\right)^2$ to

approximate the quadratic phase term of Eq. 6. Assuming an infinite input aperture, the frequency response of the system, $W(\omega)$, can be approximated by $\delta(x + \dfrac{\omega - \omega_c}{\omega}\alpha F)$, which is applied to the approximate version of Eq. 6, resulting in

$$H(x) = \exp\left[-\omega_c^2 \tau^2\left(\dfrac{x}{\alpha F} - \dfrac{x}{x + \alpha F}\right)\right]\exp\left[j\dfrac{\omega_c \Delta'' x n}{\alpha c F}\right]\exp\left[-j\dfrac{\omega_c x t_0}{x + \alpha F}\right]. \tag{7}$$

The first exponential term of Eq. 7 corresponds to a Gaussian envelope defining the aperture of the hologram. The second exponential term is a linear phase function that is linearly dependent on the signal order n, corresponding to a unique diffraction angle. The last exponential term is a phase term that depends on the frequency components (or location on spectral plane, x) and t_0 is the separation time between reference pulse and center of symmetry of the encoded bits. Placing the reference pulse to obtain $t_0 = 0$ will eliminate this spectrum dependent shift.

We analyzed space-time processors considering the effects of using ultra-short pulses for spatial-temporal encoding-decoding. These processors are shown to posses temporal phase-conjugation property necessary for distortionless communication of spatial information. Furthermore, this approach is self-referenced since when the signal and the reference are transmitted through the same distorting media (e.g., fiber link) their accumulated but identical phase distortions will be automatically compensated by the holographic recording process in the time-space processor.

References:
1. Sun, P. C. et al, *Opt. Lett.* 20, p. 1728 (1995).
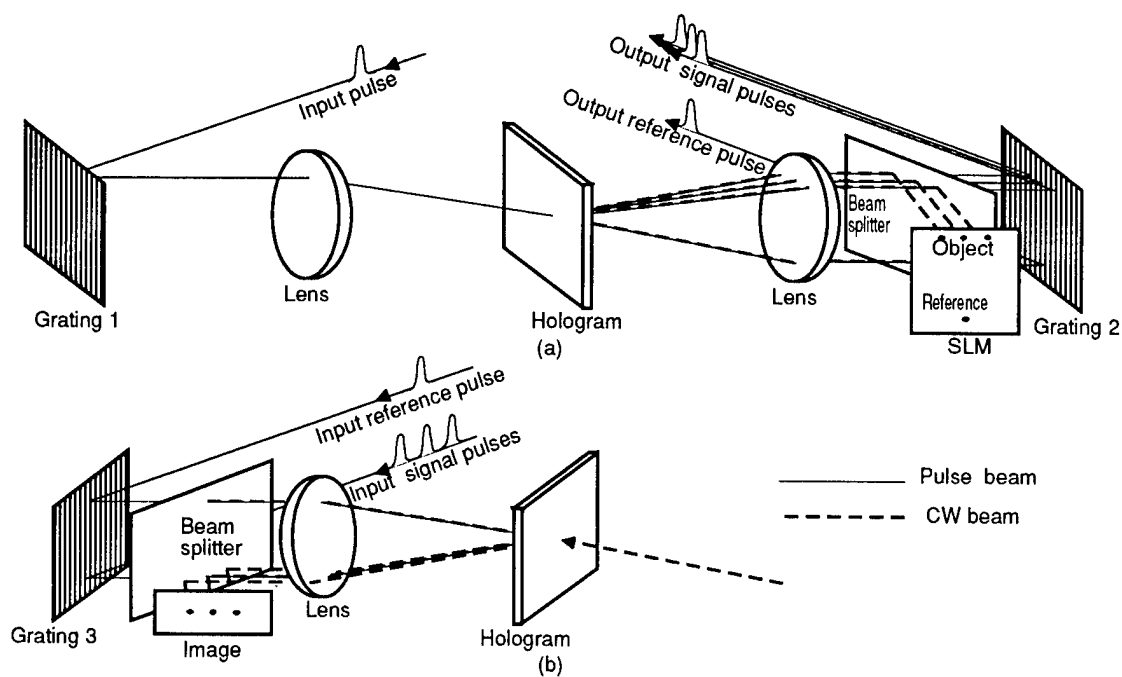2. Nuss, M. C. et al, *Opt. Lett.* 19, p. 664 (1994).

Fig.1 Schematic diagram of optical processors for (a) parallel-to-serial conversion and
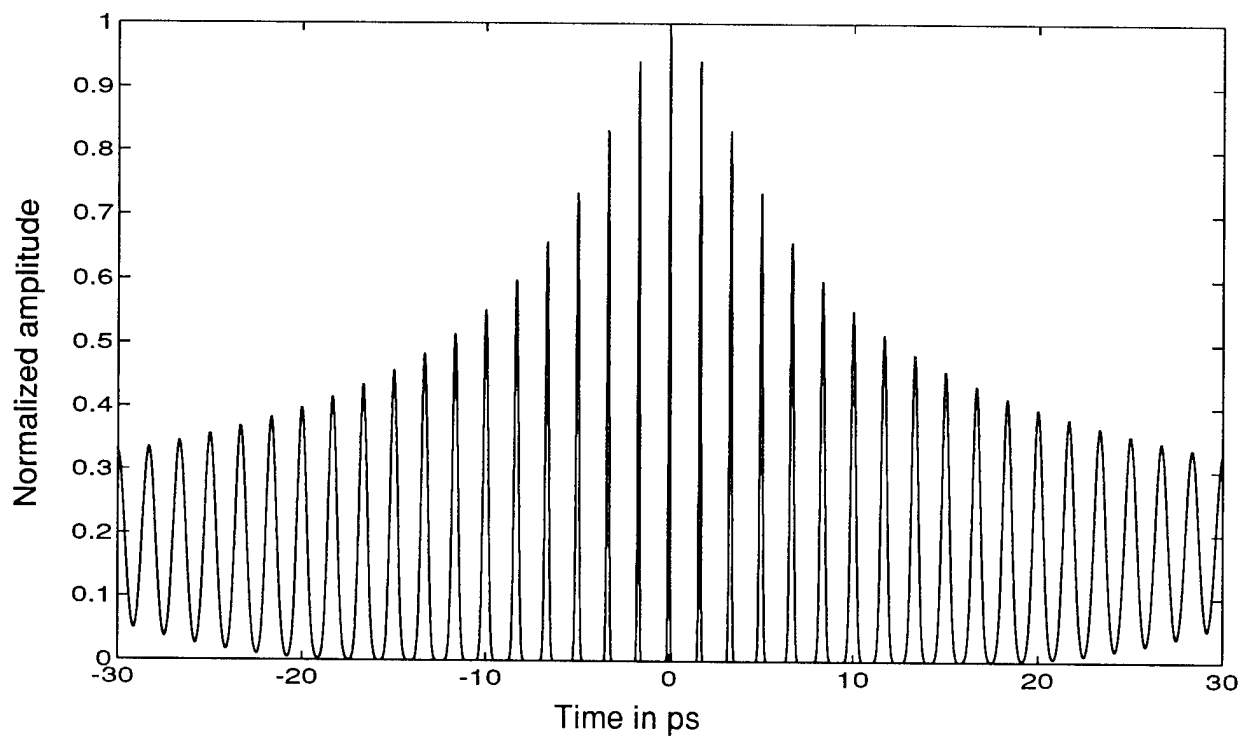(b) serial-to-parallel conversion.

Fig.2 Simulated output chirped pulses. 40 fs pulses with Δ"=0.5 mm (yielding ξ=0.52)

2D Phase Unwrapping of a Noise Contaminated Optical Interferogram

Ching-Wei Liao and M. A. Fiddy
Department of Electrical Engineering
University of Massachusetts Lowell
Lowell MA 01854
508 934 3359
fax: 508 934 3027
fiddy@cae.uml.edu

Introduction

Phase unwrapping of interference patterns is a well recognized problem, important in surface profiling and wavefront detection, [e.g. 1]. The wrapped phase function is a non-bandlimited function meaning there is no adequate sampling rate in the neighborhood of the wrapped regions. Previously, authors such as Tribolet [2] have tried to deal with 1D unwrapping uncertainties by using an adaptive sampling scheme along with continuity arguments. This approach, while frequently successful, is tedious at best. Other approaches involve taking least squares or Bayesian techniques [e.g. 3] .

In 2D there are undersampling problems in addition to those created from existence of wavefront dislocations. The lines of the wavefront dislocations are associated with the existence of real point zeros in the wavefront, which occur quite frequently in coherent wavefronts, especially those containing speckle. There is difficulty correctly estimating the phase near these lines and even the phase differences in these regions might be in error. The consequence of this is that the required phase unwrapping frequently fails and the corresponding 3D surface profile or phase profile is distorted along arbitrary erroneous paths.

In this paper we demonstrate how knowledge of the locations of the real point zeros of the complex field can remove the need for time consuming adaptive sampling schemes such as Tribolet's and directly assist with the unwrapping. Each zero defines a specific phase behavior analytically.

Since our primary goal is to recover a 3D profile, such as a landscape, surface structure or optical surface, we illustrate our approach on real data collected from the surface of a coin. We show the recovery of a surface shape estimate to high resolution from the interference pattern, which contains both noise and shows evidence of wavefront dislocations. In our experiment we use an optical interferometer which generates two tilted plane waves falling on the coin's surface. A uniform interference pattern of equidistant fringes would appear on an optically flat surface. We image this pattern and digitize it for unwrapping. The associated phase map is severely wrapped and the regions in which the wavefront dislocations are located are self-evident. The sampling of the image in these regions is fixed by the CCD and choice of magnification used. It is invariably inadequate to allow imposition of continuity arguments to unwrap the pattern and the wavefront dislocations cannot be avoided. However, we make use of the point zero locations to determine the phase unambiguously in the neighborhood of the dislocations.

We evaluate the performance of this unwrapping scheme and present the trade-offs between the choice of adaptive sampling and the precision with which we locate the zeros. In addition we discuss the significance of the chosen sampling rate compared with the accuracy of the zero locations.

References

[1]   J. C. Wyant, and K. Creath, "Advances in interferometric profiling", Int. J. Mach. Tools Manuf. 2, pp5-10, (1992).

[2]   J. Tribolet, "A new phase unwrapping algorithm", IEEE Trans. ASSP, 25 pp170-177, (1977).

[3]   H. Takajo and T. Takahashi, "Least squares phase estimation from the phase difference", J. Opt. Soc. Amer., 5, pp416 - 425, (1988).

Materials

HTuA   8:30 am-10:00 am
Commonwealth Room

Willis S. Colburn, *Presider*
Kaiser Optical Systems Inc.

Photopolymer Materials for Holography

Kirk W. Steijn, William J. Gambogi and T. John Trout
DuPont Holographic Materials
Wilmington, Delaware 19880-0352

1. Introduction

Interest in holograms as diffractive optical elements began with the early recognition of the correspondence of transmission holograms and Fresnel zone plates.[1,2] Optical designs based on holographically-generated optical elements (HOEs) and the extension of computer-based design programs to holographic gratings appeared in the late 1960s.[3,4,5] Use of HOEs in systems was limited, however, in part due to complicated processing and lack of environmental stability in available materials. Recent developments in polymeric materials for holography invite reconsideration of HOEs for emerging applications where unique function, weight, light efficiency and cost are premium considerations. OmniDex® Holographic recording films (HRFs) developed at DuPont provide benefits for the manufacturers of HOEs and optical systems that include excellent optical performance, dry processing, environmental stability, and mass reproduction. This paper reviews the holographic properties of these films and gives examples of simple HOE components.

2. Description of Films

HRFs consist of photopolymer film coated on a Mylar® polyester base (typically ~50 μm thick) in a thickness range from ~4 to >50 μm thick, depending on the application, and protected with a removable cover sheet (typically 25 μm thick Mylar). Recording typically consists of exposure to a visible-spectrum coherent light source for a total exposure of between 3 and 50 mJ/cm^2 (depending on film, wavelength, and grating type). The film is "real-time," forming a holographic grating during exposure. The film is then fixed and bleached via an incoherent flood exposure of 100-150 mJ/cm^2 of ultraviolet light. Subsequent heating of the film (typically 120° C for 2 hours) may be used to amplify the index modulation from 1.5x to 3x, depending on film type. It is useful to summarize the main types of HRFs and their typical performance.

HRF-150 is designed for use in transmission grating applications, and is normally coated at 20 μm and 38 μm thickness. The thicker coating provides diffraction efficiency that reaches 100% for 514.5 nm exposures with grating spacing of 0.4-1 μm with no heat processing.[6] Heat processing at 140° C for 2 hours will raise the achievable index modulation (Δn) from 0.009 before heating to 0.016, in which case the 20 μm thickness will achieve 100% efficiency for ~0.7 μm grating spacing.[7] Film speed is ~80 mJ/cm^2 in the blue-green spectral region.

HRF-600 is designed to achieve high index modulation in transmission gratings (Δn of 0.035-0.045 after 120° heat processing for 2 hours) for applications requiring large spectral bandwidth. The film speed is 25-35 mJ/cm^2 in the blue-green, and 100% diffraction efficiency can be achieved in films 7-8 μm thick. This film may also be used to make reflection gratings.[6]

HRF-700 is a high index modulation material for reflection gratings, achieving Δn of 0.045-0.055 with heat processing. This film has high photospeed in reflection and can be sensitized for the full visible spectrum. A number of papers have been published on full-color holography using HRF-700 film.[8,9,10] Blue sensitization (410-490 nm) provides film speeds of 5-10 mJ/cm^2 and Δn up to 0.055. Green-yellow (500-590 nm) performance is approximately 5-15 mJ/cm^2 with Δn of approximately 0.045. Red sensitization provides Δn of approximately 0.035 (600 nm to 670 nm) with a photospeed of 25-35 mJ/cm^2.

HRF-750 is also used primarily for reflection gratings and can be sensitized across the visible spectrum. This class of films has been developed for high glass adhesion, and has similar photospeed to the HRF-700 films though the index modulation is approximately 15-20% lower. HRF-750 films have also been developed that have a low-birefringence overcoating, which allows removal of the Mylar base prior to exposure and processing. These films are particularly useful for the creation of diffractive masters and other structures that are sensitive to birefringent layers. The mastering films are also used where a barrier layer is desirable, such as in the case of an applied adhesive.[7]

3. HOE Fabrication

HOE fabrication consists of four basic steps: design, mastering, replication and finishing or packaging. In the design phase, optical design software is used to determine the exposure conditions and holographic properties required to meet a given design and specification. The design software accounts for changes in the master and copies through each process step. This analysis identifies the critical physical and optical properties needed in the holographic recording films to be used in mastering and replication. Having selected the appropriate films, a diffractive master is produced for compatibility with the contact copy process. We have found that contact copy from a diffractive master results in excellent repeatability because it offers the highest mechanical and optical stability. Finishing allows packaging of the hologram for use in the system and may involve the application of adhesive, anti-scratch, anti-reflection or absorbing layers, cover layers or substrates.

4. Emerging Applications

The availability of commercial holographic photopolymers coupled with the ability to design and produce holographic elements has led to the development of innovative optical

systems using volume HOEs. The systems and designs being considered exploit the unique function, light weight, and advantageous packaging of holographic optical elements. Applications in which these performance and design advantages can be particularly important include liquid crystal display systems[11-14], lighting systems[15], and others.

5. Conclusions

With the introduction of commercial materials and production processes, applications of HOEs can now be effectively realized. Examples of simple holographic components are presented to illustrate the performance of these unique holographic materials and the HOEs that can be manufactured from them. A critical factor to the successful introduction of holographic components is a careful integration of the HOE design and performance into the complete system.

6. References

1. G. L. Rogers, "Gabor Diffraction Microscopy: the Hologram as a Generalized Zone-Plate," Nature **166** (4214) p. 237, 1950.

2. M. J. R. Schwar, T. P. Panda, and F. J. Weinberg, "Point Holograms as Optical Elements," Nature **215** (5098) pp. 239-241, 1967.

3. E. N. Leith and J. Upatnieks, "Zone Plate with Aberration Correction," J. Opt. Soc. Am. **57** (5), p. 699, 1967.

4. L. H. Lin and E. T. Doherty, "Efficient and Aberration-Free Wavefront Reconstruction from Holograms Illuminated at Wavelengths Differing from the Forming Wavelength," Applied Optics **10** (6), pp. 1313-1318, 1971.

5. J. N. Latta, "Computer-based analysis of hologram imagery and aberrations I. Hologram types and their nonchromatic aberrations," Applied Optics **10** (3) pp. 599-608, 1971.

6. W. J. Gambogi, W. A. Gerstadt, S. R. Mackara, and A. M. Weber, "Holographic transmission elements using improved photopolymer films," Proc. SPIE **1555**, pp. 256-267, 1991.

7. W. Gambogi, K. Steijn, S. Mackara, T. Duzick, B. Hamzavy and J. Kelly, "HOE Imaging in DuPont Holographic Photopolymers," Proc. SPIE **2152**, pp. 282-293, 1994.

8. W. J. Gambogi, W. K. Smothers, K. W. Steijn, S. H. Stevenson, and A. M. Weber, "Color Holography using DuPont holographic recording films," Proc. SPIE **2405**, pp. 62-73, 1995.

9. T. J. Trout, W. J. Gambogi, and S. H. Stevenson, "Photopolymer Materials for Color Holography," Proc. SPIE International Conference on Applications of Optical Holography, v. **2577**, pp. 94-105, 1995.

10. K. Steijn, "Multicolor recording in DuPont holographic recording film: determination of exposure conditions for color balance," Proc. SPIE **2688**, 1996.

11. J. Biles, "Holographic Color Filters for LCDs", SID94, pp. 403-406, 1994.

12. A. G. Chen, K. W. Jelley, G. T. Valliath, W. J. Molteni, P. J. Ralli and M. M. Wenyon, "Holographic reflective Liquid-Crystal Display", SID95 Digest, pp. 176-179, 1995.

13. N. Ichikawa, "Holographic Optical Element for Liquid Crystal Projector," Proc. Society for Information Display, Asia Display '95, pp. 727-729, 1995.

14. B. Loiseaux, C. Joubert, A. Delboulbé, J. P. Huignard, D. Battarel, "Compact Spatio-chromatic Single-LCD Projection Architecture," Proc. Society for Information Display, Asia Display '95, 1995.

15. R. Smith, "Holographic Center High-Mounted Stoplight", Proc. SPIE, **1461**, pp. 186-198, 1991.

Fast Photorefractive Multiple Quantum Well working at 1.55 μm

A. Le Corre, H. L'haridon, S. Salaün, R. Lever, M. Baudet, M. Gauneau, J.C. Keromnes, J. Pleumeekers, S. Mottet, B. Lambert, G. Moisan, C. Vaudry, C. De Matos, S. Gosselin
France Telecom CNET/LAB
Technopole Anticipa, 2 avenue Pierre Marzin
22307 LANNION Cédex France
tel: +33 96 05 15 16
fax: +33 96 05 18 16

1. Introduction

Fast optical switching devices based on resonant photorefractive (PR) phenomena in semi-insulating multiple quantum well (MQW) are very promising due to the large electrooptic effect related to Quantum Confined Stark Effect (QCSE) near the excitonic absorption peak. Up to now such structures were working at 0.8 μm in the GaAs-AlGaAs system [1,2]. This communication presents devices in the InP-GaInAs(P) system for telecommunication applications. Our aim is to obtain fast optical switching devices working at 1.55 μm with submicrosecond switching time and grating relaxation time larger than 1 microsecond.

The MQW, a series of wells (GaInAs) and barriers (GaInAsP), is sandwiched between two trapping regions. These trapping regions consist either of deep centers (InP: Fe electron traps / InP:Ti hole traps) or of InAs islands. The device was illuminated by an interference pattern at 1.32 μm (write beams) and an electric field was applied perpendicular to the MQW layers. In the illuminated regions, carriers are photogenerated and separated by the electric field. The carriers are trapped by trapping regions where they will screen the applied field. The diffraction grating results from absorption and refractive index variations induced by the modulation of space charge field and allows the diffraction of a read beam at about 1.55 μm.

2. Device optimization

In the GaAs-AlGaAs system efficient carrier escape times [3] (in the picosecond range) are obtained with $Al_xGa_{1-x}As$ barriers, the Al concentration of which is x = 29% and the width is L_B = 35 Å. So the electrons tunnel through the barriers and the holes escape by thermoionic effect [3]. Due to their heavy mass the holes cannot tunnel through the barriers. Unfortunately, in the InGaAs(P)-InP system the band offsets are reversed: for example, in the InGaAs-InP system the conduction and valence band offsets ΔE_c and ΔE_v have the values of 257 meV and 350 meV respectively. So the holes cannot escape by thermoionic effect. We chose a compromise with the quaternary (Q)

InGaAsP with a cut-off wavelength at about 1.18 µm (hereafter called $Q_{1.18}$). So the valence band offset ΔE_v is reduced to about 180 meV. In this case we may estimate the hole escape time to be in the 10 ps range [4] for 100 kV/cm field.

The PR structures are realized with a GSMBE (Gas Source Molecular Beam Epitaxy) on InP substrates. The thickness of the wells and barriers as well as the composition of GaInAs/GaInAsP MQW are optimized in order to efficiently remove both electrons and holes and separate them. As a result the change in absorption due to the QCSE remains important. The optimized structure consists of 110 periods (8.3nm)GaInAs/(8nm)GaInAsP (gap=1.05eV), surrounded by (500nm) carrier trapping layers. The semi-insulating (SI) Fe doped InP layers, grown at low temperature (460°C), show a high resistivity above 10^8 Ωcm and the resistivity of Ti and Be codoped InP is larger than 5.10^6 Ω.cm. For InAs islands, used as deep trap layers, the growth conditions have been optimized in order to develop coherent large size islands with strong luminescence at about 2 µm which demonstrates an efficient carrier trapping at room temperature [5].

In order to have an effective screening of the applied field and to avoid a short-circuit of the space charge distributions via the top electrode, a (100-200 nm) SiO_2 dielectric layer is introduced between the PR structure and a gold semi-transparent electrode. Two types of devices were realized: single and double dielectric devices. To obtain a symmetric component, the PR structure was sandwiched between two SiO_2 insulating layers and two semi-transparent conducting (100 Å of Au) layers and were Van der Waals bounded on a sapphire substrate. Both devices can work by transmission or reflection. For the reflection measurements, one of the semi-transparent gold electrodes was replaced by a reflective one, which acts as a mirror. The thicknesses of the PR structure and the SiO_2 layer can be calculated to obtain a resonant cavity.

3. Electro-absorption measurements

Electro absorption (EA) measurements have been performed on p/n junction using a Fourier transform spectrometer. Absorption spectra as a function of the electric field are reported in figure 1 and illustrate the QCSE. The absorption coefficient at the heavy hole excitonic resonance is 12200 cm^{-1} without electric field. The EA variation and the change in index of refraction, derived through Kramers-Kronig transformation, are shown in figure 2 for 100 kV/cm applied field. The maximum change in the absorption coefficient due to QCSE is about 4750 cm^{-1} at 1.56 µm and the peak value of the refractive index change is 0.073. From EA measurements the difraction efficiency has been calculated and is reported in figure 3 for a 110 well structure. The maximum diffracted signal occurs at 1.56 µm with an output diffraction efficiency of 0.5%.
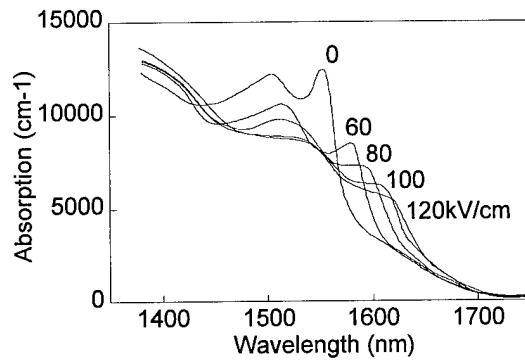
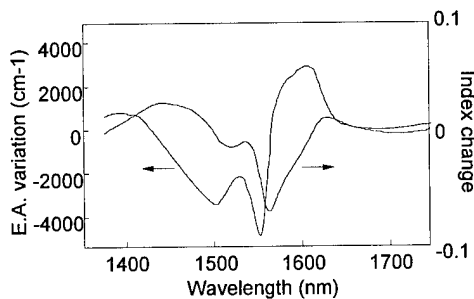Fig 1: Electroabsorption spectra for different applied electric field values

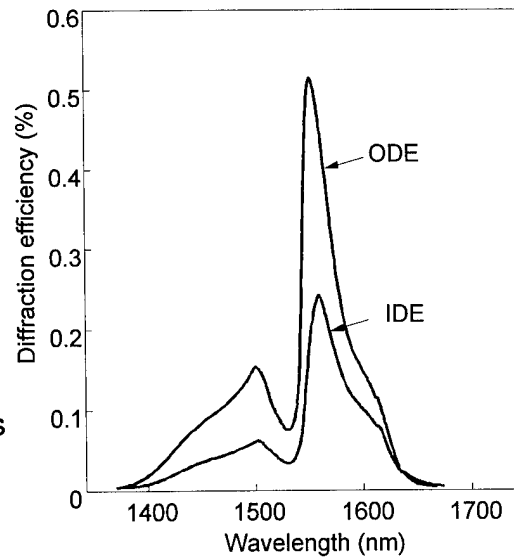Fig 2 : E.A. variation and refractive index change for a 100 kV/cm applied field

Fig 3 : Input Diffraction Efficiency (IDE) Output Diffraction Efficiency (ODE) curves calculated from E.A. experimental results of fig.2. The ODE was defined by the ratio of the power in the first-order diffraction beam (I_1) to the power of one transmitted beam (I_0) and the IDE the ratio of I_1 to the initial read beam (I_i)

4. Screening and diffraction measurements

We also investigated the time dependence of the phenomena. The beam from a 1.32 μm diode laser is modulated while a square wave voltage is applied to the device. A read laser beam at about 1.55 μm from a tunable DFB laser (Tunics) is amplified by an Er fiber amplifier (SVFO-Pirelli). In figure 4a we present the time dependant electro-absorption (TDEA) of a structure made from semi-insulating MQW and trapping regions into a p-n junction. The experiment is performed at the excitonic peak at V = 0 (1.55 μm). When we apply a negative voltage the E.A. decreases due to both the red-shift of the excitonic line and the decrease of the excitonic absorption (see figure 1). On figure 4b we see the effect of the 1.32 μm pulse (with an excitation density higher by one order of magnitude) on the TDEA. This effect corresponds to the screening of the applied field due to the photocarriers swept into the trapping regions. In opposite to structures without trapping zones, the screening effect persists after the 1.32 μm pulse.
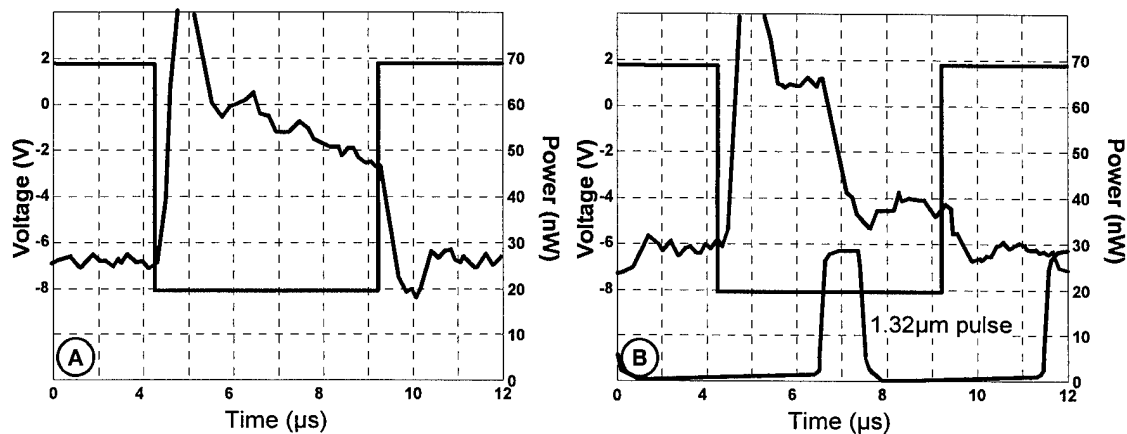
Figure 4: a/ Time resolved E.A. from a semi-insulating MQW structure Applied voltage in volts and modulated signal in nW. b/ Influence of 1.32 µm pulses.

Self-diffraction experiments with two 1.56 µm interfering beams from a tunable DFB laser (Tunics) are currently in progress. The measured ODE values are typically one order of magnitude lower than the values predicted in figure 3. This probably comes from the erasure of the grating due to lateral diffusion of carriers. We thus perform lateral diffusion measurements by shifting a 70 µm wide write slit (pulses of a few µJ/cm^2 at 1.32 µm wavelength) according to a 30 µm wide reading spot (1 µW CW at 1.56 µm wavelength). First results indicate a typical lateral diffusion length of 40 µm, increasing with the write pulse energy density and decreasing with the applied electric field.

In a next future we project to optimize the Fe and Ti doping. The Fe doping into the MQW has to be optimized to just compensate the residual donors [2]. On the contrary, increasing the Fe and Ti concentration in the trapping zones will increase the carrier trapping efficiency and thus decrease lateral diffusion. We also project in a next future to incorporate our structures into an optical microcavity (asymetric Fabry-Perot) in order to increase diffraction efficiency.

References

[1] A. Partovi, A.M. Glass, D.H. Olsoon, G.J. Zydzik, H.M. O'Brian, T.H. Chiu and W.H. Knox, ,Appl. Phys. Lett. 62 (1993) 464

[2] W.S. Rabinovich, S.R. Bowman, D.S. Katzer and C.S. Kyono Appl. Phys. Lett. 66 (1995) 1044

[3] A. Partovi, A.M. Glass, G.J. Zydzik, H.M. O'Brian, T.H. Chiu and W.H. Knox, Appl. Phys. Lett. 62 (1993) 3088

[4] H. Schneider, and K.V. Klitzing Phys. Rev. B38 (1988) 6160

[5] A. Le Corre, H. L'haridon, B. Lambert, S. Salaun and A. Ponchet, Euro-MBE - Sierra Nevada (Spain) 1995

Polymer-based Volume Hologram for a Surface-normal 3 x 3 Non-blocking Wavelength-selective Crossbar

Charles Zhou   Ray T. Chen
Microelectronics Research Center
University of Texas, Austin
Austin, TX 78758

We report the formation of a surface-normal non-blocking crossbar based on a unique wavelength switching scheme. The demonstrated device is shown in Fig. 1 where photopolymer-based volume holograms are employed in conjugation with graded index (GRIN) lenses. A prototype polymer-based volume hologram for multiple-wavelength 3 x 3 crossbar is experimentally demonstrated at 755, 765 and 775 nm. The unique beam routing property of GRIN lens reduces nine wavelengths to three wavelengths while maintaining the required nine (3 x 3) individual interconnects. The elimination of edge-coupling significantly enhances the packaging reliability. Furthermore, such a configuration is compatible with the implementation of vertical cavity surface-emitting lasers where the characteristic of azimuthal symmetry is maintained in the waveguide substrate [1].
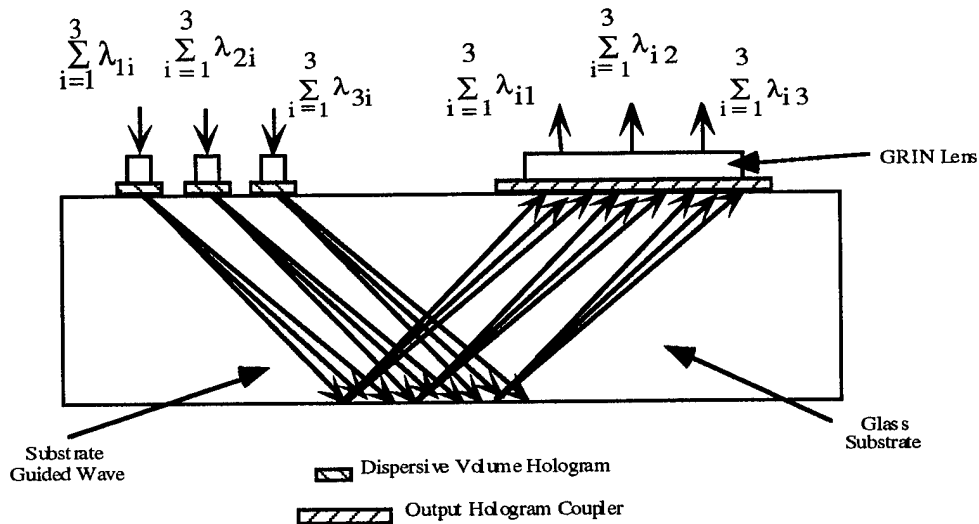
Fig. 1 Polymer-based volume hologram crossbar for a surface-normal 3 x 3 non-blocking wavelength selective crossbar. Note that the special characteristic of the GRIN lens reduces the nine wavelengths to three, i.e. $\sum_{i=1}^{3}\lambda_{i1} = \lambda_1 = 755nm$, $\sum_{i=1}^{3}\lambda_{i2} = \lambda_2 = 765nm$, $\sum_{i=1}^{3}\lambda_{i3} = \lambda_3 = 775nm$.

The phase gratings recorded in the photopolymer films are slanted, the central wavelength of the input surface-normal beam is designed to be diffracted with a maximum efficiency at the Bragg angle. The wavelengths which deviate from the center wavelength will

be dispersed at different substrate bouncing angles where discrete substrate modes are generated and zig-zaged within the substrate[2]. A GRIN lens after the output hologram coupler is used to separate channels with different angular frequencies. For a GRIN lens having a parabolic refractive index distribution profile of

$$N(y) = N(0)(1 - \frac{A^2}{2} y^2),$$ (1)

the paraxial ray path [3] can be predicted using

$$y(z) = y_0 \cos(Az) + \frac{\tan(\Delta\theta)}{A} \cdot \sin(Az),$$ (2)

where y is the radial distance from GRIN lens axis, z is axial distance from GRIN lens input surface, A is the GRIN lens constant, y_0 is the incident light radial distance and $\Delta\theta$ is the wavelength-dependent angular dispersion defined by the volume hologram.

The wavelengths and the paths equivalent to the experiment (Fig. 1) are summarized in Table 1. The results of the simulation is shown in Fig. 2 where GRIN lens is a quarter pitch, the GRIN lens constant A is 0.046 mm^{-1}. Note for Az = $\pi/2$, i.e., a quarter pitch GRIN pitch lens, only the second term of Eqn. (2) exists, therefore, incoming beams with same wavelength and $\Delta\theta$ (Table 1) will eventually come out from the same spot. In our experiment, rays with $\Delta\theta=0.5°$ ($\lambda_1=755$nm), $\Delta\theta=0°$ ($\lambda_2=765$nm), and $\Delta\theta=-0.5°$ ($\lambda_3=775$nm) were incident 1 mm off the center of the GRIN lens axis (Fig. 2). On the output surface, rays with the same initial angle of incidence converge at the same spot as we predicted. Therefore, employment of GRIN lens reduces nine wavelengths to three wavelengths while keeping the required interconnectivity. The incident angle differences are provided by the dispersive volume hologram. The use of GRIN lens provides the capability of surface mounting for holograms and fibers and thus it's more reliable and compact.

Table 1 Corresponding wavelengths and $\Delta\theta$s of the nine interconnects for 3 x 3 non-blocking crossbar.

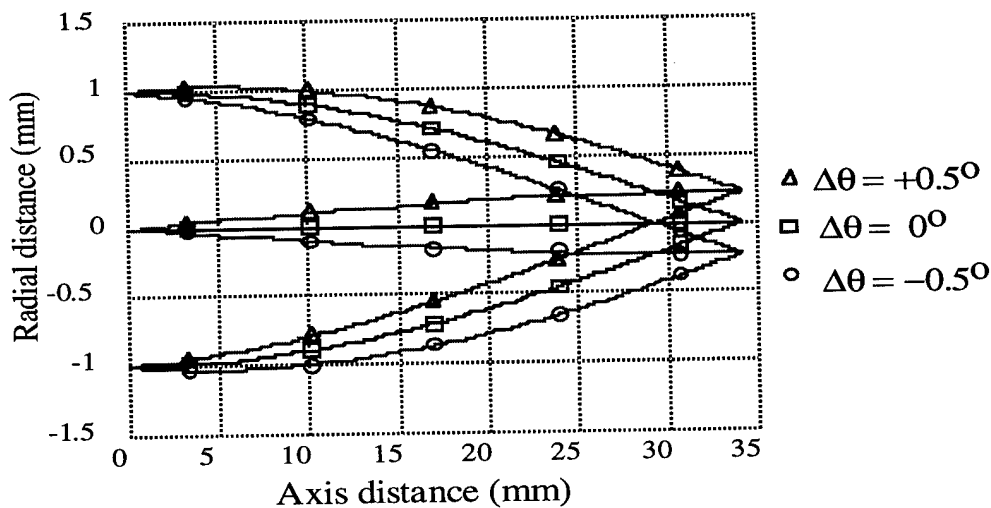| Output \ Input	1	2	3
1	$\Delta\theta=0.5°$ $\lambda_{11}=755$nm	$\Delta\theta=0.5°$ $\lambda_{21}=755$nm	$\Delta\theta=0.5°$ $\lambda_{31}=755$nm
2	$\Delta\theta=0°$ $\lambda_{12}=765$nm	$\Delta\theta=0°$ $\lambda_{22}=765$nm	$\Delta\theta=0°$ $\lambda_{23}=765$nm
3	$\Delta\theta=-0.5°$ $\lambda_{13}=775$nm	$\Delta\theta=-0.5°$ $\lambda_{23}=775$nm	$\Delta\theta=-0.5°$ $\lambda_{33}=775$nm

Fig. 2 Ray tracing of light with different incident angle in a quarter pitch GRIN lens.

In our configuration shown in Fig. 1, three input fibers each with a collimating GRIN lens on its end are attached surface normally to the input hologram coupler. The three wavelengths transmitted through one single fiber are dispersed by volume hologram at three different bouncing angles. As described by Eqn. (2), a quarter pitch output GRIN lens separates light with different colors (i.e. wavelength). The signal beams with a same wavelength from three separate input fibers are routed to the same spot at the output surface of the quarter pitch GRIN lens (Fig. 3), where a fiber array is attached (3 fibers in our case). Therefore by using only three wavelengths, a non-blocking 3 x 3 crossbar can be realized. The address of the sender in this case can be identified through the header encoded in the optical signal [4].

The experiment is conducted using a tunable Ti:Sa laser. DuPont polymer film HRF-600 having a thickness of 20 μm is employed and the hologram is recorded at 514 nm. The channel separation is measured to be 250 μm.

In summary, we present the first surface-normal non-blocking crossbar based on the wavelength dispersion of a volume hologram. 3 x 3 crossbar containing nine interconnections has been successfully demonstrated with wavelengths of 755, 765 and 775 nm. The unique property of the GRIN lens employed reduces the 9 required wavelengths to 3 while maintaining the 3 x 3 interconnections.

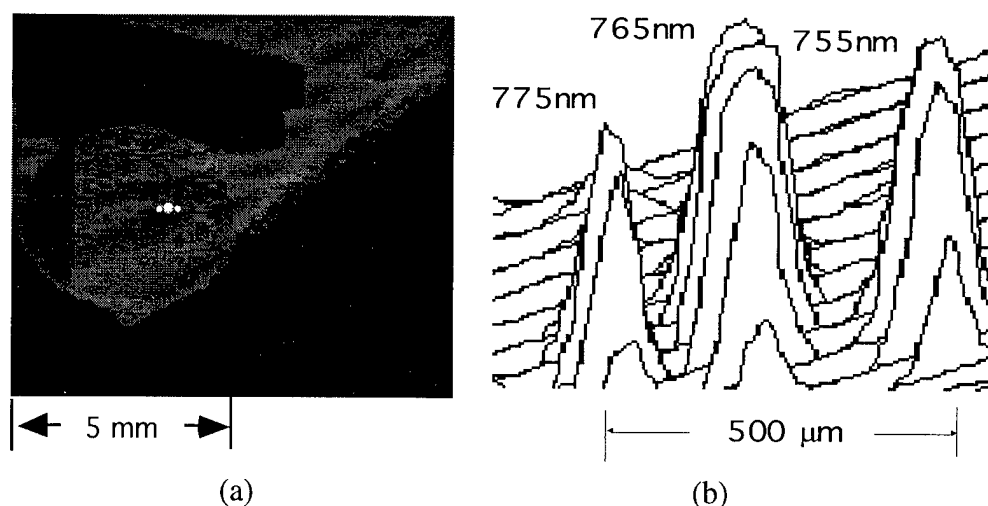(a)   (b)

Fig. 3 (a) Image of GRIN lens output surface showing three-wavelength channel separation   (b) Three-dimensional intensity profile of the three spots shown in Fig. 3(a).

Table 2   The measurement result of three-wavelength non-blocking crossbar.

Wavelength	Spot Size	Channel Separation
$\lambda_1 = 755$ nm	75 μm	
$\lambda_2 = 765$ nm	75 μm	250 μm
$\lambda_3 = 775$ nm	75 μm	

References:

1. Maggie M. Li and Ray T. Chen, "Five-channel surface-normal wavelength division demultiplexer using substrate guided waves in conjunction with polymer-based Littrow hologram," *Opt. Lett.*, Vol.20(7), pp.797, 1995.

2. Maggie M. Li and Ray T. Chen, " Two-channel surface-normal wavelength division demultiplexer using substrate guided waves in conjunction with multiplexed waveguide holograms," *Appl. Phys. Lett.,* Vol.66(3), pp.262-264, 1995.

3. W. M. Rosenblum, J. W. Blaker and M. G. Block, "Matrix methods for the evaluation of lens systems with radial gradient-index elements," American Journal of Optometry and Physiological Optics,   Vol. 65, No. 8, pp. 661-665.

4. IEEE Standard for Scalable Coherent Interface (SCI), IEEE STD 1596-1992.

HOLOGRAPHIC RECORDING KINETICS IN PHOTOPOLYMER MEDIA

E. Kovalenko, S. Sharangovich, T. Zelenskya

Department of Microwave and Quantum Electronics, Tomsk State Academy of Control Systems and Radio Electronics, 40 Lenin Avenue, Tomsk 634050, Russia. Phone: 007-3822-496224. Fax:007-3822-223262.

1. INTRODUCTION

Holographic information recording in photopolymer media is of great importance and lately has been under the thorough study [1-3]. It is found that with these materials there are some important features in comparison with the recording in photorefractive crystals. First, it is necessary to take into account the dynamic in behaviour of many medium components, involved into the process of the of the radical polymerization [4]. Second, while describing the kinetics of a holographic recording one should take into consideration medium average parameters changing in time. The diffusion processes of interaction components and also of inert component are of great importance [2]. Finally, the considerable variations of kinetic coefficients such as medium viscosity, diffusion coefficients, break reactions parameters of polymeric chain in polymerization process are also very important for description of kinetics recording [3]. All these effects require complex non-linear equations. In this work the analytical solution of the problem about the holographic information recording in photopolymer media for the cases of relatively small light diffraction on the recorded grating, the effects of self diffraction being neglected and the light field being given.

2. MAIN EQUATION

The sketchy way of radical polymerization includes some stages [4]. On the first stage the molecule of the dye absorbs the quantum of light radiation and interacting in excited condition with monomer molecule leads to formation of initial radical. On the second stage there appears a chain reaction of growth in polymeric chain as a result of interaction between the initial radicals and molecules of a monomer. The velocity of growth is defined by a chain growth parameter K_g. Finally, on the third stage the chain break is taken place as a result of interaction of two polymeric radicals and it brings to emergence of some non-active polymeric chains which are the final product of polymerization. The velocity of the break of the polymeric chain is described by a break parameter K_b.

For the mathematical description of the processes in the present scheme the theory of radical polymerization [4] is taken as a starting point. The description is much more simple, if the specific time of concentration changes of dye-stuff and monomer is longer in comparison with the excited conditions relaxation time τ_0 and the time for gaining the balance in the radical ensemble. In this case for the concentration of excited molecules of the dye K^* and for the radical concentration N we have

$$K^* = \frac{\alpha I(\mathbf{r})K}{1/\tau_0 + \beta M}; \qquad N = \sqrt{\frac{\alpha\beta K I(\mathbf{r})M}{K_b(1/\tau_0 + \beta M)}};$$

where α is a dye absorption coefficient, K is a dye concentration, β is a photoreaction parameter. As a result for the velocity of monomer concentration changes M is:

$$\frac{\partial M}{\partial t} = \mathrm{div}\big(D_m\,\mathrm{grad}\,M\big) - K_g K_b^{-1/2}\sqrt{\frac{\alpha\beta K I(\mathbf{r})}{1/\tau_0 + \beta M}}\,M^{3/2}, \qquad (1)\backslash$$

where $I(\mathbf{r})$ is an intensity of the light radiation in the point of radius-vector $\mathbf{r}$, D_m is a monomer diffusion coefficient.

Variation M in time in some point leads, due to the polymerisation process, to the changes in time of the polymeric molecules density in that point. The displacement of the inert component also occurs due to monomer diffusion processes. All the things bring about the changes in the refraction index n. To describe the variation in n let us apply the Lorentz-Lorenz formula. Then

$$\frac{\partial n}{\partial t} = \frac{\left(n^2 + 2\right)^2}{6n} \frac{4\pi}{3} \left(\alpha_m \frac{\partial N_m}{\partial t} + \alpha_p \frac{\partial N_p}{\partial t} + \alpha_i \frac{\partial N_i}{\partial t} \right), \qquad (2)$$

where N_m, N_p, N_i and $\alpha_m, \alpha_p, \alpha_i$ are the numbers of molecules in a unite of volume and polarizations of the monomer molecules, the polymer and the inert component respectively. The variation of N_m and N_p in a some points is taking place first, due to polymerization reaction, and if the average length of the polymeric change is l, then in accordance with the law of conservation of number of the participle $N_m + lN_p =$const and changes of n due to the polymerization reaction is

$$\left(\frac{\partial n}{\partial t}\right)_p = \delta n_p \left(\frac{\partial M}{\partial t}\right)_p = \delta n_p K_g K_b^{-1/2} \sqrt{\frac{\alpha\beta KI(\mathbf{r})}{1/\tau_0 + \beta M}} \cdot \frac{M^{3/2}}{M_0}.$$

Similarly, displacement of the inert component due to monomer diffusion into the illuminated area causes the changes of n in proportion to the velocity of the diffusion processes

$$\left(\frac{\partial n}{\partial t}\right)_d = \delta n_i \operatorname{div}(D_m \operatorname{grad} M),$$

where W_m is molecular weight of a monomer, δn_i is a parameter of the process,

$$\delta n_p = \frac{4\pi}{3} \cdot \frac{(n^2 + 2)}{6n} (\alpha_m - \frac{\alpha_p}{l}) \cdot \frac{M_0}{W_m},$$

As result, considering both processes of n, we have

$$\frac{\partial n}{\partial t} = \delta n_p K_g K_b^{-1/2} \sqrt{\frac{\alpha\beta KI(\mathbf{r})}{1/\tau_0 + \beta M}} \cdot \frac{M^{3/2}}{M_0} + \delta n_i \operatorname{div}(D_m \operatorname{grad} M). \qquad (3)$$

The set of equations (1),(3) is the basis for description of the hologram recording process in a photopolymeric substance.

3. ANALYTICAL DESCRIPTION OF THE RECORDING.

In a common case, to analyze the holographic recording, it is necessary to introduce the action of light beams forming the interference picture $I(\mathbf{r})$. Assuming the small diffraction efficiencies $I(\mathbf{r})$ can be taken as a given one and written

$$I(\mathbf{r}) = I_0 \left\{ 1 + \cos(\mathbf{K} \cdot \mathbf{r}) \right\}, \qquad (4)$$

where $\mathbf{K} = \mathbf{K}_1 - \mathbf{K}_2$ is a grating vector, $\mathbf{K}_1, \mathbf{K}_2$ are the wave vectors of the recording waves, whose intensity are considered to be equal.

The exact solutions of non-linear Eqs.(1),(3) can not be found. In first particular case when monomer diffusion are neglected we can find a simple exact solution for refractive index

$$n(\tau, \varphi) = n(0) + 0.5\delta n_p \left\{ 1 - \left(1 + \tau \cos(\varphi / 2)\right)^{-2} \right\}, \qquad (5)$$

where $\varphi=\mathbf{K}\cdot\mathbf{r}$, $\tau=t/T_p$, $T_p = \sqrt{\alpha\beta\tau_0 KM_nI_0}\,K_b^{1/2}/\sqrt{2}K_g$ is characteristic polymerization time. As it is seen Eq.(5) describe the nonharmonic behaviour of spatial distribution of index. In particular we can find the index average over grating period

$$n_0(\tau) = n(0) + 0{,}5\delta n_p\left\{1 - \frac{4}{\pi}\left(1-\tau^2\right)^{-3/2}\arctan\sqrt{\frac{1-\tau}{1+\tau}} + \frac{2\tau}{\pi(1-\tau^2)}\right\}. \tag{6}$$

The corresponding equation for the first harmonic amplitude of index grating has the form

$$n_1(\tau) = \frac{2\delta n_p}{\tau^2}\left\{\frac{1-3\tau^2/2}{\left(1-\tau^2\right)^{3/2}}\left(1 - \frac{2}{\pi}\arcsin\tau\right) + \frac{\tau(2-\tau^2)}{\pi(1-\tau^2)} - 1\right\}. \tag{7}$$

As a second particular case we will consider the situation when monomer diffusion make a substantial contribution to the polymerization process. In this case the zeroth and first harmonic in distributions $n(\varphi)$ and $M(\varphi)$ are principal only and the solutions of Eqs.(1),(3) can be found in the form

$$M(\tau,\varphi) = M_0(\tau) + M_1(\tau)\cos\varphi, \quad n(\tau,\varphi) = n_0(\tau) + n_1(\tau)\cos\varphi, \tag{8}$$

where we assume $M_1(\tau)\!\ll\!M_0$. In the result the index grating may be represent in the form

$$n_1(\tau) = n_{1p}(\tau) + n_{1i}(\tau), \tag{9}$$

where n_{1p} and n_{1i} characterize the contributions to first harmonic of index grating due to polymerization reaction and inert component displacement by monomer at its diffusion, respectively. For $n_{1p}(\tau)$ and $n_{1i}(\tau)$ we have

$$n_{1p}(\tau) = \delta n_p\left\{\frac{2}{9}\left(1-(1+\frac{\tau}{3})^{-2}\right) - \frac{56}{45}\Gamma(\alpha_0 - 2)\int_0^\tau(1+\frac{\tau'}{3})^{-\alpha_0-1}f(\tau')d\tau'\right\}, \tag{10}$$

$$n_{1i}(\tau) = \delta n_i\,\frac{4}{3}\frac{T_p}{T_m}\Gamma(\alpha_0-2)\int_0^\tau(1+\frac{\tau'}{3})^{-\alpha_0}f(\tau')d\tau', \tag{11}$$

where $\tau=t/T'_m$; $T'_m=\pi T_m/3$; $\alpha_0=2{,}8$; $T_m=1/|\mathbf{K}|^2 D_m$ is relaxation time of monomer grating;

$$f(\tau') = \exp\left[-3\frac{T_p}{T_m}\left(1+\frac{\tau'}{3}\right)\right]\left[\left(1+\frac{\tau'}{3}\right)^{\alpha_0-2}\gamma^*\left(\alpha_0-2;-3\frac{T_p}{T_m}\left(1+\frac{\tau'}{3}\right)\right) - \gamma^*\left(\alpha_0-2;-3\frac{T_p}{T_m}\right)\right\},$$

$\Gamma(x)$ is the Gamma-function; $\gamma^*(x,y)$ is the analytical form of the uncompleted Gamma-function.

4. CALCULATION RESULTS

The numerical results describing kinetics of index grating spatial distributions at $D_m=0$ are shown on Fig.1a (see Eq.(5)). It is seen that index grating have nearly harmonic behaviour in the region of small times and weak modulation of refractive index. The deviation from harmonic distribution are became critically at $t \geq T_p$ and are increased with time. If $t \Rightarrow \infty$ the grating has the form of the narrow lobes near the points $\varphi=\pi$ where $I(\mathbf{r})=0$. The amplitudes of the zeroth and first harmonics of refractive index (see Eqs.(6),(7)) are shown on Fig.1b as a

functions of time. As it is seen, $n_1(t)$ passes through maximum and tends to zero at $t \Rightarrow \infty$.

At $D_m \neq 0$ the dependencies of contributions $n_{1p}(\tau)$ and $n_{1i}(\tau)$ in the first harmonic amplitude calculated by Eqs.(10),(11) are represented on Figs.2(a),(b) as function of time and grating period. The last parameter are defined as $\xi = T_p/T_m = T_p |\mathbf{K}|^2 D_m$. The results in Fig.2(a),(b) indicate that the dependencies $n_{1p}(\tau)$ and $n_{1i}(\tau)$ are characteristically different. It allows to
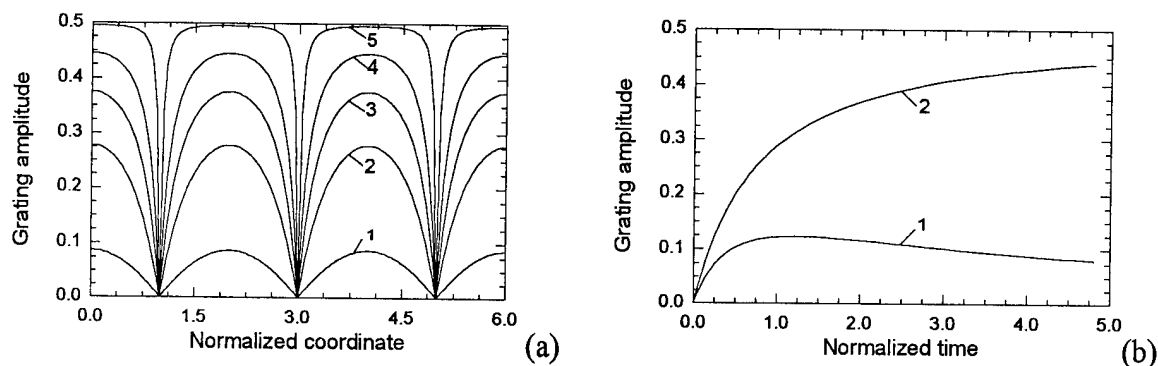
Fig.1 (a) Grating amplitude $(n(\tau,\varphi)-n(0))/\delta n_p$ as function of normalized coordinate φ/π at various $\tau = t/T_p$: (curves 1-5 ÷ 0,1;0,5;1;2;10), and (b) time dependencies of the first harmonic $n_1(\tau)/\delta n_p$ (curve 1) and the zeroth harmonic $(n_0(\tau)-n(0))/\delta n_p$ (curve 2).

separate these contributions by the corresponding processing of experimental data for holographic recording kinetics and to establish a main mechanism .of holographic recording in polymer medium under study.
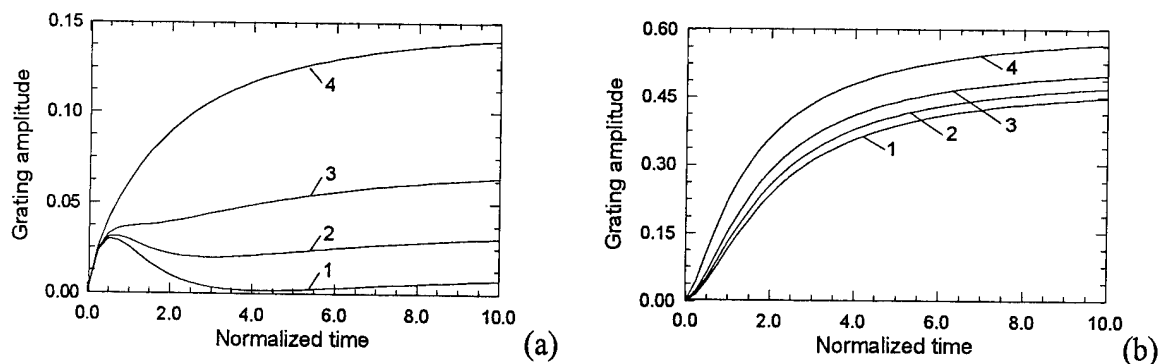
Fig.2 (a) The contributions in first harmonic grating amplitude (a) $n_{1p}(\tau)/\delta n_p$, (b) $n_{1i}(\tau)/\delta n_i$ as function of normalized time $\tau = t/T_m$ at various normalized parameters $\xi = T_p/T_m$ (curves 1-4 ÷ 1,25;1,5;2;5).

5. CONCLUSION

The analytical model of hologram recording kinetics in polymer materials is offered. The model take into account the changes of refractive index connected with the processes of photopolymerization and displacement of inert component on account of monomer diffusion. This model is in the qualitative agreement with the known experimental results and can be useful for destination and optimization of the parameters of the photopolymer materials.

REFERENCES

[1] V. Barashevsky, Proc. *SPIE*, Vol.2429, pp.12-21, 1994.
[2] E.Gulnasarov, T.Smirnova, E.Tixonov, *Journ.Techn.Phys.*, Vol.61,N10, pp.114-119,1991.
[3] A.Konstantinova, E.Pen, A.Sinyukov, V.Shelkovnikov, *Autometria*, N4, pp.31-36, 1993.
[4] H. Bagdasaryayn, *"Theory of radical polymerization"*, Nauka, Moscow, 1966.

DYNAMICAL MODEL OF RECONSTRUCTION AND AMPLIFICATION OF HOLOGRAMS IN PHOTOPOLYMER MATERIALS

Eugene S. Kovalenko , Sergey N. Sharangovich

Department of Microwave and Quantum Electronics, Tomsk State Academy of Control Systems and Radio Electronics, 40 Lenin Avenue, Tomsk 634050, Russia. Phone: 007-3822-496224. Fax:007-3822-223262.

1. INTRODUCTION

Recently it has been shown the possibility of making and using of the photopolymer materials which are organic light-sensitivity for purposes of holographic optical memory [1,2]. The main advantages of these media are the high light sensitivity and possibility to writing of holograms with the high diffraction efficiency. The experimental investigations showed that the photopolymerization peculiarities and the photopolymer composition component concentrations are significant in the dynamics of the reconstruction processes of holographic gratings [1,2]. However up to now available dinamical models of this phenomena have been developed only for composite and photorefractive materials [3,4]. These models do not give full explanation of present experimental results of kinetics peculiarities of read out process in photopolymer materials.

In this work the theoretical model describing the dinamical process of holograms reconstruction and their optical amplification in amorphous photopolymer material is developed. The peculiarities of kinetics of the hologram amplification, space-time transformation of the holographic gratings field , time evolution of the spectral-angle sensitivity of the amplification process are also discussed.

2. ASSUMPTIONS AND GENERAL EQUATIONS

We will consider the readout process of the holographic index grating with initial amplitude distribution $n_1(x,t=0)$ and grating vector $\mathbf{K}$ inside infinite layer $(0 \leq x \leq L)$ of photopolymer material as shown in Fig.1. A plane monochromatic light wave with amplitude A_0,, frequency ω and wave vector $\mathbf{k}_0$ is incident to the plane $x=0$ and is Bragg mismatched with initial grating. In the result of Bragg scattering ,.a diffracted plane wave with amplitude A_1 and wave vector $\mathbf{k}_1$ is generated. The incident and diffracted waves interfere inside photopolymer layer and form interference intensity pattern, which leads to the formation of new dinamical index grating. in the result of polymerization process. Note that dynamical grating is Bragg matched.
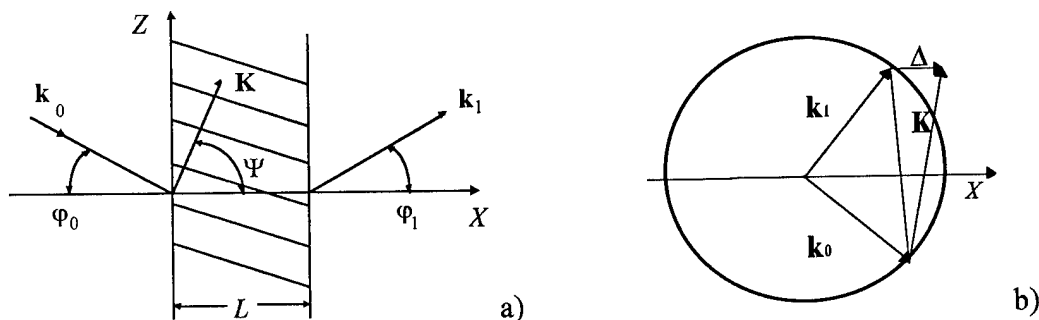

Fig.1 Diffraction geometry (a) and wave vector diagram

The spatio-temporal equations of examined problems can be derived from the wave

equation and equations of photopolymerization kinetics and components diffusion at recording process in photopolymer material Assuming the smallness of diffraction efficiency and using the slowly varying envelope approximation we can write the following system of equations

$$\frac{\partial A_1}{\partial y} = gn_1 A_0 \exp\left[-i\Delta y\right],$$ (1)

$$\frac{\partial n_1}{\partial \tau} = \left[\frac{\delta n}{1+\tau/3} - \frac{\delta n_i T_p}{T_i}\right]\frac{M_1}{M_n} + \frac{2\delta n}{3(1+\tau/3)^3}\frac{A_0^* A_1}{I_0}\exp\left[i\Delta y\right],$$ (2)

$$\frac{\partial M_1}{\partial \tau} = -\left[\frac{1}{1+\tau/3} + \frac{T_p}{T_m}\right]M_1 - \frac{2M_n}{3(1+\tau/3)^3}\frac{A_0^* A_1}{I_0}\exp\left[i\Delta y\right]$$ (3)

where $A_1 = A_1(y,\tau)$; $n_1 = n_1(y,\tau)$; $M_1 = M_1(y,\tau)$ is amplitude of induced monomer grating; $y = x/L$ and $\tau = t/T_p$ are dimensionless coordinate and time; $g = -i\omega L/(2c\cos\varphi_1)$; I_0 is a incident light intensity; T_p, T_m, T_i are the characteristic times of polymerization and diffusion of monomer and inert component, $\delta n, \delta n_i$ are the index changes due polymerization and inert component displacement by monomer at its diffusion;

$$T_i = \frac{1}{K^2 D_i}, \quad T_m = \frac{1}{K^2 D_m}, \quad T_p = \frac{2\sqrt{K_b}}{3K_g}\left[\alpha\beta\tau\langle K\rangle M_n I_0\right]^{-\frac{1}{2}},$$ (4)

M_n is monomer concentration,: K_g and K_b are growth reaction and break reaction constants; D_i and D_m are the diffusion coefficients of inert component and monomer; K is grating wave number; $\Delta = \Delta(\tau) = (k_{0x} - k_{1x} + K_x)L$ is normalized Bragg mismatch; $\alpha, \beta, \tau_0, \langle K\rangle$ are photoinitiation parameteres. Note that time dependence of phase mismatch $\Delta(\tau)$ in Eqs.(1)-(3) are caused by the photoinduced changing of mean refractive index in readout process and can be written as

$$\Delta(\tau) = \Delta + \frac{\Delta n \omega L}{c\cos\varphi_1}\left\{\cos 2\theta_B - 1 + \tan\varphi_0 \sin 2\theta_B\right\}\left[1 - \frac{1}{(1+3\tau)^2}\right],$$ (5)

where $\Delta = \Delta(\tau=0)$ is initial mismatch; θ_B. is Bragg angle. We will consider only symmetrical geometry of readout when $\varphi_1 = \varphi_1 = \theta_B$., and $\Delta(\tau) = \Delta$ and will suppose that the characteristic times T_p, T_d, T_i do not vary in time and are more less then the polymer diffusion time.

The boundary and initial conditions for solving of Eqs.(1)-(3) have the form

$$A_1(y=0,\tau) = 0, \quad n_1(y,\tau=0) = n_1(y), \quad M_1(y,\tau=0) = M_1(y).$$ (5)

3. EQUATIONS SOLUTIONS

Analytical solutions of the Eqs.(1)-(3) can be obtained by the Laplace transform technique with spatial variable y and can be expressed in the integral form in the terms of Bessel functions. In the result the index grating may be represent in the following form

$$n_1(y,\tau) = n_1(y) + n_{1p}(y,\tau) + n_{1m}(y,\tau),$$ (6)

where $n_{1p}(y,\tau)$ and $n_{1m}(y,\tau)$ are the nonstationary parts of index grating which are related with initial static polymer grating $n_1(y)$ and initial dynamic grating of monomer $M_1(y)$

respectively and can be written in the following form

$$n_{1p}(y,\tau) = -\sqrt{f(\tau)} \int_0^y n_1(y-s) \frac{\exp[i\Delta s]}{\sqrt{s}} J_1\left[2\sqrt{f(\tau)s}\right] ds, \tag{7}$$

$$n_{1m}(y,\tau) = \int_0^\tau F(\tau')\left\{ M_1(y) - \sqrt{f(\tau)-f(\tau')} \int_0^y M_1(y-s) \frac{\exp[i\Delta s]}{\sqrt{s}} J_1\left[2\sqrt{\{f(\tau)-f(\tau')\}s}\right] ds \right\} d\tau'.$$

Here $J_1[x]$ is Bessel function of the first order and are used the following notations

$$f(\tau) = -i\Gamma \frac{2T_m}{3T_p}\left\{ \left(\frac{T_m}{T_p}-C\right)\left(\exp\left[-\tau\frac{T_p}{T_m}\right]-1\right) - \frac{3T_p}{2T_m}(1+C)\left(1-\left(1+\frac{\tau}{3}\right)^{-2}\right) + \left(1-\left(1+\frac{\tau}{3}\right)^{-3}\right)\right\},$$

$$F(\tau) = \frac{\delta n}{M_0 T_p}\left\{\left(1+\frac{\tau}{3}\right)^{-1} - C\frac{T_p}{T_m}\right\}\left(1+\frac{\tau}{3}\right)^{-3}\exp\left[-\tau\frac{T_p}{T_m}\right], \tag{8}$$

where $\Gamma = ig\delta n = \omega L \delta n/2c\cos\varphi_1$ is dimensionless coupling coefficient characterizing the efficiency of interaction of light waves with index grating; $C = \delta n_i T_m /\delta n T_i$. In deriving Eq.(8) for simplicity we have used the smallness of $T_{i,m}/T_p$.

The corresponding solution of Eq.(1) defining diffracted light field may be represent in the form

$$A_1(y,\tau) = gA_0 \exp[-i\Delta y]\left\{\int_0^y n_1(y-s)\exp[i\Delta s]J_0\left[2\sqrt{f(t)s}ds\right] + \right.$$

$$\left. + \int_0^\tau F(\tau')\int_0^y M_1(y-s)\exp[i\Delta s]J_0\left[2\sqrt{\{f(\tau)-f(\tau')\}s}\right]dsd\tau'\right\}, \tag{9}$$

where $J_0[x]$ is Bessel function of the zero order. The solutions (6),(9) describes the space-time transformation of the holographic grating and diffracted light fields in the reconstruction process with taking into account the photopolymerization and diffusion kinetics..

4. CALCULATION RESULTS

The numerical results shown on Fig.2,3 have been obtained with the initial conditions for $M_1(y,t=0)=0$ and $n_1(y,t=0)=1$ whose correspond to the beginning of reconstruction after the time period $\delta T \gg T_m$ when hologram have been recorded in photopolymer material. Figure 2(a) shows the time evolution of grating amplitude $|n_1(y=1,\tau)|$ at the exit of photopolymer layer. Notice that grating amplitude first increases with time because of the additional photopolymerization and reaches the steady-state as expected. The time needed to reach steady state and amplification gain increases as the coupling coefficient Γ increases. The results in Fig.2b indicates when the time of monomer diffusion is comparable with time of polymerization the kinetics of grating amplification is more fast. This effect experimentally were observed in work [3] and is connected with the enhancing of photopolymerization velocity due to monomer diffusion from minimum to maximum of grating. It necessary to note that influence of inert component diffusion accordingly Eq.(8) is the contrary (if $C \neq 0$ and is comparable with T_m /T_p).
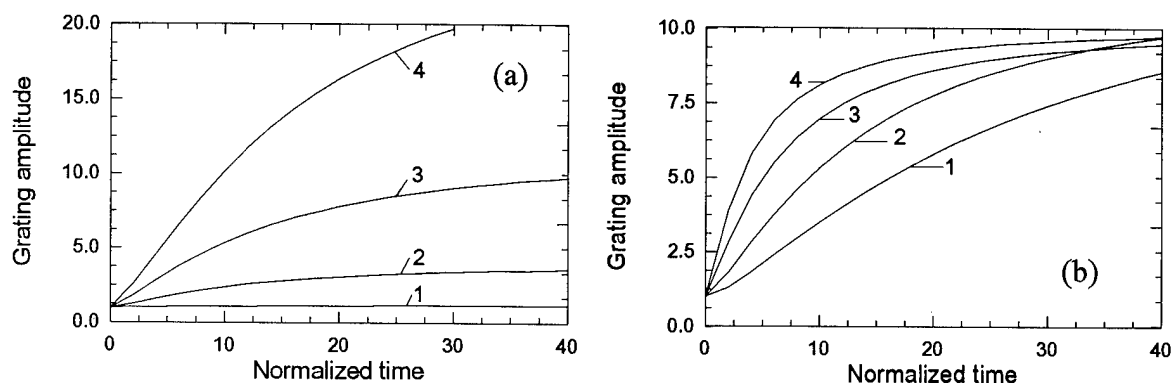
Fig.2 Grating amplitude $|n_1(y=1,\tau)|$ as function of normalized time t/T_m : (a) at various Γ (curves 1-4 $\div$ 1;5;10;15) for $T_m/T_p=0,1$; (b) at various T_m/T_p (curves 1-4 $\div$ 0,1;0,2;0,4;0,6) for coupling coefficient $\Gamma=10$ at $\Delta=0$, $|n_1(y)|=1$, $C=0$.

Figure 3(a) shows the dynamics of grating amplification in the conditions of initial phase mismatches. Note that the asymmetrical character, broadening and shifting take place and are increased with time. In the steady state as it is seen from Fig.3(b) the analogous effects are observed at the increasing of coupling constant. Analysis of solutions shows it is connected with the changing of phase shift between the initial grating and photoinduced gratings.
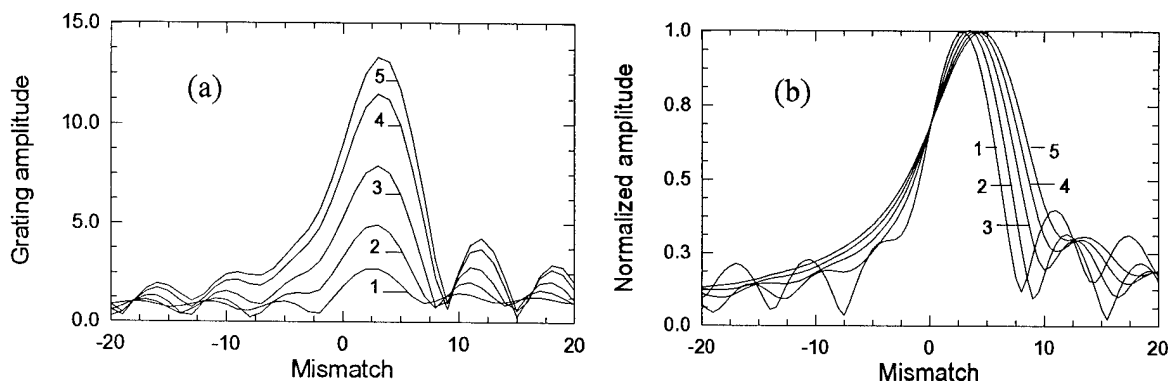
Fig.3 (a) Grating amplitude $|n_1(y=1,\tau)|$ and (b) normalized amplitude $|n_1(y=1,\tau)|/|n_1(y=1,\tau=40)|$ as function of initial mismatch Δ: (a) at various normalized time t/T_m (curves 1-5 $\div$ 2;5;10;20;30); (b) at various coupling coefficient Γ (curves 1-4 $\div$ 5;10;15;20;25) for $T_m/T_p=0,2$, $|n_1(y)|=1$, $C=0$.

5. CONCLUSION

The analytical model of hologram reconstruction in photopolymer materials based on the simultaneous solution of equations of photopolymerization kinetics, diffusion and diffraction is offered. This model is in the qualitative agreement with the known experimental results and can be useful for destination and optimization of the parameters of the photopolymer materials. In a future we will expand the analytical descriptions of above mentioned problem for slant gratings when the time evolution of geometry diffraction should be taken into account.

REFERENCES

[1] E. Gulnasarov, T. Smirnova, E. Tixonov, *Journ.Techn.Phys.*, Vol.61,N10, pp.114-119.
[2] V. Shelkovnikov, E. Pen, et al., Proc. *SPIE*, Vol.2429, pp.55-65, 1994.
[3] V. Kotov, Proc. *SPIE*, Vol.2429, pp.170-178, 1994.
[4] E. Kovalenko, S. Sharangovich, Proc. of Intern. Conf. on Photorefractive Materials, Effects and Devices, USA, Colorado. 4 p. (June 1995).

Poster Previews

JTuB 10:30 am-12:00 m
Commonwealth Room

G. Michael Morris, *Presider*
University of Rochester and Rochester Photonics Corp.

Fabrication and Experiment of Diffractive Phase Element That Implements Wavelength Demultiplexing and Focusing

Bizhen Dong, Guoqing Zhang, Guozhen Yang, Benyuan Gu,
Shihai Zheng, Dehua Li, and Yansong Chen
Institute of Physics, Academia Sinica, P. O. Box 603
Beijing 100080, China
Phone: +86-10-2559131 ext. 229   Fax: +86-10-2562605

I. Introduction

Recently, the diffractive optics has extensively attracted interest of researchers because diffractive optical elements(DOE's) can incorporate several optical functions in a single optical element.[1-4] This is important in a number of areas such as integrated optics, optical computing, optical sensors, and so on. For example, one can design diffractive optical elements to perform wavelength multiplexing/demultiplexing, and focusing. Various designs and fabrication schemes for DOE's that modulate only the phase of an incident lightwave have been proposed. In this paper we present the design and fabrication of diffractive phase element (DPE) that incorporates simultaneous wavelength demultiplexing and focusing in the optical system illuminated by a light beam with three wavelength components. Optical lithography and reactive-ion etching are used to fabricate the surface-relief structure with 8 levels. Experiments demonstrate the feasibility of three wavelength demultiplexing and focusing simultaneouslly.

II. Design and Numerical Simulation

The sketch of a typical optical system considered here is illustrated in Fig. 1. This optical system is assumed to be illuminated by a uniform beam of incident light with mutually incoherent components with different wavelength. P_1 and P_2 represent the input and output plane, respectively. A wave function at wavelength λ_α on the input planes is denoted by $U_{1\alpha}$; the corresponding wave function on the output plane is denoted by $U_{2\alpha}$. The wave functions are generally complex. For brevity of notation we consider a one-dimensional case in our design and experiment. The output wave function $U_{2\alpha}$ is linked to the input wave function $U_{1\alpha}$ at wavelength λ_α by a linear transform function $G(X_2, X_1, \lambda_\alpha)$ of the form[5]

Fig. 1 : Schematic diagram of a diffractive optical system.

$$U_2(X_2, \lambda_\alpha) = \int G(X_2, X_1, \lambda_\alpha)U_1(X_1, \lambda_\alpha)dX_1. \tag{1}$$

Equation (1) can be recast in a compact form

$$U_2(X_2, \lambda_\alpha) = \widehat{G}(\lambda_\alpha)U_1(X_1, \lambda_\alpha), \tag{2}$$

where $\widehat{G}$ represents an integral operator. In the general case or nonparaxial case, $\widehat{G}$ may be nonunitary, i. e., $\widehat{G}^+\widehat{G} = \widehat{A} \neq \widehat{I}$, where the superscript + stands for Hermitian conjugation

operation; $\hat{I}$ is an identity transform; and $\hat{A}$ is an Hermitian operator. In numerical simulations, the every continuous functions is approximately sampled in a discrete way and represented by its values at a set of sampling points (or pixels). Assume that the total numbers of the sampling points are N_1 on the input plane and $N_2 = N_{2s} \times N_\lambda$ on the output plane, where N_{2s} is the number of spatial sampling points on the output plane and N_λ is the number of different wavelengths. Thus, we have

$$U_{1n}(\lambda_\alpha) = \rho_{1n\alpha} \exp(i2\pi h_{1n}/\lambda_\alpha), \tag{3a}$$

$$U_{2m\alpha} = \rho_{2m\alpha} \exp(i\phi_{2m\alpha}), \tag{3b}$$

$$U_{2m\alpha} = \sum_{l=1}^{N_1} G_{mn}(\lambda\alpha)U_{1n\alpha},$$

$$n = 1, 2, 3, ..., N_1, \quad m = 1, 2, 3, ..., N_{2s}, \quad \alpha = 1, 2, 3, ..., N_\lambda. \tag{4}$$

The design problem of the DPE can be put into the framework of phase retrieval: If the linear transform kernel $\hat{G}$ and the amplitude information of $U_{1\alpha}$ and $U_{2\alpha}$ are known, how can the profile of the surface-relief kinoform be determined so that Eq. (2) is satisfied to a high accuracy ?

To describe the closedness of the calculated wavefront $\hat{G}U_1$ to the desired wavefront U_2, we introduce a distance measure D in an L_2 norm[5] as

$$D^2 = \sum_\alpha \| U_{2\alpha} - \hat{G}(\lambda_\alpha)U_{1\alpha} \|^2 \tag{5}$$

The design problem of the DPE's may be formulated as the search for the minimum of D^2 with respect to function arguments h_1 and $\phi_{2\gamma}$. Through evaluating the functional variations, we can derive a set of equations for determining h_1 and $\phi_{2\gamma}$.

$$\exp(i2\pi h_{1k}/\lambda_0) = \frac{\tilde{Q}_k^*}{|\tilde{Q}_k|}$$

$$k = 1, 2, 3, ..., N_1, \tag{6a}$$

where

$$\lambda_0 = \frac{\lambda_{max} + \lambda_{min}}{2}$$

$$\tilde{Q}_k = \sum_\alpha \left[\sum_{j\neq k}' \rho_{1j\alpha} \exp(-i2\pi h_{1j}/\lambda_\alpha)A_{jk}(\lambda_\alpha) - \sum_j \rho_{2j\alpha} \exp(-i\phi_{2j\alpha})G_{jk}(\lambda_\alpha) \right]$$

$$\times (2\pi/\lambda_\alpha)\rho_{1k\alpha} \exp[i(2\pi h_{1k}/\lambda_0)(\lambda_0/\lambda_\alpha - 1)].$$

$$\exp(-i\phi_{2k\gamma}) = \frac{\sum_j G_{kj}(\lambda_\gamma)\rho_{1j\gamma} \exp(i2\pi h_{1j}/\lambda_\gamma)}{\left| \sum_j G_{kj}(\lambda_\gamma)\rho_{1j\gamma} \exp(i2\pi h_{1j}/\lambda_\gamma) \right|}$$

$$k = 1, 2, 3, ..., N_{2s}, \quad \gamma = 1, 2, 3, ..., N_\lambda. \tag{6b}$$

Generally speaking, no analytical solutions to Eqs.(6a) and (6b) may be expected, but they can be numerically solved by use of Yang-Gu iterative algorithm described in Refs.

[6-7] in detail. According to the general theory of optical wave propagation, this system shown in Fig. 1 performs the linear transform given by Eq.(1) with a transform kernel $G(x_2, x_1; l, \lambda_\alpha)$ at wavelength λ_α. In the paraxial approximation, G can be expressed as

$$G(x_2, x_1; l, \lambda_\alpha) = \left(\frac{1}{i\lambda_\alpha l}\right)^{1/2} \exp(i2\pi l/\lambda_\alpha) \exp[i\pi(x_2 - x_1)^2/\lambda_\alpha l]. \qquad (7)$$

The relevant physical and structural parameter values were chosen as follows: The number of wavelengths of illumination light is $N_\lambda = 3$. The corresponding wavelengths are $\lambda_1 = 0.5145\mu m$, $\lambda_2 = 0.5900\mu m$, and $\lambda_3 = 0.6328\mu m$. The central wavelength is $\lambda_0 = 0.5(\lambda_1 + \lambda_3) = 0.57365\mu m$. The sizes of the apertures on the input and output planes are $x_{1max} = 7.66mm$ and $x_{2max} = 15.32mm$. The numbers of sampling points on the input and output planes are $N_1 = 256$ and $N_{2s} = 12$, respectively. A uniform intensity at all wavelengths on the input plane is assumed, i.e., $\rho_{1\alpha}$ is a constant. The intensity and positions of diffractive light focused in the focal plane, and focal distance can be arbitrary. In our design, the intensities of three wavelength demultiplexing are assumed identical, the consecutive positions of three wavelength foci are designed 0.128mm and 0.256mm, and the focal spacing between the input and output planes also is designed $l = 400mm$. Fig. 2 shows the designed quantized relief depth of 8-level DPE, and the numerical simulation of the intensity distribution generated by the DPE on the output plane is displayed in Fig. 3. From Fig. 3 it can be seen that a local maximum of intensity for each wavelength is demultiplexed and occurred at its predesignated position in the desired plane.
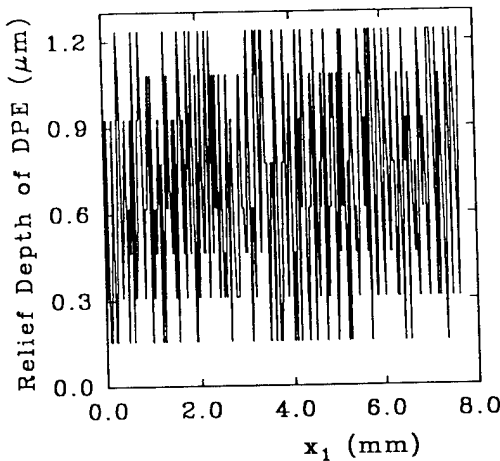
Fig. 2 : Profile of 8-level relief depth of the DPE.
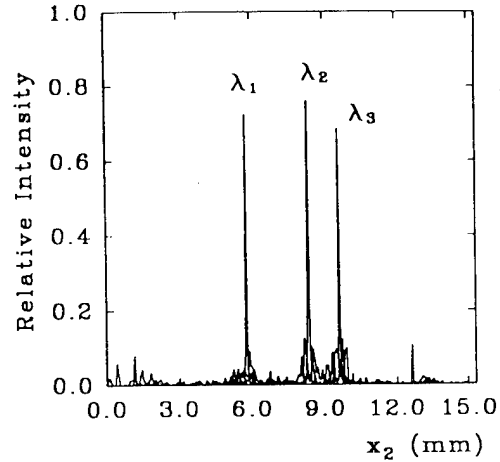
Fig. 3 : Numerical simulation of output pattern generated by the DPE.

III. Fabrication and Experimental Results

Optical lithography and reactive-ion etching are used in forming the surface-relief structure of the designed DPE. To fabricate the surface-relief structure with 8 levels, three lithographic masks shown in Fig. 4 were designed and used to fabricate the surface-relief structure in our experiment. The DPE was fabricated in fused silica(index refraction = 1.459). To demonstrate the validity of the numerical simulation, a optical system shown in Fig. 5 was chosen as the experimental setup. Identical intensities of three laser beams with

wavelength, $\lambda = 0.6328\mu m$ (He-Ne laser), $\lambda = 0.5145\mu m$ (Argon laser), and $\lambda = 0.5900\mu m$ (Dye laser), consist a coaxial collimated beam to illuminate the DPE.
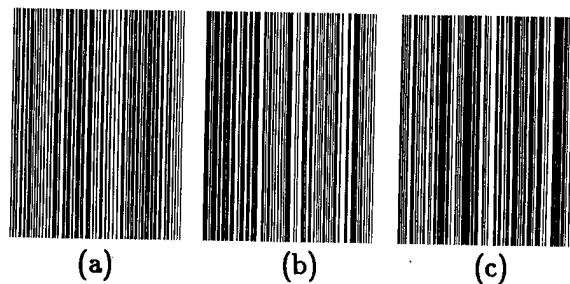

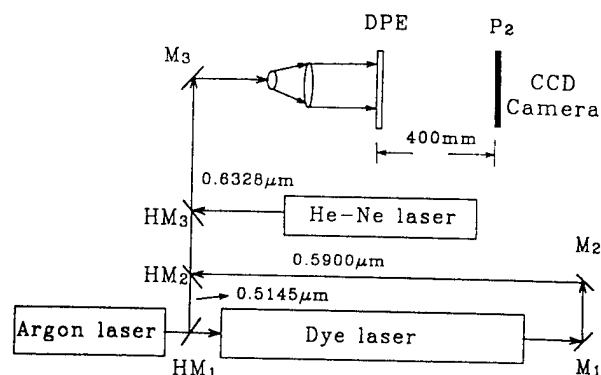Fig. 4 : Lithographic masks for 8-level DPE, (a) mask1, (b) mask2 and (c) mask3.

Fig. 5 : Experimental setup.

Figs. 6 depict the experimental output images recorded by the CCD camera and photo camera, respectively, at the focal plane for three wavelength demultiplexing and focusing from the DPE. It is clear that the experimental results shown in Fig. 6(a) are in good coincidence with the numerical simulation shown in Fig. 3.
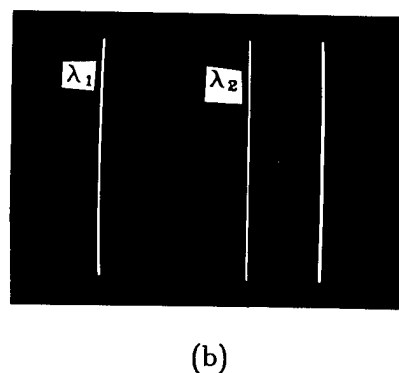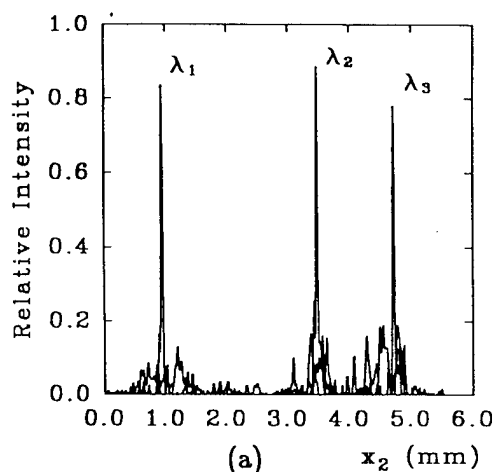
Fig. 6 : Experimental results for three wavelength demultiplexing and focusing:
(a) Intensity distribution measured by CCD camera; (b) Photography.

References

[1] M. Kato and K. Sakuda, Appl. Opt. **30**, 630–635(1992).

[2] M. Bernhardt, F. Wyrowski, and O. Bryngdahl, Appl. Opt. **30**, 4629–4639(1991).

[3] Y. Ishii and T. Kubota, Appl. Opt. **32**, 4415–4422(1993).

[4] Y. Amitai, Opt. Commun. **98**, 24–28(1993).

[5] G. Z. Yang, B. Z. Dong, B. Y. Gu, J. Y. Zhuang, and O. K. Ersoy, Appl. Opt. **33**, 209–218(1994).

[6] B. Y. Gu, G. Z. Yang, B. Z. Dong, J. Y. Zhuang, and O. K. Ersoy, Appl. Opt. **34**, 2564–2570(1995).

[7] M. P. Chang, O. K. Ersoy, B. Dong, G. Yang, B. Gu, Appl. Opt. **34**, 3069–3076(1995).

A New Kind of Diffractive Phase Elements Applied to Wavelength Demultiplexing and Annular Focusing

Benyuan Gu, Guoqing Zhang, Bizhen Dong, Guozhen Yang
Institute of Physics, Academia Sinica, P. O. Box 603
Beijing 100080, P. R. China
Phone: +86-10-2559131 ext. 229   Fax: +86-10-2562605
e-mail: guby@aphy01.iphy.ac.cn

1. Introduction

In recent years much effort has been devoted to the designs of diffractive optical elements (DOE's) because of considerable progress in DOE microfabrication technology. In the previous papers various designs of DOE's have been presented, these elements produce focal annuli for monochromatic illuminating system[1], or implement wavelength demultiplexing and straight line or spot focusing.[2-5]

The goal of this article is to propose a design of a new kind of diffractive phase elements (DPE's), these DPE's are able to integrated above all functions, i.e. DPE's implement simultaneously wavelength demultiplexing and produce annuli with each wavelength focusing at desired focal plane.

2. Formulas Used for the Design of DPE's

A schematic representation of a typical optical system for design DPE's is shown in Fig. 1. The system is assumed to be illuminated by a beam of incident light consisting of mutually incoherent components with different wavelengths. P_1 and P_2 represent the input plane and output planes, respectively. A wave function at wavelength λ_α on the input plane P_1 is denoted by $U_{1\alpha}$; the corresponding wave function on the output plane P_2 is denoted by $U_{2\alpha}$. The wave functions are generally complex. In numerical simulations, the every continuous functions are sampled and represented by their values at a set of sampling points(or pixels). Consequently, at a given wavelength λ_α, the wave function on the input plane is

Fig. 1 : Configuration of a diffractive optical system.

$$U_{1n}(\lambda_\alpha) = \rho_{1n\alpha} \exp(i2\pi h_{1n}/\lambda_\alpha),$$

$$n = 1, 2, 3...N_1, \quad \alpha = 1, 2, 3...N_\lambda. \tag{1}$$

The corresponding wave function on the output plane is

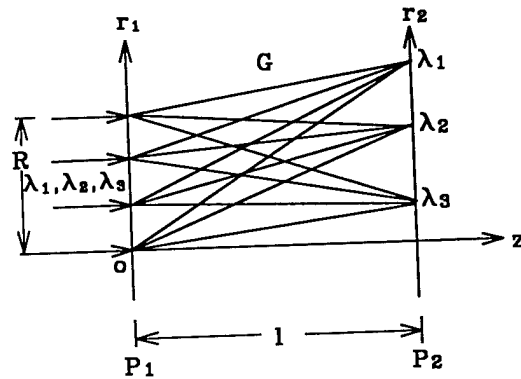$$U_{2m\alpha} = \rho_{2m\alpha} \exp(i\phi_{2m\alpha}), \quad m = 1, 2, 3..N_{2s}. \tag{2}$$

The coordinate system is such that the z-axis is along the optical axis of the system, the system considered here is rotationally symmetric, our description can be in terms of polar coordinates, radial coordinates on the input and output planes are described r_1 and r_2. The output wave function is linked to the input wave function at wavelength λ_α by a linear transform function $G(r_2, r_1, \lambda_\alpha)$ of the form

$$U_{2m\alpha} = \sum_{n=1}^{N_1} G_{mn}(\lambda_\alpha) U_{1n\alpha}. \tag{3}$$

The design problem for the DPE's can be generally addressed as follows : From known the transform kernel G and the amplitudes of $U_{1\alpha}$ and $U_{2\alpha}$ determinate the profile of the surface-relief kinoform, satisfying Eq. (3) to a high accuracy.

To describe the closeness of the calculated wavefront $\widehat{G}U_1$ to the desired wavefront U_2, we introduce a distance measure D^2 in an L_2 norm[6],

$$D^2 = \sum_\alpha || [U_{2\alpha} - \widehat{G}(\lambda_\alpha) U_{1\alpha}] ||^2 . \tag{4}$$

By evaluating the functional variation of D^2 with respect to h_1 and $\phi_{2k\gamma}$, one obtain

$$\exp(i2\pi h_{1k}/\lambda_0) = \frac{\widetilde{Q}_k^*}{| \widetilde{Q}_k |}, \quad k = 1, 2, 3....N_1, \tag{5}$$

where λ_0 is the mean wavelength, and can be chosen as the center wavelength, given by $\lambda = (\lambda_{max} + \lambda_{min})/2$, λ_{max} and λ_{min} are maximum and minimum of wavelengths in polychromatic illumination. and

$$\widetilde{Q}_k = \sum_\alpha \{ \sum_{j \neq k}^{\prime} \rho_{1j\alpha} \exp(-i2\pi h_{1j}/\lambda_\alpha) A_{jk}(\lambda_\alpha)$$

$$- \sum_j \rho_{2j\alpha} \exp(-i\phi_{2j\alpha}) G_{jk}(\lambda_\alpha) \} (2\pi/\lambda_\alpha) \rho_{1k\alpha} \exp[i(2\pi h_{1k}/\lambda_0)(\lambda_0/\lambda_\alpha - 1)].$$

and

$$\exp(i\phi_{2k\gamma}) = \frac{\sum_j G_{kj}(\lambda_\gamma) \rho_{1j\gamma} \exp(i2\pi h_{1j}/\lambda_\gamma)}{| \sum_j G_{kj}(\lambda_\gamma) \rho_{1j\gamma} \exp(i2\pi h_{1j}/\lambda_\gamma) |},$$

$$k = 1, 2, 3....N_{2s}, \quad \gamma = 1, 2, 3...N_\lambda. \tag{6}$$

Eqs. (5) and (6) can be numerically solved with use of the YG iterative algorithm described in Ref. 6.

3. Numerical Simulation Results for the Design of DPE's

In Fig. 1 the focal spacing between the input plane P_1 and the output plane P_2 is l, and the DPE is placed on the input plane. According to the general theory of optical wave propagation,[7] this system performs the linear transform given by Eq.(3) with a transform kernel at wavelength λ_α,

$$G(r_2, r_1; l, \lambda_\alpha) = \frac{2\pi}{i\lambda_\alpha l} \exp(i2\pi l/\lambda_\alpha) \exp[i\pi(r_2^2 + r_1^2)/\lambda_\alpha l] \times J_0(\frac{2\pi r_2 r_1}{\lambda_\alpha l}) r_1. \tag{7}$$

where J_0 is the zeroth–order Bessel function of the first kind.

We now present the results obtained in the design of DPE's which simultaneously perform wavelength demultiplexing and annular focusing of each wavelength. In our computations, the number of wavelengths of illumination light of the optical system, intensities and radii of diffractive annuli focused in the focal plane, and focal distance can be arbitrarily chosen. The relevant physical and structural parameter values chosen as follows: The sizes of the apertures on the input and output planes are $R_1 = 3.0mm$ and $R_2 = 9.0mm$. The numbers of sampling points on the input and output planes are $N_1 = 512$ and $N_{2s} = 32$, respectively. A uniform intensity at all wavelengths on the input plane is assumed, i.e., $\rho_{1\alpha}$ is a constant. In our design, the intensities of focusing annuli for wavelength demultiplexing are assumed identical, and the focal spacing between the input and output planes also is predesignated $l = 400mm$.

In the first two examples of design, the number of wavelengths of illumination light is chosen $N_\lambda = 2$. Figs.2 (a) and (b) show a depth distribution of the designed DPE and corresponding intensity of focusing annuli, respectively. In Fig. 2(b) two peaks of intensity with each wavelength ($\lambda = 0.6328\mu m$ and $0.5145\mu m$) occur at predesignated radii $r_2 = 5.28mm$ and $7.29mm$, respectively. It means that the designed DPE implements simultaneously two annuli with each wavelength separating and focusing at desired positions.
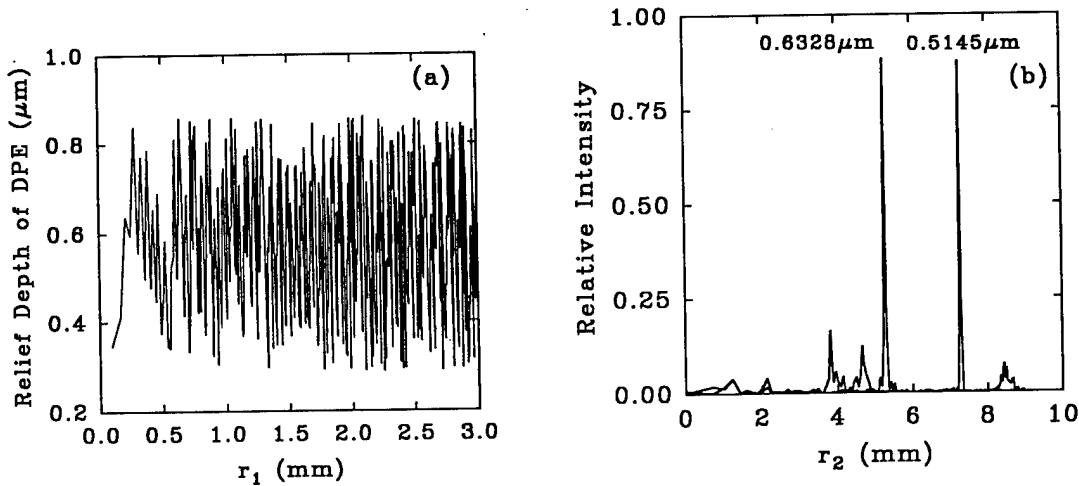
Fig. 2: (a) Profile of depth of the designed DPE, (b)Output pattern with two wavelengths demultilexing and annuli focusing generalized from the designed DPE shown in Fig.2 (a).

To verify further the validity of the design method, we now demonstrate more examples by changing the relevant parameter values. Fig. 3 also present successful result by using different wavelengths and radii from that in Fig. 2. Fig. 3 describes the corresponding output pattern of intensity, two annuli with each wavelength ($\lambda = 0.5145\mu m$ and $0.5900\mu m$) are divided and focusing at desired radii $r_2 = 3.56mm$ and $6.56mm$, respectively.

For second example, N_λ is taken 3, and radii of focal annuli are predesignated ar-

bitrarily. Fig. 4 present a satisfactory design again. Three peaks of intensity raise in the output pattern shown in Fig. 4, the peaks with each wavelength ($\lambda = 0.5900\mu m$, $0.6328\mu m$, and $0.5145\mu m$) still demultiplex, and focus at expected radii $r_2 = 1.59mm$, $3.89mm$, and $7.29mm$, respectively, in the focal plane.
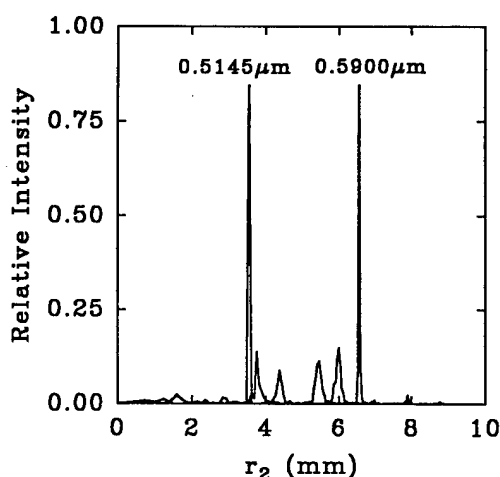

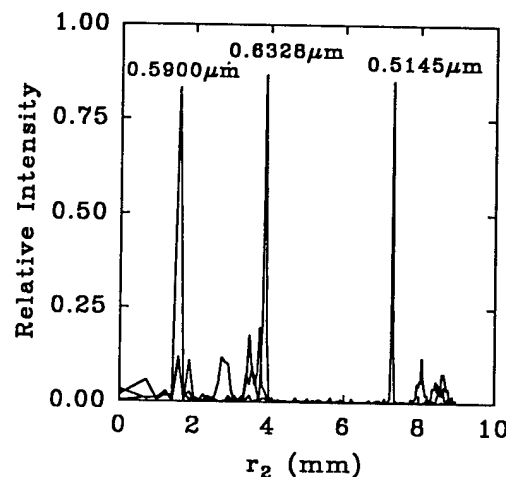Fig. 3 : Output pattern with two wavelengths demultilexing and annuli focusing generated from the designed DPE.

Fig. 3 : Output pattern with three wavelengths demultilexing and annuli focusing generated from the designed DPE.

4. Conclusions

The design of DPE's that simultaneously implement wavelength demultiplexing and annular focusing is present based on the theory of amplitude-phase retrieval and an iterative YG algorithm. The calculated results shows that the diffractive patterns obtained by the designed DPE's are in good agreement with the desired patterns. It may be expected that this design method will be useful and effective for the design of DPE's in micro-optical system.

References

1. G. Zhang, G. Yang, and B. Gu, Appl. Opt. **35**, 1995. in press.
2. M. Kato and K. Sakuda, Appl. Opt. **30**, 630-635 (1992).
3. Y. Amitai, Optics Communications **98**, 24-28 (1993).
4. B. Gu, G. Yang, B. Dong, M–P. Chang, and O. K. Ersoy, Appl. Opt. **34** , 2564-2570 (1995).
5. M–P. Chang, O. K. Ersoy, B. Dong, G. Yang, and B. Gu, Appl. Opt. **34** , 3069-3076 (1995).
6. G. Z. Yang, B. Z. Dong, B. Y. Gu, J. Y. Zhuang and O. K. Ersoy, Appl. Opt. **33**, 209–218 (1994).
7 J. W. Goodman, Introduction to Fourier Optics (McGraw-Hill, San Francisco, 1969).

Off-axis Talbot effect and array generation in planar optics

Markus Testorf, Jürgen Jahns

FernUniversität Hagen, LG ONT, Elberfelderstr. 95, 58084 Hagen, Germany,
fax.: +49-2331-332904, e-mail: markus.testorf@fernuni-hagen.de.

Nikolay A. Khilo, Andrey M. Goncharenko

Division for Optical Problems in Information Technology (DOPIT), Belarussian Academy of
Sciences, P.O. B. 1, Minsk 220072, Republic of Belarus, fax: +375-172-324553
e-mail: dopit@bas.minsk.by

I. Introduction

Recently, planar optics was introduced as a concept for the micro integration of free space optics[1]. For the planar optics approach passive optical elements are arranged on the surface of a thick transparent substrate. The light signal travels within the substrate along a folded zig-zag path, reflected at the surfaces of the substrate. Since planar optics was first proposed, various applications were successfully demonstrated, like integrated split and shift modules[2] or integrated optical imaging systems[3].

Typically, the light signal reflects off the optical elements, positioned on the surfaces of the substrate under a certain angle with respect to the plane in which the elements are located. The oblique angle of light propagation has to be considered for the analysis of planar optics and related optical systems. In order to develope a foundation for the treatment of integrated planar optical systems incorporating self-imaging phenomena, we investigate the Talbot effect for oblique angles of light propagation.

II. Free space propagation and self-imaging
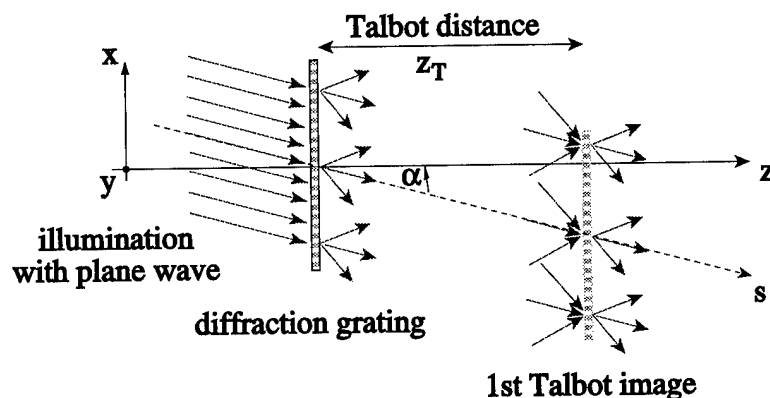
We consider the configuration shown in Fig. 1. A grating is illuminated by a tilted plane wave. The transmission function of the grating is assumed to be separable in x and y. The propagation direction s of the initial wave front and the grating axis z deviate by an angle α within the x-z plane.

Fig. 1: Configuration for observing the off-axis Talbot effect

As self-imaging is based on free space propagation of diffracted wave fields, we first calculate the transfer function $\tilde{h}(k_x, k_y, z)$ of free space starting from the solution of Helmholtz's equation in frequency space[4]. We assume small diffraction angles centered around the propagation direction $k_{x0} = (2\pi/\lambda) \cdot \sin(\alpha)$ of the incident wave. Substituting $k'_x = k_x - k_{x0}$ and disregarding constant factors we find

$$\tilde{h}(k'_x, k_y, z) = \exp\left[\underbrace{-i\, k'_x z \tan(\alpha)}_{\text{shift in space}} \underbrace{- \frac{i\, k_x'^2 z}{2k\cos^3(\alpha)} - \frac{i\, k_y^2 z}{2k\cos(\alpha)}}_{\text{parabolic approximation}} \underbrace{- \frac{i\, k_x'^3 z \sin(\alpha)}{2k^2 \cos^5(\alpha)} - \frac{i\, k'_x k_y^2 z \sin(\alpha)}{k^2 \cos^3(a)}}_{\text{aberrations}} \right] \quad (1)$$

with $k=2\pi/\lambda$. Eq. (1), can be split into three terms. The phase linear in k'_x corresponds to a lateral shift of the diffraction pattern in real space. The second part contains the parabolic approximation, including on-axis Fresnel diffraction ($\alpha=0$) as a special case. The last term describes aberrations which arise from the off-axis propagation of the light signal.

The effect of self-imaging can be explained within the parabolic approximation. From the parabolic term, in Eq. (1), we find different Talbot distances for x and y:

$$z_{T,x} = m_x \frac{2d_x^2}{\lambda} \cos^3(\alpha); \quad \text{and} \quad z_{T,y} = m_y \frac{2d_y^2}{\lambda} \cos(\alpha) \quad \text{with} \quad m_x, m_y = 1,2,3,\ldots, \quad (2)$$

where indices x and y denote the lateral coordinates. For self-imaging of two dimensional gratings both conditions in Eq. (2) have to be fulfilled simultaneously.

III. Experimental verification

A) The Talbot distance

To verify Eq. (2) experimentally a one-dimensional amplitude Ronchi grating with a period $d=50\mu m$ was illuminated under different angles α by a collimated laser beam (He-Ne laser $\lambda=0.633mm$). The grating lines were oriented in y-direction. For angles $\alpha=5$, 10, 15 and 20 degrees we determined the Talbot distance. The results are summarized in Fig. 2 where the measurements are compared to the theoretical values. The deviations of the experimental
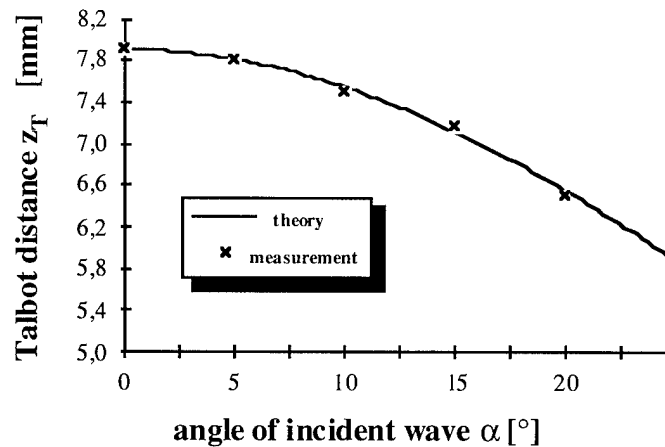

Fig. 2: Determination of the Talbot distance

and the theoretical results were found to be approximately 1%.
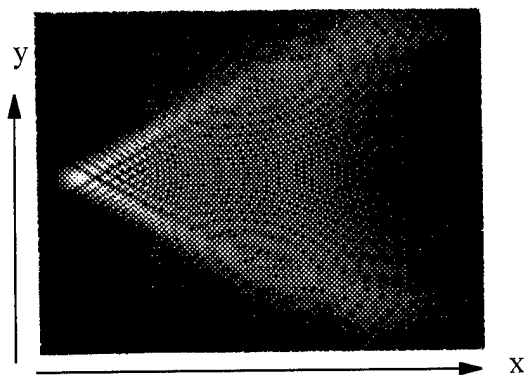
B) Aberrations

Fig. 3: Point-spread function of aberrations

To study the aberrations we numerically calculate the Fourier transformation of the last term in Eq. (1). The result, presented qualitatively in Fig. 3 as a gray scale picture, can be regarded as the point spread function for off-axis self-imaging. The ideal self-image has to be convoluted by a coma like amplitude distribution.

To compare the numerical calculations with experiments we use again a one-dimensional amplitude Ronchi grating with a period of 50μm. The grating consists of 200 lines which is sufficient to avoid edge effects at the center of the grating image. We determine the intensity distribution of the diffracted wave front of the grating at the first Talbot plane (Fig. 4a). The intensity line scan, Fig. 4a shows strongly modulated bright lines and a moderate contribution of background noise.

For comparison we computed the theoretical intensity distribution from Eq (1). The resulting intensity distribution, Fig. 4b, corresponds fairly good to the measurement, in Fig. 4a. Deviations are caused by intensity variations of the illuminating laser beam and alignment errors. During the experiment, we found that the shape of the fringes strongly depends on α and z.

a)

b)
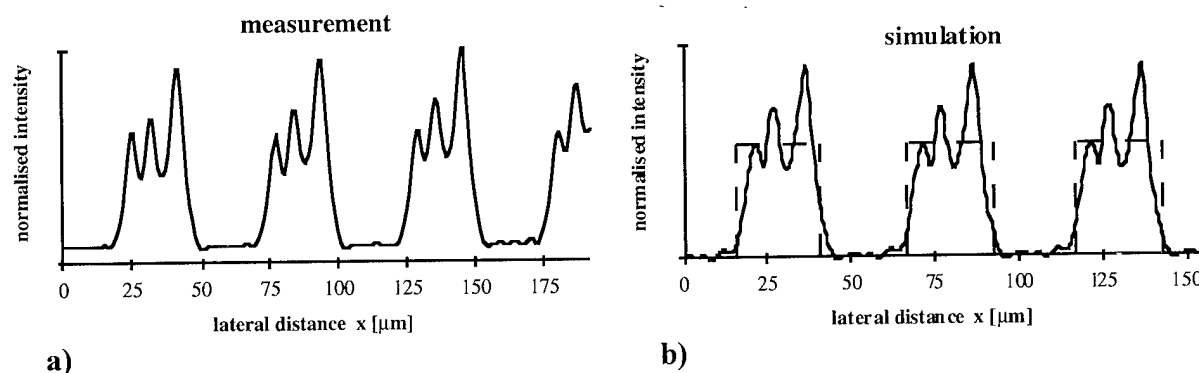
Fig. 4: Experiment and simulation of the intesity pattern in the first Talbot plane.

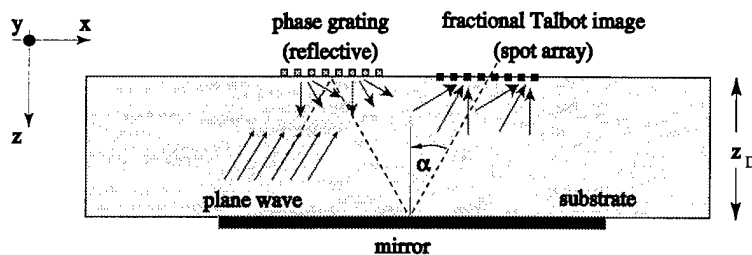# IV. Application to planar optics: spot array generation

Fig. 5: Planar optical setup

One useful application for the off-axis Talbot effect is array illumination[5]. This can be efficiently performed by use of the fractional Talbot effect, where the diffraction grating is a phase only element and the bright spots appear in rational fractions of the Talbot distance[6]. A planar optical configuration is shown in Fig. 5.

For array illumination, the portion of light intensity diffracted to the desired output spots is important rather than the specific shape of the spots. Therefore, aberrations of the self-images are of less importance as long as only the line shape is influenced. From simulations we found that more than 95% of the light energy can be used in a planar optical setup. This portion, depending on α, is found to be a maximum for angles between $\alpha=20°$ and $\alpha=30°$.

V. Conclusion

In this paper we investigated the Talbot effect for oblique angles of light incidence. The Talbot distance depending on the illumination angles turns out to be different for both lateral coordinates. Aberrations arising from the off-axis configuration cause a significant modulation and distortion of the ideal self-images. For array generation by means of the fractional Talbot effect, however, these distortions are of less importance. Therefore, Talbot array illuminators are well applicable to planar optical integration.

References

1. J. Jahns and A. Huang, "Planar integration of free space optical components," Appl. Opt. 28, 1602 (1989).
2. J. Jahns and B. A. Brumback, "Integrated-optical split and shift module based on planar optics," Opt. Comm. 79(5,6), 318 (1989).
3. J. Jahns and J. S. Walker, "Imaging with planar optical systems," Opt. Comm. 76(5,6), 313 (1990).
4. J. Goodman, Introduction to Fourier optics, (McGraw Hill, New York 1968).
5. N. Streibl, "Beam shaping with optical array generators," J. Mod. Opt. 36, 1559-1573 (1989).
6. J. R. Leger and G. J. Swanson,"Efficient array illuminators using binary-optics phase plates at fractional Talbot planes," Opt. Lett. 15, 288 (1990).

Diffractive Elements Developed for Uniform Illumination in Inertial Confinement Fusion

Qiu Yue   Fan Dianyuan   Deng Ximing

Shanghai Institute of Optics and Fine Mechanics, Chinese Academy of Sciences
P.O.Box 800-211, Shanghai 201800, P.R.China
Tel: 86-21-59534890 Ext.291, Fax: 86-21-59528812

Deng Xuegong   Li Yongpin

Department of Physics, China University of Science and Technology
Hefei Anhui 230026, P.R.China

1. Introduction

In inertial confinement fusion(ICF) experimental researches, especially in direct drive ICF experimental researches, energy of the incident high power laser beam must be focused onto the target surface very uniformly. To achieve high illumination uniformity for target, several techniques have been developed, such as random phase plate (PR)[1], induced spatial incoherence (ISI)[2], smoothing by spectral dispersion (SSD)[3], lenslet array (LA)[4], etc.. Although these techniques have proven valuable in ICF applications, all of them have some limitations and can't meet all of the requirements of the applications.

Recently, we've been investigating the possibility of introducing the diffractive optical technology into our uniform illumination for ICF applications. Using a modified Gerchberg-Saxton algorithm, a kind of pure-phase elements (PPE)s are designed[5,6]. The results show it is a very promising method. Meanwhile, scientists in Lawrence Livermore National Laboratory developed a kind of kinoform phase plate for ICF uniform illumination[7,8]. In this paper, we will give out our fabricate and experiment results of PPE.

2. Design

We've developed a 2-D PPE design code according to a modified Gerchberg-Saxton algorithm[5,6], which enable us to design PPEs which can generate focal spots of arbitrary shapes and sizes with varied intensity profiles. During the design of the PPE, we

choose $\lambda=0.6328\mu m.$, the size is 40mm × 40mm. The iteration is start up with a lens like initial phase profile. With a uniform plane incident beam, the focal spot intensity profile is chosen to be a super-Gaussian function:

$$U_t(x_t, y_t) = \exp\left(\left|\tfrac{x}{w_x}\right|^n + \left|\tfrac{y}{w_y}\right|^n\right) \tag{1}$$

with n=50 and $w_x=w_y$=500μm. Figure 1(a) shows the phase distribution of the PPE after 100 iterations, Figure 1(b) is the focal spot intensity distribution. As we expect, the focal spot is of very sharp edge and low sidelobes. Statistically, the intensity profile tends to have a flat-top envelope, but resembles a speckle pattern with very large intensity modulations. This may be caused by the limits of the algorithm, such as self-trapping phenomena, etc. It is a problem need to be solved. However, by using PPE array, the modulation nonuniformity can be statistically averaged out, furthermore, the intensity distribution on the target plane will not be sensitive to the near-field distribution of the incident laser beam[4]. The interference fringes can also be smoothed out with some existing techniques, such as SSD or partially coherent light, etc.. To make a PPE array is very difficult and very expensive, but it is the most effective method available up date.
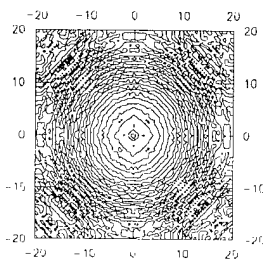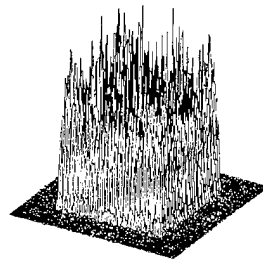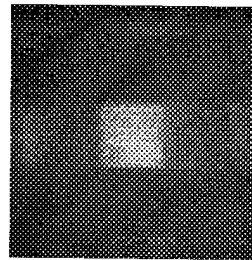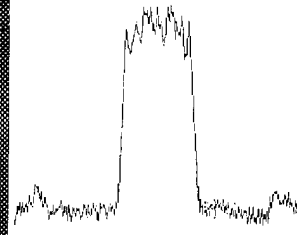

Figure 1. (a) The profile of the PPE obtained by the iterative algorithm (b) The intensity of the focal spot

Figure 2. (a) The experimental focal spot pattern. (b) Horizontal line-scan through the profile.

3. Experiment

Using technology of ion etching, a 40mm × 40mm in square size, 16 levels PPE has been fabricated. We have tested the PPE's performance using a 2D-image measurement system. An expanded He-Ne laser beam incident to the PPE and focused by a main focusing lens with a focal length of 340mm. A 500 × 582 pixel, 1/3" CCD imager is fixed in the target position. Figure 2(a) is the focal spot intensity profile, and Figure 2(b) is the horizontal line-scans through the profile. As expected, the focal spot is a 500μm × 500μm in size with very sharp edges. The intensity distribution within the spot is very modulated. These properties are fit with the theoretical result in the previous section. However, the pattern is a little different from the theoretical result in detail because of the drawback during the PPE's fabrication and the near-field distortion of the incident beam. The size of

the PPE is a little larger than that is fit to the ion etching equipment, this reduces the accurate of the masks' alignment. The misalignment cause a additional grating structure with a period of about 200μm in horizontal and vertical direction on the PPE's surface phase relief pattern, especially in the horizontal direction, as shown in Figure 2. We believe that this drawback can be overcome by enhance the accurate of the masks' alignment during the PPE's fabrication. Another simple but effective technique to fabricate the PPE is under developing.

Reference

[1] Y.Kato & K.Mima, "Random Phase Shifting of Laser Beam for Absorption Profile Smoothing and Instability Suppression in Laser Produced Plasmas", *Appl.Phys.B:* , 29(3), 186, (1982)

[2] R.H.Lehmberg & S.P.Oenschain, "Use of Induced Spatial Incoherence for Uniform Illumination of Laser Fusion Targets", *Opt.Commun.*, 46(1), 27, (1983)

[3] S.Skupsky, R.W.Short, T.Kessler, et al, "Improved Laser-Beam Uniformity Using the Angular Dispersion of Frequency-Modulated Light", *J.Appl.Phys.*, 66(8), 3456, (1989)

[4] Ximing Deng, Xiangchun Liang, Zezun Chen, et al, "Uniform Illumination of large targets Using a Lens Array", *Appl. Opt.* , 25(3), 377, (1986)

[5] Qiu Yue, Wen Guojun, Fan Dianyuan, Dengximing, Li Yongping, Deng Xuegong, "Using Kinoform Phase Plates to Generate Uniform Focal Profiles", *International Atomic Energy Agency Technical Committee Meeting on Drives for Inertial Confinement Fusion, Paris, France*, Nov.1994.

[6] Deng Xuegong, Li Yongping, Qiu Yue, Fan Dianyuan, "Phase-Mixture Algorithm Applied to Design of Pure Phase Elements", *Chinese Journal of Lasers* B4(5), 447, (1995)

[7] J.K.Lawson, S.N.Dixit, D.Eimerl, et al, "Phase Screens for the Control of the Focal Irradiance of the Nova Laser", *Proc. SPIE*, 1870, 88, (1993)

[8] S.N.Dixit, J.K.Lawson, K.R.Manes, et al, "Kinoform Phase Plates for Focal Plane Irradiance Profile Control", *Opt.Lett.* 19(6), 417, (1994)

Achromatization for Multiple Narrowband Sources using Hybrid Multi-Order Diffractive Lenses

Kevin J. McIntyre and G. Michael Morris, Institute of Optics, University of Rochester
Rochester, NY 14627, (716) 275-2322, (716) 271-1027 (FAX)

Introduction

Surface relief diffractive lenses that utilize multiple diffracted orders were first introduced by Sweeney and Sommargren[1] and Morris and Faklis[2]. More comprehensive discussions of these lenses were later presented[3,4,5]. These multi-order diffractive (MOD) lenses were shown to have the same optical power at a discrete set of resonance wavelengths within a chosen spectral region. The physical difference between a standard diffractive lens and a MOD lens is that the OPD at the zone boundaries of a standard diffractive lens is equal to the design wavelength, whereas, for a MOD lens the OPD is equal to an integer (>1) multiple of the design wavelength. As a result, the diffraction efficiency for each order of a MOD lens has a reduced spectral bandwidth. This efficiency reduction indicates that MOD lenses may be best suited for optical systems which utilize discrete wavelength sources as opposed to broadband sources. This paper will investigate the use of MOD lenses in this class of systems by examining the combination of refractive and diffractive lens power to achieve proper achromatic control in a manner analogous to the standard hybrid lens approach. These hybrid lens combinations may be well suited for applications such as color laser printing and laser machining. Several first order design examples are provided including a two-color hybrid achromat with nearly 100% diffraction efficiency and a three-color hybrid apochromat made from a single material.

Background

The expression for the power of a MOD lens is given as $\Phi(\lambda) = m\lambda\phi_0/p\lambda_0$, where m is the diffracted order, λ is the wavelength, ϕ_0 is the design power, p is a physical design parameter (integer), and λ_0 is the design wavelength. At the resonance wavelengths given by, $\lambda_{res} = p\lambda_0/m$, the optical power of the lens is equal to ϕ_0. It is likely that the operating wavelengths of a given system will not be the same as the resonance wavelengths making it necessary to add refractive power to achromatize the lens. To make use of the unique spectral properties of MOD lenses and to ensure a minimum level of diffraction efficiency, the operating wavelengths should be nearly equal to the resonance wavelengths. In terms of diffraction efficiency, the ideal operating wavelengths are those for which the efficiency equals 100 %. These wavelengths can be determined through use of the expression for the mth order diffraction efficiency, $\eta_m = sinc^2[\alpha(\lambda)p - m]$, where $\alpha(\lambda) = [\lambda_0(n(\lambda)-1)]/[\lambda(n(\lambda_0)-1)]$ is a wavelength detuning factor, and $n(\lambda)$ is the refractive index of the material. Since the effect of material dispersion is relatively small, the efficiency maxima occur near the resonance wavelengths.

Adding refractive power also results in a reduction in the rate of change of power as a function of wavelength. This dispersion reduction may be enough to accommodate the spectral fluctuations exhibited by diode lasers. The design bandwidth for such devices it typically 20 nm. For diode systems which are relatively fast, this dispersion may need to be constrained directly in the first-order design.

Theory

The concept of overlaying multiple diffractive lenses was recently introduced[1] for a broadband imaging application. In this case a standard diffractive lens was combined with a MOD lens to offset the effects of material dispersion. Generalizing this idea, the following expression is written for the power of N_{ref} thin refractive lenses and N_{diff} diffractive lenses in contact at an operating wavelength, λ_k,

$$\Phi(\lambda_k) = \sum_{i=1}^{N_{ref}} c_i\,(n_i(\lambda_k)-1) \;+\; \sum_{j=1}^{N_{diff}} A_j\,m_{jk}\,\lambda_k \;. \tag{1}$$

The curvature and refractive index of the ith refractive element are given by c_i and n_i, respectively. The factor, m_{jk}, represents the diffraction order of the jth diffractive element for the wavelength, λ_k, and A_j is a physical design parameter given by

$$A_j = \frac{\phi_j}{p_j(\lambda_{des})_j}\;. \tag{2}$$

In this expression p_j is an integer that specifies the integer number of waves of OPD at the edge of each diffractive zone, $(\lambda_{des})_j$ is the design wavelength of the jth diffractive lens, and ϕ_j is the power of the jth diffractive lens at the resonant wavelengths, $p(\lambda_{des})_j$ /m . The parameter, A_j, is analogous to the curvature c_i, since it describes the physical structure of a lens and remains unchanged as the operating wavelength, λ_k, is varied. A similar expression for the derivative of the lens power can be written as

$$\Phi'(\lambda_k) = \sum_{i=1}^{N_{ref}} c_i\,n_i{}'(\lambda_k) \;+\; \sum_{j=1}^{N_{diff}} A_j\,m_{jk} \tag{3}$$

where the prime symbol denotes the derivative with respect to wavelength. The resulting system of equations can be expressed as

$$
\begin{bmatrix}
n_1(\lambda_1)-1 & n_2(\lambda_1)-1 & \cdots & m_{11}\,\lambda_1 & m_{21}\,\lambda_1 & \cdots \\
n_1(\lambda_2)-1 & n_2(\lambda_2)-1 & \cdots & m_{12}\,\lambda_2 & m_{22}\,\lambda_2 & \cdots \\
\cdots & \cdots & \cdots & \cdots & \cdots & \cdots \\
n_1{}'(\lambda_1) & n_2{}'(\lambda_1) & \cdots & m_{11} & m_{21} & \cdots \\
n_1{}'(\lambda_2) & n_2{}'(\lambda_2) & \cdots & m_{12} & m_{22} & \cdots \\
\cdots & \cdots & \cdots & \cdots & \cdots & \cdots
\end{bmatrix}
\cdot
\begin{bmatrix}
c_1 \\ c_2 \\ \cdots \\ A_1 \\ A_2 \\ \cdots
\end{bmatrix}
=
\begin{bmatrix}
\Phi_{tot} \\ \Phi_{tot} \\ \cdots \\ 0 \\ 0 \\ \cdots
\end{bmatrix}
\tag{4}
$$

where Φ_{tot} represents the target power at each of the operating wavelengths, and the value of the derivative of the power is arbitrarily set equal to zero. Each row corresponds to a specific operating wavelength and each column corresponds to a specific lens element. If the number of rows in the matrix equals the number of variables given in the column vector on the LHS, then at least one solution exists. This assumes that no two columns in the matrix are multiples of one another since they could be combined causing a reduction in the number of variables by one. This assumption implies a restriction on overlapping multiple diffractive lenses which can be expressed solely in terms of the diffraction orders as

$$\frac{m_{jk}}{m_{j'k}} = constant, \qquad \text{for all k in two columns } (j \neq j'). \tag{5}$$

If this condition is satisfied, the two diffractive lenses are not independent and therefore degenerate into one. This restriction prohibits designing a diffractive lens by simply multiplying the values for p and m of another diffractive lens by a fixed scale factor. Note that this degeneracy condition is analogous to defining two refractive lenses with the same material (i.e. refractive index). Examples of valid combinations of overlaid diffractive lenses include: 1) a diffractive lens which uses the same diffracted order for two or more operating wavelengths combined with another diffractive lens which utilizes at least two different orders for different operating wavelengths 2) a MOD lens, used in a system of three operating wavelengths, which uses three consecutive diffracted orders and a second MOD lens which utilizes orders such that there are an unequal number of orders between the operating wavelengths.

Design Examples

In all of the following examples, the glass is BK7 and the nominal focal length is 60 mm. The diffraction efficiency for multiple diffractive lenses is calculated as the product of the individual lens efficiencies at each wavelength.

Three-color hybrid apochromat

This lens is designed to have the same power at three different wavelengths and is formed with a single refractive lens and two overlaid diffractive lenses. A potential application for this lens type is a color laser writer which writes to a spectrally sensitive substrate such as photographic film. This type of application may require a relatively fast system making achromatic correction particularly important. The following operating wavelengths are assumed: $\lambda_1 = 670$ nm, $\lambda_2 = 750$ nm, $\lambda_3 = 880$ nm. The first diffractive lens is the conventional type ($p = 1$; $m = 1$) with a design wavelength given by $(\lambda_{des})_1 = \lambda_2 = 750$ nm. The second diffractive lens is a MOD lens with following design parameters, which are chosen to maximize the diffraction efficiency at each of the operating wavelengths: $p = 6$; $m = 6, 7, 8$; $(\lambda_{des})_2 = 880$ nm. The resonance wavelengths of the MOD lens are $\lambda_{res,8} = 660$ nm, $\lambda_{res,7} = 754$ nm, and $\lambda_{res,6} = 880$ nm. Using equation 4, one can solve for the refractive lens curvature, c, and the diffractive lens parameters, A_1 and A_2. The total power of the hybrid lens is distributed among the three lenses as: 101.63% : 2.69% : -4.32% (ref : standard diff : mod).

The chromatic behavior of this lens is illustrated in Fig. 1(a) which shows the focal length and the diffraction efficiency as functions of wavelength. The diffraction efficiencies at each of the operating wavelengths (shortest to longest) are equal to 94%, 98%, and 93%, respectively. The slopes of the focal length curves are roughly the same and given by 3.7μm/nm. A wavelength shift of 10 nm for one of the lasers results in a focus error of 0.037 mm. For an F/5 system, this is nearly equal to the depth of focus. In this case the laser spectral output would have to be better controlled. For slower systems, this focus error may be tolerable but it might be more appropriate to use a standard hybrid achromat designed to unite the focii for the wavelengths, λ_1 and λ_3.

Two-color hybrid achromat

This lens is designed to have the same power at two wavelengths and a value of zero for the derivative of the power at one of the wavelengths. It is formed with a single refractive lens and two overlaid diffractive lenses. Such chromatic properties may be appropriate for a high speed system which incorporates a diode alignment laser without any special controls over the emitted wavelength and a spectrally stable laser. A potential application is high resolution laser machining. The following wavelengths are assumed: $\lambda_1 = 500$ nm (primary beam), $\lambda_2 = 670$ nm (diode). The derivative of the power is set equal to zero at the diode wavelength. The first diffractive lens is the conventional type ($p = 1$; $m = 1$) with a design wavelength given by $(\lambda_{des})_1 = \lambda_1 = 500$ nm. The second diffractive lens is a MOD lens with the following design parameters: $p = 4$; $m = 3, 4$; $(\lambda_{des})_2 = \lambda_1 = 500$ nm. The resonance wavelengths of the MOD lens are $\lambda_{res,4} = 500$ nm and $\lambda_{res,3} = 667$ nm. The total power of the hybrid lens is distributed among the three lenses as: 97.69% : 0.92% : 1.39% (ref : standard diff : mod).

Fig. 1(b) shows the focal length and the diffraction efficiency as functions of wavelength. The diffraction efficiencies at each of the operating wavelengths, λ_1 and λ_2, are 100% and 79%, respectively. The reduced efficiency for λ_2 results from setting the design wavelength of the standard diffractive lens to be equal to λ_1.

Two-color hybrid achromat

This lens is similar to the previous two-color hybrid achromat but with no constraint on the derivative of the power and is formed with a single refractive lens and a single MOD lens. This lens type may be useful in a two laser application where the diffraction efficiencies must approach 100% at both of the operating wavelengths. The following relevant parameters are assumed: $\lambda_1 = 500$ nm, $\lambda_2 = 670$ nm ; $p = 3$; $m = 4, 3$; $(\lambda_{des})_1 = 665$ nm. The total power of the hybrid lens is distributed among the two lenses as: 25.77% : 74.23% (ref : mod).

Fig. 1(c) shows the focal length and the diffraction efficiency as functions of wavelength. The diffraction efficiencies at each of the operating wavelengths, λ_1 and λ_2, are 99.3% and 99.8 %, respectively. The relatively steep slope of the focal length curves, due to the strong diffractive component, dictates that the laser wavelengths should not deviate from their design values.

Summary

By combining multiple diffractive lenses with one or more refractive lenses, a variety of achromatic lens types can be designed. These lenses are particularly suited to laser applications which require achromatic behavior at a discrete set of operating wavelengths. These lens types offer the same advantages that conventional hybrid achromats provide including fewer lens materials (i.e. elements) and reduced surface curvatures. In fact, it is possible to design a three-color apochromat using a single lens material. The design of these lenses involves making judicious choices for the diffractive design wavelengths as well as the physical parameter, p, described earlier. For a system where the operating wavelengths are relatively close to one another, a conventional doublet design (either refractive or standard hybrid) may be the most appropriate choice, since the change in power over the small spectral band may be tolerable. However, for high speed systems in which chromatic aberration must be tightly controlled or systems in which the spectral separation is relatively large, these new hybrid lenses provide an alternative to existing achromatic design forms.

(a)

(b)

(c)
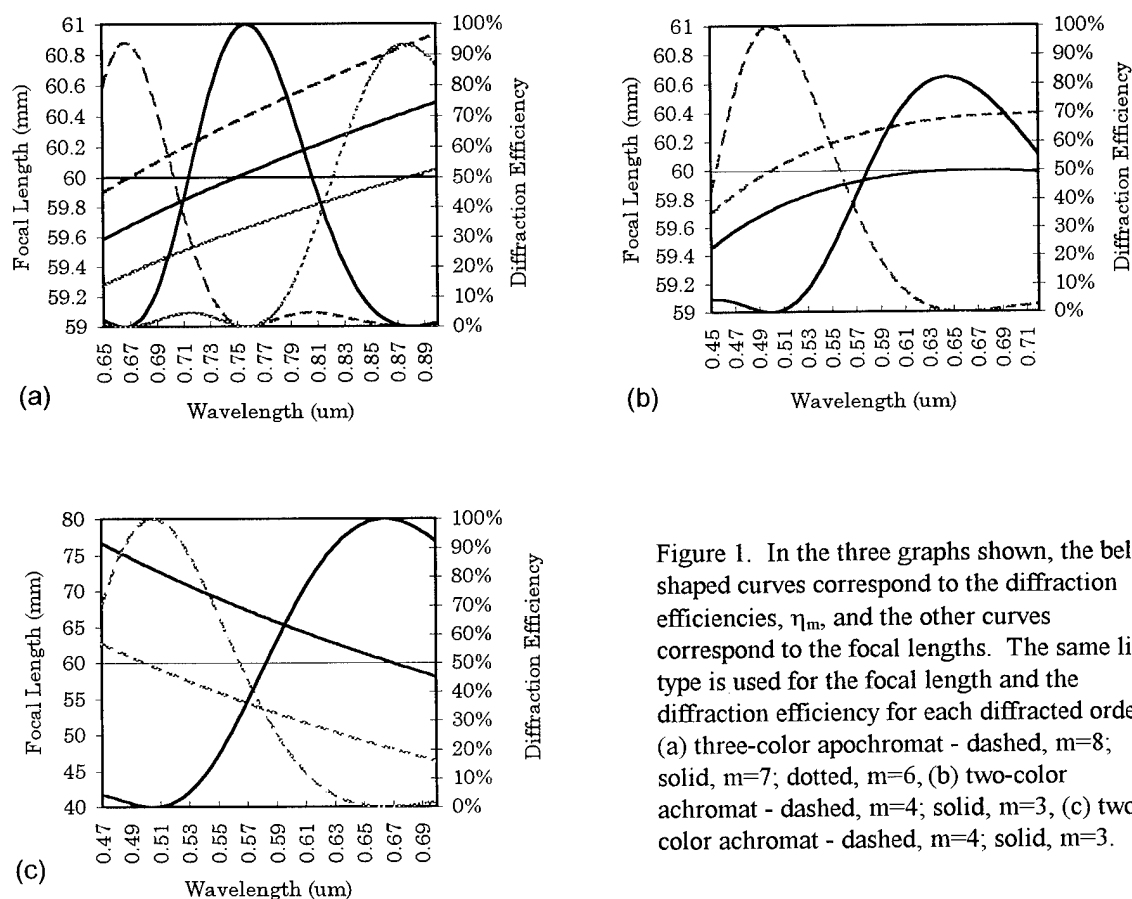
Figure 1. In the three graphs shown, the bell shaped curves correspond to the diffraction efficiencies, η_m, and the other curves correspond to the focal lengths. The same line type is used for the focal length and the diffraction efficiency for each diffracted order. (a) three-color apochromat - dashed, m=8; solid, m=7; dotted, m=6, (b) two-color achromat - dashed, m=4; solid, m=3, (c) two-color achromat - dashed, m=4; solid, m=3.

References

[1] D. W. Sweeney and G. Sommargren, "Single element achromatic diffractive lens", in Diffractive Optics, Vol. 11 of 1994 OSA Technical Digest Series (Optical Society of America, Washington, D.C., 1994), pp. 26-29

[2] G. M. Morris and D. Faklis, "Achromatic and apochromatic diffractive singlets", in Diffractive Optics, Vol. 11 of 1994 OSA Technical Digest Series (Optical Society of America, Washington, D.C., 1994), pp. 53-56

[3] D. Faklis and G. M. Morris, "Spectral properties of multiorder diffractive lenses", Appl. Opt. 34, 2462-2468 (1995)

[4] D. W. Sweeney and G. Sommargren, "Harmonic diffractive lenses", Appl. Opt. 34, 2469-2475 (1995)

[5] M. Rossi, R.E. Kunz, and H.P. Herzig, "Refractive and Diffractive Properties of Planar Micro-Optical Elements", Appl. Opt. 34, 5996-6007 (1995)

Array Generator Design for an Optical Analog-to-Digital Converter

Joseph N. Mait
U.S. Army Research Laboratory
AMSRL-SE-EO
2800 Powder Mill Road
Adelphi, Maryland 20783
e-mail: mait@arl.mil

Barry L. Shoop
Photonics Research Center
Department of Electrical Engineering and Computer Science
United States Military Academy
West Point, New York 10996

Within the context of image processing, digital image halftoning is an important class of analog-to-digital (A/D) conversion. Halftoning can be thought of as an image compression technique whereby a continuous-tone, gray-scale image is printed or displayed using only binary-valued pixels. One method to achieve digital halftoning is error diffusion, wherein the error associated with a nonlinear quantization process is diffused within a local region. One of us (BLS) has developed a neural network architecture based on the mathematical foundation of the error diffusion algorithm that is called an error diffusion neural network [1]. The error diffusion neural network computes the halftoned image asymptotically faster than a conventional Hopfield-type neural network, provides full-rank connectivity across the entire image (other error diffusion techniques provide only local error diffusion), and, because of its parallel implementation, does not generate any artifacts commonly associated with sequential halftoning. Figure 1 is a representation of a smart-pixel-based architecture for an optical implementation of the error diffusion algorithm. The functionality required of the error diffusion neural network is implemented using gallium arsenide (GaAs) and aluminum gallium arsenide (AlGaAs) multiple quantum well modulators. The two-dimensional spatial distribution and intensity weighting required of the error diffusion filter is accomplished using a diffractive array generator. We report here on the design of the array generator.

The desired diffusion matrix is

0.0003	0.0019	0.0051	0.0068	0.0051	0.0019	0.0003
0.0019	0.0103	0.0248	0.0328	0.0248	0.0103	0.0019
0.0051	0.0248	0.0583	0.0766	0.0583	0.0248	0.0051
0.0068	0.0328	0.0766	0	0.0766	0.0328	0.0068
0.0051	0.0248	0.0583	0.0766	0.0583	0.0248	0.0051
0.0019	0.0103	0.0248	0.0328	0.0248	0.0103	0.0019
0.0003	0.0019	0.0051	0.0068	0.0051	0.0019	0.0003

These weights describe the intensity of the desired generated array. Because of the sensitivity of the human visual system to directional artifacts, circular symmetry of the frequency response is a key requirement in the design of this filter. If an eight-level phase-only array generator is assumed, the diffraction efficiency upper bound for this array is 91.15% [2]. We used the upper

bound solution as an initial input to the iterative Fourier transform algorithm [3] to design a 128 × 128 eight-level phase-only array generator. The phase function for a single period of the array generator is represented in Fig. 2. The calculated diffraction efficiency of the array generator is 91.97% and root-mean-square fluctuation in amplitude is only 0.0026.

The geometry of the opto-electronics is such that the horizontal spacing between quantum well modulators is twice that of the vertical. This is evident in Fig. 3, which is a representation of the mask set necessary to fabricate the array generator. The element has been submitted for fabrication to the diffractive optics foundry run sponsored by the ARPA CO-OP. The specifics of the design are indicated below.

Given
wavelength $\lambda = 850$ nm
focal length $f = 50$ mm
spot spacing $d_x \times d_y = 160\ \mu m \times 80\ \mu m$
DOE size $D_x \times D_y = 1\ cm \times 1\ cm$
minimum feature $\Delta_x \times \Delta_y = 2.1\ \mu m \times 4.2\ \mu m$

Calculated
grating period $W_x \times W_y = \lambda f/d_x \times \lambda f/d_y = 265.625\ \mu m \times 531.25\ \mu m$
number of replicas $M_x \times M_y = D_x/W_x \times D_y/W_y = 37.647 \times 18.824$
lattice size $L_x \times L_y = W_x/\Delta_x \times W_y/\Delta_y = 126.49 \times 126.49$

Designed
128 × 128 array generator replicated 37 × 18 times
grating period $(128 \cdot 2.1\ \mu m) \times (128 \cdot 4.2\ \mu m) = 268.8\ \mu m \times 537.6\ \mu m$
DOE size $(37 \cdot 268.8\ \mu m) \times (18 \cdot 537.6\ \mu m) = 9.9456\ mm \times 9.6768\ mm$
spot spacing $(850\ nm \cdot 50\ mm) \cdot (1/268.8\ \mu m \times 1/537.6\ \mu m) = 158.11\ \mu m \times 79.06\ \mu m$
spot size ~$(850\ nm \cdot 50\ mm)/1\ cm = 4.25\ \mu m$

1. B. L. Shoop, J. N. Mait, and E. K. Ressler, "Optical error diffusion for analog-to-digital conversion," submitted to the 1996 Army Science Conference.
2. F. Wyrowski, Opt. Lett. 16, 1915-1917 (1991).
3. F. Wyrowski, J. Opt. Soc. Am. A 10, 1553-1561 (1993).

Figure 1. Architecture for optical implementation
of error diffusion neural network.

128 x 128 8-level phase-only diffusion matrix array generator

Figure 2. Representation of single period of phase for
an eight-phase level diffusion matrix array generator.

Figure 3. Representation of single period of mask set necessary to fabricate eight-phase level diffusion
matrix array generator. Binary mask for (a) π-phase, (b) $\pi/2$-phase, and (c) $\pi/4$-phase etches.

Electric Fields and Poynting Vectors
in Dielectric Gratings

Bruce W. Shore
Lawrence Livermore National Laboratory, Livermore CA 94550
phone (510) 455-0627 email shore2@LLNL.GOV
Lifeng Li
Optical Sciences Center, University of Arizona, Tucson AZ 85721
and Michael D. Feit
Lawrence Livermore National Laboratory, Livermore CA 94550

The electric field E is the most significant of the several fields of electromagnetic radiation, because it indicates regions of dielectric response. The nodes and antinodes of plane wave structure are clearly visible in plots of the E field, as are regions of localized enhancement near grating surfaces. It is in these enhanced field regions that one expects to find the strongest photoelectric response, or the first damage as the field is increased.

The electromagnetic energy density W , though uniform for simple standing wave patterns (above a mirror or high efficiency grating) reveals more structure around the grating interface than does the E field. It reveals mode structure and evanescent waves. However, patterns of nodes and antinodes in energy density do not become visible through photoelectric response, and regions of high energy density are not necessarily the regions in which damage occurs.

When there are no dissipative or absorptive sources and sinks of electromagnetic radiation, as is the case for an ideal dielectric material, then the Poynting vector S is a divergenceless field. It can have curls and saddle points as well as planes along which there is uniform flow. These structures do not correspond in an intuitively obvious way with the more important structure of nodes and peaks of the electric field, although the patterns of the two fields are closely tied.

When applied to resistive electromagnetic circuits, the Poynting vector describes Joule heating. The Poynting vector has been used to provide insight into the behavior of metallic gratings, whose surfaces are, like resistors, sinks for electromagnetic energy . In particular, Popov [1-3] has offered plots of the Poynting vector as a means of understanding how grating efficiency varies with groove depth, passing through regimes of high and low diffraction efficiency, interspersed with regimes of high and low specular reflection [3].

Such studies have had great value for the understanding of metal gratings. It is natural to hope that the Poynting vector will offer insight into the behavior of all-dielectric gratings.

Our studies, based on numerical solutions to the Maxwell equations using the multilayer modal method [4], have shown that although it is possible to associate changes of S with changes in grating construction, not all of these changes are evident in the far field. It is particularly noteworthy that small changes in groove shape of a dielectric grating may, without influencing the far field pattern (i.e. the grating efficiency) or the near E field cause

dramatic changes in the near-field Poynting vector: rows of curls may shift from above grating valleys to above grating peaks. Furthermore, the planes of steady flow of **S** may flow in either direction. Unlike the situation with absorbing material (metallic surfaces), the flow lines of **S** in a dielectric do not provide indication of Joule heating or other observable effects.

From examining the appearance of E, W and S in representative cases, we conclude that plots of **S** may not be as useful for dielectric gratings as they are for metallic structures. The energy density W is a much more intuitive field to examine than is **S**

References

[1]. E. Popov, L. Tsonev and D. Maystre, "Gratings - general properties of the Littrow mounting and energy flow distribution" J. Mod. Opt. **37,** 367-377 (1990)

[2]. E. Popov, L. Tsonev and D. Maystre, "Losses of plasmon surface waves on metallic grating" J. Mod. Opt. **37,** 379-387 (1990)

[3]. E. Popov and L. Tsonev, "Total absorption of light by metallic gratings and energy flow distribution" Surface Science **230,** 290-294 (1990)

[4]. L. Li, "Multilayer modal method for diffraction gratings of arbitrary profile, depth, and permittivity" JOSA A **10,** 2581-91 (1993)

Diffractive-refractive achromatic optical processor for white-light spatial filtering

P. Andrés, E. Tajahuerce*, J. Lancis*, V. Climent*, and M. Fernández-Alonso*

Universidad de Valencia, Departamento de Optica, 46100 Burjassot, Spain.
Universitat Jaume I, Departamento de Ciencias Experimentales, 12080 Castellón, Spain.

1. INTRODUCTION

White-light Fourier processing techniques allow to improve the signal-to-noise ratio, to use non-laser sources, and, of course, to deal with color input signals. Nevertheless, conventional optical processing operations performed with broadband illumination are severally limited due to the wavelength dependence of the diffraction phenomenon. In this way, the Fraunhofer diffraction pattern of the input transparency is chromatic dispersed, both axial and laterally and, furthermore, the insertion of spatial filters at the frequency plane produces additional chromatic effects at the output plane.

Achromatic Fourier transformers are designed to partially compensate for the chromatic dispersion of the Fraunhofer diffraction pattern [1]. In this direction, two different optical architectures, constituted by a small number of diffractive lenses and achromatic objectives, providing the achromatic representation of the optical Fourier transform of any color input signal with low chromatic aberration under white-light point source illumination have been recently proposed [2,3]. The optical Fourier transform provided by the above optical setups is located, in a first-order approximation, in a single real plane and with the same magnification for all the wavelengths of the incident light. In a different context, it is also possible to design achromatic imaging systems using diffractive optical elements and conventional lenses [4,5].

Combining both achromatic Fourier transforming concepts and diffractive imaging methods, in this contribution we report a novel achromatic Fourier processor under white-light point source illumination. The first part of our optical proposal is an achromatic Fourier transformer that uses solely two on-axis blazed diffractive lenses. By adding only an achromatic objective and a third zone plate, the whole arrangement acts as an achromatic imaging configuration that, thus, images the input transparency into the output plane preserving the achromatic correction in the intermediate Fraunhofer plane. With a different approach, other achromatic Fourier processors have been previously reported [6-8]. However, they are constituted by a large number of optical components and/or the residual chromatic errors are very important. The formation of the final image can be understood in all the above cases as a double achromatic Fourier transforming process in cascade.

Our configuration provides an intermediate achromatic Fourier transform with low chromatic aberration and, neglecting the secondary chromatic aberration of the refractive objective, a final image with no chromatic error. This achromatic optical processor is well-adapted to extend the conventional monochromatic spatial filtering techniques to white-light with noteworthy results. Now, our optical processor can perform the same spatial filtering operation for all the spectral components of the broadband illumination simultaneously.

2. ACHROMATIC FOURIER TRANSFORMER

Let us consider an input transparency illuminated by a broadband spherical wavefront beam converging towards the point source S located at a normal distance z from the aperture. It is possible to recognize that a separated diffractive doublet, which consists of two on-axis zone plates ZP_1 and ZP_2 in such a way that ZP_2 is positioned at the source plane, is able to provide an achromatic representation of the Fourier transform of the input, as is depicted in Fig.1. If we denote Z_0 and Z'_0 as the focal length of ZP_1 and ZP_2, respectively, for the reference wave number σ_0, the achromatic condition leads to the constraint [3]

Figure 1.

$$d^2 = -Z_0 \, Z'_0 \quad , \qquad (1)$$

where d is the separation between the two zone plates.

In this way, the Fraunhofer diffraction pattern of the diffracting screen is obtained, in a first-order approximation, at a distance D'_0 from ZP_2 such that

$$D'_0 = \frac{-d^2}{d + 2 Z_0} = \frac{\alpha}{\sqrt{\alpha} - 2} Z_0 \quad , \qquad (2)$$

where the dimensionless parameter α is defined as $\alpha = -Z'_0 / Z_0$. In order to manipulate the spectral content of the input object we must obtain a real achromatic Fraunhofer plane, i.e. $D'_0 > 0$. This later fact implies that ZP_1 and ZP_2 should be a diverging and a converging zone plate, respectively, and α must satisfy the inequality $0 < \alpha < 4$.

Since we develop a first-order theory, the setup suffers from residual chromatic aberrations. For $\sigma_o = \sqrt{\sigma_1 \sigma_2}$, being σ_1 and σ_2 the end wave numbers of the incoming radiation, it is possible to show that the greatest value of both the axial and the lateral geometrical chromatic error, CA_M, expressed as a percentage, is given by

$$CA_M = \frac{100}{1 + \beta \, (2 - \sqrt{\alpha})} \quad , \qquad (3)$$

where $\beta = \sqrt{\sigma_1 \sigma_2} / (\sqrt{\sigma_1} - \sqrt{\sigma_2})^2$ takes into account the spectral bandwidth of the incident light. It is important to note that the achromatization of the Fourier transforming process in intensity remains unaltered by the position of the input along the optical axis of the system.

3. ACHROMATIC IMAGING SYSTEM

In order to design the achromatic Fourier processor we think about the whole optical setup as an achromatic imaging system whose first half performs an achromatic Fourier transformation of the input transparency. Following Morris' study [5], we consider an imaging system constituted by two on-axis zone plates, ZP_2 and ZP_3, with focal length Z'_0 and Z''_0, respectively, for the design wave number σ_0, and an achromatic objective L, with focal distance f, located between the two, as is shown in Fig.2.
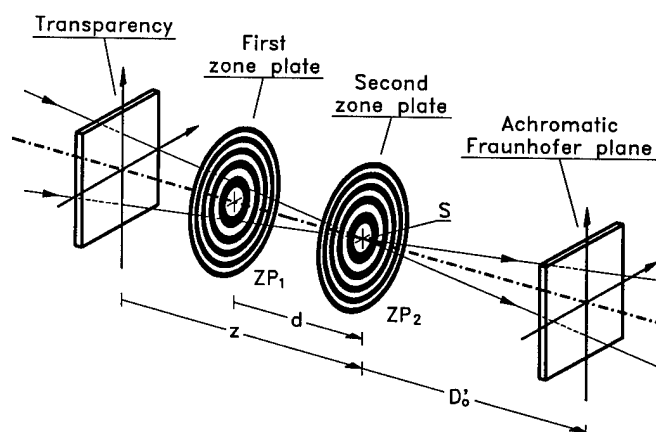
Let an input object O, illuminated by a polychromatic light beam, be located at a distance d of ZP_2. It is apparent that if we are able, in some way, to compensate the action of the two zone plates, the final image, O', supplied by the optical system will be simply given by the action of the refractive objective L. Thus, neglecting the secondary chromatic aberration of the achromatic lens, we will obtain a wavelength-independent image at the output plane. It is easy to recognize that this compensation

Figure 2.

can be accomplished if the next two conditions are satisfied. First, ZP_2 and ZP_3 are located at conjugate planes through the lens L. In mathematical terms, the distances l and l' (see Fig.2) must be related by

$$l' = \frac{l\,f}{l - f} = -M\,l \quad , \tag{4}$$

where M is the lateral magnification between the conjugate planes. Second, in order that the image of ZP_2 through L has the same scale than ZP_3, i.e., the same focal distance (aside from a sign change), the focal lengths Z'_0 and Z''_0 must be linked by the relation

$$Z''_0 = -M^2\,Z'_0 \quad . \tag{5}$$

In this way, the image O' appears just at the conjugate plane of O through L. That is, at a distance I'_0 from ZP_3 such that

$$I'_0 = \frac{-f^2\,d}{(l - f)(l + d - f)} = -M\,M_0\,d \quad , \tag{6}$$

where M_0 is the lateral magnification between O and O' given by the objective. Although I'_0 is in principle negative, a real final image can be obtained by simply adding a second achromatic objective at the end of the setup.

4. ACHROMATIC PROCESSOR

The appropriate combination of the optical setups shown in Figs.1 and 2 provides an achromatic Fourier processor as we show next. The whole setup corresponding to our optical processor is shown in Fig.3. The first two zone plates, ZP_1 and ZP_2, perform the achromatic Fourier transformation of the input transparency. Our Fourier-transform configuration is constructed following the prescriptions of section 3. Thus, the achromatic condition is fixed by Eq.(1) and the achromatic Fraunhofer plane is located at a distance D'_0 from ZP_2 given by Eq.(2). The Fourier processor is then achieved by adding the achromatic objective L and the third zone plate ZP_3 in such a way that the position and the focal length of ZP_3 are determined by Eqs.(4) and (5), respectively. In this way, the three optical elements ZP_2, L, and ZP_3 act as an achromatic imaging system provided that the input transparency be located just against the first zone plate ZP_1. The final image plane is then located at a distance I'_0 from
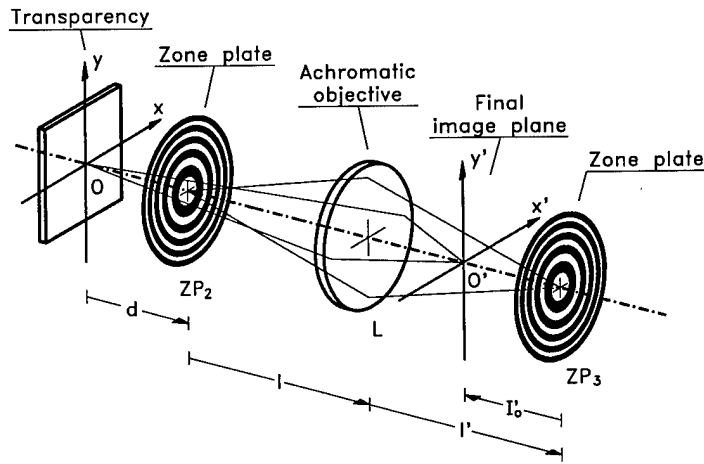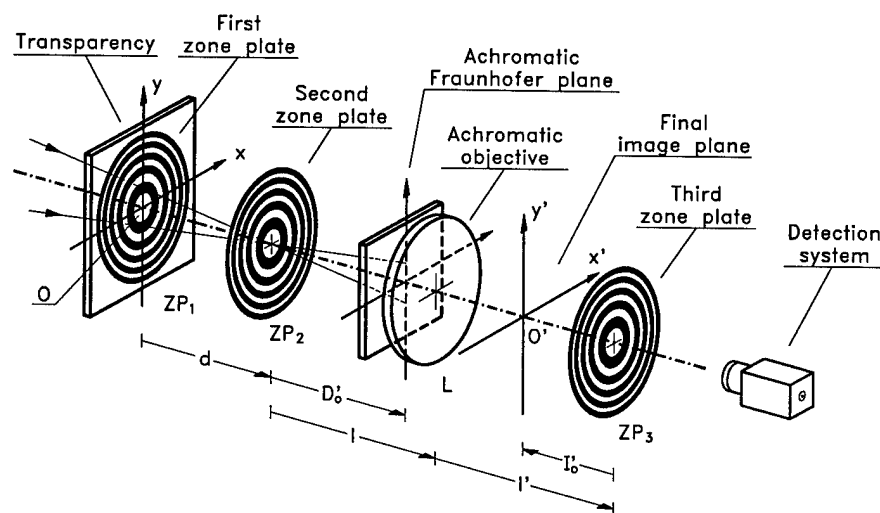
Figure 3.

ZP_3 given by Eq.(6). We can define the total length of our processor as the distance $e = d + l + l'$.

To optimize the optical system, the focal distances Z_0 and Z'_0 are selected in such a way that α has a small value. In this way, we obtain the Fourier transform of the input with low residual chromatic aberrations. To minimize the total length of the setup, it is convenient to choose l' such that $l' = l = 2f$, and thus $M = -1$. By inserting this result into Eq.(5), we derive that $Z''_0 = - Z'_0$. Finally, for inserting a spatial filter at the achromatic Fraunhofer plane of the setup the distance l must be grater than D'_0 and, thus, the focal length f must fulfill the inequality $f > D'_0/2$.

We will report some experimental verifications of the above procedure. In particular, the novel spatial filtering capabilities of our achromatic Fourier processor will be illustrated in a color multiple imaging experiment.

5. REFERENCES

1. G. M. Morris, "Diffraction theory for an achromatic Fourier transformer," Appl. Opt. **20**, 2017-2025 (1981).

2. P. Andrés, J. Lancis, and W. D. Furlan, "White-light Fourier transform with low chromatic aberration," Appl. Opt. **31**, 4682-4687 (1992).

3. J. Lancis, P. Andrés, W. D. Furlan, and A. Pons, "All-diffractive achromatic Fourier transform setup," Opt. Lett. **19**, 402-404 (1994).

4. S. J. Bennet, "Achromatic combinations of hologram optical elements," Appl. Opt. **15**, 542-545 (1976).

5. D. Faklis and G. M. Morris, "Broadband imaging with holographic lenses," Opt. Eng. **28**, 592-598 (1989).

6. R. H. Katyl, "Compensating optical systems. Part 3: Achromatic Fourier transformation," Appl. Opt. **11**, 1255-1260 (1972).

7. G. M. Morris and N. George, "Frequency-plane filtering with an achromatic optical transform," J. Opt. Soc. Am. **5**, 446-448 (1980).

8. S. Leon and E. N. Leith, "Optical processing and holography with polychromatic point source illumination," Appl. Opt. **24**, 3638-3642 (1985).

Diffractive Optical Elements for Tracking and Receiving in Optical Space Communication Systems

P. Blattner, H. P. Herzig, K. J. Weible
Institute of Microtechnology, University of Neuchâtel,
Rue A.- L. Breguet 2, 2000 Neuchâtel, Switzerland
Tel +41 38 234 494, Fax +41 38 254 276

1 Introduction

The design of first generation free space laser communication systems is based on laser diodes with output powers in the order of 100 mW [1]. The data rate transmission is in the order of 100 Mbit/s. This leads to terminals with large transmitter and receiver telescope diameters and, consequently, to high terminal mass and dimensions. The optical systems are usually designed with refractive lenses and reflective mirrors. Alternatives are planar diffractive optical elements (DOEs). By relying on diffraction and interference rather than on reflection and refraction, unique and novel properties can be realized. Almost any structure shape, including non–rotationally symmetric aspherics, can be manufactured, which provides all degrees of freedom for the design. Other interesting aspects of DOEs are their low weight, their strong dispersion, and the possibility to make segmented elements, large arrays of elements, beamsplitters, and polarizers. These properties are useful for many applications of DOEs in space, including: filters for image data processing [2], beam shaping [3, 4], and antireflection structures [5, 6]. Furthermore, the combination of refractive and diffractive surfaces (hybrid elements) offers new possibilities for optical design. The negative dispersion of DOEs can be used to compensate the chromatic aberrations of refractive lenses [7, 8]. Hybrid elements can also be used to compensate the temperature induced variations of their mounting system [9, 10]. Diffractive optical elements for space applications must comply with a number of requirements, including mechanical, thermal and optical stability [8]. Suitable techniques for realizing the microstructures in space qualified materials are based on a variety of high resolution lithographic and optical processes [11].

In this paper, we discuss the design and experimental realization of a ring pattern generator allowing tracking and data transmission within one optical element. This work has been done in the framework of an ESA project [12, 13].

2 Tracking/Receiver System

A schematic of a typical tracking/receiver system of the optical head of a laser communication system is shown Fig. 1. The tracking sensor consists of a 4-quadrant detector with a central hole which acts as a field stop for the subsequent receiver optics. The specific task of the diffractive optical element, situated at the entrance of the tracking/receiver system, consists of focusing the incoming beam into the central hole (receiver signal) while generating a ring intensity pattern in the tracking detector
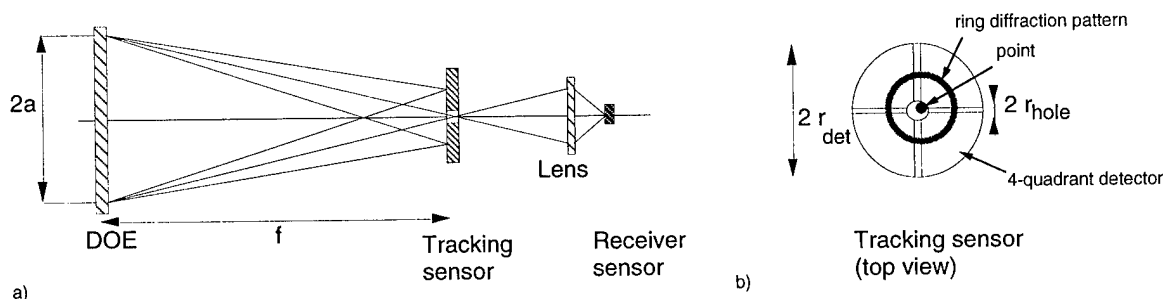

Figure 1: Principles of the tracking/receiving system. a) side view, b) top view. Changes of the relative positions of the sending and receiving communication terminals are directly translated into a shift of the ring intensity pattern on the tracking sensor, which can be measured by means of the 4-quadrant detector.

plane (tracking signal). Changes of the relative positions of the sending and receiving communication terminals are directly translated into a shift of the ring intensity pattern on the tracking sensor, which can be measured by means of the 4–quadrant detector.

Different design methods exist for the tracking/receiver DOE. The two specific tasks may be made by a segmented element. This means that the surface of the DOE is divided into two parts: A simple lens function in one part for the focusing point, and a radially shifted lens function in the other part for generation of the ring pattern (segmented aperture design). An alternative technique is to generate the ring pattern by the first diffraction order of a rotational blazed grating structure combined with a focusing function. The focal point in the center is then realized by the zero order of the grating structure. In this case, both functions are generated by the whole element, thus have the same aperture (common aperture design). The two design strategies are shown in Fig. 2 a) and b).
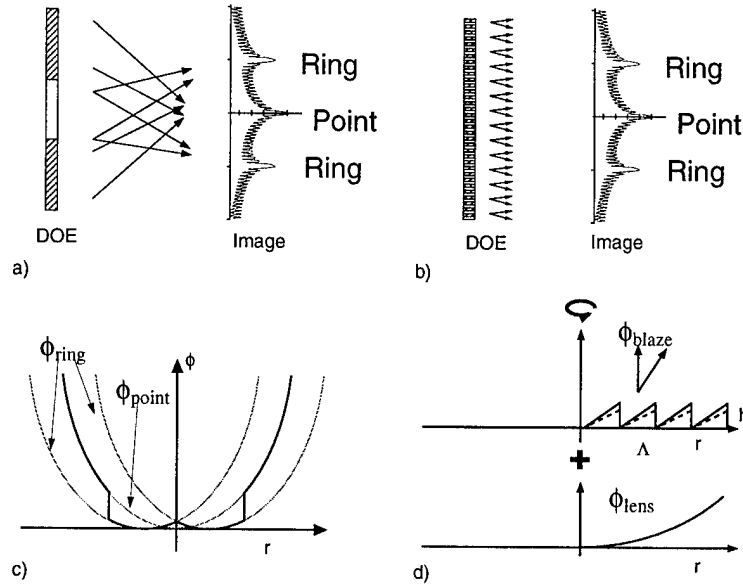
Figure 2: Two different design approaches for the tracking/receiver element. a) Segmented aperture design, b) common aperture design, c) the phase function of the segmented element, d) the phase function of the common aperture element.

DOEs are mainly described by their phase function. For the segmented aperture design each segment has its own phase function. In the case of the tracking/receiver DOE the phase function ϕ is then given by

$$
y = \begin{cases} -\dfrac{k}{2f}r^2 & for \quad r_{seg} < r < a \\[2em] -\dfrac{k}{2f}(r - r_{ring})^2 & for \quad 0 < r < r_{seg} \end{cases} , \tag{1}
$$

where k is the wave vector, f the focal length of the tracking system, r_{ring} the radius of the ring intensity pattern on the 4-quadrant detector, $2a$ the diameter of the DOE, and r_{seg} the radius of separation of the two different segments. The function $\phi(r)$ is shown in Fig. 2 c). The advantage of this concept is that the ratio of the energy used for tracking (ring) and the energy used for the receiver (focal point) is directly given by the ratio of the surfaces of the two segments (i.e. $(r_{seg}/a)^2$). Furthermore, the two optical functions can be tested and characterized independently by covering one of the segments. However, a drawback of this concept might be that the system is not shift invariant, i.e. a change of the input intensity distribution directly affects the output functions. Also, the radius of the diffraction spot of the focus and the width of the ring are given by the aperture of the corresponding segments. This can lead to design problems. In particular, if much more energy has to be in the central point than in the ring, the surface of the segment used to generated the ring becomes small, thus, the width of the ring gets very large due to diffraction. On the other hand, if much more energy has to be in the ring than in the point, the point becomes very large. Depending on the design specifications the segmented approach may not be satisfying. The above mentioned problem can be avoided by the common aperture design.

The phase function of the common aperture design is composed of a lens function and a blazed grating structure defined over the entire aperture

$$\phi(r) = -\frac{k}{2f}r^2 + h \; \text{mod}(\frac{r}{\Lambda}, 1),$$ (2)

where Λ is the period of the grating structure, h is the phase depth of the grating structure and $mod(a, b)$ is the modulo function (also referred to the fractional part of the division a/b) . The phase function $\phi(r)$ is shown in Fig. 2 d). The grating period Λ determines the beam deflection of the first diffraction order, thus, the radius of the ring, while the phase depth of the grating structure h determines the energy distribution in the different diffraction orders. The diffraction efficiency of the first order of a blazed phase grating is given by

$$\eta_1 = \sin^2\left(\frac{h}{4}\right).$$ (3)

For a 2π-deep blazed structure only the first diffraction order has energy, therefore, only a ring structure without central peak is generated. If the phase depth differs from 2π, then the zero order will also get some energy, but also higher orders appear, i. e. rings of radius $2r_{ring}$, $3r_{ring}$, etc are created. However, these higher order rings don't affect the functionality of the tracking system. In this approach the diameter of the diffraction spot is given by the aperture of the whole DOE, and is therefore smaller than in the first approach.

Based on the design discussed above a set of visible light demonstrators (633 nm) for the ring/point-generation has been made, with a focal length of 400 mm and a diameter of the generated ring of 15 mm. The DOE were realized in fused silica. The resulting 8-phase level elements have smallest features in the order of 4 μm for the segemented design, respectively, 1 μm for the common aperture design.

Figure Fig. 3 a) shows the diffraction pattern of the common aperture design. Scans trough the focus in the image plan, together with the calculated function are presented in Fig. 3 b) and c) for the segmented aperture and the common aperture design, respectively. The measured intensity distribution shows excellent agreement with the expected theoretical data. The difference between theory and measurements can be explained by etch depth errors in the fabrication. Also it turned out that the common aperture element is more sensitive to etch depth errors than the segment element.
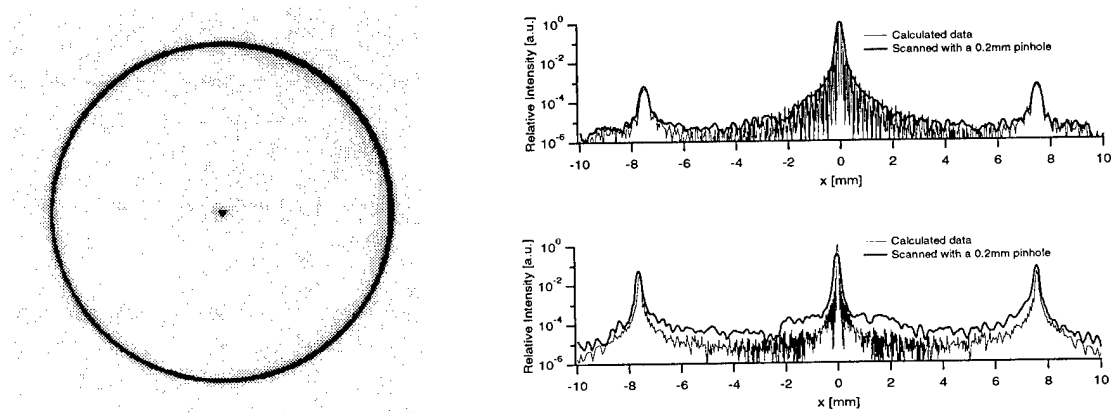
Figure 3: a) The diffraction pattern of the common aperture design. b) and c) Scans trough the focus in the image plan together with the calculated curve for the segment aperture, for the common aperture design, respectively.

3 Conclusions

On the example of the tracking/receiving element, it has been shown that diffractive optical elements may simplify optical systems, by including several functionalities in a single DOE. The task of this DOE is to generate a point/ring pattern. For this purpose two different design strategies have been investigated. One is based on a segmented aperture, the other on a common aperture approach. The realized elements showed a good agreement with the theory for both types of design. However, it

turned out that the segmented aperture based system may give some problems for specific point-ring energy ratios. The elements have satisfied the given severe specifications for space applications, which encourages to use DOEs in other systems.

References

[1] R. H. Czichy, M. Wittig, "Diffractive optics for advanced free space laser communication terminals," IEE Conference Publication No 379, Holographic Systems, Components and Applications, Neuchâtel, 1993, 255 - 259.

[2] F. Wyrowski, "Digital phase encoded inverse filters for optical pattern recognition", Appl. Opt. **30**, 4650-4657 (1991).

[3] M. T. Eisenmann, A. M. Tai, J. N. Cederquist, "Iterative design of a holographic beamformer," Appl. Opt. **28**, 2641-2650 (1989).

[4] P. Ehbets, H. P. Herzig, R. Dändliker, P. Regnault and I. Kjelberg, " Beam shaping of high power laser diode arrays by continous surface-relief elements," J. Mod. Opt. **40**, 637-645 (1993).

[5] Y. Ono, Y. Kimura, Y. Ohta, N. Nishida, "Antireflection effect in ultrahihg spatial-frequency holographic relief gratings," Appl. Opt. **26**, 1142-1146 (1987).

[6] D. Raguin and G. M. Morris, " Analysis of antireflection-structured surfaces with continous one-dimensional surface profiles," Appl. Opt. **32**, 2582-2598 (1993).

[7] T. Stones and N. George, "Hybrid diffractive-refractive lenses and achromats", App. Opt. **27**, 2960-2971 (1988).

[8] R. H. Czichy, "Hybrid optics for space applications," ESA Scientific/Technical Monographs SP–1158, ESA Publications Division, The Netherlands, 1993.

[9] G. P. Bohrmann and J. P. Bowen, "Influence of temperature on diffractive lens performance," Appl. Opt. **32**, 2483-2489 (1993).

[10] C. Londoño, et al., "Athermalization of a single-component lens with low diffractive optics", Appl. Opt. **32**, 2295-2302 (1972).

[11] H. P. Herzig, et al., "Diffractive components: Computer generated elements," in Perspectives for Parallel Interconnects, Ph. Lalanne, P. Chavel, eds. (Springer, Berlin, 1993) 71-107.

[12] ESA project Co10566/93/NL/JV

[13] R. H. Czichy, "Miniaturised optical tracking sensor/receiver combination," ESA/PAT/274 (1992)

Scalar Design of Diffractive Elements using Direct and Indirect Optimization

Joseph N. Mait
U.S. Army Research Laboratory
AMSRL-SE-EO
2800 Powder Mill Road
Adelphi, Maryland 20783
e-mail: mait@arl.mil

1. Introduction

Although analysis of diffractive optical elements (DOEs) is critical to an understanding of the technology, equally important for their widespread application is an understanding of their design or, in counterpoint to analysis, their synthesis. The problem of design is essentially a casting of a designer's understanding of physics into an optimization problem: the DOE is to be determined so that it achieves some desired performance, preferably optimally, subject to the constraints of fabrication.

A large portion of the design literature consists of a discussion of algorithms. Unfortunately, this clouds a more fundamental distinction in synthesis, namely, whether the design is "direct" or "indirect." Direct designs are those that attempt to optimize directly the desired performance measure, subject to the constraints of fabrication. In contrast, indirect designs are those that first seek to determine a solution to the design problem unconstrained by fabrication and then impose the constraints of fabrication onto the unconstrained solution. To make this point clear, rather than concentrating on design for only a single application, the design of DOEs is considered for different applications, including focussing, array generation, and correlation. For each application the same methodic approach to design is followed: model the optical system, model the DOE fabrication, identify freedoms available for design, and define a performance measure. The problem is then solved in both a direct and an indirect manner. To insure that the discussion remains uncluttered, only design in the scalar domain is considered. However, the procedure is general enough that is easily applicable to the vector design of DOEs.

2. Design Procedure

The design of DOEs can be divided into three basic stages: understand the physics of the design problem (analysis); translate the physical understanding into mathematics and define an appropriate optimization problem (synthesis); and execute the design and fabricate the element (implementation). Each of these stages can be broken down further as indicated in the following.

Analysis: Understand the physics of image formation using the DOE.
Understand the fabrication of the DOE from data generated by computer.

These first two steps are perhaps obvious, but are critical to design. By *understand* we mean to imply the selection of a model. In this work, we consider only applications where scalar diffraction theory is valid. Simple integral transforms can then be used to model optical systems and the DOE is modelled as a thin phase transformation element. In selecting a fabrication model,

the designer must address how much detail to include. In our examples we model the DOE as a multilevel quantized phase element.

Synthesis: Define the design metric.
Define the optimization problem.

The essence of the synthesis step is to cast the design into an appropriate optimization problem. However, two basic approaches to optimization have emerged in the DOE literature: indirect and direct approaches. The distinction between the two is represented in Fig. 1. For both approaches, it is necessary to define a design metric based on those physical parameters that are used to characterize system performance. Whereas a direct approach to the design problem optimizes the design metric subject to the constraints of fabrication, in an indirect approach, the design metric is optimized without regard to these constraints. The solution to the unconstrained problem is then mapped onto the fabrication constraints using an alternative design metric.

The uni-directional and bi-directional methods refered to are based on the error-reduction and input-output algorithms defined by Fienup [1]. We prefer the nomenclature bidirectional and unidirectional to indicate the nature of data flow.

Implementation: Select a design algorithm and perform the optimization.
Fabricate the DOE from the computer-generated data.
Test the DOE.

The implementation steps are straight forward, but require many practical decisions to be made and, most importantly, considerable expenditure of resources. As indicated in Fig. 1, for direct approaches it is the primary design metric that is optimized. For indirect approaches, optimization of an alternate metric is necessary to solve the mapping problem, which is the imposition of fabrication constraints onto the unconstrained solution.

3. Diffractive Lens Design

The first design example is that of a diffractive lens. The function of the desired, but as yet unknown, DOE is to focus the energy from an incident plane wave to a point in space at a distance z_0 behind the lens. Under the assumptions of scalar diffraction theory the relationship between the input wavefield and the output wavefield is given by Fresnel diffraction [2]. For DOE fabrication, we assume a multiple-step etch procedure with binary masks, which achieves multilevel quantized phase. Further, we assume that the ability of the DOE to focus light is measured by its diffraction efficiency at the focal point.

The solution of the unconstrained problem is a quadratic phase function which maximizes the diffraction efficiency to unity. One can impose the constraints of fabrication by quantizing the unconstrained phase values to the constrained values. Table 1 summarizes the calculated diffraction efficiencies for a 100-μm diameter $f/1$ lens designed by quantization with a minimum feature size of 1.0 and 0.5 μm [3]. Direct solution of the lens design problem has been achieved with the rotationally symmetric iterative discrete on-axis (RSIDO) method [4,5]. The improvement in diffraction efficiency for lens designs generated by RSIDO is also presented in Table 1 [3].

4. Fourier Array Generator

We consider next DOEs that produce an array of point sources with illumination from a single point source. A coherent Fourier optical system is used to achieve this, thus a Fourier transform relationship exists between the diffractive element in the pupil plane and its response in the image plane. We assume again that the diffractive element is fabricated to have multilevel quantized phase. The performance of the diffractive array generator is measured by its ability to generate the desired spot array with high diffraction efficiency and minimum intensity error. To measure this we use the absolute distance measure between the generated intensity and the intensity that corresponds to the upper bound solution [6].

The upper bound solution is the solution to the unconstrained problem, but, unlike diffractive lens design, it does not have an analytic expression. However, upper bound arrays have been reported for a few one- and two-dimensional fan-outs [7,8]. As in Sec. 3, one can impose the constraints of fabrication via quantization. Table 2 summarizes the performance of 3 × 3 array generators designed by sampling and quantization. The results of the direct solution to the design problem using both the iterative Fourier transform algorithm and simulated annealing are also summarized in Table 2.

5. Correlation Filter

The details of the correlation design problem are presented in Ref. 9, however the results of both direct and indirect optimizations are presented in Table 3.

6. Conclusion

The examples and designs presented herein have been chosen for pedagogical reasons and are meant to be illustrative. That is, the intent of this work is not to make specific contributions to the design of diffractive lenses, array generators, and correlation filters, nor to endorse a particular design algorithm. Rather, it is to highlight the design process and also the distinctions between direct and indirect approaches that have not been adequately explored.

1. J. R. Fienup, Opt. Eng. **19**, 297-306 (1980).
2. J. W. Goodman, *Introduction to Fourier Optics* (McGraw-Hill, New York, 1968), chap. 3.
3. Data supplied by Michael Feldman through personal communication.
4. J. R. Rowlette, T. Bowen, R. Roff, J. Stack, J. E. Morris, W. H. Welch, and M. R. Feldman, Proc. Annual Meeting IEEE LEOS (93CH3297-9), 474-475 (1993).
5. W. H. Welch, J. E. Morris, and M. R. Feldman, ``Design and fabrication of radially symmetric computer generated holograms," Annual Meeting of the Optical Society of America (1991).
6. F. Wyrowski, Opt. Lett. **16**, 1915-1917 (1991).
7. U. Krackhardt, J. N. Mait, and N. Streibl, Appl. Opt. **31**, 27-37 (1992).
8. J. N. Mait, *Holographic Optics: Computer and Optically Generated*, I. N. Cindrich and S.-H. Lee, eds., Proc. SPIE **1555**, 53-62 (1991).
9. J. N. Mait, J. Opt. Soc. Am. A **10**, 2145-2158 (1995).
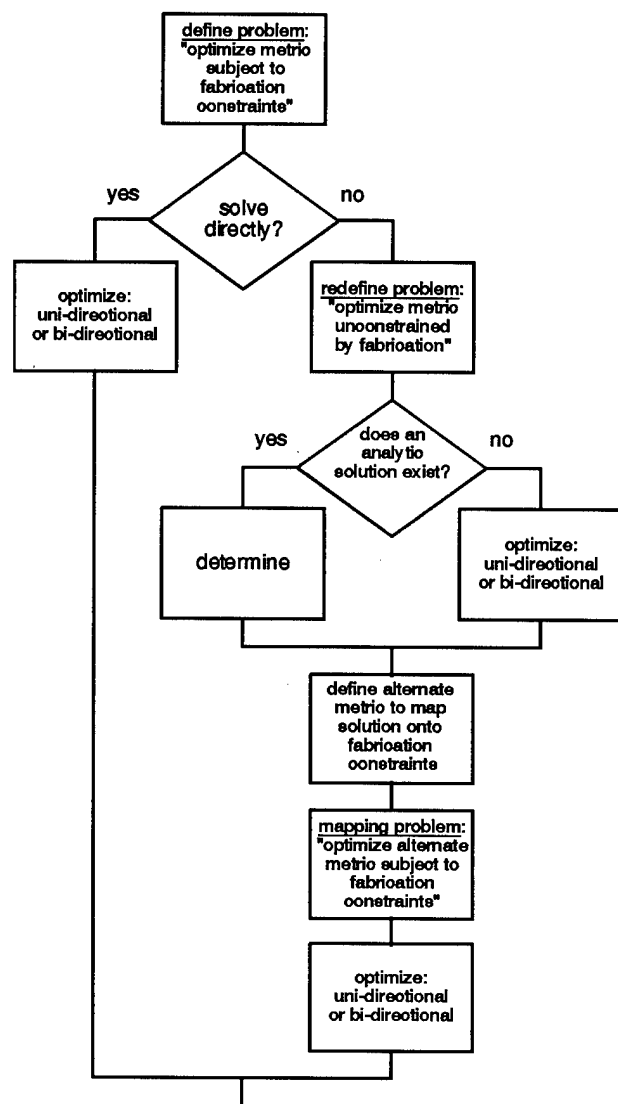
Fig. 1 Flowchart representation of design highlighting the distinction between direct and indirect designs.

phase levels	η_{ub} (%)	minimum feature size (μm)	design	η (%)
2	40.5	0.5	quantization	29.0
			RSIDO	32.0
		1.0	quantization	24.0
			RSIDO	31.0
4	81.0	0.5	quantization	61.0
			RSIDO	64.0
		1.0	quantization	41.0
			RSIDO	46.0

Table 1. Performance of diffractive $f/1$ lenses with 100-μm diameter.

phase levels	η_{ub} (%)	design	η (%)	error ($\times 10^{-4}$)
2	75.74	quantized	79.77	247.08
		iterated	67.51	79.83
		annealed	67.94	79.35
4	78.81	quantized	77.52	31.45
		iterated	77.26	31.90
		annealed	76.84	33.90
8	89.73	quantized	89.44	4.98
		iterated	89.25	2.72
		annealed	89.23	2.60
16	92.94	quantized	93.02	3.22
		iterated	92.72	0.21
		annealed	92.44	0.29
∞	94.06	quantized	94.13	3.69
		iterated	93.88	0.00

Table 2. Performance of multilevel quantized phase array generators designed to generate a 3×3 fan-out.

DOE performance measure	design	$c1(x,y)$	$c2(x,y)$
MACE filter		1	1
indirect			
minimum mean square error	quantized	757.76	675.16
	iterated	628.04	593.15
minimum (average energy plus correlation peak energy)	quantized	609.98	595.54
direct			
minimum (average energy plus correlation peak energy)	annealed	609.97	609.97

Table 3. Performance of binary-phase diffractive elements designed to perform as correlation filters.

High Efficiency Dielectric Reflection Gratings

B. W. Shore, M. D. Perry, J. A. Britten, R. D. Boyd, M. D. Feit, H. Nguyen,

R. Chow, G. Loomis,

Lawrence Livermore National Laboratory, PO Box 808, Livermore Ca 94550

and Lifeng Li

Optical Sciences Center, University Of Arizona, Tucson AZ 85721

Summary

We discuss examples of designs for all-dielectric high-efficiency reflection gratings that tolerate high intensity laser pulses and are, in theory, capable of placing 99% of the incident light into a single diffraction order. The designs are based on placing a dielectric transmission grating atop a high-reflectivity multilayer dielectric stack. We comment on the connection between transmission gratings and reflection gratings and note that many combinations of gratings and multilayer stacks offer high efficiency. Thus it is possible to attain secondary objectives in the design. We describe examples of such designs aimed toward improving fabrication and lowering the susceptibility to laser-induced damage.

Introduction

A reflection grating must incorporate two optical functions: it must combine high reflectivity with diffraction. Traditional metallic gratings combine these two functions in a single conducting surface. The conductivity of the metal forces reflection, while periodic grooves create diffraction. Because metallic gratings owe their reflectivity to conductivity, expressible as a complex-valued refractive index, they have a disadvantage for applications that subject the grating to intense radiation. The absorption of radiation causes heating and damage [1]. Transparent dielectric materials have much smaller absorption coefficients than do metals, and therefore optical devices based on dielectrics have potential for withstanding intense radiation [2]. When used to create grating structures, they have unique properties that can offer additional benefits [3].

Contemporary techniques of interference lithography (or holographic grating fabrication) offer opportunities for producing a variety of all-dielectric gratings. Such gratings, useful for a variety of applications as transmission gratings, can be combined with suitable all-dielectric multilayer structures to create reflection gratings. In our work the multilayer thin-film stack is used as a substrate for the grating, which we create using previously described procedures[1] .In brief, we first coat the substrate with a carefully controlled uniform layer of photoresist. Next we expose this photosensitive surface to the stabilized interference pattern at the intersection of two collimated laser beams in a two-arm interferometer. We develop the latent image to create a corrugated surface, using in-situ monitoring to control the profile by terminating the development step at the optimal moment

[4]. Although the developed photoresist could serve as the grating [5], it is more fragile than other materials. To create a more robust structure, the photoresist can be overcoated with dielectric material or, as in our work, the pattern can be transferred to the underlying substrate using lithographic etching techniques.

For use in chirped pulse amplification [6], diffraction gratings must be able to withstand intense radiation. This requirement imposes restrictions on the acceptable materials, largely to such transparent oxides as hafnia, scandia and silica [7]. There remain many possibilities for grating profile and material thicknesses. As we shall show, the action of the combined grating-multilayer structure can be considered in two parts, the diffractive transmission and the reflection. In particular, the required highly reflective multilayer stack can be designed in many ways. This variety of designs allows us to impose additional constraints on the design, beyond the primary requirement of producing high reflectivity.

Our designs are based on numerical modeling of discretized grating profiles and the transcription of the exact Maxwell equations into coupled algebraic equations using the multilayer modal method of Li [8]. The computer codes provide not only efficiencies but also field distributions within the grating.

Relationship between transmission and reflection

Our gratings owe their high efficiency, in part, to the choice of groove spacing and angle of incidence: the spacing $d < 3\lambda/2$ and near-Littrow mount (angle of incidence equal to diffraction angle) allows only orders 0 and -1 to propagate. Under such conditions both the simple single-dielectric transmission grating and the multilayer dielectric reflection grating exhibit regular maxima and minima of diffraction efficiency as a function of groove depth. However, conditions which produce high diffraction efficiency for transmission will produce low diffraction efficiency for reflection. This result is because the reflection grating requires interference between the two transmitted orders, after reflection, in order to place the radiation into order -1 rather than as specular reflection into order 0. When a dielectric transmission grating places a large fraction of the incident light either into order -1 or 0 of transmission (light incident at angle θ_i and emerging at angle θ_t say), then the time reversed situation (radiation at angle θ_t within the medium flowing out of the grating from below into angle θ_i), will also apply. Detailed computations, to be exhibited, bear out this intuitive observation.

Multilayer Grating Designs

Multilayer stacks of thin dielectric films are widely used in the optics industry as antireflection coatings, polarizers, beam splitters, filters, and highly reflecting mirrors. Rather than relying on conductivity or absorption to produce reflection, multilayer dielectric stacks rely on interference. A succession of horizontal plane layers are created with thicknesses such that, for light of a specified wavelength and polarization, incident from above at a given angle, the phases of upward and downward traveling waves within each layer either reinforce the upward wave (for reflection, or HR coating) or the downward wave (for transmission, or AR coating).

It is obviously desirable to have a point design that has relatively little sensitivity to small variations in design parameters, such as layer thicknesses, groove depth, and duty cycle. From a purely theoretical standpoint (disregarding fabrication considerations), robust designs can be obtained by allowing some portion of the top layer to lie beneath the grooves -- the grooves are not etched entirely through the top layer. However, it is often simpler to produce a grating whose groove depth is fixed by a discontinuity in chemical

composition, i.e. a grating whose grooves extend entirely through the uppermost layer. This is one of several subsidiary constraints that may be imposed upon the overall structure, in addition to having high efficiency.

The quarter wave stack

The most common form of highly reflecting multilayer dielectric stack is the $(H\ L)^{\wedge}n$ stack based on n pairs of high index (H) and low index (L) material, each of which offers one quarter wave of phase shift at the desired angle [9]. As the number of layers increases, the reflectance approaches closer to unity, within a wavelength band whose width is set by the ratio of refractive indices. With this stack in mind, the simplest high efficiency multilayer grating designs are based on placing a dielectric grating atop such a quarter-wave stack. Either an H or L layer may be made the top layer; in general the grooves will be shallower the higher is the index of refraction of the grating layer. The design problem then becomes one of choosing the thickness of the grating layer and the depth and shape of the grooves. (That is, the exact structure of the HR stack need not be considered, only the ability to reflect waves .)

Problems with quarter-wave stacks

The quarter-wave stack provides one easily-understood possibility for creating a high efficiency reflection grating. However, in our holographic method it has one drawback. The dielectric stack, intended to be highly reflecting at the use angle of 52° for 1053 nm light, is also highly reflecting near the exposure angle of 17° for 413 light. (This light is near the reflectivity maximum associated with third harmonic of the design wavelength). This undesired reflectance can be diminished by altering various layer thicknesses.

The HLL design

A very simple alternative to the quarter wave design $(HL)^{\wedge}n$ is an $(HLL)^{\wedge}n$ design, comprising quarter waves of high index material H and half waves of low index material L. Rather than define the quarter waves for the usage wavelength and angle, we choose a shorter wavelength and normal incidence. We have chosen for the stack-design wavelength 830 nm (a choice that simplifies the monitoring of the layer deposition). Such a design greatly diminishes the reflected exposure light and thereby eliminates the need for special antireflection or absorbing coatings between the photoresist and the stack.

As with the quarter wave designs, grating designs based on this stack can achieve reflection efficiency exceeding 99%. Such high efficiencies are available for a range of groove depths and duty cycles, and with either the H or the L dielectric as the uppermost layer.

The efficiencies obtained with the HLL design (at the usage wavelength and angle) are almost indistinguishable from those obtained with the quarter wave stack: Both designs have the same far-field Rayleigh expansion. However, the two designs differ appreciable in the near-field region within the grating grooves. Because the designs have high efficiency, there is a strong standing wave pattern of electric field, with antinodal planes where the electric field is twice the value of a free-space traveling wave. With the quarter wave design, the enhanced-field regions extend into the surface, where they may cause photo-induced breakdown and damage. With the HLL design, the enhanced-field regions fall within the grooves, where they have no harmful effects on damage.

Acknowledgments

References

[1]. R. Boyd, J. Britten, D. Decker, B. W. Shore, B. Stuart, M. D. Perry and L. Li, "High-efficiency metallic diffraction gratings for laser applications" Appl. Opt. **34,** 1697-1706 (1995)

[2]. B. C. Stuart, M. D. Feit, A. M. Rubenchik, B. W. Shore and M. D. Perry, "Laser-induced damage in dielectrics with nanosecond to subpicosecond pulses" Phys. Rev. Lett. **74,** 2248-2251 (1995)

[3]. M. D. Perry, R. D. Boyd, J. A. Britten, D. Decker, B. W. Shore, C. Shannon, E. Shults and L. Li, "High-efficiency multilayer dielectric diffraction gratings" Optics Lett. **20,** 940-2 (1995)

[4]. J. A. Britten, R. D. Boyd and B. W. Shore, "In situ end-point detection during development of submicrometer grating structures in photoresist" Opt. Eng. **34,** 474-9 (1995)

[5]. M. G. Moharam, T. K. Gaylord, G. T. Sincerbox, H. Werlich and B. Yung, "Diffraction characteristics of photoresist surface-relief gratings." Appl. Opt **23,** 3214-20 (1984)

[6]. M. D. Perry and G. Mourou, "Terawatt to petawatt subpicosecond lasers" Science **264,** 917-924 (1994)

[7]. M. R. Kozlowski, R. Chow and I. M. Thomas, "Optical coatings for high power lasers" in *CRC Handbook of Laser Science and Technology Supplement 2* ed. M. J. Weber (CRC Press, Boca Raton, 1995), pp. 767-812

[8]. L. Li, "Multilayer modal method for diffraction gratings of arbitrary profile, depth, and permittivity" J. opt. Soc. Am. A **10,** 2581-91 (1993)

[9]. A. MacCloud, *Thin Film Optical Filters* (Adam Hilger, Bristol, 1986)

Design of phase–shifting masks for enhanced–resolution optical lithography

Guo–Zhen Yang, Zhi–Yuan Li, Bi–Zhen Dong, Ben–Yuan GU, and Guo–Qing Zhang

Institute of Physics,Academia Sinica, P. O. Box 603, Beijing 100080, China

Phone : 086–10–2553101,   Fax. : 086–10–2562605

1. Introduction

As integrated circuit (IC) technology continues to push further into the submicrometer regime, considerable effort has been devoted to finding new approaches for extending the resolution limits of optical lithographic systems. The idea of using phase–shifting masks in optical lithography is one of such resolution–enhancing techniques and is commonly attributed to Levenson.[1] The problem of the design of phase–shifting mask is how to determine the phase of the mask that produces a predesignated image. There are several approaches to deal with this problem such as simulated annealing algorithm[2] and optimal coherent approximations.[3] In this paper we present an approach of the design of the phase–shifting mask for the enhancement of optical resolution in lithography based on general theory of amplitude–phase retrieval in optical system and an iteration algorithm. For several model objects the numerical investigating results are given.

2. Theoretical formulas

The schematic of a typical optical system considered is shown in Fig. 1. This optical system is composed of an input plane P_1, one Fourier–transform lens and an output plane P_2. The spacings between the two consecutive planes are l_1 and l_2, respectively. The focal length of the lens is l_f. The wave functions on the input plane P_1 and output plane P_2 are denoted by

$$U_1(x_1, y_1) = \rho_1 \exp(i\phi_1) \quad \text{and} \quad U_2(x_2, y_2) = \rho_2 \exp(i\phi_2),$$

respectively. The z-axis is chosen along the optical axis of the system. The output wave function is related to the input wave function by a linear transform function $G(x_2, y_2; x_1, y_1)$ in the form

$$U_2(x_2, y_2) = \int \int G(x_2, y_2; x_1, y_1) U_1(x_1, y_1) dx_1 dy_1. \tag{1}$$

As the discrete form we have

$$U_{1l} = \rho_{1l} \exp(i\phi_{1l}), \quad U_{2m} = \rho_{2m} \exp(i\phi_{2m}), \tag{2}$$

and

$$U_{2m} = \sum_{l=1}^{N_1} G_{ml} U_{1l}, \quad l = 1, 2, 3 ... N_1, \quad m = 1, 2, 3 .. N_2, \tag{3}$$

where N_1 and N_2 are the numbers of sampling points for the input and the output wave functions, respectively. Consequently, the design of phase–shifting masks for the imaging system can be generally addressed as follows: Given the linear transform $\widehat{G}$ and amplitudes of $U_1(x_1, y_1)$ and $U_2(x_2, y_2)$,how can we determine the phase distribution ϕ_1 in the input plane to satisfy Eq. (3) to high accuracy?

To describe the closeness of $\widehat{G}U_1$ to U_2, we introduce a distance measure equal to the L_2 norm as

$$D(\rho_1, \phi_1; \rho_2, \phi_2) = \| U_2 - \widehat{G}U_1 \| = [\sum_{m=1}^{N_2} | U_{2m} - (\widehat{G}U_1)_m |^2]^{1/2}. \tag{4}$$

The problem may thus be formulated as the search for the extremum of the function D^2 with respect to the function arguments ϕ_1 and ϕ_2.

Through standard algebraic manipulations, we can derive a set of equations satisfied by ϕ_1, and ϕ_2 as follows[4]

$$\phi_{1k} = \arg[\frac{1}{A_{kk}}[\sum G_{jk}^* \rho_{2j} \exp(i\phi_{2j}) - \sum_{j \neq k}' A_{kj}\rho_{1j} \exp(i\phi_{1j})]], \tag{5a}$$

$$\phi_{2k} = \arg[\sum_j G_{kj}\rho_{1j} \exp(i\phi_{1j})], \tag{5b}$$

where $\widehat{A} = \widehat{G}^+\widehat{G}$ is an hermitian operator. Equations (5a) and (5b) can be numerically solved by an iterative algorithm starting with an arbitrary initial phase of ϕ_1.[4]

3. Numerical Simulations

According to the general theory of the optical transform,[5] when the lens law is satisfied, i.e., $1/l_1 + 1/l_2 = 1/l_f$, this system performs a linear transform as

$$G(x_2, y_2; x_1, y_1) = \frac{1}{\lambda^2 l_1 l_2} \exp[i\frac{\pi}{\lambda l_2}(x_2^2 + y_2^2)]\exp[i\frac{\pi}{\lambda l_1}(x_1^2 + y_1^2)]$$

$$\times \int \int P_a(x, y) \exp\{-i\frac{2\pi}{\lambda l_2}[(x_2 + Mx_1)x + (y_2 + My_1)y]\}dxdy, \tag{6}$$

where P_a represents the finite aperture of the lens defined by $P_a(x) = 1$, for $| x | \leq a$, $| y | \leq a$; and 0, otherwise. $M = l_2/l_1$ is the amplification factor of the system. Performing the integral operation and neglecting the irrelevant phase factor $\exp[i\pi(x_2^2 + y_2^2)/\lambda l_2]$, we obtain a simple form of the transfer kernel

$$G(x_2, y_2; x_1, y_1) = M \exp[i\frac{\pi}{\lambda l_1}(x_1^2 + y_1^2)] \frac{\sin[2\pi a(x_2 + Mx_1)/\lambda l_2]}{\pi(x_2 + Mx_1)}$$

$$\times \frac{\sin[2\pi a(y_2 + My_1)/\lambda l_2]}{\pi(y_2 + My_1)}. \tag{7}$$

In the case of 1–D system, we have the transform function as

$$G(x_2; x_1) = \sqrt{M} \exp[i\frac{\pi}{\lambda l_1}x_1^2] \frac{\sin[2\pi a(x_2 + Mx_1)/\lambda l_2]}{\pi(x_2 + Mx_1)}. \tag{8}$$

In the simulations we choose system parameters as follows : Wave length of the illumination light $\lambda = 365nm$, the numerical number $NA = 0.5$, the focal length $l_f = 40cm$, the diameter of the lens aperture $2a = 40cm$. The system amplification is $M = 0.01$. In the typical optical lithographic system, it requires that the amplitude of output function is proportional to that of the input function, i.e., $U_2(x_2) = \sqrt{1/M}U_1(-x_2/M)$ for 1–D system while for 2–D system $U_2(x_2, y_2) = (1/M)U_1(-x_2/M, -y_2/M)$. Therefore, in solving to Eqs. (5a) and (5b) we set $\rho_2(x_2) = \sqrt{1/M}\rho_1(-x_2/M)$ for 1–D case and $\rho_2(x_2, y_2) = (1/M)\rho_1(-x_2/M, -y_2/M)$ for 2–D case.

We first investigate the design of the phase–shifting–masks for 1–D model images that consist of equal–spacing lines with submicron width, such as two lines, three lines, and four lines, as shown in Fig. 2(a), (b), (c),respectively. The patterns generated by the conventional transmission mask and the designed mask are also shown in Fig. 2. It is evident that the performance of the optical resolution has been substantially improved when using the phase–shifting–mask, compared to conventional imaging system. Therefore, the new algorithm has been proven to be effective. The binary phase distribution (0 and π) for ϕ_1 is automatically derived, as shown in Fig. 3(a), (b), (c),respectively. This is the first time by means of solving the inverse problems to derive the well–known result due to Levenson.[1] As for 2–D system we investigate more complex image shown in Fig. 4(a). Our algorithm also presents an improved result compared to the conventional imaging system, as shown in Fig. 4(b), (c).
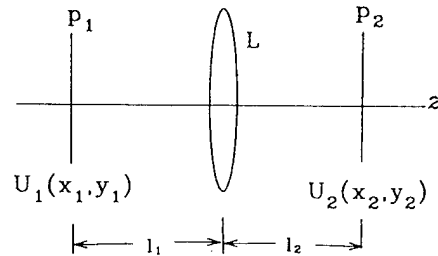
Fig.1. Schematic of an imaging system
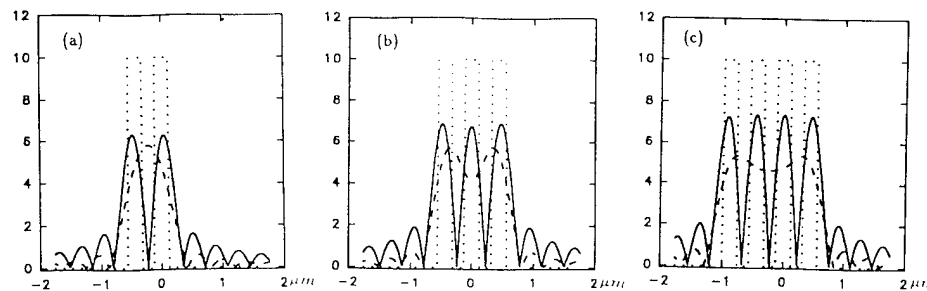
Fig.2. Phase–shifting mask design for 1–D 0.22μm equal-spacing lines. Dotted lines, dashed lines and solid lines correspond to ideal images, conventional transmission masks and designed masks,respectively.
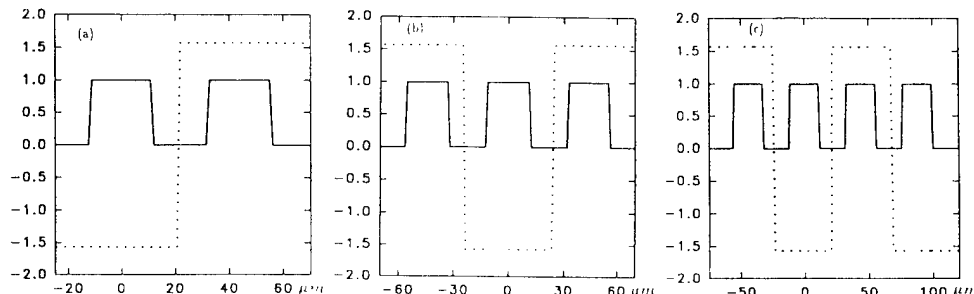
Fig.3. Binary phase distribution of ϕ_1(dotted lines) for designed masks. Solid lines correspond to distribution functions of objects.
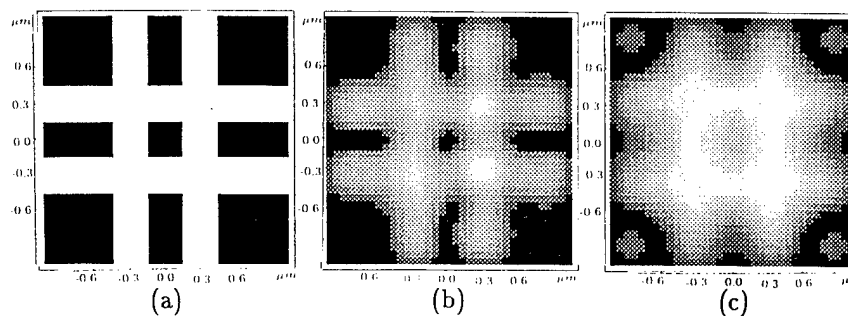
Fig.4. Phase–shifting mask design for 2–D image.(a) The ideal image with 0.30μm space between two lines.(b) Image due to designed mask.(c) Image due to conventional transmission mask.

3. References

[1] M. D. Levenson, N. S. Viswanathan, and R. A. Simpson, IEEE Trans.Electron Devices **ED–29**, 1828 (1982).

[2] Y. Liu and A. Zakhor, IEEE Trans.Semicon. Mfg. **5**, 138 (1992).

[3] Y. C. Pati and T. Kailath, J. Opt. Soc. Am. A **11**, 2438 (1994).

[4] Guo–Zhen Yang, Ben–Yuan Gu, Bi–Zhen Dong, Jie–Yao Zhuang, and Okan K. Ersoy, Appl. Opt. **33**, 209 (1994).

[5] J. W. Goodman, *Introduction to Fourier Optics* (McGraw–Hill, New York, 1968).

Flattop Beam Generation Using An Iteratively-Designed Binary Phase Grating

Jun Amako and Tomio Sonehara
Seiko Epson Corp., R & D Division
Owa 3-3-5, Suwa-shi, Nagano-ken, 392 Japan
Tel: 0266-52-3131 /Fax: 0266-58-9848

1. Introduction

Various approaches for flattop beam generation have been reported.[1-4] Here we focus on a grating approach in which a phase grating is used to modulate a beam wavefront and shape its Fourier spectrum. We designed a grating-type beam shaper in an iterative manner, where an optimal grating phase is sought under the constraints of amplitude and phase both in the grating and Fourier planes.

Generating a flattop intensity distribution, which is a uniform amplitude and phase distribution, requires that we consider the phases as well as amplitudes of diffracted waves when designing the grating. This phase consideration enables the adjoining diffracted waves to be produced in phase so they can interfere constructively to form a flat-topped field.

2. Physical Basis

Our beam shaper consists of a window and a binary phase grating[5] (see Fig. 1). The function of the window is auxiliary but important.
We let the phase depth of the grating equal π. If a phase function comprising 0 and π is even-symmetric, its Fourier field is also real and even and has the phase of 0 and π. Using this relation makes it easy to find grating structures meeting the demand that some adjacent waves acting for the beam shaping (the wanted waves) have to be in phase. For a depth other than π, its Fourier transform will become complex, which means the diffracted waves can be proven out of phase. The four requirements for grating design are given below.
(1) As much light energy as possible should be directed to the wanted waves, from the -mth to the +mth order. Other higher orders should be so fully suppressed that their interference with the wanted waves can be minimized.
(2) The wanted waves should have equal amplitudes.
(3) There must be no phase jumps among the wanted waves.
(4) The grating's smallest feature should be made as large as possible.

3. Grating Design and Fabrication

By using the simulated-annealing (SA) algorithm,[6] we sought a one-dimensional binary phase structure that reconstructs three in-phase diffracted waves, the 0th, and ±1st orders. One period of a grating is divided into plural segments. Each segment has a phase value of 0 or π, alternately. The positions of these dividing points are optimized under the afore-mentioned requirements. Solutions obtained for 187 iterations and their diffraction properties are given in Table 1 and Table 2, respectively. The efficiency is the summation of the diffraction efficiencies of the three waves. The uniformity is the ratio of minimum and maximum intensity among these waves. S/N is defined as the ratio of the minimum intensity of the three orders to the maximum intensity of the higher orders (up to ±100th).

We fabricated the grating by means of projection-photolithography and a reactive ion-etching technique. In the translation of the design output into computer-aided design data used to operate a mask writer (laser beam), the quantizing-error was $\leqq \pm 0.0625 \mu$m. The photo mask was manufactured by the mask writer which can write a line-width of $\geqq$ 2μm with a positioning accuracy of $<0.1\mu$m. The resist-patterned quartz glass substrate was etched at a rate of 400Å/min.; using CHF^3 the RF power was 70W and the pressure was 26mTorr.

4. Simulations and Experiments

By computer simulation we examined the profile's dependence on the incident beam width and the window width for a given grating period. We then determined the optimal dimensions of these factors for the grating period of 8.0mm, the lens focal length of 2000mm, and the beam wavelength of 0.633μm: the beam was 8.0mm ($1/e^2$) wide and the window was 9.0mm wide. Figure 2 shows the results; on the horizontal axis the width of 20 divisions equals 326μm.

In the experiment, the aperture slit, 2.0mm in height and adjustable in width, was placed before the grating. A He-Ne laser beam (0.633μm) hit the grating and the transmitted wavefront was optically Fourier-transformed by a lens. The focused intensity distribution was detected by a CCD camera and the camera's video output was fed, via a frame memory, to a computer for display and analysis. Figure 3 shows the results; on the horizontal axis the width of 20 divisions equals 222μm. Our estimate of the light use efficiency is ~50% from both the grating's efficiency of 57% and the window width which is greater than the beam width ($1/e^2$).

5. Conclusion

We recommend the use of a compact beam shaper composed of a window and a binary phase grating. By computer-simulating the shaped profiles, we have obtained the optimal relation among the beam width, the window width, and the grating period. Through optical experiment we confirmed that the shaper achieves a good approximation to a flattop profile.

References

1) W.W. Simmons, G.W. Leppelmeier and B.C. Johnson, Appl. Opt., 13 (1974) 1629.
2) J.W. Ogland, Appl. Opt., 17 (1978) 2917.
3) P.W. Rhodes and D.L. Shealy, Appl. Opt., 19 (1980) 3545.
4) W.B. Veldkamp and C.J. Kastner, Appl. Opt. 21 (1982) 345.
5) J. Amako and T. Sonehara, Opt. Rev. 2 (1995) 339.
6) M.R. Taghizadech, J.I.B. Wilson, J. Turunen, A. Vasara, and J. Westerholm, Appl. Phys. Lett. 54 (1989) 1492.
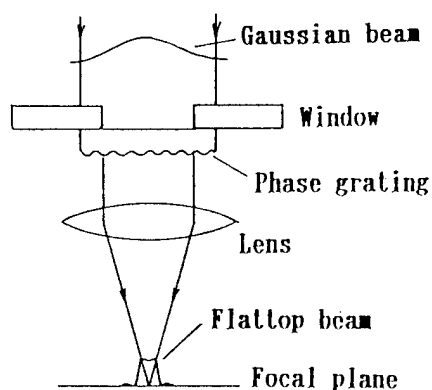
Fig. 1. Schematic drawing of the beam conversion using our beam shaper.

Table 1. Data for a Binary Phase Grating

Dividing positions (in fraction of period)

0.039166	0.069447	0.133235	0.148085
0.185804	0.814196	0.851915	0.866765
0.930553	0.960834		

Table 2. Diffraction properties

Items	Simulated results
Efficiency	57 %
Uniformity	0.99
S/N	8.1
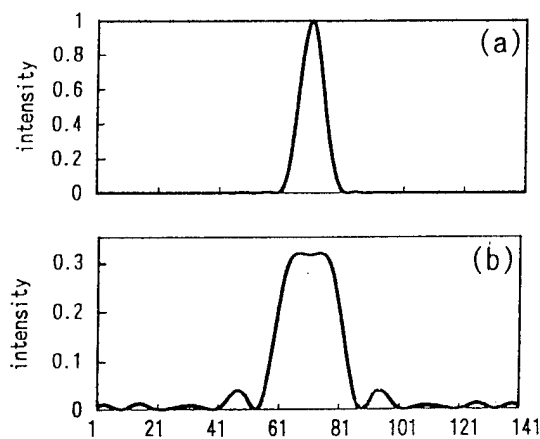
Fig. 2. Computer-simulated profiles
(a) without any grating, (b) with the grating.
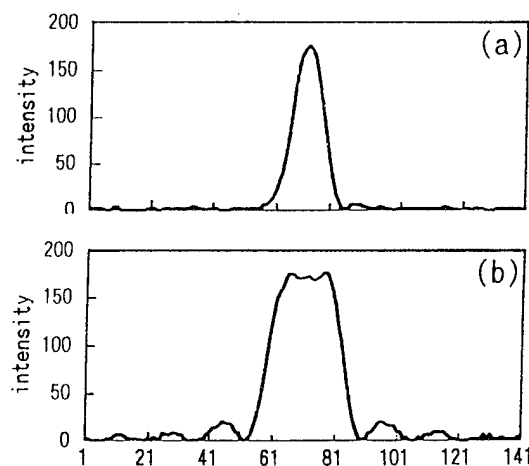
Fig. 3. Experimentally-obtained profiles
(a) without any grating, (b) with the grating.

Surface-relief Gratings with Sharp Edges: Improvement of the Convergence of the Coordinate Transformation Method

Lifeng Li

Optical Sciences Center, University of Arizona, Tucson, Arizona 85721
Tel: (520) 621-1789, Fax: (520) 621-4358

1. Introduction

Since it was first proposed one and a half decades ago, the coordinate transformation method of Chandezon *et al.*[1] (the C method) for analyzing surface-relief gratings has gone through many stages of improvement and extension.[2-10] By now, it is truly one of the most efficient and versatile theoretical tools for modeling gratings of arbitrary permittivity and (reasonably) arbitrary profiles. The most distinctive features of the C method, not shared with any other rigorous grating methods, are its virtually uniform convergence with respect to the incident polarization (TE, TM, or conical) and the medium permittivity (dielectric or metal), and its perfect suitability for modeling multilayer-coated gratings.

However, one weakness of the C method remains: it converges slowly at large depth-to-period ratios ($h/d \sim 1$) when the groove profile has sharp edges. This weakness prevents effective application of the C method to some practically important cases, such as triangular and trapezoidal gratings.

In this paper, the C method is reformulated using the recently developed proper procedure for Fourier-analyzing the differential equations that contain periodic discontinuities.[11] The newly formulated C method converges much faster than the old one for grating profiles with sharp edges.

2. Review of the C method

For the purpose of this paper, it suffices to consider only one periodic triangular interface, as shown in Fig. 1. $Oxyz$ is a rectangular Cartesian coordinate system. The profile function $a(x)$ is independent of z and its period is d. Furthermore, it is only necessary to consider the TE polarization (the electric field vector parallel to the grooves) because, as explained in Ref. 5, the solutions of Maxwell's equations for the TM polarization and conical mounts can be obtained easily from the TE solutions. Here, only a sketch of the steps of the C method leading to the eigenvalue equation is given. The reader is referred to the above-cited papers for more details.

In the C method, a curvilinear coordinate system is introduced in the *x-y* plane:

$$v = x, \quad u = y - a(x). \tag{1}$$

The relevant Maxwell's equations expressed in this coordinate system are

$$\frac{\partial E_z}{\partial u} = i \mu k_0 (H_v - \dot{a} H_u), \tag{2a}$$

$$\frac{\partial E_z}{\partial v} = i \mu k_0 [\dot{a} H_v - (1 + \dot{a}^2) H_u], \tag{2b}$$

$$\frac{\partial H_v}{\partial u} - \frac{\partial H_u}{\partial v} = i \epsilon k_0 E_z, \tag{2c}$$

Fig. 1. The Cartesian Coordinate system and a triangular grating profile.

where k_0 is the vacuum wavevector, $\mu = 1$, ϵ is the permittivity, $\dot{a}$ denotes the derivative of $a(v)$, and H_v, H_u, and E_z are the covariant component of the field vectors. In this paper, the Gaussian

system of units and the time dependence $\exp(-i\omega t)$ are used. Eliminating H_u from Eqs. (2), we have

$$\frac{\partial E_z}{\partial u} = D(v) \frac{\partial E_z}{\partial v} + i\,\mu\,k_0\,C(v)\,H_v,$$ (3a)

$$\frac{\partial H_v}{\partial u} = \frac{\partial}{\partial v}[\,D(v)\,H_v\,] + i\,\epsilon\,k_0\,E_z + \frac{i}{\mu\,k_0}\frac{\partial}{\partial v}\left[\,C(v)\,\frac{\partial E_z}{\partial v}\,\right],$$ (3b)

where

$$C(v) = \frac{1}{1 + \dot{a}^2(v)}, \qquad D(v) = \frac{\dot{a}(v)}{1 + \dot{a}^2(v)}.$$ (4)

Since the fields are pseudo-periodic in v, we can convert Eqs. (3) into their counterparts in the discrete Fourier space by simply using the transformation rules:

$$\phi \rightarrow \phi_m, \qquad \frac{\partial}{\partial v} \rightarrow i\,\alpha_m,$$ (5)

where ϕ is any term in the equations, ϕ_m is its Fourier coefficient, and $\alpha_m = \alpha_0 + m\,K$, with $K = 2\pi/d$ and α_0 being the Floquet exponent. If ϕ is a product of functions of v, we suppose that the following rule applies:

$$fg \rightarrow \sum_n f_{m-n}\,g_n.$$ (6)

Thus, Eqs. (3) become,

$$\frac{1}{i}\frac{d}{du} F = M\,F,$$ (7)

with

$$M = \begin{pmatrix} D_{m-n}\,\alpha_n & \mu\,k_0\,C_{m-n} \\ \dfrac{1}{\mu\,k_0}(\epsilon\,\mu\,k_0^2\,\delta_{mn} - \alpha_m\,C_{m-n}\,\alpha_n) & \alpha_m\,D_{m-n} \end{pmatrix},$$ (8)

and $F = (E_{zm}, H_{vm})^{\mathrm{T}}$, where E_{zm}, H_{vm}, C_m, and D_m are Fourier coefficients of the corresponding non-subscripted quantities. The total fields everywhere in the grating structure are given by the superpositions of the eigen-solutions of Eq. (7), which can be solved by standard techniques. Hence, the solution of the grating problem is completed.

3. Reformulation of the C method

Although a computer program based on the theory outlined in Section 2 converges quickly for gratings with smooth profiles, it does not do so for gratings whose profiles have sharp edges. The source of the problem lies in the use of the Fourier factorization rule, Eq. (6), for a product of two functions that have complementary jumps.[11] Two functions, f and g, are said to have a pair of complementary jumps at x_0 if both functions have jumps at x_0 but their product remains continuous there. In Ref. 11, it is proved that in the case of complementary jumps the following Fourier factorization rule should be used, instead of Eq. (6):

$$fg \rightarrow \sum_n [\![\,1/f\,]\!]^{-1}_{mn}\,g_n,$$ (9)

where $[\![\phi]\!]$ denotes the matrix generated by ϕ_m. If the jumps of f and g are concurrent but not complementary, then neither Eq. (6) nor Eq. (9) is valid. In addition, the procedures for correctly Fourier-analyzing the differential equations resulting from Maxwell's equations are also given in Ref. 11. In the sequel, these procedures are followed to reformulate the eigenvalue problem. We first need to identify the continuous and discontinuous functions of v in Eqs. (2).

Within a homogeneous medium characterized by a constant ϵ, the continuous functions of v in Eqs. (2) are E_z, H_u, $\partial E_z/\partial u$, and $H_v - \dot{a}\,H_u$, and the discontinuous functions are $\dot{a}$, $\dot{a}^2$, H_v, $\partial E_z/\partial v$, $\partial H_u/\partial v$, and $\partial H_v/\partial u$. The reader is reminded that the field components here are the covariant components in the curvilinear coordinate system. Perhaps the best way to verify the above classification of field components and their derivatives is to consider the field components at $v_0 + 0$ and at $v_0 - 0$ as being associated with two distinct local coordinate systems, where v_0 is one of the abscissae of the discontinuities of $\dot{a}$. Then, by applying the tensorial transformation rule for the covariant vector components, the nature of the field components can be easily identified.

Equations (2a) and (2c) can be readily Fourier analyzed, yielding

$$\frac{\partial E_{zn}}{\partial u} = i\,\mu\,k_0\left(H_{vn} - \sum_m [\dot{a}]_{n-m} H_{um}\right), \tag{10a}$$

$$\frac{\partial H_{vn}}{\partial u} - i\,\alpha_n H_{un} = i\,\epsilon\,k_0 E_{zn}, \tag{10c}$$

because they do not contain products that have complementary jumps. Equation (2b) contains the product $\dot{a}\,H_v$, which has a pair of non-complementary jumps at v_0. To circumvent this problem, we rewrite it as follows,

$$\frac{\partial E_z}{\partial v} = i\,\mu\,k_0\left[\,-H_u + \dot{a}\,(H_v - \dot{a}\,H_u)\,\right]. \tag{11}$$

Now, the second term on the right hand side is a product of a continuous function and a discontinuous function, for which Eq. (6) is valid. To complete the missing part in Eqs. (10), we have

$$\alpha_n E_{zn} = \mu\,k_0\left[\,-H_{un} + \sum_m [\dot{a}]_{n-m}\left(H_{vm} - \sum_p [\dot{a}]_{m-p} H_{up}\right)\right]. \tag{10b}$$

From Eqs. (10a), (10c) and (10b), we rederive an equation identical to Eq. (7), but this time with the M matrix of Eq. (8) replaced by

$$M' = \begin{pmatrix} \mathbb{C}\,[\![\dot{a}]\!]\,\alpha & \mu\,k_0\,\mathbb{C} \\[2ex] \dfrac{1}{\mu\,k_0}\,(\,\epsilon\,\mu\,k_0^2 - \alpha\,\mathbb{C}\,\alpha\,) & \alpha\,\mathbb{C}\,[\![\dot{a}]\!] \end{pmatrix}, \tag{12}$$

where α is a diagonal matrix with α_n along the diagonal and

$$\mathbb{C} = (\,1 + [\![\dot{a}]\!][\![\dot{a}]\!]\,)^{-1}. \tag{13}$$

Once the eigen-solutions of M' are found, the remaining tasks in solving the grating problem are the same as in the conventional C method.

4. Numerical Results

For all numerical examples in this section, the wavelength $\lambda = 1.0$, the incident medium $n_2 = 1.0$,

the truncation order N is half of the matrix dimension of M or M', the solid and dashed lines correspond to TM and TE polarizations, respectively, and the thick and thin lines correspond to the improved and the old C methods, respectively. For the C method, the sum of all diffraction efficiencies is a good indicator of the convergence of individual diffraction orders, therefore only the efficiency sums are presented here.
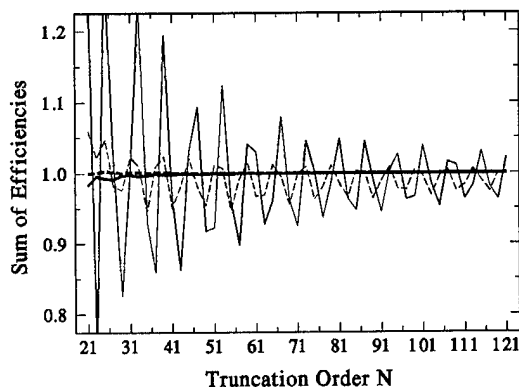

Fig. 2

Fig. 3

Figure 2 is for a triangular grating at -1 order Littrow mount, with $d = h = 1.7$, $d_1 = 0.5$, and $n_1 = 0 + i\,5$. Figure 3 is for a symmetrical trapezoidal grating at 45° incident angle, with $d = h = 2.0$, and $n_1 = 0.3 + i\,7.0$. The upper width of the trapezoid is 0.75 and the lower one is 1.25. Figure 4 is for the same geometry as in Fig. 3, but $n_1 = 1.5$. The substantial improvement of convergence by the newly formulated C method is evident.
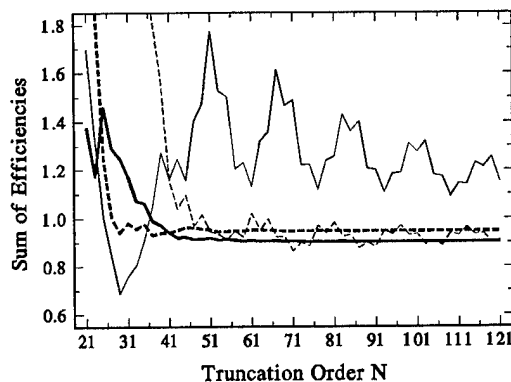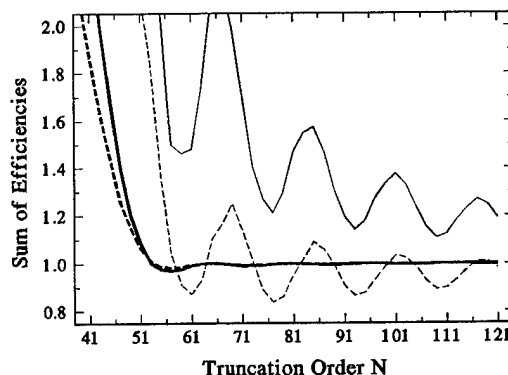
Fig. 4

5. Conclusion

The convergence of the C method for grating profiles with sharp edges has been improved by the reformulation of the eigenvalue equation. Without the mathematical understanding developed in Ref. 11, this improvement would have been impossible.

References

1.   J. Chandezon, D. Maystre, and G. Raoult, J. Optics (Paris) 11, 235 (1980).
2.   J. Chandezon, M. T. Dupuis, G. Cornet, and D. Maystre, J. Opt. Soc. Am. 72, 839 (1982).
3.   E. Popov and L. Mashev, J. Opt. (Paris) 17, 175 (1986).
4.   S. J. Elston, G. P. Bryan-Brown, and J. R. Sambles, Phys. Rev. B 44, 6393 (1991).
5.   L. Li, J. Opt. Soc. Am. A 11(11), 2816 (1994).
6.   N. P. K. Cotter, T. W. Preist, and J. R. Sambles, J. Opt. Soc. Am. A 12, 1097 (1995).
7.   G. Granet, J. P. Plumey, and J. Chandezon, Pure Appl. Opt. 4, 1 (1995).
8.   T. W. Preist, N. P. K. Cotter, and J. R. Sambles, J. Opt. Soc. Am. A 12, 1740 (1995).
9.   L. Li, G. Granet, J. P. Plumey, and J. Chandezon, Pure Appl. Opt. (to be published).
10.   J. B. Harris, T. W. Preist, and J. R. Sambles, J. Opt. Soc. Am. A 12, 1965 (1995).
11.   L. Li, "Use of Fourier series in the analysis of discontinuous periodic structures," J. Opt. Soc. Am. A (to be published).

Liquid Crystal Phase Modulation Technique to Reduce the Spatial Frequency of Interferometric Fringes

P. Douglas Knight, Jr.
UNC-Charlotte Physics Department
University of North Carolina at Charlotte
Charlotte, NC 28223
Phone: 704-547-2536   Fax: 704-547-3160

Interferometric surface analysis involves looking at a fringe pattern and deriving information concerning the surface being imaged. By counting the fringes, one is able to find the surface deformation relative to a reference point. But a problem is encountered when the fringes are too dense for the fringe analysis software to count them. This limits the resolution of the system. But if a spatial light modulator (SLM) could modulate the phase profile in one arm of the interferometer so that the spatial frequency of the fringes is decreased enough to be counted, this problem would be solved.

The technique to reduce interferometric fringe density involves placing a liquid crystal television (LCTV), acting as a phase modulating SLM, in one arm of an interferometer. A phase profile is then imaged onto the SLM that reduces the fringe density in the region of interest. Assume we have an interferometric pattern where the phase of the pattern varies linearly across the pattern. If we select a point on a fringe pattern captured by a CCD to have a phase shift of zero, then we can express the phase of another point on the image as a function of position as

$$\phi_1(x) = 2\pi(x/a) \tag{1}$$

Here a is the change in image pixel position that gives a phase shift of 2π. Now let us assume we have a phase ramp on the LCTV that mimics the effect of a glass wedge placed in one arm of an interferometer. Therefore we now have phase varying linearly with respect to position across the LCTV. We now write a function for the variance of phase across the LCTV as

$$\phi_2(x) = 2\pi(x/b) \tag{2}$$

where b is the number of pixels (change in x) across the LCTV that gives a phase shift of 2π. Since the LCTV acts as an SLM that retards phase, the SLM in the measurand arm of the interferometer will cause the resulting phase of that point on the output image to be the difference between ϕ_1 and ϕ_2. Notice this only occurs if the region of interest on the SLM and the region of interest on the captured image have a one-to-one correspondence. Therefore the phase-modulated captured image phase has the form of

$$\phi_3(x) = 2\pi x\left(\frac{1}{a} - \frac{1}{b}\right) \tag{3}$$

where $\phi_3(x)$ is the phase as a function of position of this captured image. Since a and b are changes in position for a phase shift of 2π, they are also the change in position of one fringe pattern (light to dark to light). So then $1/a$ and $1/b$ can be thought of as fringe spatial frequencies f_a and f_b. Equation 3 then becomes

$$\phi_3(x) = 2\pi x(f_a - f_b) \tag{4}$$

So if f_b is less than f_a and in the same direction, the resulting fringe pattern would have a phase shift that has a lower spatial frequency than the original pattern. Since this lower spatial frequency in phase corresponds to a lower spatial frequency of fringes in the interferometric pattern, we now have a theoretical technique able to lower output fringe density. Note that if f_b is greater than f_a or in the opposite direction, the resulting fringe pattern would have a phase shift with a greater spatial frequency and/or opposite direction than the original pattern. Also note that equation 4 is valid for any direction as long as f_a and f_b are in the same direction. If we wish to reconstruct the original fringe pattern, we easily see that the original phase can be found using

$$\phi_1(x) = \phi_2(x) + \phi_3(x). \tag{5}$$

Since the modulated fringe pattern and the phase profile on the LCTV each have phase intensity values for each pixel, a reconstructed fringe pattern of the original interferometric output can be generated to prove the initial image is recoverable from the resulting fringe pattern and the phase profile placed on the SLM.

For the twisted, nematic liquid crystal display to produce mainly phase modulation, certain modifications are necessary. Initially, the crossed polarizers on opposite ends of the LCTV are removed to eliminate amplitude modulation due to polarization. Also, the polarization angle of the laser beam is aligned to be parallel to the liquid crystal alignment at the front surface of the LCTV. Also, the bias voltage value for the LCTV is set below the optical threshold to reduce polarization modulation while inside the device.

Referring to Figure 1 as the optical apparatus, a Mach-Zender interferometer is set up using a 488 nm argon laser to produce the fringes. This beam is incident on P1 aligned with the plane of polarization angle of the AR laser. The light is then incident on a half-wave plate
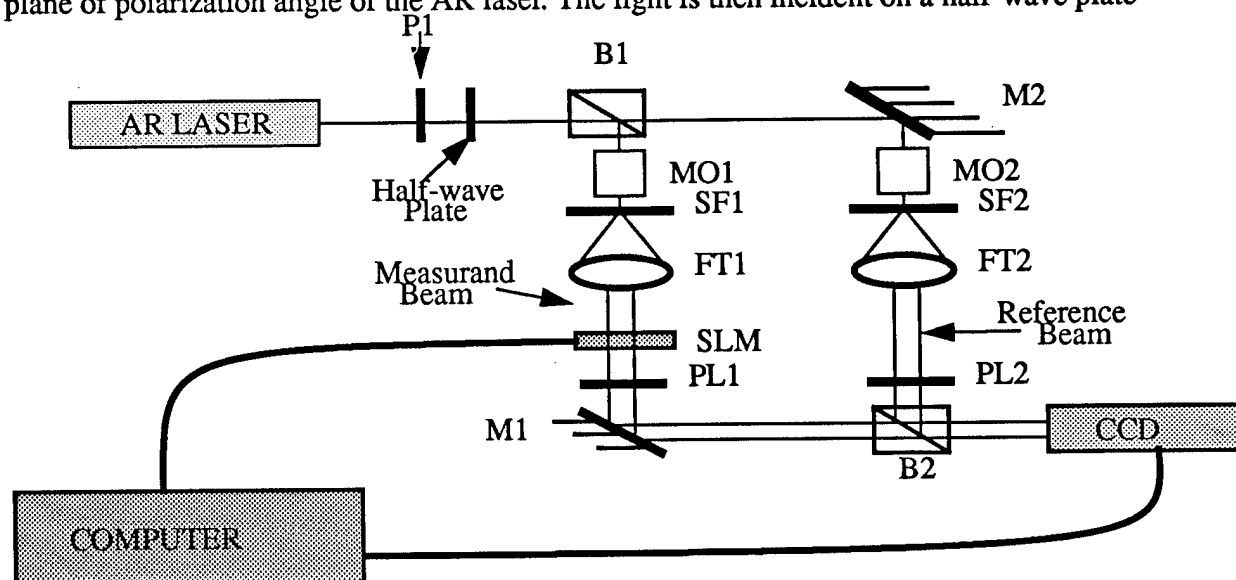
Figure 1

B1, B2, B3: Beamsplitters
MO1, MO2: Microscope Objectives
FT1, FT2: Fourier Transform Lens
SLM: Spatial Light Modulator

M1: Mirror, P1: Polarizer
SF1, SF2: Spatial Filters
CCD: Imaging Camera
PL1,PL2: Plastic Lens

that is oriented so that the outgoing polarization angle is parallel to the alignment of the liquid crystals on the front surface of the SLM. Next, B1 amplitude divides the beam into the reference and measurand arm of the interferometer. For the measurand arm, MO1 focuses the light through pinhole SF1 that spatially filters the beam. FT1 then is placed a focal length away from SF1 so that a plane wave exits FT1. This plane wave is then modulated by a SLM placed perpendicular to the direction of propagation of the wave. M1 then directs the beam so that it is recombined with the reference wave by B2 and imaged onto the CCD. For the reference arm, a plane wave is created similar to how the plane wave for the measurand arm is created. The only difference is the absence of a phase modulator in the reference arm of the interferometer. Plastic lenses of n=1.498 are then used as phase objects. PL1 is placed in the measurand arm right after the LCTV and before M1. PL2 is placed between FT2 and B2 of the reference arm. These are placed at positions appropriate to create a viable interference pattern. For coarser fringe patterns, another phase object (a small piece of clear 35 mm film) is placed before PL2 in the reference arm of the interferometer. Depending on the angular position of the phase object or objects relative to the reference beam, varying coarse phase patterns are generated.

A somewhat linear fringe pattern is initially created by the interferometer. A phase ramp similar to Figure 2a is imaged upon the SLM. This phase ramp is a linear pattern of intensity 0 to intensity b scaled across a set width of pixels. For Figure 2a, the phase ramp width is 20 pixels and b has an intensity of 170. Figure 2b shows fringe density reduction for a fringe pattern of increasing density within the region of interest. Notice the phase ramp is modeled to be similar in form to the fringe pattern. This is necessary for this fringe reduction technique to be valid.
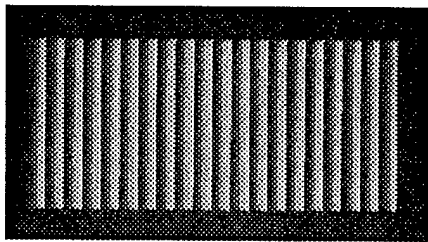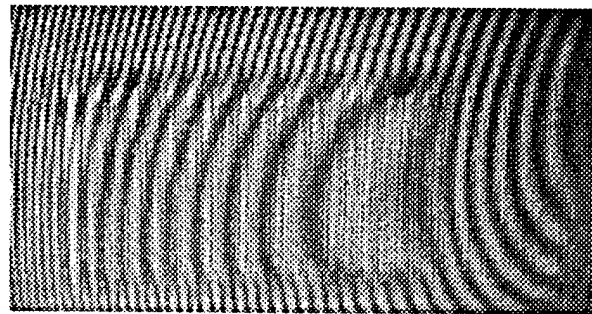
Figure 2a   Figure 2b

With the goal of the research being increased resolution of surface profiles, the initial fringe pattern needs to be recoverable. Therefore a technique must be developed to reconstruct the original fringe pattern. Using equation 5, the modulated fringe pattern must first be mapped from an intensity pattern to a phase distribution. Using a gradient technique to map phase, the modulated fringe pattern was mapped to a phase-related intensity distribution using the formula

$$I_2 = \left(\frac{b}{2\pi}\right)a\sin\left(\frac{I_1 - A_1}{B_1}\right). \tag{6}$$

where I_2 is the phase related intensity of the modulated fringe pattern, b is as defined earlier, I_1 is the intensity of the modulated fringe pattern, A_1 is the bias intensity of the fringe pattern, and B_1 is the amplitude intensity of the fringe pattern. Equation 6 is derived from equation 2 and the equation for the intensity of a fringe pattern,

$$I_1 = A_1 + B_1\sin\phi. \tag{7}$$

The intensity distribution from equation 6 and the intensities of the phase ramp placed on the

SLM are then added to get the original phase mapped intensities. These are converted to CCD pixel intensities using equation 7 to reconstruct the original fringe pattern. Figure 3a shows the original fringe pattern, 3b shows the phase ramp imaged onto the SLM, 3c shows the resulting modulated fringe pattern, and Figure 3d shows the computer generated fringe pattern using the described reconstruction technique. The noise in Figure 3d comes mainly from Figure 3c.
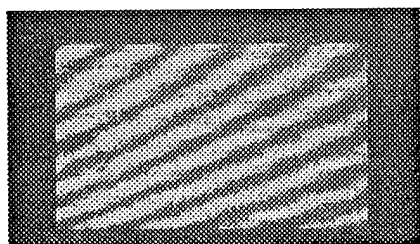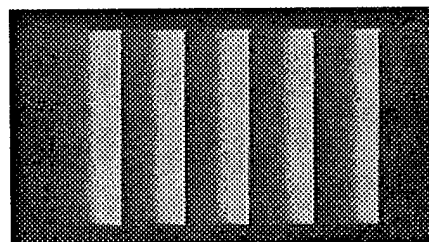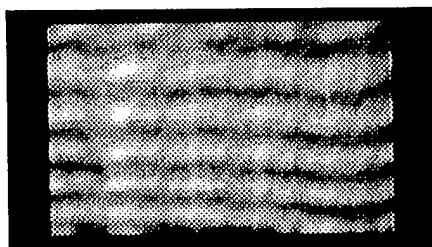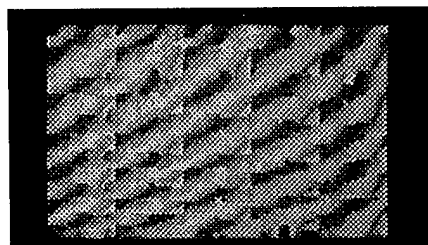
Figure 3a

Figure 3b

Figure 3c

Figure 3d

From Figure 2, it is shown that the spatial frequency of an interferometric fringe pattern can be reduced using an LCTV as a phase modulating SLM. From Figure 3d, it is shown that the original fringe pattern can be recovered using a computational technique. This allows the original fringe pattern to be known only from the phase function placed on the SLM and the resultant modulated fringe pattern captured by a CCD.

Applications of this technique are varied. Flat surfaces with large bumps or pits not mappable using interferometric means could now be mapped. This would involve circular or elliptical phase ramps to initially try to reduce the fringe density.Also, curved surfaces with bumps or pits could be mapped using a phase ramp modeled to fit the surface anomaly. Path noise could also be removed using this technique similar to an adaptive optics system. Currently, pixel size and response time limit the use of LCTV as phase modulating SLMs. With future improvements, applications toward more detailed and complex analysis should be possible.

The author wishes to thank Dr. Eddy Tam for his guidance during the project.

References
1. N. Konforti, et al, Phase-only Modulation with Twisted Nematic Liquid-Crystal Spatial Light Modulators, Optics Letters, Vol. **13**, 251-253 (1988).
2. Eddy Tam, Modulation Properties of a TNLC SLM and its Applications in a Joint Transform Correlator, (1990).
3. Jurgen R. Meyer-Arndt, Introduction to Classical and Modern Optics, Prentice-Hall, (1984).
4. Clifford R. Pollock, Fundamentals of Optoelectronics, Irwin, Chicago (1995).
5. Rafael C. Ganzalez and Paul Wintz, Digital Image Processing, Addison-Wesley, Reading, Mass. (1987).
6. Rensheng Dou and Michael Giles, Closed-Loop Adaptive-Optics system with a Liquid-Crystal Television as a Phase Retarder, Optics Letters, Vol **20**, 1583-5 (1995).

Synthesis of fully continuous phase screens for tailoring the focal plane irradiance profiles

Sham Dixit and Mike Feit

Lawrence Livermore National Laboratory
L-493, P. O. Box 5508, Livermore, California 94551

Tel: (510) 423-7321   Fax: (510) 422-1930
e-mail: dixit1@llnl.gov

In laser driven inertial confinement fusion systems, it is desirable to produce smooth focal plane intensity profiles [1]. Traditionally, binary random phase plates (RPPs) have been used to produce a focal plane irradiance profile which consists of a smooth Airy function shaped envelope and a superimposed fine scale speckle pattern. The speckle is smoothed by conduction smoothing in the laser produced plasma and/or by externally imposed temporal smoothing methods. Although easy to fabricate and use, the RPPs have very limited flexibility in producing arbitrary shaped irradiance profiles. In addition, the secondary maxima of the Airy profile lead to a 15% loss of the energy from the desired region in the focal plane. This loss of the laser energy requires the operation of the fusion lasers at higher energies thereby increasing their cost of operation. Additionally the scattered energy could also cause optical damage to detection equipment near the target.

In order to overcome these limitations of the RPPs, we have recently proposed [2] new phase plate designs for producing arbitrary shaped focal plane intensity profiles which contain greater than 95% of the incident energy. We presented a robust, iterative algorithm based on the phase retrieval algorithms for generating the appropriate phase screens (called kinoform phase plates or KPPs) for producing quite complex intensity profiles in the focal plane. In this procedure, an initial random phase screen is systematically improved upon by repeatedly transforming the complex electric fields between the near-field and the far-field planes and applying appropriately chosen constraints in each plane. The process was successfully

applied to design KPPs that produce complex far-field profiles such as the logo of our Laboratory.

As robust as the algorithm is, it suffers from one serious limitation: if one launches the iterative process using a random phase screen as an initial guess, the algorithm stagnates at the positions of the intensity zeros in the near-field and phase vortices are introduced at these points. Further iterations are unable to remove these vortices. These vortices lead to ~ 2:1 intensity modulations immediately following the phase screen and also to a few percent scattering loss of energy in the focal plane. The inherent singularities at these vortices also make it impossible to unwrap the phase screen into a continuous phase profile.

Continuously varying phase screens offer several advantages over those containing 2π discontinuities. One important advantage is that the propagated field past such a KPP exhibits a low level of intensity modulation. This should minimize the damage threat to the downstream optics. Since the phase appears continuous for the fundamental and harmonic wavelengths as well, the intensity modulations remain small at these wavelengths and hence the unconverted laser light also does not experience any significantly increased level of intensity modulation because of the KPP. The absence of 2π jumps also eliminates the large angle scattering losses from these edges and increases the energy concentration inside the central spot. Phase screens without 2π discontinuities are also useful when fabrication techniques such as ion exchange methods or volume holographic methods are used.

In spite of the advantages of continuous phase screens, the problem of designing such phase screens has eluded us for some time. Typically, smoothly varying phase screens lead to Gaussian envelopes in the far-field whose size is related to the correlation length and the variance of the phase profile. Recent attempts [3] to improve on the iterative algorithm have been unsuccessful where the authors used a continuous phase as a starting point in an iterative algorithm and concluded that the 2π line discontinuities crept in after only two iterations.

We have developed an iterative procedure for constructing fully continuous phase profiles for producing arbitrary focal plane intensity profiles. While continuous phase screens can be easily designed in simpler situations such as circularly symmetric phase profiles and x-y separable phase profiles, the new algorithm is applicable to fully two-dimensional non-

separable situation. The algorithm is launched with a continuous phase profile as an initial guess. The continuous nature of the phase is maintained throughout the iteration cycles by a careful application of the constraints in the near-field and the far-field. The details of the procedure will be presented during the presentation.

We have applied this new algorithm to generate continuous phase profiles for producing superGaussian focal plane intensity distributions. The converged phase continuous phase screen and its corresponding far-field intensity profile are shown in figure 1. The azimuthally averaged far-field profile corresponds to an approximately 12th power superGaussian and contains greater than 98% of the incident energy inside it. We have also applied the algorithm to generate complex far-field profiles. The results will be presented.

References:

[1]   J. D. Lindl et al *Physics Today* **45** 32 (1992)

[2]   S. N. Dixit et al *Opt Lett* **19** 417 (1994)

[3]   Y. Lin et al *Opt. Lett.* **20** 764 (1995).
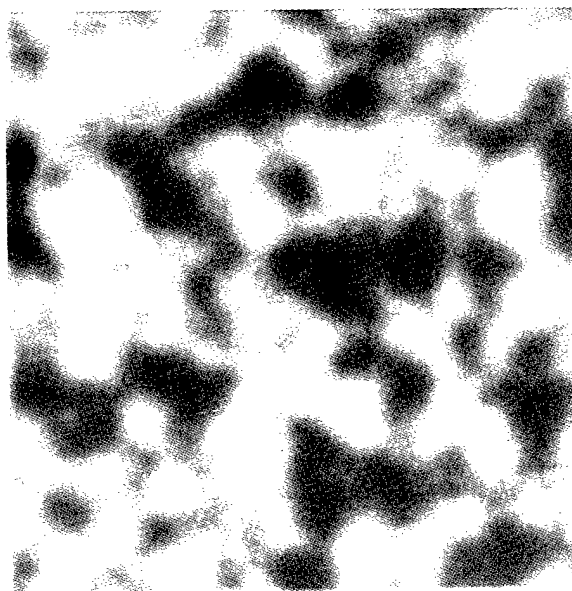
Figure 1a.   Continuous phase screen for producing a superGaussian focal plane intensity profile. The phase values range from 0 (black) to 43 radians (white). The gray scale is linear between black and white.
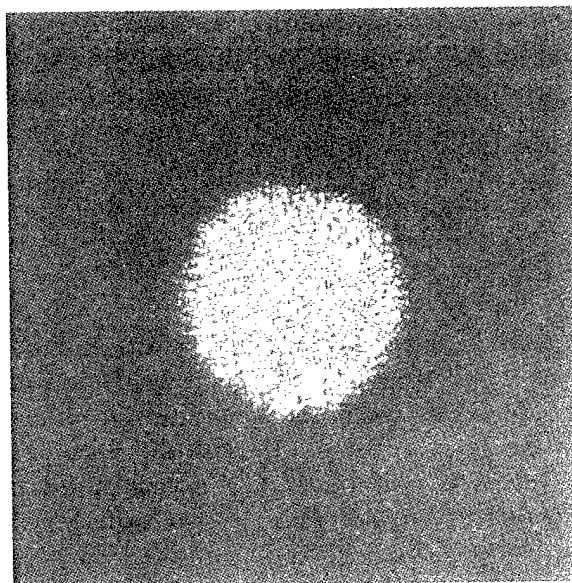
Figure 1b.   Far-field intensity distribution produced by the phase screen shown in figure 1a. The far-field has an approximately 12th power superGaussian profile and contains 98% of the incident energy inside it.

Fabrication of large aperture kinoform phase plates in fused silica for smoothing focal plane intensity profiles

Mike Rushford, Sham Dixit, Ian Thomas and Mike Perry

Lawrence Livermore National Laboratory
L-493, P. O. Box 5508, Livermore, California 94551

Tel: (510) 423-7321   Fax: (510) 422-1930

e-mail: dixit1@llnl.gov

In laser driven inertial confinement fusion systems, it is necessary to produce smooth focal plane intensity profiles [1]. The desired intensity distribution consists of a superGaussian envelope with a superimposed speckle on it. The speckle pattern is smoothed either by the plasma or by other temporal smoothing techniques. Binary random phase plates (RPPs) are inadequate for spatial smoothing as they lead to Airy function envelopes in the far-field and are only 84 % efficient. Furthermore RPPs also introduce large intensity modulations in the propagated intensity past the RPP which can potentially damage the optics downstream from the RPPs.

In order to overcome these limitations of the RPPs, we have recently designed new phase plates for producing superGaussian focal plane intensity profiles. Such phase plates consist of smoothly varying phase profiles only a few waves deep. The propagated field past such a KPP exhibits a low level of intensity modulation. The absence of 2π jumps also eliminates the large angle scattering losses from these edges and increases the energy concentration inside the central spot. The calculated far-field profile contains greater than 98% of the incident energy inside the superGaussian spot.

The kinoform phase plates can be fabricated either as a several waves deep smooth surface relief pattern or as a one-wave deep pattern after re-wrapping the phase. The latter design contains 2π jumps that occur either as closed loop structures or as lines extending from one edge to another edge on the input aperture. Use of the phase plates in fusion laser systems also requires that they be resistant to optical damage under high fluence

irradiances (several J/cm2). Moreover, the phase plates have to be located at the end of the fusion laser chains (where the laser beam size is large ~ 40 cm for the Beamlet laser) in order to prevent any potential optical damage to downstream optics. These requirements imply that the phase plates have to fabricated on large fused silica substrates.

Fabrication of continuous phase plates requires patterning the required surface relief structure in a photoresist layer and its subsequent transferring into fused silica by some form of dry etching (reactive ion etching or chemically assisted ion beam etching). The aperture sizes that can be fabricated using this approach are currently limited to a few centimeters in diameter due the size of available ion etching machines. On the other hand, a one wave deep, mod-2π phase profile can be easily fabricated using the lithographic process with binary masks and wet etching of fused silica in hydrofluoric acid. We have demonstrated the scalability of such process to large apertures (up to 80-cm diameter) in our binary RPP fabrication for smoothing the Nova laser focal spot. For these reasons we have chosen to fabricate 40-cm size KPPs in fused silica using the multiple-mask, wet-etch method.

The continuous KPP phase screen was first rewrapped to a one-wave deep structure and was quantized to 16 levels. This quantized phase screen can be fabricated using four binary masks combined with differential etching for each mask step. This quantization leads to about 1% decrease in the efficiency.

The required binary masks were patterned in chrome coated fused silica substrates by patterning an overlayer of photoresist and etching away the unprotected chrome. We used fused silica substrates for the masks as well in order to equalize the thermal expansion coefficients of the KPP and the mask substrates. The mask substrates (also ~40 cm)were chrome coated by vapor deposition and were subsequently coated with a ~ 350 nm layer of photoresist using a large aperture meniscus coater developed at our Laboratory. The patterning of the photoresist was done on a large aperture photoplotter developed in our laboratory. Here the photoresist is exposed by delivering the 414 nm light from an Kr-ion laser through a 300 μm aperture placed approximately 15 μm above the substrate. The long time required for writing the masks (~3 days for each mask) required us to control the temperature of the plotter table (made of aluminum) to 0.02 degrees

centigrade throughout the plotting period. This enabled us to prepare the binary masks with about 1μm precision (positioning as well as pixel size) over the entire aperture.

The KPP was fabricated by transferring these binary patterns into a photoresist layer deposited over the fused silica substrate by exposing under a UV lamp, developing away the exposed resist and etching the unprotected fused silica in a buffered hydrofluoric acid solution. This process was repeated for each of the four masks. The etch depth for the first mask step is $\lambda/2(n-1)$ where λ is the operating wavelength (351nm) and n the substrate refractive index at this wavelength. It is reduced by a factor of 2 with each subsequent mask step. The alignment accuracy between various masks is about 1-2μm.

To evaluate the optical performance of the 16-level KPP, we illuminated a 30-cm diameter portion of the KPP by a spatially coherent 351 nm laser and investigated the focal plane irradiance distribution produced by it. Preliminary results indicate that the far-field spot resembles a super-Gaussian and contains approximately 94% of the incident energy inside it. This compares well with the predicted efficiency of about 97% after allowing for the quantization and mask misalignment losses. Detailed results including the sources of the efficiency loss will be discussed during the presentation.

References:

[1]   J. D. Lindl et al *Physics Today* **45** 32 (1992)
[2]   S. N. Dixit et al (preceding paper).

Speckle-free phase Fresnel holograms and beam shaping elements

Luiz Gonçalves Neto* and Yunlong Sheng

Université Laval, Centre d'Optique, Photonique et Laser
Département de Physique, Québec, Canada G1K 7P4, sheng@phy.ulaval.ca
*Address after January 1996: São Paulo University, Laboratory of Integrated Systems
EPUSP, Dept. Engenharia Eletrônica, C.P.8174, 01065-970 São Paulo, SP, Brazil
Fax:(55)(11)211-4574, lgneto@lsi.usp.br

1. Introduction

Computer-generated holograms (CGH's) have proved effective as non-periodic diffractive elements for beam shaping. The elements are usually designed with the iterative algorithms based on the Gerchberg-Saxton Algorithm [1-3]. However, the initial random phase and the phase freedom in the image plane used in those algorithms introduce speckle noise in the reconstructed image [4]. Several techniques have been proposed for designing speckle-free CGH's.

In this paper we describe speckle-free phase-mostly Fresnel holograms. In our design we use the linear spatial filter for computing the Fresnel transform and apply the band-limitation constraint on the Fourier spectrum of the reconstructed image. We choose the constant initial phase for iterations, that can avoid the speckles caused by isolated point zeros in the reconstruction plane. We show that the constant initial phase is suitable in the case of Fresnel holograms as the spherical initial phase is suitable for Fourier holograms. We demonstrate good quality speckle-free phase-only Fresnel holograms using a coupled-mode modulation LCTV as phase-mostly spatial light modulator (SLM) [5].

The design technique is also used for a non-periodic beam-shaping Fresnel hologram which is under fabrication in Honeywell through the CO-OP/ARPA diffractive optics workshop. The element was designed to shape a laser diode elliptical pattern into a square flat top pattern. In the design we consider that the laser diode pattern is approximately a gaussian energy distribution in the x-y plane.

2. Speckle-free design technique

When designing a CGH or a non-periodic beam shaping element a random phase is usually added to the image in order to spread out its Fourier spectrum. Also with the iterative method, the phase of the image in the reconstruction plane is used as a free parameter in order to provide the degree of freedom for the iteration to converge. However, in the optical implementation of such holograms the introduction of the random phase can cause problems because the Fourier spectrum of the image can be spread over the entire Fourier plane, whereas the CGH is of finite size. As a result, a severe information loss will occur and the optically reconstructed image from the resultant CGH will contain strong speckle noise [6], which is not desirable in many applications.

The speckle noise can do not appear in the design of the CGH, because the discrete Fourier transform in the computation gives the amplitude and phase information of the reconstructed image only at the sampled points. However, the optical reconstruction is continuous. The finite CGH aperture leads to interpolation among the sampled image values by a sinc function. When the image with random phase is not a band limited function, the interpolation with the sinc function leads to large intensity variations, e.g. speckle noise, on the optically reconstructed image.

Figure 1 shows how the random phase affects the optical reconstruction. The top part of figure 1 depicts 16 sample values of an one-dimensional image $|f_m|$. We multiply $|f_m|$ by a phase function, compute its Fourier transform and then reconstruct the image. In the example of Fig.1b the phase is constant, resulting in no changes of the image bandwidth. The interpolation with the sinc function does not lead to a large amplitude variation in the reconstructed image. In the example of Fig.1a the phase function is $\exp(2\pi n_m)$, where n_m is a white noise. The random phase introduces higher frequency components and enlarges the bandwidth of the image spectrum, resulting in large amplitude variations in between the sampled values of the reconstructed $|f_m|$. To show the effect of the interpolation with sinc functions in the computer simulation, we increase the sampling rate of the reconstructed image. The bottom part of Fig.1 shows 32 sample values of the reconstructed image at the double sampling rate. The reconstructed image $|f_m|$ in the example of figure Fig.1b is smooth, and that in the example of Fig.1a has large amplitude variations,e.g. speckle noise. Note, however, that the 16 sample values of $|f_m|$ at the initial sampling locations are still equal to that of the original image $|f_m|$ in both examples.
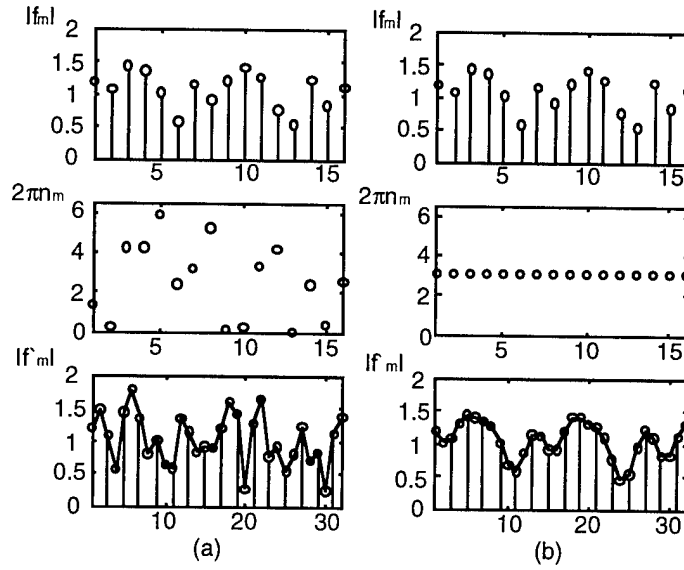
Figure 1: Top: Sampled image; Middle: phase factors added to the image; Bottom: Reconstructed images from $f_m \exp[j2\pi n_m]$ with a double sampling rate.

Three factors should be considered in the iterative designing of the speckle-free CGH's. One is that the sampling rate should be increased in the reconstruction plane in order to simulate the speckle noise which will appear in the optical reconstruction. Another factor is that a Fourier plane constraint should be applied, such that the reconstructed image is a band-limited function. Finally, as shown by Wyrowski et.al., although the iterative technique with band-limitation constraint can smooth out most π-phase jumps in the reconstructed image, and remove most speckle noise, there could be still some isolated point zeros in the reconstructed image. Tracing the phase along a closed circle around those point zeros, the phase can shift by 2π. When a π-jump on those circle is removed by the iteration, a new π-jump will occur on the same circle, so that those point zeros can not be removed by the iteration. Wyrowski suggested to choose initial phase of the iteration and Teiwes [4] used an initial spherical phase to effectively remove those isolated point zeros in Fourier holograms. We show below the implementation of the above three considerations in the design of speckle-free Fresnel holograms.

3. Speckle-free phase-mostly Fresnel holograms

Figure 2 shows the design scheme. We start the design by positioning the desired image $a_{mn} = i_{mn}^{1/2}$ in window of M x N size centered in a 2M x 2N matrix, that results in a image $f_{mn,z}$ in the reconstruction plane. Inside the reconstruction window we have freedom of phase. Outside the window we have freedom of phase and amplitude. The initial phase is chosen as a constant phase.

$$f_{mn,z} = FT^{-1}\left[F_{kl,z}\right] = FT^{-1}\left\{AF_{kl,0}\exp\left[j2\pi\frac{z}{\lambda}\sqrt{1 - \left(\lambda\frac{k}{Md_x}\right)^2 - \left(\lambda\frac{l}{Nd_y}\right)^2}\right]\right\} \quad (1)$$

The Fresnel diffraction is calculated using a linear spatial filtering [7]. The free propagation at a distance z from the hologram $f_{mn,0}$ to the reconstructed image $f_{mn,z}$ is described by Eq.1 where $F_{kl,0}$ is the Fourier transform of $f_{mn,0}$; $F_{kl,z}$ is the Fourier transform of $f_{mn,z}$; m and n are the image plane coordinates, k and l are the Fourier plane coordinates; A is the amplitude of the plane wave; λ is the wave length; MxN are the number of elements of the hologram matrix structure and d_x and d_y are the size of each hologram element. From Eq.(1) the free propagation is characterized by a transfer function $H_{kl,z}$, given by:

$$H_{kl,z} = \frac{F_{kl,z}}{F_{kl,0}} = A\exp\left[j2\pi\frac{z}{\lambda}\sqrt{1 - \left(\lambda\frac{k}{Md_x}\right)^2 - \left(\lambda\frac{l}{Nd_y}\right)^2}\right] \quad (2)$$

To calculate the inverse propagation from the reconstruction plane to the hologram plane, we apply the inverse propagation filter

$$f_{mn,0} = FT^{-1}\left[\frac{F_{kl,z}}{H_{kl,z}}\right] \tag{3}$$

The constraint in the hologram plane is the phase modulation characteristic of the SLM, which is a phase-mostly liquid crystal television (LCTV) with a slight coupled amplitude modulation [6].
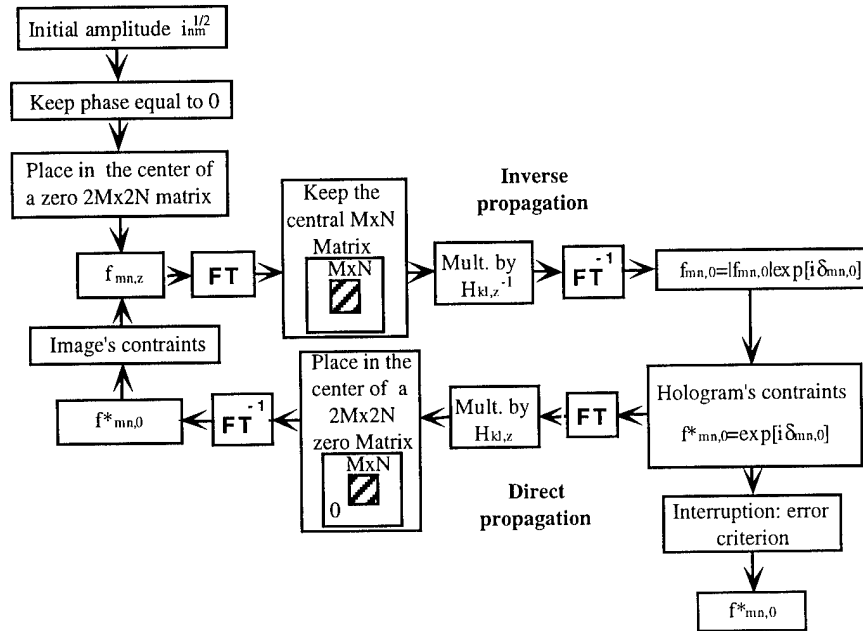

Figure 2: The Iterative Algorithm applied in design of speckle free phase-only fresnel holograms.

The hologram is of M x N size. For computing the free propagation from the hologram plan to the image plan, we use the Fourier transform of $f_{mn,0}$ which is $F_{kl,0}$ of M x N size. We multiply it with $H_{kl,z}$. In this step we introduce the M x N spectrum $F_{kl,0}H_{kl,z}$ inside a 2M x 2N zero matrix before computing the reconstructed image, that doubles the sampling rate of the image in order to simulate the optical reconstructed image with the speckle noise.

The image plane constraint is that the amplitude $|f_{mn,z}|$ must be proportional to a_{mn} inside the reconstruction window g_r. The band-limited constraint is applied on the Fourier transform $F_{kl,z}$ of the image $f_{mn,z}$, that is $F_{kl,z} = 0$ outside a center square of M x N size. The new information $f_{mn,z}$ is used in the next iteration. The iterations continues until no significant reduction in the mean square error is achieved.

(a)   (b)   (c)
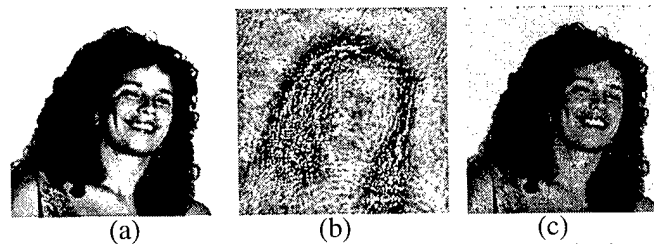
Figure 3: (a) desired reconstruction; (b) resulted hologram; (c) speckle-free reconstruction

For Fourier holograms, the initial spherical phase is a suitable choice because it is naturally band limited in the Fourier plane (hologram plane). By adjusting its radius we can spread the light only in the region of the

hologram. For Fresnel holograms, the initial constant phase is a suitable choice because we are forcing the spectrum of the function $F_{kl,z}$ to be concentrated in the center of the Fourier plane, and consequently, band limited. During the calculus of the inverse and direct propagation, the phase variation of the phase function $H_{kl,z}$ is more smooth in the center of the frequency plane, what does not introduces a strong phase variation (deviation) in $F_{kl,z}$, resulting in a smooth hologram.

4 Experimental results

We designed a phase-mostly Fresnel hologram with the dimensions of 200 x 200 pixels, that is to be displayed in a coupled-mode LCTV [5]. The desired reconstruction is the intensity of the image shown in figure 3a with a size of 400 x 400 pixels. This image is placed in a reconstruction region g_r with the same size, 400x400 pixels (we use only the freedom of phase in the reconstruction). Figures 3b and 3c show the computer generated hologram and computer reconstruction after 50 iterations. The distance z for the free propagation is 3 m, the LCTV pixels size are $d_x=10.9 \cdot 10^{-5}$ m and $d_y=9.0 \cdot 10^{-5}$ m, and the light wavelength is $\lambda=632.8 \cdot 10^{-9}$ m. The figure 4a shows the optical reconstruction. We note the absence of the speckle noise. To compare the quality of our result, we generated a Fresnel hologram using a initial random phase and an iterative algorithm without force the reconstruction $f_{mn,z}$ to be a band limited distribution. Figure 4b shows the noisy optical reconstruction.

(a)   (b)
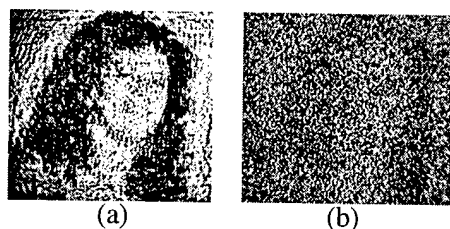
Figure 4: (a) optical speckle-free
reconstruction; (b) noisy optical
reconstruction

References

1. R.W. Gerchberg and W.O. Saxton. A Practical Algorithm for the Determination of Phase from image and Diffraction Plane Pictures, Optick 35, 237-46, 1972.
2. J.R. Fienup. Iterative method applied to image reconstruction and computer-generated holograms. Optical Engineering, vol.19 no.3, p.297-305, June 1980.
3. Frank Wyrowski. Iterative quantization of digital amplitude holograms. Applied Optics, vol.28 no.18, p.3864-3870, Sep. 15, 1989.
4. Stephan Teiwes, Heiko Schwarzer, Harald Aagedal, Michael Schimid, Thomas Beth, Frank Reichel and Frank Wyrowski, Speckle-free signal reconstruction with non-periodic diffractive elements on liquid-crystal SLM, OSA topical meeting, spatial light modulator, thech. Digest series, vol.9, 24-27 (1995).
5. Luiz Gonçalves Neto, Danny Roberge and Yunlong Sheng. Programmable optical phase-mostly holograms with coupled-mode modulation liquid-crystal television. Applied Optics, Vol. 34, No. 11, p.1944-1950, 10 april 1995.
6. Luiz Gonçalves Neto and Yunlong Sheng. Optical implementation of image encryption. Submitted to Optical Engineering, October 1995.
7 Joseph W. Goodman. Introduction to Fourier Optics. McGraw-Hill Publishing Company, p.48 54, 1968, 1988.

High efficiency fast diffractive lens
for beam coupling

Yunlong Sheng and Dazeng Feng
Université Laval, Centre d'Optique, Photonique et Laser,
Département de Physique, Québec, Canada G1K 7P4.
Tel: 418 656 3908, Fax: 418 656 2623 sheng@phy.ulaval.ca

Diffractive lenses for laser diode beam focusing collimating and coupling have wide applications. Large numerical aperture and high light efficiency are important issues for the coupling lenses. Numerical aperture of a typical laser diode beam can be as large as NA ~ 0.5. To capture the highly divergent beam the lens must have a low F-number of F/1 ~ F/2. Coupling the laser beam into an optic fiber with an acceptance angle of NA ~ 0.1 - 0.2 needs even larger numerical aperture of the lens.

We designed a focusing and shaping lens which is fabricated in the Honeywell/CO-OP diffractive optics workshop. The lens is of $\phi = 5$ mm, minimum feature size $\delta = 1.5$ μm and phase levels N = 8 for wavelength $\lambda = 850$ nm. With the conventional design the outermost Fresnel zone will have a minimum width of $N\delta = 12$ μm, resulting a lens of about F/7. Reducing the phase levels to N = 2 leads to a minimum zone width $N\delta = 3$ μm and F/1.7, resulting in a diffraction efficiency of 40%. The uniform etching depths in the workshop foundry does not allow us to make multi-order lens[1].

To design a high efficiency fast focusing lens we choose the method proposed by Welch et.al.[2], which is useful for encoding radially symmetric discrete phase lenses. In the encoding the photomask resolution $\Delta\rho$ is used instead of the minimum feature size δ as the sampling interval. The minimum feature size δ is still respected. The feature sizes become δ, $\delta+\Delta\rho$, $\delta+2\Delta\rho$ ... instead of δ, 2δ, 3δ ... Since $\Delta\rho$ << δ the degrees of freedom for the iterative simulated annealing optimization are dramatically increased. In this paper we design high efficiency large aperture focusing and shaping lenses with elliptical incident beam using this technique. We estimate aberrations and effects of the sampling rate and of the fabrication errors of those particular type lenses.

1. Simulated annealing algorithm

In the photolithographic process the position accuracy of mask features is determined by the e-beam mask writing, while the minimum feature size δ depends on the mask alignment. We divide a radially symmetric diffractive lens into P ring-shaped cells of equal radial width of $\Delta\rho$, where $\Delta\rho$ << δ is the resolution of the photomasks. Then, we regroup the cells into T rings. Each ring has a constant phase $\phi(\rho)$ for $\rho_t \leq \rho \leq \rho_{t+1}$ and the minimum feature size is respected $\rho_{t+1} - \rho_t \geq \delta$.

In the simulated annealing[3] we change randomly the phase value ϕ_t and the locations of the phase transition points ρ_t and ρ_{t+1}. The latter corresponds to change the number of cells in a ring. Then, we calculate the cost function. When the cost is reduced the change is accepted. When the cost is augmented the change is accepted with a probability, which decreases with the decrease of a temperature parameter. In one iteration all the rings are visited consecutively from the innermost to outermost ring. The iteration is then repeated with a lower temperature until the temperature becomes sufficiently low. The initial state of the lens should not affect the final solution of the simulated annealing if the initial temperature is sufficiently high.

The near field diffraction of the fast lens is computed with the Rayleigh-Sommerfeld formula as,

$$U(r,\psi) = \frac{1}{j\lambda} \iint_\Sigma A(\rho,\theta) \exp[j\phi(\rho)]$$

$$\frac{\exp(jkr_{01})}{r_{01}} \cos(\hat{n}, \hat{r}_{01}) \rho d\rho d\theta \qquad (1)$$

where $j = \sqrt{-1}$, λ is the wavelength, $k = 2\pi/\lambda$, $A(\rho,\theta)$ is the incident amplitude, $\exp[j\phi(\rho)]$ is the lens, r_{01} is the displacement vector from a point (ρ,θ) in the lens plane to a point (r,ψ) in the focal plane. The directional factor $\cos(n,r_{01}) = f/r_{01}$, where f is the focal length. For a given $A(\rho,\theta)$ the integral with respect to θ in the right-hand side of Eq.(1) is independent of the lens and can be computed and stored in the computer before the design. Hence, the diffraction output can be updated quickly for each change in the simulated annealing process. The cost function is defined for maximizing the diffraction efficiency η as,

$$e_1 = 1 - \eta = 1 - \frac{\sum_m \sum_n |U_{mn}|^2 m (\Delta r)^2 (\Delta \psi)}{I} \quad (2)$$

where I is the incident power on the lens and U_{mn} is sampled $U(r,\psi)$ with $r = m\Delta r$ and $\psi = n\Delta\psi$. The η is calculated in an area of five times of the Airy size of the lens.

Optimized for high efficiency, the designed lens can have discrete phase levels N at the center, but less than N in the outer region of the lens. Welch et. al. obtained η = 90% for a F/1 lens with the minimum feature size δ = 0.7 μm and λ = 1.3 μm. We obtain η = 89% for a F/3 lens with δ = 1.5 μm for λ = 0.85 μm. We note that the efficiency was high only for a Gaussian incident beam and was much lower for a uniform incident beam. The loss of power due to the lower number of phase levels in the outer region of the lens is less important for Gaussian beam than for uniform beam.

2. Design considerations

(1) Elliptical incident beam: When $A(\rho,\theta)$ is radially symmetric the diffraction output $U(r,\psi)$ is also radially symmetric, we need to compute the output only on one radius in the focal plane. The integral with respect to θ in Eq.(1) becomes a function only of the radial coordinates ρ in the lens plane and r in the focal plane. The data stored in the computer for fast updating the cost function is a 2-D array. When $\Delta\rho$ = 0.1 μm for sampling the lens radius R_0 = 2.5 mm and r = m(Δr) is sampled with m =0, 1, ... 30, for radially sampling the focal plane the storage requires 6 Mbytes memory.

We designed focusing lenses for elliptical laser diode incident beam $A(\rho,\theta)$. In this case the diffraction output is no longer radially symmetric. The data to be stored are a 3-D array, which depends on ρ, r and the angular coordinate ψ in the focal plane. The storage requires a much larger memory. Fortunately, for on-axis focusing the diffraction pattern $U(r,\psi)$ has a reflection symmetry. We need to compute the data only for a quarter of the focal plane. The focal plane was sampled by m = 30 points in the radial direction and by every 6° in angular direction. We had to use a larger sampling interval for the lens with $\Delta\rho$ = 0.5 μm, the storage memory was about 18 Mbytes. We needed about 3 hours in the Silicon Graphic Power Indigo 2 Computer for calculating the 3-D array and one hour for optimizing the lens with the simulated annealing.

(2) Sampling interval: In the Rayleigh-Sommerfeld diffraction Eq.1, the phase term $\exp(jkr_{01})$ is very sensitive to r_{01}, the sampling rate $\Delta\rho$ must satisfies the following condition,

$$k\Delta\rho \left\{ \frac{\partial r_{01}}{\partial \rho} \right\}_{max} < 2\pi \quad (3)$$

The maximum value of $\partial r_{01}/\partial\rho$ occurs at $\rho = R_0$ for the on-axis focal point, where R_0 is the lens radius. Hence, we have,

$$\Delta\rho < \lambda\sqrt{1 + (2F/\#)^2} \quad (4)$$

The $\Delta\rho$ is limited by the accuracy in mask writing and by the size of the 3-D data stored in the computer. We find that when $\Delta\rho$ varies from 0.05 μm to 0.5 μm for F/# = 1 and 3 the diffraction efficiency varies less than 5%, because in this case the sampling interval,

$$\Delta\rho \approx 0.1\lambda F/\# \quad \sim \quad 0.2\lambda F/\# \quad (5)$$

the condition described in Eq.4 is satisfied.

(3) Beam shaping: With the elliptical incident beam the focal spot is elliptical(see Fig.1). We designed a lens that shapes the beam to yield a circular focal spot. In the design we added one term in the cost function e_1 as,

$$e_2 - e_1 + \frac{\displaystyle\sum_m \sum_n (|U_{mn}|^2 - |U_{m0}|^2) m (\Delta r)^2 \Delta \psi}{I} \quad (6)$$

where U_{m0} is a target circular amplitude distribution whose diameter is equal to the long axis of the elliptical focal spot. The elliptical focus is then expanded along the short axis to a circular spot(see Fig.2). The lens is still radially symmetrical. Its focal length is in fact changed by the simulated annealing, resulting in the circular spot in the original focal plane for the elliptical incident beam.
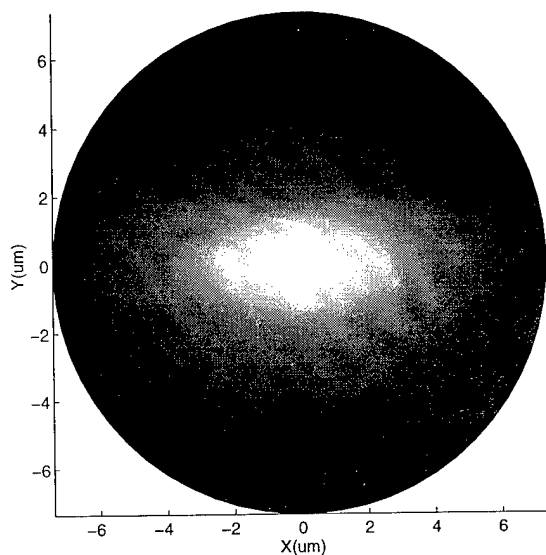
Figure 1. The intensity distribution of the elliptical spot.

(4) Aberrations: The encoding process optimizes the discrete phase values and the locations of the phase transition points in order to maximize the diffraction efficiency. As a consequence, the zone boundaries and phase profile of a diffractive lens are violated, resulting in an important wavefront aberration. We interpolated the discrete phase profile of the designed lenses with a polynomial and estimated the spherical aberrations with the CODE V. Figure 3 shows the axial spherical aberration of the designed focusing and shaping lens of F/3. The transverse spherical aberration (TSA) is smaller than the Airy size for ray heights smaller than 68% of the maximum ray height. Outer this region the TSA increases very fast with the ray height. As a result the lens focuses most energy of the Gaussian beam into
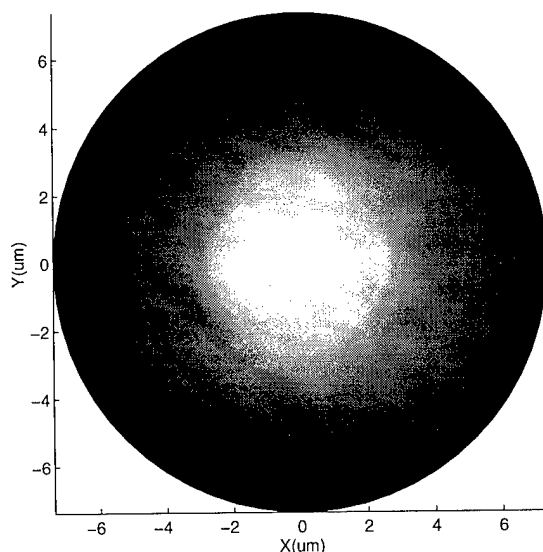
Figure 2. The intensity distribution of the circular spot.

the diffraction limited focal spot. The outer region of the Gaussian incident beam go far beyond the focal point. Its energy is lost.
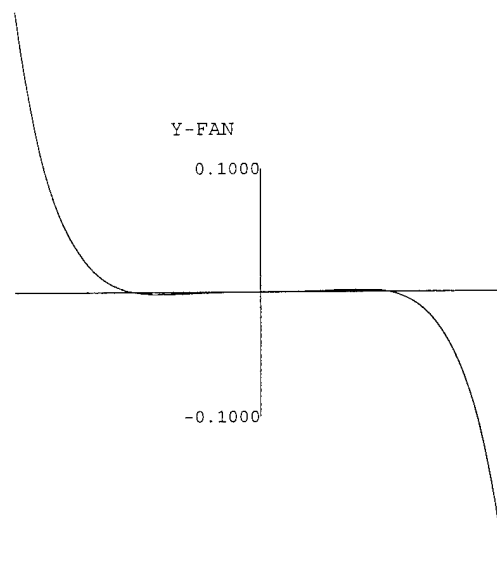
Figure 3. Axial spherical aberration.

3. Estimation of fabrication error effect

There are basically two systematic errors in the photolithographic fabrication: that in the etching depth and that in the mask alignment. Their effects on the lens diffraction efficiency can be estimated by numerical simulation.

For simulating the etching depth error we introduced random phase errors $\Delta\phi_n$ in each of three etching process with n = 1, 2, 3. The values of $\Delta\phi_n$ were randomly distributed within $-\Delta\phi_{max} \leq \Delta\phi \leq \Delta\phi_{max}$. The mean value of η and the standard deviation σ were computed as a function of $\Delta\phi_{max}$ and $\eta\pm\sigma$ are plotted in Fig.4. One sees that when the etching depth errors are controlled under 300 A (0.24 rad for $\lambda = 0.85$ μm), the efficiency decreases only by 1 - 3 % for both F/1 and F/3 lenses.
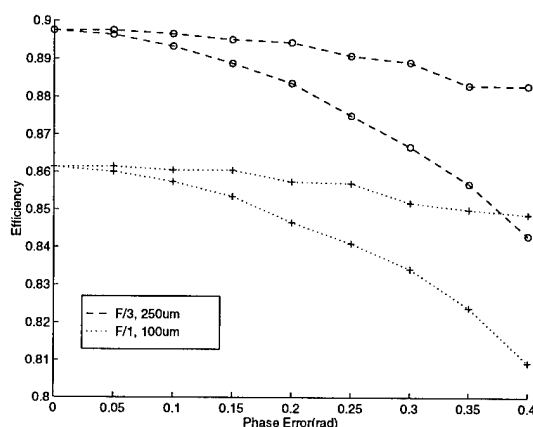
Figure 4. Etching depth error

For simulating the mask alignment error, we shifted the second mask in the x-axis by a distance of Δ with respect to the first mask and the third mask in y-axis by the same distance. With those alignment errors the diffractive lens were no longer radially symmetric. The focal plane light amplitude distribution was calculated with the Rayleigh-Sommerfeld formula. The Efficiency η is computed as a function of Δ and is plotted in Fig.5. The efficiency is reduced by 10% for F/3 lens when Δ = 0.4 μm and by 15% for F/1 lens when Δ = 0.2 μm. Misalignment of the mask can introduce new high spatial frequency features to the lens and reduce the diffraction efficiency significantly.
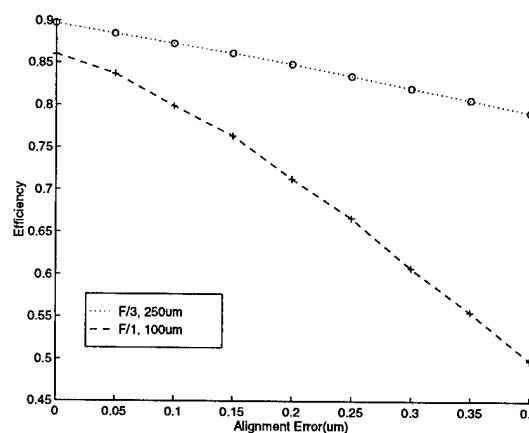
Figure 5. Mask alignment error

5. Results

We have designed focusing and shaping lenses for elliptical shaped input beams. The phase levels of the lenses is N = 8 in the center and N < 8 in outer regions. The TSA of the lens is estimated. The rays within the circle of 68% radius of the lens are focused into the Airy circle. High efficiency is only for Gaussian input beams. For uniform beam the efficiency was poor. Our best design provides efficiency of 89.4% for F/3 lens for minimum feature size of 1.5 μm and $\lambda = 0.85$ μm.

References

1. G. M. Morris, D. Faklis, "Achromatic and apochromatic diffractive singlets", OSA Topical Meeting "Diffractive Optics", Tech. Digest 11, 57-60 (1994).
2. W. H. Welch, J. E. Morris and M. R. Feldman, "Iterative discrete on-axis encoding of radially symmetric computer-generated holograms", J. Opt. Soc. Am. A, 10, 1729-1738 (1993).
3. S. Kirkpatrick, C. D. Gelatt Jr. and M. P. Vecchi, "Optimization by simulated annealing ", Science, 220, 671-680 (1983).

Effective medium theory of symmetric two-dimensional subwavelength periodic structures

Philippe Lalanne
Institut d'Optique Théorique et Appliquée, CNRS, BP 147, 91403 Orsay Cedex, France
tel: 33-1-69-41-68-46   fax: 33-1-69-41-31-92   e-mail: philippe.lalanne@iota.u-psud.fr

1. Introduction

Recent experimental and theoretical investigations have shown that periodic subwavelength structured surfaces with periods small compared to the illumination wavelength behave as homogeneous medium, and have suggested interesting applications, such as fabrication of anti-reflection coatings[1,2,3], quarter wave plates[4], polarizers[5], and graded-phase diffractive elements[6]. The replacement of the periodic structure by a homogeneous medium is often referred as homogenization or effective medium theory (EMT). EMT can be applied to a large variety of physical material properties, such as diffusion constant, magnetic permeability, thermal conductivity, etc. To facilitate the design and fabrication of artificial dielectric elements, one must be able to relate the effective index of the subwavelength structured surface in a simple way.

The properties of one-dimensional (1-D) periodic structures have been analyzed in great detail, and the equivalence of 1-D gratings and homogeneous uniaxial thin films has been rigorously derived in the long wavelength limit. Limited research has been done in the area of two-dimensional (2-D) gratings. Jackson and Coriell[7] derived upper and lower bounds of the zeroth-order effective index of 2-D periodic structures. More recently, Grann et al.[21] used rigorous coupled-wave analysis (RCWA) to estimate the effective index of 2-D gratings by computer simulations.

In this paper we study the EMT of 2-D symmetric periodic structures for a wave propagating normally to the grating. We use a Fourier expansion method. Closed-forms of the zeroth- and second-order effective indices are provided. By 2-D symmetric structures, we mean structures presenting a center of symmetry. It does not imply that the periods are the same, and for gratings composed of parallelepipeds of one given medium immersed in an other medium, it does not imply that the two fill factors are equal. To our knowledge, this work is the first to present a rigorous approach for the EMT of 2-D periodic structures.

2. Effective medium theory

Notations

To establish our notation, let us first consider a 2-D periodic structure along the x and y axis with an arbitrary relative permittivity profile $\varepsilon(x,y)$. Two examples are shown in Fig. 1. The structure is assumed to be constant in the z direction perpendicular to the plane of Fig. 1. The grating period along the y direction is noted Λ. The period in the x direction Λ_x can be simply written $\Lambda_x = \Lambda/\rho$, where ρ is a dimensionless coefficient. The grating vector K is simply defined as $K = 2\pi/\Lambda$. Using ε_{mn} to denote the (m,n)th Fourier coefficient of periodic structures, we have

$$\varepsilon(x,y) = \sum_{m,n} \varepsilon_{mn} \exp jK(\rho mx + ny). \tag{1}$$

Similarly a_{mn} will be used to denote the (m,n)th Fourier coefficients of the inverse relative permittivity. In the following, we restrict the discussion to symmetric periodic structures with

$$\varepsilon_{m,n} = \varepsilon_{-m,n} = \varepsilon_{m,-n} = \varepsilon_{-m,-n}. \tag{2}$$

Note that it does not imply the equality of the periods along the x and y directions, but simply that a center of symmetry exists.

Methodology

We consider a wave with wavelength λ in a vacuum and wave vector k ($k = 2\pi/\lambda$). The wave is propagating in the periodic structure along the z-direction and is polarized in either the x or y direction. In the following, only a

polarization along the y direction will be investigated for the sake of simplicity. The z-dependence of the wave is assumed to be

$$\exp(j\sqrt{\eta}\,kz),$$ (3)

where the constant η is read as the square of the effective index of the periodic structures for the z direction and the given polarization.

We look for a wave propagating in the z direction and periodic in the x and y direction with period $\rho\Lambda$ and Λ, respectively. Expending the x and y components of the wave electric field in a Fourier series, we have

$$E_x = \exp jk\sqrt{\eta}z \sum_{(m,n)\neq(0,0)} s_{xmn} \exp jK(m\rho x + ny)$$ (4a)

$$E_y = \exp jk\sqrt{\eta}z \sum_{m,n} s_{ymn} \exp jK(m\rho x + ny),$$ (4b)

where s_{xmn} and s_{ymn} are constants, and only E_y has a DC component. On spatial averaging along the x and y directions of the periodic structure, E_x equals zero and E_y equals s_{y00}, since only E_x has a non-null DC component. Note that when looking for a wave polarized in the x direction, Eqs. 4 hold except that, in that case, only E_x has a DC component (i.e. $s_{y00}=0$ and $s_{x00} \neq 0$).

The wave electric field of Eq. 4 is used in satisfying Maxwell's equations inside the periodic structure. Obviously such a solution is not correct. But for small period-to-wavelength ratios, an approximate solution can be derived[8] by expanding η, s_{xmn} and s_{ymn} in a power series of $\alpha = \lambda/\Lambda$. The EMT expansion for η can be written

$$\eta = \eta_0 + \eta_1\alpha^{-1} + \eta_2\alpha^{-2} + ...,$$ (4)

where η_o is the square of the zeroth-order effective index and η_i, i=1,...,N is the ith-order coefficient of the series expansion. In general η depends on the permittivity ε, the period Λ, the wavelength λ, and on ρ for 2-D periodic structures. (2)

Solution

By solving Maxwell's equations inside the periodic structure, we find[9]

$$\eta_0 = \varepsilon_{00} - \sum_{p,q\neq 0} \sum_{m\geq 0,n>0} \varepsilon_{m,n} a^{p,q}_{m,n} \varepsilon_{p,q} n,$$ (5a)

$$\eta_1 = 0,$$ (5b)

$$\eta_2 = \sum_{p,q\neq 0} \sum_{m\geq 0,n>0} \varepsilon_{p,q} a^{p,q}_{m,n} c_{mn} + \sum_{p\neq 0} \frac{\varepsilon_{p,0}}{p^2\rho^2}\left(\varepsilon_{p,0} - \sum_{\substack{(r,t)\neq(0,0) \\ u\geq 0,v>0}} \varepsilon_{p-r,t} a^{u,v}_{r,t} \varepsilon_{r,t} t \right).$$ (5c)

For numerical purpose, the Fourier series of Eq. 4 have to be truncated. We denote by M the truncation rank so that, in Eq. 4, m and n vary between -M and M. The computation of $a^{p,q}_{m,n}$ and c_{mn} coefficients requires the inversion of a $M(M+1)\times M(M+1)$ matrix not defined here.

3. Comparison with rigorous computations

3.1 Jackson and Coriell[7] derived upper and lower bound expressions for the zeroth-order EMT of several simple symmetric periodic structures composed of two-phase materials, like those of Fig. 1. These structures are composed of two homogeneous media indexed by 1 and 2. In our simulation, media 1 and 2 have optical permittivities equal to 1 and 16, respectively. The periodic structure of Fig. 1a is composed of parallelepipeds of high index inserted in a medium of low index. Similarly, the periodic structure of Fig. 1b is composed of cylinders of low index inserted

in a medium of high index. We define the fill factor of the two structures as the ratio between the width (resp. the diameter) of the parallelepiped (resp. cylinder) and the period Λ. The solid lines of Fig. 2 are the upper and lower bounds derived by Jackson and Coriell[7]. They are plotted as a function of the fill factor. Circle-, cross-, and plus-marks are the zeroth-order (η_0) effective index obtained for different truncation ranks. Circle-marks were derived with M = 40, cross marks with M = 20, and plus-marks with M = 7. Basically, the EMT prediction of Eq. 5a lies in between the upper and lower bounds. For the parallelepiped case and for fill factors about 0.8 and 0.9, it is noticeable that the truncated expansion is slowly converging. For a fill factor equal to 0.9, even with M = 40, η_0 remains just above the upper bound.

3.2 In Fig. 3, the transmittance for normal incidence of a 6-grid stack of alternate layers is shown as a function a the wavelength. Each grid is composed an homogeneous thin film of relative permittivity 13 and a 2-D grating with a cubic filling geometries of relative permittivity 1 immersed in a medium of relative permittivity 13. The grating period, fill factor and depth are 0.16, 0.56 and 0.09, respectively. The homogeneous layer depth is 0.07. The solid curve is obtained with rigorous computation and the dashed curve is derived with the second-order EMT of Eqs. 5. Once homogenized, the periodic structure is equivalent to a thin film stack. Basically, there is a good agreement between rigorous computation and the EMT prediction. A significant mismatch is visible for wavelength smaller than 0.6, i.e. for period-to-wavelength ratios larger than 0.27. In that case, the 2-D EMT presented in this paper is a valuable technique to explain and predict the existence of a gap for wavelength larger than 0.9 and smaller than 1.2.

References

[1] T.K. Gaylord, W.E. Baird and M.G. Moharam, "Zero-reflectivity high spatial-frequency rectangular-groove dielectric surface-relief gratings", Appl. Opt. 25(24), 4562-4567 (1986)

[2] Y. Ono, Y. Kimura, Y Otha and N. Nishida, "Antireflection effects in ultrahigh spatial-frequency holographic relief gratings", Appl. Opt. 26(6), 1142-1146 (1987)

[3] D.H. Raguin and G.M. Morris, "Antireflection structured surfaces for the infrared spectral region", Appl. Opt. 32(7), 1154-1167 (1993)

[4] L. H. Cescato, E. Gluch and N. Sreibl, "Holographic quaterwave plates", Appl. Opt. 29(15), 3286-3290 (1990)

[5] P. Yeh, "A new optical model for wire grid polarizers", Opt. Comm. 26(4), 289-292 (1978)

[6] F.T. Chen and H.G. Craighead, "Diffractive phase elements based on two-dimensional artificial dielectrics", Opt. Lett. 20(2), 121-123 (1995)

[7] J.L. Jackson and S.R. Coriell, "Transport coefficients of composite materials", Journ. Appl. Phys. 39(5), 2349-2354 (1968)

[8] Ph. Lalanne and D. Lemercier-Lalanne, "On the effective medium theory of subwavelength periodic structures", submitted for publication.
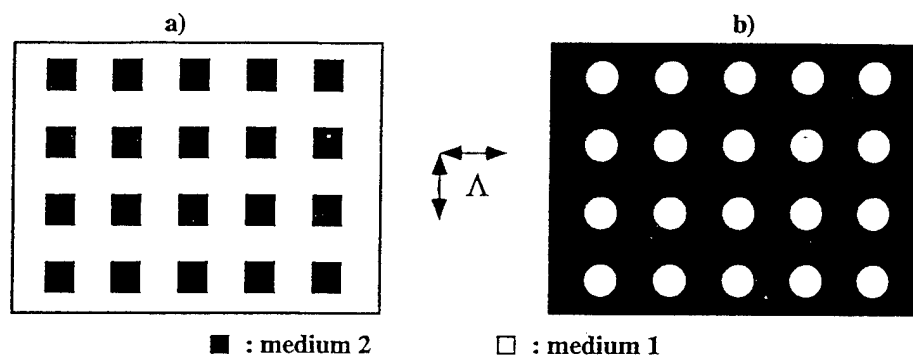
Fig.1 a) periodic structure composed of parallelepipeds of high index inserted in a medium of low index
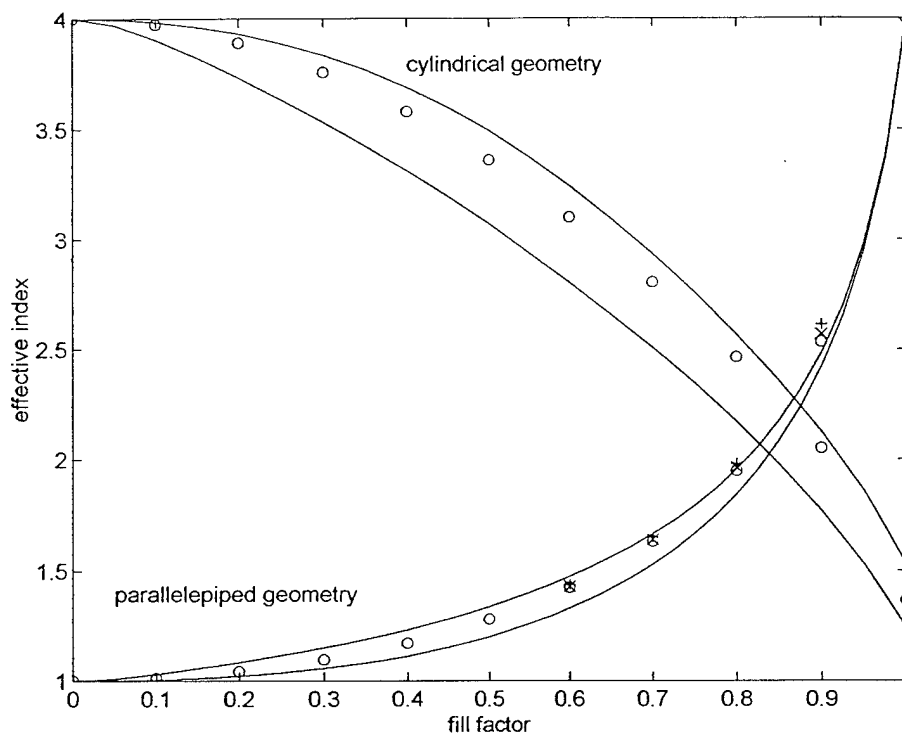b) periodic structure composed of cylinders of low index inserted in a medium of high index

Fig.2 Zeroth-order effective index. The solid curves are the upper and lower bounds derived in Ref. 7 for the zeroth-order effective index and for the periodic structures of Fig. 1. Plus-marks, cross-marks and circle-marks are respectively the effective indices of Eq. 5a for truncation ranks M equal to 8, 20 and 40.
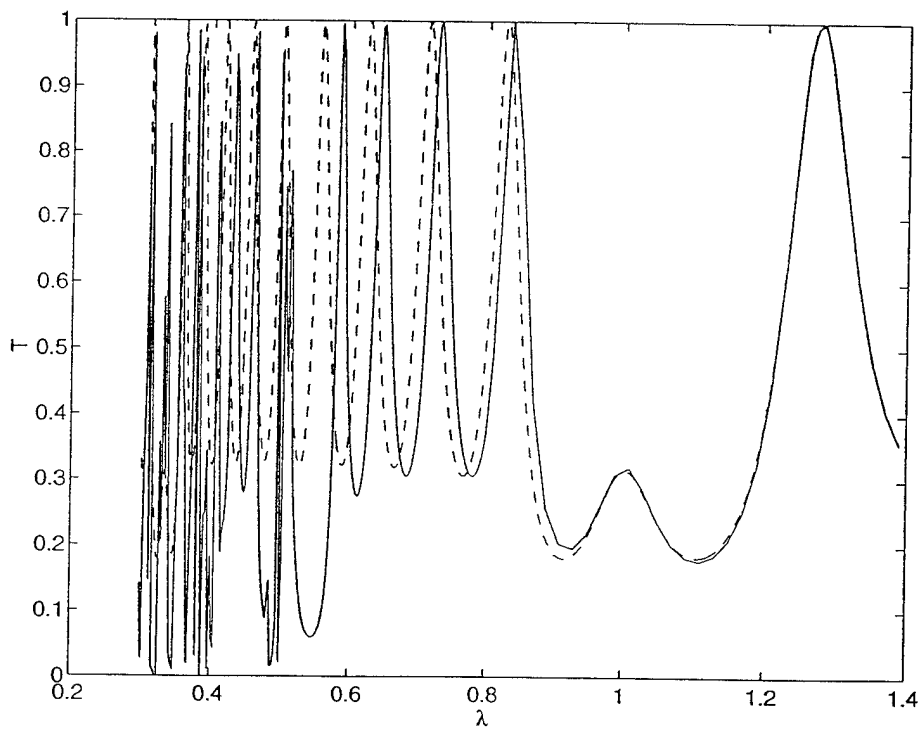

Fig.3 Comparison between the EMT prediction of Eq.5 and rigourous computations.

Z-Scan Measurement in Amorphous As$_2$S$_3$ Thin Film

Yeung Joon Sohn, Chong Hoon Kwak, Ok Shik Choe

Department of Physics, Yeungnam University,

Kyongsan, 712-749, Korea

(Fax:+82-53-813-4465, e-mail:chkwa@ynucc.yeungnam.ac.kr)

1. Introduction

Z-scan technique is very useful method for measuring the magnitude and the sign of the nonlinear refractive index due to its simple geometry and high sensitivity compared with nonlinear interferometry, degenerate four-wave mixing, nearly degenerate three-wave mixing, ellipse rotation, beam distortion measurement.[1, 2] With this technique the measurements and analysis for several nonlinear optical materials such as CS$_2$, ZnSe, GaAs, CdTe had been succesfully acomplished by using high power pulse laser.[1-3] In this paper, we present a cw pump-probe z-scan method for determining the optical nonlinearity of an amorphous As$_2$S$_3$ thin film. In an amorphous chalcogenide As$_2$S$_3$, thin film the optical nonlinearity originates from the photostructural changes of the material by band gap illumination (bandgap energy of E$_g$ ≃2.5eV corresponding to Ar-ion laser wavelength of 514nm), which results in photodarkening and photoanisotropy. These effects have been extensively investigated as holographic recording medium for optical information processing, polarization hologram and binary phase gratings such as Dammann grating.[4-6]

2. CW Pump-probe Z-Sscan Experiments

Figure 1 shows the experimental geometry for pump-probe Z-scan method. The sample to be measured is placed and scanned along the z direction in the focal region of two focused laser beams: the one is strong pump beam of Ar-ion laser with wavelength of 514.5nm and the other weak probe beam of He-Ne laser with 632.8 nm. Amorphous As$_2$S$_3$ thin film is prepared on slide glass by vacuum evaporation and the thickness is about 4μm. The transmitted intensity through an aperture is detected in the far field region by photodiode and stored in IBM-PC. The sample is mounted on the sample holder and scanned by using a linear moter along the z-direction. We performed three kinds of experiments: (i) pump inducing-probe scanning method, (ii) (probe inducing) probe scanning method, and (iii) (pump inducing) pump scanning method. These experiments are conducted by controlling shutters S$_1$ and S$_2$, as shown in Fig. 1.

3. Experimental Results and Discussions

Figure 2 illustrates the typical experimental results of the z-scan measurements obtained by using (a) pump inducing-probe scanning method, and (b) (probe inducing) probe scanning method, as mentioned above. In obtaining Fig. 2(a), the sample is illuminated with a strong pump beam of $100mW/cm^2$ for a long time (about 10 min.) in order for making the refractive index changes unaltered for further pump beam illumination before Z-scan experiment by probe beam. It is also noted in Fig. 2(b) that although the probe beam intensity is weak compared with pump beam intensity and the wavelenth of the probe beam corresponds to the transparent regions of the material, the intensity near the focal point of the lens is sufficient to induce nonlinear refractive index changes. The sign of the nonlinear refractive index n_2 can be determined from the type of the z scan curve and the magnitude from the valley-peak difference in normalized transmittance. It is found from Fig. 2 that amorphous As_2S_3 thin film is a kind of self-focusing material having a positive Kerr coefficient. We also estimate $\triangle n \simeq 10^{-4}$ for Ar-ion laser intensity of $100mW/cm^2$, which is reasonably agree with that of obtained by holographic method.[4, 6] The curves of two kinds of measurement look like similar to each other except for their relative magnitude of valley to peak value. Figure 3 illustrates the experimental curves for (pump inducing) pump scanning method with various sizes of apertures and depicts the deep well curves. It can be understood from the strong nonlinear absorption of Ar-ion laser wavelength of 514.5nm. Since the absorption coefficient of As_2S_3 for 514.5nm wavelength (about $3x10^3cm^{-1}$) is much larger than that for 632.8 nm (about $3x10^2cm^{-1}$), the absorption significantly influences the z scan curve rather than the nonlinear refraction, and so the absorption curve is predominate over the nonlinear refraction curve.

References

[1] M. Sheik-Bahae, A. A. Said, and E. W. Van Stryland, Opt. Lett. **14**, 955 (1989).

[2] M. Sheik-Bahae, A. A. Said, T. Wei, D. J. Hagan, E. W. Van Stryland, IEEE J. Quantum Electron. **26**, 760 (1990).

[3] A. A Said et al., J. Opt. Soc. Am. **B9**, 405 (1992).

[4] C. H. Kwak, J. T. Kim, and S. S. Lee, Opt. Lett. **13**, 437 (1988).

[5] C. H. Kwak, J. T. Kim, and S. S. Lee, Appl. Opt. **28**, 737 (1989).

[6] C. H. Kwak, S. Y. Park, H. M. Kim, and E.-H. Lee, Opt. Comm. **88**, 249 (1992).
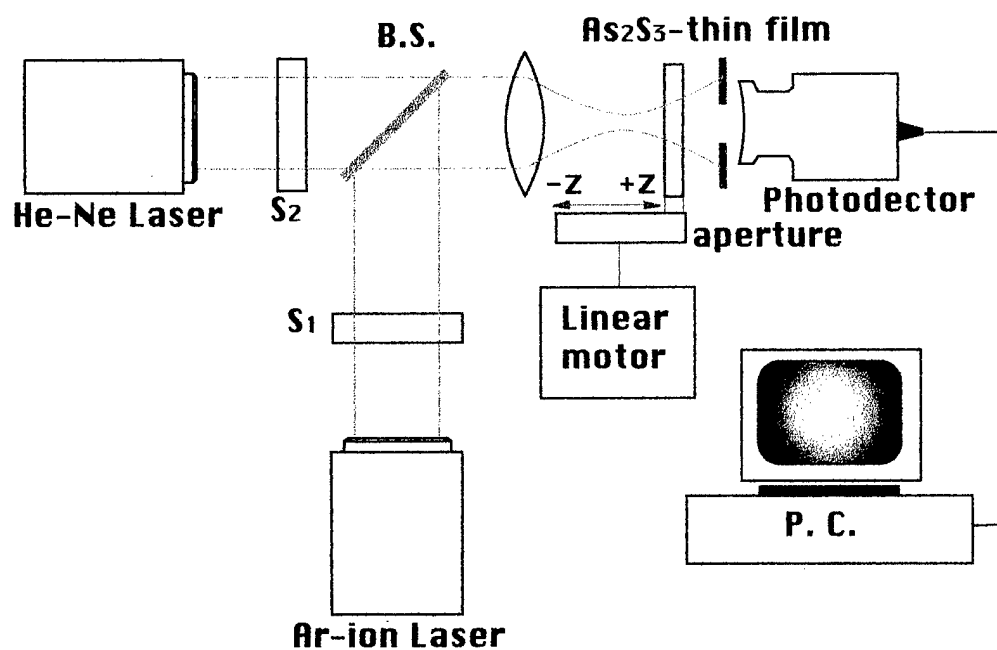
Fig. 1. Experimental geometry for pump-probe z-scan technique.
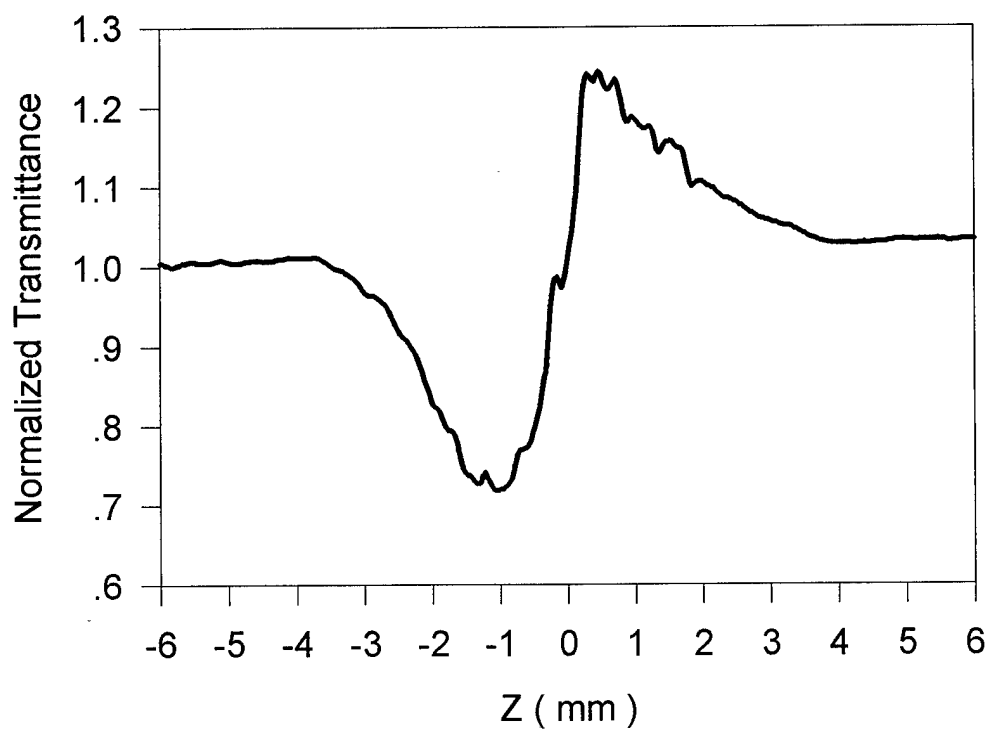
Fig. 2. Experimental z-scan curves for normalized transmittance: (a) pump inducing and probe scanning data and (b) probe beam alone(the next page)

(b) probe beam alone
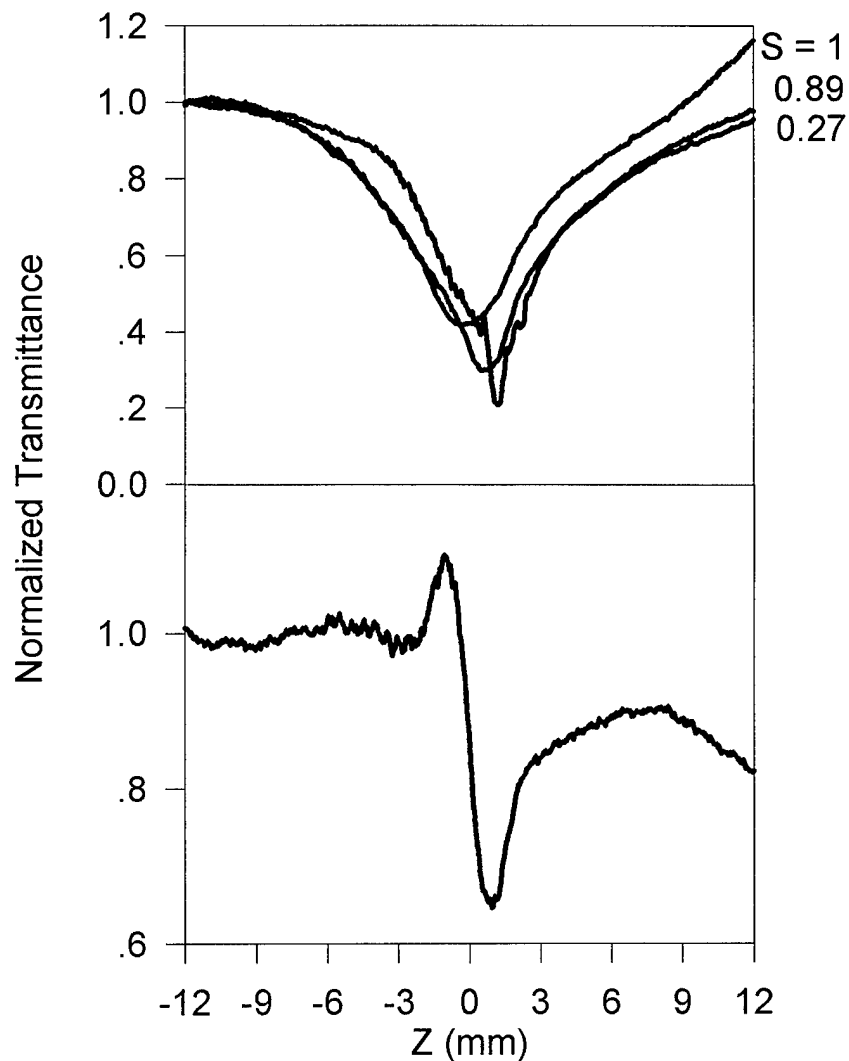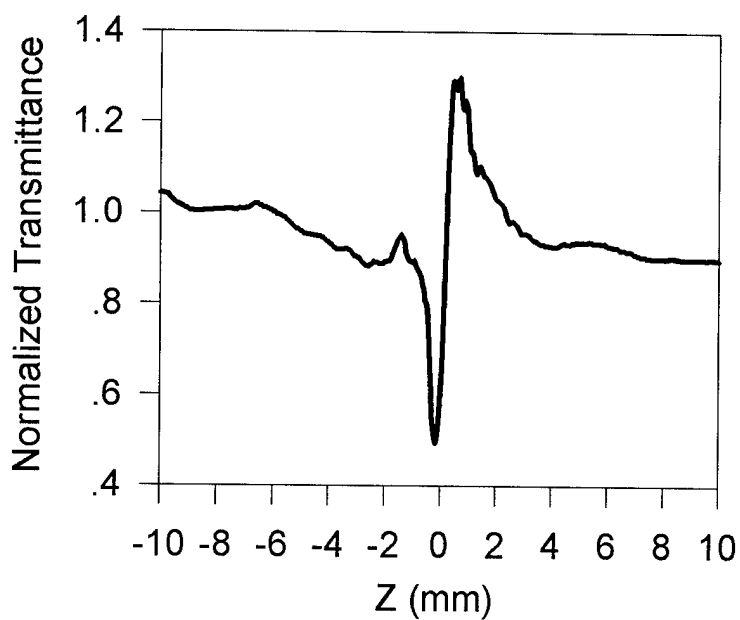
Fig. 3. Experimental z-scan curves obtained from pump beam alone.: (a) Normalized transmittance against sample position for various aperture transmittance S, (b) Aperture transmittance(S=0.4) divided by open aperture transmittance(S=1).

Simplified Processing Method of Dichromated Gelatin Derived from Agfa 8E75HD Plates

Yong Seok Im, Young Lak Lee, Chong Hoon Kwak and Ok Shik Choe
Department of Physics, Yeungnam University,
Kyongsan, 712-749, Korea.
(Fax: +82-53-813-4465, e-mail: chkwak @ynucc.yeungnam.ac.kr)

Sang Cheol Kim
Samsung Aerospace Industries, LTD.
P.O. Box111, Suwon, 440-600, Korea

Introduction

Dichromated gelatin (DCG) is one of the best recording materials for phase volume holograms. Since DCG has large refractive-index modulation, high resolution, high diffraction efficiency (DE), and good signal-to-noise ratio, it is suitable for preparing holographic optical elements. Several papers on the hologram formation mechanism in DCG have been reported in the literature.[1-5] The simplest way to obtain a good hologram is by use of photographic plates, dissolving the silver halide in a fixing bath, and sensitizing it with a solution of ammonium dichromate. Upto now, most of the works has been done using the gelatin layer of Kodak 649F plates. Oliva et al.,[8] presented the holographic characteristics of the DCG plates obtained from Agfa 8E75HD plates. The processing procedures for preparing high-quality DCG holographic optical elements (HOEs) developed by Oliva, however, are tedious, since it takes at least 12 hours to process one HOEs. In this work, we present very simple method for making highly efficient DCG hologram starting with Agfa 8E75HD plates. Beginning with Agfa 8E75HD plates, the complete processing time including preprocessing, sensitization, and development is just 2 hours. In addition, DCG hologram has a high DE of 81.5%.

Basic Principle

Assuming the refractive-index modulation of gelatin film is due to a hardness differential,[3-7] the DE of the DCG hologram would be dependent on the initial degree of hardening of the gelatin layer. If the initial hardening is too high, the refractive-index modulation capability will be reduced. Whereas if it is too low, the gelatin will be partially dissolved in the development bath and noisy holograms of low DE will be formed. The degree of hardness of the gelatin layer can be measured by swelling factor and is expressed as a percentage increase in weight, $k_p=(W-W_o)/W_o(\%)$, where W_o is the weight of the dry film and W is that of the swelled film. During development, the initial refractive index modulation in water, $\triangle n_w$, depends on the hardness differential $\triangle h$ between the exposed and unexposed regions and the two swelling factors $\triangle k_p$ and $\triangle k_w$, i.e.,

$$\triangle n_w = k_p k_w \triangle h \qquad (1)$$

where k_w is the swelling factor during the water development. The initial refractive index modulation $\triangle n_w$ is further amplified by the final alcohol development. The final refractive index modulation $\triangle n$ can be expressed by

$$\triangle n = k_f \triangle n_w \qquad (2)$$

where k_f is a constant gain factor or swelling factor. According to the Kogelnik's coupled wave theory, the diffraction efficiency for transmission phase volume holograms is given by

$$DE = \sin^2 \left(\frac{\pi \triangle nd}{\lambda \cos \theta_0} \right) \qquad (3)$$

where λ is the reconstruction wavelength in air, θ_0 is the Bragg angle, and d is the hologram thickness.

Experimental Results and Discussion

To study the effects of various parameters and holographic exposure characteristics on the high drying method of the sensitized DCG plate, transmission holographic gratings with spatial frequency of about 1500 lines/mm have been recorded by using Ar-ion laser with a wavelength of 457nm. The irradiance of each beam was taken to be equal, and the angle between the two beams was 40°. The Agfa 8E75HD plates whose gelatin thickness is about 7μm. The physical characteristics investigated include DE, absorption spectrum of the sensitized DCG, Bragg angle deviation, and degree of hardness. All the chemicals are dissolved in tap water (pH 7.63) and the processes are conducted at room temperature. The detailed preparation and development method for DCG plate developed in this work is shown in Table I.

The DE was measured simultaneously during the hologram recording by placing a detector in one of the diffracted beams of the He-Ne laser at 633nm wavelength.(Fig. 1) He-Ne laser beam is not absorbed by the Cr ions in DCG and does not affect the hologram formations. Figure 2 illustrates the typical experimental result for DE against exposure time. The absorbance of the unexposed DCG at 457nm light is the order of 0.28. From the experimental curve, we estimated the maximum refractive index modulation was about $\triangle n$=0.022, and the corresponding phase shift is $\triangle \psi_{max}$=1.126. We also measured the reconstruction angle response as shown in Fig. 3. It is noted that after the development processing the maximum reconstruction angle corresponding to maxmium DE is shifted about 1.4 degree from Bragg angle at the initial recording. Figure 3(a) shows the reconstruction angle of the maxmium DE as a function of exposure and Fig. 3(b) shows angular response of the grating (1500 lines/mm) in the gelatin layer.

Figure 4 represent the DE curves according to various processing conditions. The final hologram thickness mainly depends upon two step preprocessing parameters.

The curve C represents the DE of the gratings formed by Georgekutty and Liu's method.[6] The maximum DE is obtained about 28%. There are swelling proportion of 3.8 times as compared with curve D method. The curve D presents the DE of the gratings formed by Table-I, which is obtained from the process without hot water (step 5) and using hardener fixer instead of non-hardener fixer (step 1). The maximum DE were

obtained about 8.6%. This result indicates that the gelatin of Agfa 8E75HD plates is extremely hard. The curve B presents the DE by method of Table I without hot water (step 5) and using non-hardener fixer (step 1). The maximum DE is about 38%. The relative swelling value increases to the proportion of 5.4 times as compared with curve D method. The curve A presents the DE by method of Table- I . The maximum DE is about 80%. The relative swelling value increases to the proportion of 9.2 times as compared with curve D method. The crucial step in producing the efficient strong phase hologram recording is immersion in non-hardener fixer and hot water (80℃). We think that the process increases the optical path length differences of the plate such a large value that efficient phase holograms can be produced. The gelatin hardness is an important parameter because it almost influences the optical property of DCG holograms. The result implies that DE depends on non-hardener fixer and hot water (step 5) in processing method. Finally, our simplified method also includes the baking the sensitized DCG plate in the oven (85±5℃) for 10 min. This is not necessary to have overnight drying of the gelatin plate in stringent temperature and relative humidity conditions proposed by Oliva's method. In conclusion, a simple method preparing high efficient DCG plates from Agfa 8E75HD plates, is presented, and it is easy to obtain DCG HOE's of high diffraction efficiency over 80%. Furthermore, one can see that the whole process only requires 2 hours, and the present process is relatively less sensitive to relative humidity when compared to Oliva's process.

Table I . Simplified Fabrication Procedures of DCG film with Agfa 8E75HD Plates

(1) Soak in non-hardener fixer for 15 min.
(2) Wash in running water for 15 min.
(3) Soak in methyl alcohol for 10 min.
(4) Soak in clean methyl alcohol for 10 min.
(5) Soak in hot water (80℃) for 10 min.
(6) Soak in 5% ammonium dichromate solution (with 1% of Kodak photo-flo 200) for 15 min.
(7) Bake for 10 min at 90±5℃.
(8) Exposure (Ar+ laser, λ =457nm)
(9) Soak in 0.5% ammonium dichromate solution for 5 min.
(10) Wash in running water for 10 min.
(11) Dehydrate in 50% isopropyl alcohol for 5 min.
(12) Dehydrate in 100% isopropyl alcohol for 5 min.
(13) Dry over 10 min with flowing hot air at 85±5℃.

REFERENCES

[1] T. A. Shankoff, Appl. Opt. 7, 2101 (1968).
[2] R. K. Curran and T. A. Shankoff, Appl. Opt. 9, 1651 (1970).
[3] D. Meyerhofer, Appl. Opt. 10, 416 (1971).
[4] D. Meyerhofer, RCA Rev. 33, 110 (1972).
[5] B. J. Chang and C. D. Leonard, Appl. Opt. 18, 2407 (1979).
[6] T. G. Georgekutty and H-K. Liu, Appl. Opt. 26, 372 (1987).
[7] T. Keinonen and O. Salminen, Appl. Opt. 27, 2573 (1988).
[8] J. Oliva, P. G. Boj and M. Pardo, Appl. Opt. 23, 196 (1984).
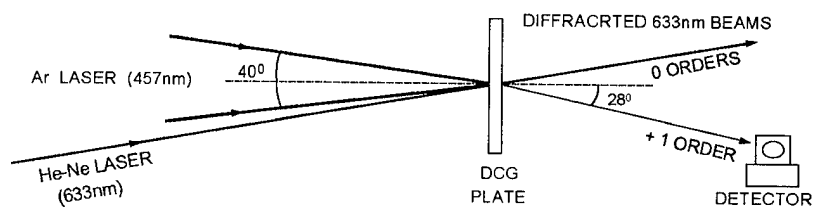
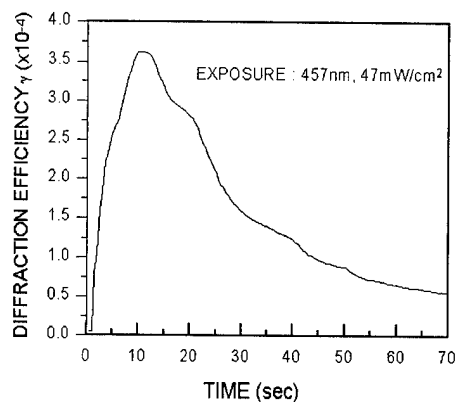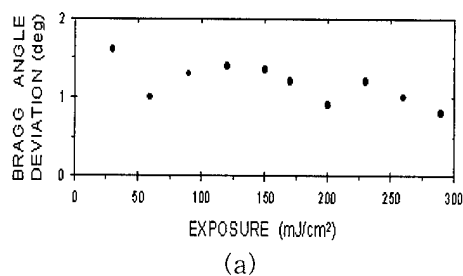Fig. 1. Experimental arrangement for measuring the phase change due to exposure alone.

(a)

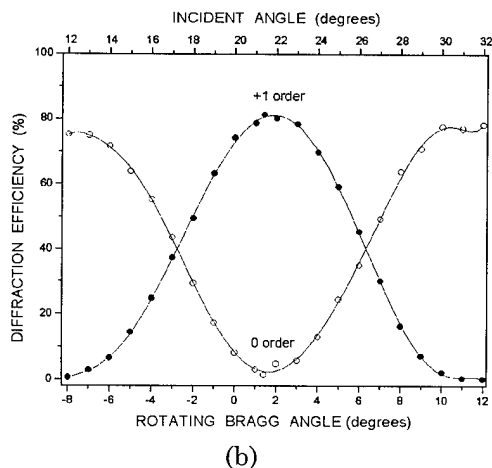Fig. 2. Diffraction efficiency against time

(b)

Fig. 3. (a) Reconstruction angle for obtaining maximum diffraction efficiency, and
(b) Angular response of the diffraction efficiency against Bragg angle deviation.
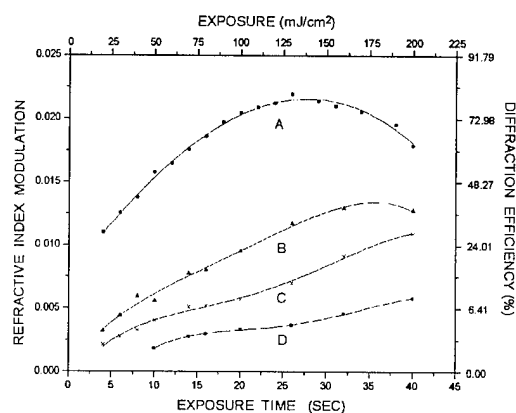

Fig. 4. Effect of the initial degree of hardening on the diffraction efficiency (measured at 457nm).

Analysis of Focal Tolerance and Fine Pattern Resolutions Formed by Phase Conjugation in Dichromated Gelatin Hologram

Yong Seok Im, Young Lak Lee, Chong Hoon Kwak and Ok Shik Choe
Department of Physics, Yeungnam University,
Kyongsan, 712-749, Korea
(Fax: +82-53-813-4465, e-mail: chkwak @ynucc.yeungnam.ac.kr)

Introduction

Submicrometer photolithography necessitates high resolution imaging system. Optical holography is one of the promising candidates for realizing such high resolution imaging systems. Several optical system utilizing holograms have been demonstrated until now including far-field holograms, image holograms, and focused image holograms. In order to achieve the required high resolution, there is to decreasing the wavelength or to increasing the numerical aperture. Two fundamental parameters limiting an optical system are the numerical aperture, NA, and the size of the image field of the imaging optics.[1] For a given wavelength, the resolution is improved by increasing the numerical aperture. As a result, the increasing NA lead to decreasing the focal tolerance. In this paper we present the high resolution holographic imaging system using a focused imaging hologram with phase conjugate wave and demonstrated a long focal tolerance of an image.

Holographic Principles

Figure 1 illustrates the focused holographic construction and reconstruction processing. The minimum construction beam angle, θ_{min}, required to insure that the re-constructed image can be observed without any interference from its twin image as well as from the surrounding halo of scattered light is given by[2]

$$\theta_{min} = \sin^{-1}(3NA_{hologram}) \qquad (1)$$

The use of a lens to focus the image onto the holographic recording material permits a larger numerical aperture. The numerical aperture as seen by the high resolution recording material is defined as

$$NA_{hologram} = \frac{NA_{object}}{M_{mag}} \qquad (2)$$

where $NA_{hologram}$ is the numerical aperture at the hologram plane, NA_{object} is the numerical aperture at the object plane, and M_{mag} is the magnification of the

object at the hologram plane. The spatial frequency is frequently used to refer to either the angular direction of propagation of a plane-wave component of a complex wavefront or to the spatial rate of change of the holographically recorded interference pattern. When it used to define the direction of propagation of a plane wave component, the spatial frequency refers to the spatial rate of change of the phase of the wavefront across a suitably chosen the axis of an optical system. The spatial frequency is related to the angle of the wavefront (θ) by[3]

$$\nu_w = \frac{\sin \theta}{\lambda} \tag{3}$$

When this wavefront is allowed to interfere with a reference wavefront, whose angle of arrival is ψ, the resulting interference pattern has a spatial frequency give by

$$\nu_r = \frac{\sin \theta - \sin \psi}{\lambda} \tag{4}$$

When the reference wave propagates along the normal to the observation plane

$$\nu_w = \nu_r \tag{5}$$

The intensity distribution near focus is of particular importance in estimating the tolerance in the setting of the receiving plane in an image-forming system. The properties of the out-of-focus monochromatic images of a point source by a circular aperture were first discussed in Ref. [4]. It follows that focal tolerance $\triangle z$ is approximately given by[4]

$$\triangle z = \pm 3.2 \frac{\lambda}{2\pi} \left(\frac{f}{a}\right)^2 \tag{6}$$

where f is the distance of the focal plane from the hologram mask of aperture, a is the radius of the hologram mask of aperture. Since the numerical aperture of the hologram is given by $NA_{hologram} = a/fq$, for the case of $f \gg a$, $q \approx 1$ (equivalently $f \cong fq$). Hence, the ratio a/f can be defined as the numerical aperture of hologram. We have the expression for the focal torelence of the hologram of the form:

$$\triangle z \approx \pm 3.2 \frac{\lambda}{2\pi} \left(\frac{1}{NA_{hologram}}\right)^2 \approx \pm \frac{4.58}{\lambda \nu^2} \tag{7}$$

Experimental Results and Discussion

The holographic imaging system for both constructing a hologram of the mask and reconstructing the image of the mask is shown in Fig. 1. The theoretical resolution of the fully coherent imaging system is $\lambda/2NA=0.57\mu m$ (λ=457nm, NA=0.4). Figure 2 shows the theoretical maximum resolution of the imaging system. The numerical aperture $NA_{hologram}$ of the hologram is plotted as a function of line width. TEM_{00} mode of Ar-ion laser at 457nm wavelength is used as a

light source. A light beam is splitted into two beams by using a variable beam splitter. Both illuminating beams are first focused to a diffraction limited spot with a microscope objective, and then collimated with a lens corrected for infinite image to object ratio. To form a focused hologram, the beam is focused by a condenser lens to trans-illuminate the mask by imaging the source into the entrance pupil of the imaging lens. The hologram mask is formed at this plane using the dichromated gelatin (DCG) as the high resolution recording material.[5-6] The preparation and the development of DCG derived from Agfa 8E75HD plates. The DCG is exposed simultaneously to both the focused image and the second collimated beam, as shown in Fig. 1(a). The focused image holograms were constructed using the IC pattern mask or the USAF-1951 resolution target mask. In order to test the focal tolerance of an image formed by the holographic phase conjugation, the recorded images are reconstructed at the focal point and then the hologram mask is scanned along the optic axis by using the linear motor (Encoder Mike: $0.05 \mu m$/sec) along optical axis. Theoretical focal tolerance of $1 \mu m$ and $2.2 \mu m$ line width of the hologram mask were $\pm 40.12 \mu m$ and $\pm 192.94 \mu m$, respectively. The corresponding focal tolerance observed are about $\pm 37 \mu m$ and $\pm 180 \mu m$, respectively. Figure 3(a) shows a photo-micrograph of the reconstructed image ($1 \mu m$ line width of the IC pattern mask) in the forward moved position of $37 \mu m$, and Fig. 3(b) is a photo-micrograph of the reconstructed image ($2.2 \mu m$ line width of the USAF-1951 resolution target mask) in the forward moved position of $180 \mu m$.

References

1. Victor Pol, James H, Bennewitz, Gary C. Escher, Martin Feldman, Victor A. Firtion, Tanya E. Jewell, Bruce E. Wilcomb, and James T. Clemens, "Excimer laser-based lithography: a deep ultraviolet wafer stepper", Optical/Laser Microlithography V, **633**, 6-16, SPIE, (1986).

2. G. Addiego and W.G. Oldham, "High-Resolution Imaging Using Focused-Image Holography with Wave-Front Conjugation", Optical/Laser Microlithography, **922**, 18-25, SPIE, March2-4, (1988).

3. Marvin J. Weber, "*Handbook of Laser Science and Technology*", Vol **V**, CRC Press, Florida, (1988).

4. Max Born and Emil Wolf, "*Principles of Optics*", Pergamon Press, Oxford, 1983.

5. J. Oliva, p. G. Boj, and M. Pardo, "Dichromated gelatin holograms derived from Agfa 8E75HD plates", Applied Optics, **23**, 196, (1984).

6. B. J. Chang and C. D. Leonard, "Dichromated gelatin for the fabrication of holographic optical elements", Applied Optics, **18**, 2407, (1979).
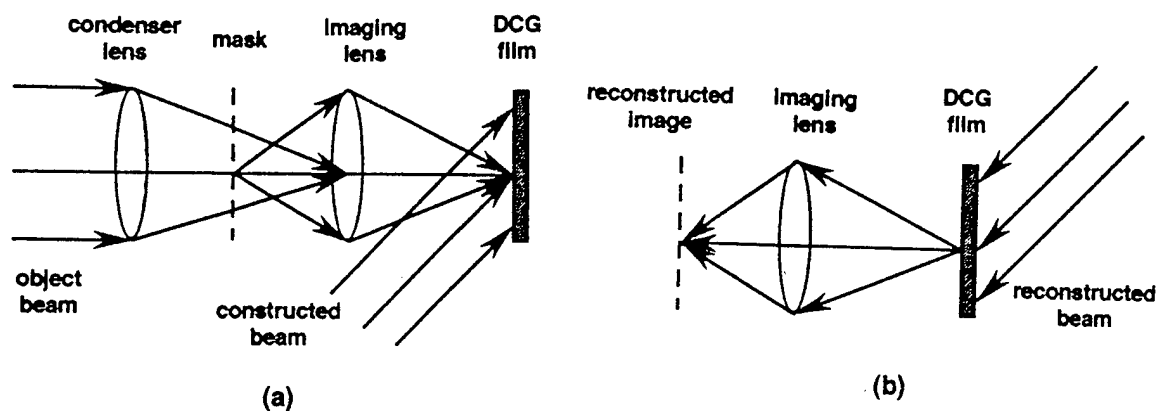
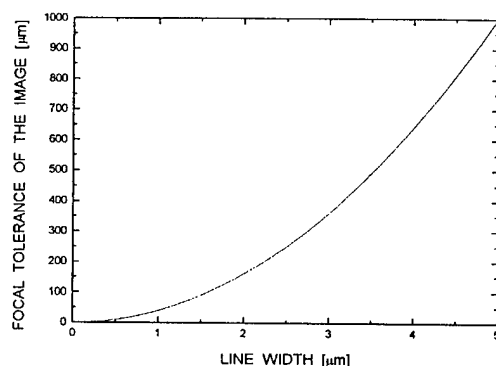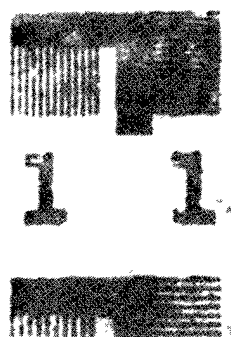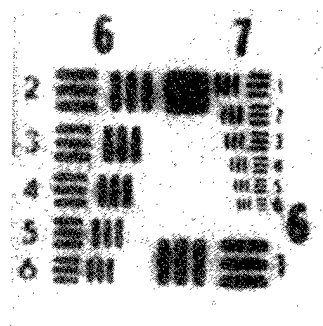Figure 1. Schematic of the construction and reconstruction process for focused image holography.

Figure 2. Theoretical focal tolerance $\triangle z$ of the imaging system versus the line width of the hologram mask.

(a) Imaging of 1μm line width position of 37μm in the forward

(b) Imaging of 2.2μm line width position of 180μm in the backward.

Figure 3. Photo-micrograph of the reconstructed aerial image of the hologram mask.

Wavelength agile fluorescence microscopy filter using photorefractive barium titanate.

Robert Kersten and Salvador Fernandez
Ciencia Inc.
111 Roberts St, Suite C
East Hartford, CT 06108.

George Fischer and Robert Boyd
Institute of Optics
University of Rochester
Rochester, NY 14627.

We describe a wavelength-agile holographic notch filter (WAHNF) suitable for attenuating scattered laser light from the fluorescence signal in laser induced fluorescence (LIF) applications. The WAHNF utilizes a photorefractive material, specifically $BaTiO_3$, and the technique of two beam coupling to attenuate the coherent portion of the signal to be detected[1]. Static holograms recorded in film emulsions are routinely used for this purpose but have the limitation that they are fixed notch-band devices. In contrast, the WAHNF enables tuning or switching the excitation wavelength while passively adapting to maintain the notch band centered on the laser wavelength.

Two-beam coupling, with its ability to transfer energy from one beam to another, is the method chosen to accomplish the filtering[2]. A 5mm x 5mm x 5mm $BaTiO_3$ crystal with a 90 degree C axis geometry is used and oriented so that the energy from the object beam is transferred to the transmitted reference beam. In LIF applications, the signal is comprised of the very narrow band portion from the excitation laser light and the broad band fluorescence emission which is Stokes-shifted away from the excitation light .

The experimental configuration shown in Figure 1 was initially used without the LED to demonstrate the WAHNF's wavelength-agility. First, two-beam coupling was achieved at 514nm and the extinction coefficient measured; then the wavelength from the argon ion laser was changed to 488nm and the extinction coefficient was measured again. The photorefractive holographic filter was shown to maintain good energy transfer at both wavelengths without any adjustments to the experimental configuration.

Figure 1
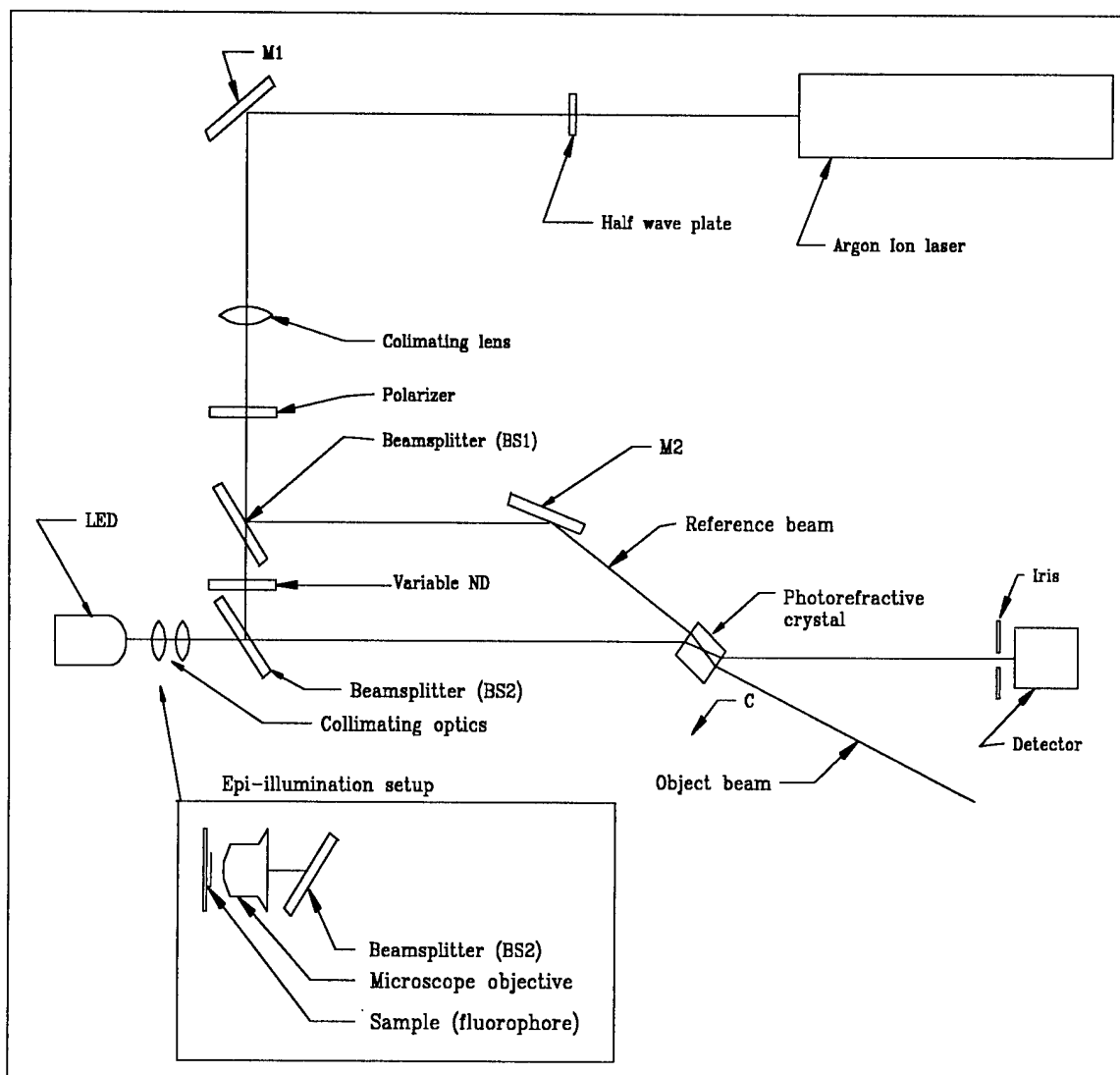
For the next step, a broad band 650 nm LED light source was made colinear with the object beam by inserting a dielectric beamsplitter in the position of BS 2. The 650nm wavelength was chosen because it was the highest power visible LED available. This setup demonstrates the WAHNF's capability to attenuate the coherent laser light while passing the broad band LED incoherent light which

simulates the fluorescence emission that would be obtained in a LIF application. The final step was to replace the LED setup with an epi-illumination fluorescence microscopy arrangement as shown in the box in figure 1. The object beam is reflected off BS 2 into a microscope objective and onto a small cuvette which holds the fluorophore. At the detector, the laser excitation light is attenuated by approximately two orders of magnitude while the Stokes-shifted fluorescence is unaffected. Rhodamine was used as a fluorophore since it exhibits significant excitation at both 488nm and 514nm, allowing us to demonstrate wavelength-agility with this configuration.

Our results demonstrates the ability to use a wavelength-agile photorefractive holographic filter in a biological application to achieve greater spectral flexibility. This is important in many LIF applications where multiparameter or ratiometric measurements at more than one excitation wavelength are required.

References.

1. Theo Tschudi, Andreas Herden, Joachim Goltz, Harald Klumb, Franco Laert and Johan Albers, IEEE J. Quantum Electron., QE-22, Aug 1986, p. 1493-1502.
2. S.W. McCahon and M.B. Klein, SPIE 1105, 1989, p.119-122.

Holographic Interferometry Methods for Conducting
Stress Analysis on Quartz Crystal Components

Jill A. Brosig
Senior Development Engineer
Motorola, Quartz Products Division
1301 E. Algonquin Rd.
Schaumburg, IL, 60196
Phone 708-576-5673
Fax 708-576-1689

The technique of holographic interferometry has aided in Motorola's Quartz Products Division's continuous pursuit of higher quality quartz crystal components. QPD's portfolio consists of several models of quartz crystals, which are sold as resonators, oscillators, and filters. The crystal frequency for the various products ranges from 12 MHz to 100 MHz.

Products discussed in this paper include AT-cut quartz resonators and quartz filters. Both leaded and surface mount packages were studied. Surface mount parts are attached directly to the radio board whereas the lead formed pieces are hand soldered on.

An oscillator is any device that resonates at a selected frequency or range of frequencies. In simple terms, a tuning fork is an oscillator. In the electronics industry, however, an oscillator is a device that uses the principles of the piezoelectric effect to produce a predetermined output frequency. The basic construction consists of a resonator, in this case a quartz crystal, a power source, and required circuitry. The quartz crystal resonator is equivalent to an inductor connected in series with a capacitor and a resistor.

A crystal filter is a device which allows the receiver circuitry to efficiently select and process the chosen frequency. This is necessary since the overflow of wireless communications has limited the number of radio channels. As the radio channel spacing becomes tighter, the need for higher performing filters increases.

The production of an AT quartz crystal component begins with the cutting of 2" x 2" wafers from a bar of manmade or cultured quartz. The angle at which the quartz bar is cut determines the end product's frequency stability over temperature, and the thickness of the cut wafer determines the frequency. After the cutting process, a series of metals are then deposited on the wafers, followed by a photolithographic process which produces 140 crystals per wafer. The finished crystals are then mounted in appropriate housings.

When an AT cut crystal approaches the infinite plate approximation and is in a stress free environment, the generalized frequency-temperature relationship follow what is known as Bechmann curves. Within this scenario, the inflection temperature is 26 C. Depending on how stress affects the crystal lattice, the inflection temperature can range from as low as 22 C to well above 30 C. By lowering the inflection temperature, the frequency stability of the crystal becomes more controlled. As the industry moves to smaller and smaller telecommunication devices, these types of components become highly desirable as they can replace their larger counterpart, the oscillator.

One theory as to how the inflection temperature can be lower than that at the stress free condition is through the presence of a beneficial stress, either tensile or compression. The beneficial stress hypothesis can be accepted or nullified by using holographic interferometry to relate stress patterns to yields.

Understanding the mechanics of the leaded and surface package will aid in optimizing both product lines. Through the use of holographic interferometry, studies were conducted which determined the stress patterns of the quartz crystal over several environmental perturbations, including temperature, vibration, and drive level. The temperature studies will be discussed here.

The first objects used in the first holographic interferometry experiments consisted of crystal resonators. These crystals were 300 mil in diameter, set at 19.1 MHz, had an unpolished surface, and were mounted in leaded packages. These units were built on two different designs, either a clamp or slot post, and using two types of adhesives, referred to as A and B. At 25 C the slotted mount exerted a tensile stress on the blank, while the clamp design held the quartz under compression. Those products, which recorded inflection temperatures between 22 and 24 C, used a slotted mount design.

The experimental parts were manufactured identical to those run through production, except they were not sealed or plated. The sealing process prevents the blank from being seen and the gold plating interferes with hologram developing by reflecting the laser beam rather than diffusing the light.

These pieces were tested for both in-plane and out-of-plane displacements over the temperature ranges 25 C to 70 C, 35 C to 70 C, and 45 C to 70 C. All the various build cells of this experiment were studied simultaneously, in order to eliminate time and temperature as factors between successive runs. Unfortunately, the equipment used in the crystal design experiment was not capable of performing sandwich holography. Instead, real time holography was used with reference holograms taken at 25 C, 35 C, and 45 C.

The holography setup used was a workstation, manufactured by the Newport Corporation. The light source was a HeNe laser, with a wavelength of 632.8 nm. The system consisted of a free standing enclosed unit and a control console, which creates a hologram within one to two minutes.

These crystal resonators were cycled through temperature vial a hot plate, which was controlled by a Thermo/cense temperature controller. The temperature controller used an RTD capable of accurately reading temperature to +/- 0.2 C. The temperature controller resided outside the optics table for easy access and viewing during the holographic studies.

The holocamera consisted of the camera module and the electronics module. The former holds the thermoplastic plate, on which the hologram is recorded, and the components needed for the recording process. The later module contains the operating panel, control logic and power supplies. The electronics have the capability of activating a variety of holocamera functions.

Throughout the holographic experiments they are viewed via both a video monitor and computer monitor. The resulting fringe patterns are stored on video taper for future viewing and image analysis. The software used for image analysis is manufactured by Automatix, Inc. of Billerica, MA. In conjunction with McRail software, strain is calculated in the x-y direction. This software is limited by only being able to measure strain in two dimensions, however due to the geometric nature of the quartz blank this is sufficient.

The interference patterns obtained from these experiments were examined for fringe number, movement, and location. Experiments were then replicated for repeatability. These additional experiments eliminated part location and orientation as a factory.

The fringe patterns for the out-of-plane displacement studies showed the greatest movement occurred with the clamp mount and adhesive B. For example, when examining those runs where the reference hologram was taken at 25 C, the fringe rotation of this design was 360 degrees. The designs of the adhesive A and the clamp mount and adhesive B and the slot mount showed comparable fringe movement, both near 180 degrees. Adhesive A and the slot mount showed the least movement with under a 90 degree fringe rotation. Initial in-plane displacement measurements did not detect localized strains.

In addition to those crystal packages built for holography, similar production pieces were plated and sealed. These units were then placed in an environmental chamber and run through a temperature cycle (-30 C to 70 C), which measured frequency and resistance at eight temperature points. Corresponding inflection temperature values were derived from this data.

In general, the higher the inflection temperature, the greater the displacement over temperature. It is interesting to note that regardless of the mount design, and inflection temperature near 27.75 C is recorded when the adhesive B is in contact with the quartz. In fact, this is true across product lines. This indicates that adhesive B decouples any stress associated with the mounting package, and only introduces a localized stress between itself and the quartz blank.

Note that at 25 C the slot mount holds the quartz blank in a tensile state, while the clamp mount holds the piece in compression. When adhesive A is used, the quartz blank can be thought of as coupling directly to the mount. The clamp mount has a wider range since holographic results indicated that it undergoes up to twice as much movement as the slot design. In fact, it may surpass the tensile value of the slot mount on the cold temperature end.

Therefore, this experiment used holographic interferometry to aid in optimizing the crystal package by relating stresses exerted on the blanks due to mount design. The observed fringe patterns showed object displacement as a function of time and temperature. Results were that the rigid clamp mount undergoes greater change of displacement than the more forgiving slot mount. A direct relationship was made between quartz displacement and the inflection temperature. The quartz blanks, which were mounted with adhesive B, showed more movement that those on the same design mounted with adhesive A. Results indicated that adhesive A coupled the blank to the mount, similar to a C-clamp, while adhesive B acted like a spring between the two interfaces. Therefore, based on this experiment, QPD was able to optimize the frequency stability of their round blank crystal resonator products by going to a slot mount design and using adhesive A.

Similar experiments are also being conducted on crystal filters. As with the crystal resonators, these parts are being cycled through temperature, however in this case the initial cure phase is also being studied. It appears that the curing process, in conjunction with the makeup and placement of the adhesive, is producing a localized stress upon the quartz blank. The introduction of this stress is resulting in broken blanks as a function of normal usage. Various types and placements of adhesives are being studied via holographic interferometry in order to correct this issue.

A Computational Model for Holographic Sensing

Ben Bakker
University of Massachusetts at Lowell
Val Bykovski
VirTek, Inc. and University of Massachusetts at Lowell

1. *Introduction.* An existing analytical concept based on spectral decomposition has been developed more than hundred years ago, and is presently close to its limits in terms of performance and reliability, in particular, for complex samples. For molecules, a spectrum is a very complex pattern of sharp lines and continuous bands. So, in a classical spectrometer, detection is pruned to *overlapping* errors when two or more components of a sample have overlapping lines, and their separation is, generally, *a non-unique* problem. Indeed, a line can be assigned to, at least, two different transitions (in the same or different atom/molecules in a sample). Such an assignment based on line positions and transitions has limitations, and may not work at all for complex samples. As samples are getting more and more complex, the problem becomes increasingly intractable. In particular, algorithms and data processing to analyze complex spectra become very complex, require sophisticated peak analysis, etc. A mathematical "inversion" procedure for assignment and identification of components (species) also becomes unstable. That is, the current situation has all signs of a *critical bottleneck*, and requires an innovative approach. Meanwhile, *selectivity* is the first priority for many industries and applications. For instance, in the field of air toxics detection, the US EPA requires 189 components to be detected and regulated, and it is highly doubtful that any existing spectrometer is able to analyze reliably such a complex gaseous medium.

2. *An approach* [4]. The proposed approach *revises* the existing analytical paradigm and is aimed to create a foundation for a new class of high performance *knowledge-based* sensors. We replace a "dumb" prism or diffraction grating (DG) by a recordable optical holographic storage which makes the sensor a programmable *knowledge-based* device that is able to store light patterns for various species. Light from a sample interacts with the *reference* light patterns recorded holographically in the sensor memory and reconstructs *an output species mapping*, for example, a position-sensitive mapping of the species in the sample. It may be detected, say, by a CCD array and then used for any process control application. In other words, the holographic sensor is a *knowledge-based* one, and can be species- or application-specific. It makes analysis easier as the primary measurement immediately generates the final result, a sample composition, without any need for sophisticated data analysis and processing such as peak identification.

Holographic recording of a spectrum was first demonstrated by Stroke and Funkhouser [1]. They used a holographic method of Fourier-transform (FT) spectroscopy which permits one "to obtain the spectrum without any computation, and indeed in an interferometric system having completely stationary elements and medium". The interference fringe system was proportional to a non-coherent superposition of the monochromatic fringe systems for each wavelength λ. Experimentally, a light of a cold mercury arc has been recorded holographically on a photoplate and then successfully reconstructed with the 632 nm HeNe laser. A symmetrical spectrum has been obtained

with all characteristic mercury line systems. Holographic FT spectroscopy allows one "recording" spectra on a lensless, slitless and completely static interferometric assembly of two mirrors, simply pointed in the general direction of a diffuse source. Another way to record interferometrically mercury spectrum has been demonstrated in [2].

The proposed method combines two normally separated functions: (1) identification (recognition) of a light pattern (not necessarily a spectral one) from a sample and (2) its decomposition or mapping in the "space of species" rather than in the spectral, wavelength space. Another advantage of the proposed detection concept is that the holographic sensor is highly selective (it is a volume Bragg selective grating), whereas the conventional dispersing element, a periodical diffraction grating is, in fact, an extreme case of *nonselectiveness*. In the proposed method, a multi-wavelength light pattern rather than a single spectral line of a species is used for detection and mapping. This is why the *overlapping error* is quite unlikely.

The holographic sensor may as well respond to a *combination* of components of a sample which seems to be important for many applications. The optical holographic sensors do not require sophisticated data processing thus opening a way to compact, reliable, *in-situ* sensors/analyzers. Additionally, an *all-optical* sensor is noise-resistant in industrial and combat environments. Power supply may also be not needed as optical output may indicate directly a species detected (say, by its position on a calibrated range).

3. *A model.* We consider a simplified model of computer-generated holographic sensor (CGHS). We use a species spectrum to build CGHS. A software was developed to select the n major peaks from an absorption spectrum. An n-plexed hologram was created using a point source object and plane wave reference beam in each case. Figure 1 shows 256 gray-scale image of an CGHS for acetone (CH_3COCH_3). The computational resolution is 500x500 pixels. Seven peaks were selected and multiplexed. Spectral data was obtained from the EPA/AEDC Spectral Database.
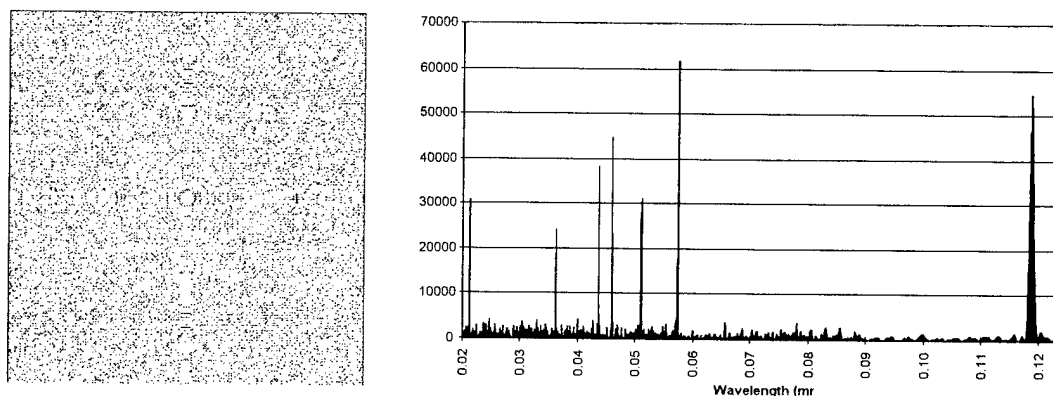
Fig. 1: (a) Computed 256 gray-scale image of multiplexed CGHS for seven spectral peaks from acetone. (b) A spectral response obtained by multiplexing of a scanned spectrum of acetone (7 lines are taken). Each of the seven original acetone peaks is reconstructed, and a high spectral selectivity of the CGHS is obvious.

Both recording and reconstruction were accomplished using a discretized Fresnel integral. The reconstruction using the original acetone spectrum generates a response at the central maximum which is more than 100 times greater than the reconstruction is done with a spectrum of toluene. Further computational experiments revealed a nearly linear dependence on the number of acetone lines present. With five acetone lines present (0.0211, 0.0362, 0.0437, 0.0460, and 0.0576 mm), the intensity of the central maximum was 228,814. With two acetone lines present (0.0437 and 0.0576 mm) the central maximum was 106,155. That is, the proposed detection method is robust to individual spectral lines that may be removed from spectrum without affecting significantly the response. Simply flat "white" background which simulates a thermal one leads to response .016 times acetone response. That, in turn, means that the detection is robust to thermal background.

Further simulation results will be presented including the demonstration of *generalization* capabilities of the holographic sensor which can be designed and built to detect families of chemical components such as "toxic metals", "aromatic cancerogenes", etc.

References:

1. G.W. Stroke, A.T.Funkhouser, "Fourier-Transform Spectroscopy Using Holographic Imaging without Computing and with Stationary Interferometers", *Physics Letts.* **16**, n3, pp.271-74 (1965)
2. K. Yoshihara, A. Kitade, "Holographic Spectra Using a Triangle Path Interferometer", *Japanese J. Appl. Phys.* **6**, 167 (1967)
3. H.J. Caulfield, "Holographic Spectroscopy", *In: Advances in Holography*, v.2, Dekker, N.Y., 1976
4. V. Bykoski, M. A. Fiddy, "A Novel Holographic Analyzer Concept and Apparatus". *Patent Pending*, 1995

Computer-generated hologram for reconstruction of unusual mode image

Gao Wenqi   Tan Suqing   Zhou Jin
(Department of Physics, Nanjing University, Nanjing210093)

Introduction

Usually in reconstruction of Fourier computer-generated hologram[FCGH] the lens is necessary to make imaging at finite distance instead of imaging at infinite originally. The reconstructed images are mutual inverted (one upright image,another inverted image) both appear in a same plane. Whether the imaging lens in reconstruction FCGH will be able to omit? Whether two reconstructed images will be able to separate in spatial? Whether two images have an identical direction and different shape in the same plane? It is the motivation for us to do this study.Through theoretic analysis and experimental reconstruction these assume can be realized essentially.

Principle

In reconstruction configuration of FCGH, as shown in Fig.1 only by virtue of the Fourier lens (F.T.lens) to complete Fourier transform,computer-generated Fourier hologram can reconstruct the image of original object and the conjugate image.The transmission function of Fourier lens in reconstructive geometry is :

$$T = \exp[-jk(x^2 +y^2) / 2f] = \exp[i\,\theta\,(x,y)]^1 \tag{1}$$

where f indicates the focal length of a lens, k is wave number, $k=2\pi/\lambda$, λ is the wave length. Here the constant phase delay associated with the lens has been omitted since it dose not affect the result in any significant way .

Thus it can be seen that the effect of a lens in reconstruction is equal to introduce a qudratic phase factor $\exp[-jk(x^2+y^2) / 2f]$.If U(x,y) expresses optical field behind FCGH, thus the optical field U'(x,y) behind the positive lens is:

$$U'(x,y) = U(x,y)\exp[-jk(x^2 +y^2) / 2f] \tag{2}$$

That shows the quadratic phase factor may be added in frequency spectrum of FCGH directly.
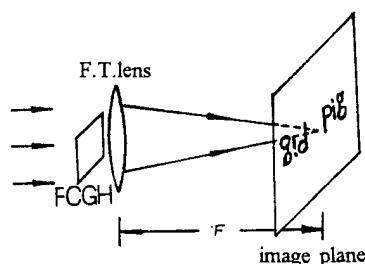
Fig1. The reconstruction configuration
of the usual FCGH
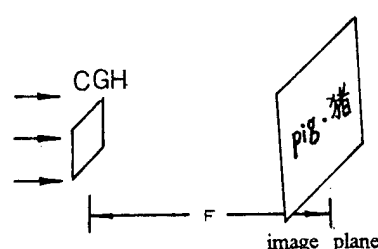
Fig2. The reconstruction configuration
of the unusual CGH

Following,this hologram has been further discussed dividing into three cases. In order to explain physical principle conveniently, the continuous function is adopted in discussion instead of discrete form in practical calculation.

1). Adding directly positive lens factor into frequency spectrum of a object.

Assuming objecte function is f(x,y),object's frequency spectrum function is$\mathscr{F}$f(x,y), when adding the quadratic phase factor the optical filed is:

$$U(f_x,f_y) = \mathscr{F}f(x,y) \cdot \exp[i\,\theta\,(f_x,f_y)] \tag{3}$$

where θ $(f_x, f_y)]$ is the added quadratic phase factor,

θ $(f_x, f_y)] = [-k(f_x^2 + f_y^2) / 2f]$

When CGH has recorded information of $U(f_x, f_y)$, the optical filed +f distance away from this CGH is:

$U_0(x_0, y_0) = [\exp(jkf)] / j \lambda f \cdot \exp[jk(x_0^2 + y_0^2) / 2f] \cdot$

$\iint U(f_x, f_y) \cdot \exp[jk(f_x^2 + f_y^2) / 2f] \cdot \exp[-j2 \pi (x_0 f_x + y_0 f_y) / 2f] df_x df_y$

$= [\exp(jkf)] / j \lambda f \cdot \exp[jk(x_0^2 + y_0^2) / 2f] \cdot \mathcal{F}[\mathcal{F}[f(x,y)]]$　　　　(4)

In formula, except phase factor the $\mathcal{F}[\mathcal{F}[f(x,y)]]$ is Fourier transform of object's frequency spectrum, i.e. $\mathcal{F}[\mathcal{F}[f(x,y)]]$ is the image filed of original object, the phase factor not acts on observing intensity.

Because detour phase encoding method[2-3] is adopted in CGH, the phase of +1 order and -1 order are mutual conjugate in reconstruction.When adding the positive lens phase factors, image of original object can be reconstructed exactly on +1 order. For -1 order, the added positive quadratic phase factor converts sign that is equal to qudratic phase factor of negative lens $\exp[-i\theta]$. For -1 order, the optical filed also became $U^*(f_x, f_y)$, thus, inverted image of original object can be recontructed on -1 order -f distance away from the CGH. Therefore, when unit-amplitude parallel light illumnates this CGH, one reconstructed image appears on +1 order location; For -1 order, which is equivalent to add a negative lens, a light spot is seen in -1 order location　and -1 order reconstructed image is actually in negative focal length -f (here the light spot is defocussed image of -1 order reconstructed image). Thus, the lensless spatial separation of reconstructed images at +1 order and -1 order comes ture. Similarly, adding negative quadratic　phase factors into frequency spectrum of object, conjugate image appear in -1 order location and a light spot appears in +1 order location.

2). Adding positive lens factors into frequency spectrum of object and adding negative lens factors into conjugate frequency spectrum of object.

Assuming object function is $f(x,y)$, the function of object's frequency spectrum is:

$\mathcal{F}[f(x,y)] = A(f_x, f_y) \exp[i \phi (f_x, f_y)]$　　　　(5)

the function of object's conjugate frequency spectrum is:

$\mathcal{F}^*[f(x,y)] = A(f_x, f_y) \exp[-i \phi (f_x, f_y)]$　　　　(6)

let formula (5) add positive lens factor $\exp[i \theta (f_x, f_y)]$ and formula (6) add negative lens factor $\exp[-i \theta (f_x, f_y)]$ respectively then adding:

$A(f_x, f_y) \exp i[\phi (f_x, f_y) + \theta (f_x, f_y)] + A(f_x, f_y) \exp{-i}[\phi (f_x, f_y) + \theta (f_x, f_y)]$

$= 2A(f_x, f_y) \cdot \cos[\phi (f_x, f_y) + \theta (f_x, f_y)]$　　　　(7)

obviously, now only two times real part exist, virtual part vanish.Thus, two identical　direction images appear simultaneously at +1order location and - 1 order location on the same plane when reconstructing.

3). Adding positive lens factor into frequency specturm of oneobject and negative lens factors into conjugate frequency spectrum of another different object respectively.

Assuming a object $f(x,y)$ through Fourier transform, function of object's frequency spectrum is:

$\mathcal{F}[f(x,y)] = A(f_x, f_y) \exp[i \phi _A(f_x, f_y)]$　　　　(8)

Assuming another object $g(x,y)$ through Fourier transform, function of object's conjugate frequency spectrum is:

$\mathcal{F}^*[g(x,y)] = B(f_x, f_y) \exp[-i \phi _B(f_x, f_y)]$　　　　(9)

Let formula (8) add positive lens factor $\exp[i \theta (f_x, f_y)]$ and formula (9) add negative lens factor $\exp[-i \theta (f_x, f_y)]$ repectively then adding:

$$A(f_x,f_y) \, expi[\, \phi_A(f_x,f_y) + \theta \, (f_x,f_y)] + B(f_x,f_y) \, exp\text{-}i[\, \phi_B(f_x,f_y) + \theta \, (f_x,f_y)]$$

$$= C(f_x,f_y) \, expi[\, \beta \, (f_x,f_y)] \tag{10}$$

where $C(f_x,f_y)$ and $\beta \, (f_x,f_y)$ express amplitude and phase of combined frequency spectrum repectively. when unit-amplitude parallel light illumnates this type CGH,two identical directional different reconstructed images appear simultaneously at +1 order location and -1 order location on the same plane away from the CGH

Experiment

Lee's delay sampling method[4-5] is adopted in CGH. The sampling point of object is 64 × 64. Before FFT transform, the object function adds a random phase factor to prvent dynamic range of Fourier frequency spectrum too big. The size of the CGH drawing by plotter is 256 × 256mm^2 , then reducing the drawing (100x) by photograph, the required CGH is obtained.

When reconstructing, the parallel He-Ne laser (λ =633nm) illuminates the CGH, the configuration is shown in figure 2. Because of adding the quadratic phase factor (which is equavalent to a lens),the CGH has the function of self-focusing.The reconstruction image will be a focal length f away from the CGH (in our experiment f is 61cm). For the CGH that positive lens factor is added in frequency spectrum of the object (English word 'pig'), one upright image of originally object appear in +1 order location and one light spot appear in -1 order location when reconstructing as shown in figure.3 (a)

For the CGH that positive lens factor is added into frequency spectrum of the object and negative lens factors is added into conjugate frequency spectrum of the object respectively, two image having identical direction appear at +1 order location and -1orderlocation on the same plane when reconstructing as shown in figure.3 (b)

For the CGH adding positive lens factor into frequency specturm of one object and negative lens factors into conjugate frequency spectrum of another different object repectively, two identical direction different reconstructed images appear at +1 order location and -1 order location on thesame plane f away from the CGH. The reconstructed image of this CGHis shown in figure.3 (c)

If illumnating the CGH is not parallel light,the position of reconstructing image plane may be calculated by lens equation, which is decided by the divergence and convergence of incident light.The experimental results is identical to thoeretic analysis but the noise is largger in latter two situations .

For the convenience of comparison, the reconstructed images of usual CGH is shown in figure 3.(d)

(a)   (b)   (c)   (d)
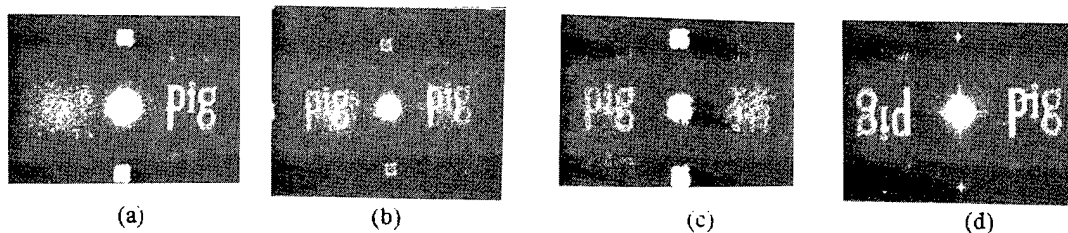
Fig.3. reconstructed images of CGH's unusual mode and usual mode. (a). spatial spectrum of two recontruction images. (b).two reconstruction images having an identiacal direction .(c).two different shape reconstruction images having identical direction . (d).two mutual inverted recontruction images.

Conclusion

The new type CGH that the quadratic phase factor is directly added in frequency spectrum of object has the function of self-focusing and self-imaging objectively, the imaging lens can be omitted in CGH's reconstruction. The optical configuration becomes more simple and more compact.The reconstructed images break through traditional mode (one upright ,another inverted both appear in a same plane), The spatial separation of reconstructed

images comes true. +1 order's upright image and -1 order's inverted image may be appear in diffenert plane respectively When reconstructing;two upright image (having identical direction) of same object or different object appear at +1 order location and -1 order location respectively in the same plane.This study explores a singnificant new way for making particalar reconstructive demand CGH, if increasing diffraction efficiency and the signal-to-noise ratio, a good future for application could be exepected.

Refenerce:
1. "Introduction To Fourier Optics" J.W. Goodman McGraw-Hill Inc.
2. A.W.Lohmann and D.P.Paris, Appl. Opt., 6, 1139 (1967)
3. R.J.Colleir, et al., Optical Holograpy, Academic press, New York and london ,(1971)
4. W.H.Lee, Appl.Opt., 9,639 (1970)
5. W.H.Lee, Progress in Optics, ed. by E.Wolfe, Vol.XVI (1978)

Measurement and Analysis of Compound Amplitude and Phase Holographic Gratings

Y. J. Wang[1], M. A. Fiddy[1], Y. Y. Teng[2], D. A. Pommet[1], and L. Malley[1]

Center for Electromagnetic Materials and Optical Systems
[1] Department of Electrical Engineering
[2] Department of Physics
University of Massachusetts Lowell
Lowell, MA 01854
508 934 3359; fax 3024

Abstract

This paper describes the effect on the reconstruction of a bleached hologram, of the inevitable presence of a residual amplitude hologram which is usually neglected. The modeling of this offers insights into its possible exploitation for some applications.

Introduction

A hologram on which an interference pattern is recorded, appears transparent after exposure, developing and bleaching. However, these types of holographic transparencies are found to have both some periodic variations of optical density and surface relief when measured using microdensitometer and profilometer. We refer to this kind of holographic grating as a compound hologram, i.e. it contains variations in both amplitude and phase.

It is well known that the diffraction efficiency of this kind of bleached holographic grating is a function of the exposure. Under ideal conditions one can control the exposure and bleaching process to maximize the diffraction efficiency of the first order diffracted beam (approaching 33%) or one of the higher order diffracted beams.

We analyze the diffraction property of this kind of grating below. We assume that the transmittance function of a compound holographic grating is

$$t(x',y') = \{[(1/2) + (m_a/2)\sin(2\pi f x')]\exp[j(m_p/2)\sin(2\pi f x')]\} * \text{rect}(x'/L)\text{rect}(y'/L) \qquad (1)$$

where m_a is the peak to peak excursion of the amplitude transmittance
          m_p is the peak to peak excursion of the phase delay
          L   is the width of the square aperture bounding the grating

The sinusoidal variation of the amplitude is caused by the residual amplitude of the partially bleached grating. The sinusoidal variation of the phase is caused by refractive index variation associated with the surface relief of the bleached emulsion. The variations of both amplitude and phase are in phase. Substituting the identity

$$\exp[j(m_p/2)\sin 2\pi f x'] = \sum_{q=-\infty}^{\infty} J_q(m_p/2)\exp(j2\pi qf x')$$

where J_q is the Bessel function of the first kind, of order q, into equation (1) gives the expression for the transmittance function,

$$t (x',y') = \{(1/2) \sum J_q (m_p /2)\exp(j2 \pi qf x') +(m_a/4j) \sum J_q (m_p /2)\exp(j2 \pi (qf + f)x')$$

$$- (m_a/4j) \sum J_q (m_p /2)\exp(j2 \pi (qf - f)x')\} *rect(x'/L)rect(y'/L) \tag{2}$$

Thus, when a compound grating is illuminated by a normalized monochromatic wave, the field distribution just behind the aperture is assumed proportional to t (x',y'). Fourier transforming this field distribution and using the shifting property of δ - functions, we obtain

$$FT [t (x', y')] = L^2 sinc(Lf_y)\{(1/2) \sum J_q (m_p /2)sinc[L(f_x - qf_0)]$$

$$+ (m_a/4j) \sum J_q (m_p /2)sinc[L(f_x - qf - f)]$$

$$- (m_a /4j) \sum J_q (m_p /2)sinc[L(f_x - qf - f)] \tag{3}$$

After substituting $f_x = x/ \lambda z$, $f_y =y/ \lambda z$, it is simple to show that the intensity distribution is

$$I (x,y) = (L^2 /2 \lambda z)^2 sinc^2 (Ly/ \lambda z) \sum J_q^2 (m_p /2)sinc^2 [(L/ \lambda z)(x - qf \lambda z)]$$

$$+ (m_a^2 /4) \sum J_q^2 (m_p /2)sinc^2 [(L/ \lambda z)(x - qf \lambda z - f \lambda z)]$$

$$+ (m_a^2 /4) \sum J_q^2 (m_p /2)sinc^2 [(L/ \lambda z)(x - qf \lambda z + f \lambda z)]\} \tag{4}$$

Equation (4) is thus the diffraction pattern of a compound holographic grating. If we choose $m_p = 0$, then

$$\sum J_q (m_p /2) = J_0 (0) = 1$$

The intensity distribution reduces to the diffraction pattern of a pure sinusoidal amplitude grating. If $m_a = 0$ then expresses the diffracted intensity distribution of a pure sinusoidal phase grating. If we assume that q = 0 in Eq. (4), we have

$$I_0 (x,y) = (L^2 /2 \lambda z)^2 sinc^2 (Ly/ \lambda z)[J_0^2 (m_p /2)sinc^2 [(L/\lambda z)x]$$

$$+ (m_a^2 /4) J_0^2 (m_p /2) sinc^2 [(L/ \lambda z)(x - f \lambda z)]$$

$$+ (m_a^2 /4) J_0^2 (m_p /2) sinc^2 [(L/ \lambda z)(x + f \lambda z)] \tag{5}$$

While $q = \pm 1$, it becomes

$$I_{\pm1}(x,y) = (L^2/2\lambda z)^2 \text{sinc}^2 (Ly/\lambda z)[J_{\pm1}^2 (m_p/2)\text{sinc}^2 [(L/\lambda z)(x^-_+ f\lambda z)]$$

$$+ (m_a^2/4)J_{\pm1}^2 (m_p/2)\text{sinc}^2 [(L/\lambda z)(x^-_+ 2f\lambda z)]$$

$$+ (m_a^2/4)J_{\pm1}^2 (m_p/2)\text{sinc}^2 [(L/\lambda z)x\} \tag{6}$$

Eqs (5) and (6) indicate that there always exist three terms for any one of the values of q. These terms are similar to the three components diffracted by a pure sinusoidal amplitude grating. In other words, each diffraction order of a compound grating actually consists of three components: the central maximum of q order, and the two side maxima of (q+1) and (q-1) orders. From Eq. (4) we can explain the behavior of the diffraction efficiency. When the exposure time increases, m_p increases also. The phase component of a compound grating plays an increasingly important role in diffraction with increasing m_p. The maximum diffraction efficiency evolves from the zero order to higher order terms due to the properties of the Bessel function of the first kind.

Since the sinusoidal amplitude grating is always present, then in a compound hologram, every order of the Bessel function is actually diffracted into three components. When m_p is such that the diffracted intensity of the qth order of a pure phase grating is equal to zero, then there will still be the left side maximum of (q+1) order and the right side maximum of (q-1) order at the position of the qth order for the grating. Therefore the order is not absent.

References

1. M. C. Hutley, Diffraction Gratings, Academic Press Inc. Ltd., London, 1982.
2. J. W. Goodman, Introduction to Fourier Optics, McGraw--Hill, 1968.
3. F. T. S. Yu, Appl. Opt., **8**, 2350, 1969.
4. J. N. Latta, Appl. Opt., **7**, 2409, 1968.
5. W. T. Cathey, Jr., J. Opt. Soc. Amer., **56**, 1167, 1966.

Joint Session on Diffractive and Micro-Optics and Holography II

JTuC 1:30 pm-3:00 pm
Gardner A&B

Michael Gale, *Presider*
Paul Scherrer Institute

Diffraction Optics - A century from basic studies to mass production

Erwin G. Loewen
Spectronic Instruments, Inc.
Rochester, NY 14625

Introduction:

Diffractive Optics, defined as the use of diffraction to aid or perform the imaging process, belongs to the large familiy of 19th century concepts in optics that have moved from obscurity to important technology thanks to a fascinating confluence of recently discovered needs with development of a whole collection of new enabling technologies. These include computational methods, optical materials, and finally precision engineering processes that convert the impossible into the possible . Not one of these basic developments originated because of demands from the Diffraction Optics community. They came from the outside world and were conveniently appropriated as needs arose.

Early History

The first serious study of possibilities of diffraction modified imaging was due to Cornu, who was stimulated by reports of the effects of systematic groove spacing errors on diffraction gratings, which shifted the focal plane of his imaging optics. An 1875 paper describes his work, first with standard gratings, but quickly recognizeing that results apply equally well for spherical waves combined with circular grooved gratings. He went so far as to build a special ruling engine designed to allow deliberate program errors to be introduced. He ruled Fresnel patterns into a layer of soot on glass, with 8.5 mm focal length. He noted other orders at integral multiples. Further work was reported in 1893, but practical applications were not on his mind.

Lord Rayleigh experimented with Fresnel Zone plates at about the same time, and noting that no more than 10% was imaged in any one plane suggested that the opaque zones be replaced with transparent ones etched deep enough to give them a $\pi/2$ phase difference. It remained for R.W. Wood some 25 years later to produce such a 'lens' and he was happy to find as much as 40% in the principal image plane. Excessive stray light inhibited any thought he might have had of

actually using it.

Wood, who was the first to blaze a standard diffraction grating by giving the grooves a triangular shape (~1910), must have considered applying this idea to his lens, but evidently could find no good way to actually carry out the idea. This was to take another 40 years, which gives a clear indication of how difficult a job this is.

Enabling Technology for Blazing

The first outside development that proved critical to diffractive optics was precision diamond turning machines. Originally built at Phillips research labs, passed on to DuPont, it found its first U.S. home in Oak Ridge and Lawrence Livermore Labs. The first applications were for generating precision spheres, but they were also treated as an academic prospect (1960). These machines were not only equipped with accurate slides, but were the first to apply programmable digital interferometric feedback position control. Crucial also were the recently developed air bearing spindles with axial run-out at the 50 nm level or better, and finally they taught the all important lesson that temperature of the entire machine and its environment both could and should be held constant to 0.01 C or less. The development of corresponding diamond tools should not be overlooked.

A quite different and to some extent more versatile approach was introduced in the 1980's capable of giving similar results. This was the oddly named concept of binary optics, which rested on the proposition that there is little optical difference between a smooth triangular groove face and its approximation by a series of steps (4 to 16). It could never have been put to use without the great advances in microlithography, in all its aspects. It requires a set of accurately made masks and means to align them. Making masks requires special pattern generators, 'writing' with either laser or electron beams. The latter can write finer patterns, but are slow, expensive, and work in a vacuum. Thanks to digital programming they have the advantage of being able to produce off axis and other non-symmetrical patterns when required, hardly reasonable to do on lathes.

Replication

An important step in making volume diffraction optic elements is replicating the modulated surface of a master onto the product optic. The goal invariably is how to combine high fidelity

with low cost. This describes injection molding quite well, but presupposes that limitations inherent in a plastic lens are acceptable, especially changes of index with temperature. More accurate, but much slower, is the casting process. The master is 'glued' to the glass product with a low viscosity monomer which is then polymerized, usually with the aid of UV radiation. If properly prepared, the two surfaces can be separated without damage, so that the process can quickly be repeated. Another potentially useful process involves embossing the master pattern, usually in the form of a nickel electroform, against the product that has been coated with a special film that must adhere tightly to the substrate, is readily deformed and finally cured with UV light.

Some applications

The simplest diffractive lens, and used in the greatest volume, is the small collimating lens found in every CD system for the last 15 years. It is made by a molding process. At the other end of the scale are large high grade IR lenses made out of germanium. The material is heavy and expensive, giving every incentive to use singlets. To reduce resulting aberrations and chromatism with a diffractive surface is an excellent solution. With volume low, it makes sense to turn the pattern directly into the surface of each lens.

Quite another problem is a reflecting system where simple design calls for skew rays, yet all mirrors are required to be spheres for low cost. A diffractive optic with skew pattern provides an ideal tool for suppressing aberrations. One cannot overlook in such cases the fact that any diffractive surface will change its angular behavior with wavelength. This is desirable for taking advantage of chromatizing possibilities, but it may in some instances limit the wavelength band over which it can be used.

A totally unique application of diffractive optics is found in the vacuum alignment tunnel of the Stanford Linear Accelerator. It supplies the straightness reference over the full 2 miles to an accuracy of 0.025 mm, as checked every 8 m. This is done with a set of 296 Fresnel lenses made by etching their patterns into 10 inch square sheets of 0.01 inch thick nickel. There is a laser illuminated pinhole at one end and an elegant quadrant detector at the other, which recognizes any off axis condition of the lenses (1 at a time) with accuracy to spare. This was set up in 1966 and to this day no alternative concept has been proposed that could do the job.

Liquid crystal grating based on modulation of circularly polarized light.

Jay E. Stockley,

NSF Optoelectronic Computing Systems Center University of Colorado at Boulder, Boulder, Colorado 80309-0525 phone (303) 492-2195 fax (303) 492-3674

Gary D. Sharp, Steven A. Serati, and Ping Wang,

Boulder Nonlinear Systems, Inc. 1898 S. Flatiron Ct. Boulder, Colorado 80301 phone (303) 786-8958 fax (303) 786-8598

Kristina M. Johnson

NSF Optoelectronic Computing Systems Center University of Colorado at Boulder, Boulder, Colorado 80309-0525 phone (303) 492-7967 fax (303) 492-3674

Introduction

Liquid crystals are frequently used as active diffractive optical elements [1,2]. These materials offer several advantages, including rapid response [3], large aperture, and low cost. The simplest liquid crystal diffractive structure is a one dimensional grating comprised of a linear array of electrodes [4]. Application of different voltages along the electrode array results in a multi-level phase structure which may take the form of a blazed grating or phased array. For such devices, the phase front across the grating aperture is constructed from periodic and quantized phase steps up to 2π.

Conventionally, birefringence modulation has been used to obtain the phase modulation for liquid crystal gratings. This is achieved by electrically changing the extraordinary refractive index encountered by the optical field. Changing the birefringence to induce a phase modulation is inherently chromatic. That is, the phase difference, Φ, induced on the field is wavelength dependent and is in general given by:

$$\Phi = 2\pi n_{ex}(V)d/\lambda \quad . \tag{1}$$

Here $n_{ex}(V)$ is the voltage induced change in the extraordinary index of refraction, d is the liquid crystal thickness, and λ is the wavelength of the optical field.

If instead the phase is due purely to polarization modulation, as is the case described here, the phase induced on the optical field is achromatic. This is because the phase modulation depends on the optic axis orientation of the liquid crystal retarder in the plane transverse to the direction of propagation and not on the refractive indices.

Such a broad band active grating structure has a distinct advantage over conventional phase modulation based on retardation. If the reset phase of 2π for the grating is independent of wavelength, then there will be no material dispersion and the only dispersive effects will be due to the grating structure itself. Grating dispersion is a consequence of the far field propagation of the diffracted light. Such propagation effects can be theoretically compensated for by a diffractive system, such as an achromatic Fourier transformer [5].

Phase Modulators Using Chiral Smectic Liquid Crystals

Multiple phase levels can be achieved by rotating the optic axis of a half-wave plate in a plane transverse to a circularly polarized optical field [6]. A few microns of planar aligned chiral smectic liquid crystal (CSLC) between electrodes results in an electrically activated half-wave plate with a rotatable optic

axis. The phase induced on a circularly polarized field is equal to twice the rotation of the optic axis of the half-wave retarder with respect to a reference orientation.

$$\Phi = 2k\alpha \ . \tag{2}$$

Where k is the number of half-wave retarders or the number of passes through a half-wave retarder and α is the optic axis rotation. The advantage of CSLC's is that the optic axis can be reoriented within submicrosecond times [3].

There are several structures that can produce such a phase modulation. The basic structure is a CSLC half-wave retarder sandwiched between two passive quarter-wave retarders [6]. Here the induced phase is $\Phi = 2\alpha$, where α is the relative optic axis orientation of the CSLC retarder. These materials exhibit maximum optic axis reorientations that vary from a few degrees for electroclinic [7] materials to nearly 90° for Smectic C^* materials [8]. Since the phase is twice the reorientation of the optic axis per pass through a half-wave retarder, multiple half-wave plates, reflection-mode configurations or resonantly enhanced devices are needed to obtain enough phase to produce efficient diffractive elements having more than two phase levels.

We have recently implemented a reflection-mode modulator at 632.8 nm using a ferroelectric half-wave retarder and polymer cholesteric liquid crystal mirror [9]. The device demonstrated nearly 2π radians of analog phase modulation.

In this meeting one of the things we will present is our continued effort to obtain large analog phase modulation using a single active device. One such structure, a resonant device which employs a quarter-wave thick retarder of electroclinic material between a high reflector and a partially reflecting (65%) cholesteric mirror has been implemented at 1064 nm. This device demonstrated a phase modulation of $\Phi = 8\alpha$, or just over π radians. This is the first integrated active resonant device using a cholesteric mirror and conventional mirror. Another new phase modulator is a two pass device which is an extension of the phase modulator discussed in reference 9. A $4\mu m$ thick CSLC retarder was fabricated onto a $8.5\mu m$ thick polymer cholesteric mirror which reflected 86% of left hand circularly polarized light at 1064 nm. An analog phase modulation depth of over $3\pi/2$ radians was observed. Figure 1 is a plot of the phase modulation as a function of electric field demonstrated by this new modulator.

Chiral Smectic Liquid Crystal Gratings

The diffraction characteristics of the liquid crystal grating depend on the aspect ratio of the grating thickness and grating period [10]. For a large grating period the diffraction efficiency may be obtained using scalar diffraction theory. As the grating period becomes smaller and the diffraction angles increase, the theoretical diffraction efficiency must be obtained using rigorous coupled wave theory [11]. A system of equations has been derived from Maxwell's curl equations and implemented numerically.

The number of resolvable spots can be shown to first order to vary as twice the square root of the number of electrodes, $2\sqrt{m_e}$, [12]. However, the flexibility of addressing imparted by the electrode structure allows a significant increase in the number of resolvable spots over $2\sqrt{m_e}$.

The chromatic effects of the liquid crystal retarder have also been determined. The retardation change on switching results in a small amplitude grating which will direct some of the incident light to the -1 and +3 orders. However, for a typical amplitude modulation of 10% the amount of light directed to these undesired orders is 0.2% each. Moreover, this amplitude grating does not reduce the number of resolvable spots.

Theoretical results including diffraction efficiency, number of resolvable spots, and chromatic effects will be presented at the meeting.

We will also present, for the first time, experimental results obtained from the implementation of a reflection mode liquid crystal grating using a quarter-wave CSLC retarder and a two pass configuration. The device exhibits a preferential direction for the primary diffracted beam depending on the direction of

increasing phase. Preliminary results indicate a 5:1 contrast ratio between the ±1 orders.

A reflection-mode grating which employs a half-wave CSLC retarder and a polymer cholesteric mirror as the back plane is currently being fabricated. A schematic of this device is shown in Figure 2. The diffraction characteristics of this grating will also be presented at the meeting.

Acknowledgements

References

[1] S. T. Kowel, D. S. Cleverly, and P. G. Kornreich, Appl. Opt. 23, p.278, 1984.

[2] G. D. Love, J. V. Major, and A. Purvis, Opt. Lett., 19, p.1170, 1994.

[3] N. A. Clark, and S. T. Lagerwall, Appl. Phys. Lett., 36, p.899, 1980.

[4] P. F. McManamon, E. A. Watson, T. A. Dorschner, and L. J. Barnes, Opt. Eng., 32, p.2657, 1993.

[5] G. M. Morris, Appl. Opt. 20, p.2017, 1981.

[6] G. D. Sharp Ph. D. Thesis University of Colorado 1992.

[7] S. Garoff and R. B. Meyer, Phys. Rev. Lett. 38, p.848, 1977.

[8] J. S. Patel and J. W. Goodby, Mol. Cryst. Liq. Cryst., 144, p.117, 1987.

[9] J. E. Stockley, G. D. Sharp, S. A. Serati, and K. M. Johnson, Opt. Lett., 20, p.2441, 1995.

[10] T. K. Gaylord, and M. G. Moharam, Appl. Opt. 20, p.3271, 1981.

[11] E. N. Glytsis and T. K. Gaylord, J.O.S.A. 4, p.2061, 1987.

[12] J. D. Zook, Appl. Opt. 13, p.875, 1974.

Phase Modulation as a function of Applied Electric Field
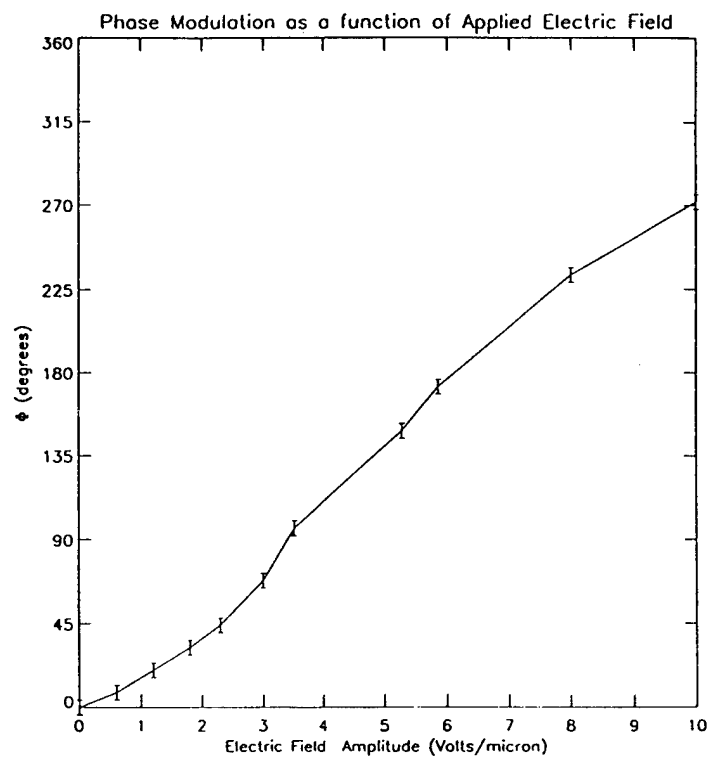
Figure 1. Experimental measurements of phase modulation as a function of electric field for the integrated two-pass modulator.

Incident Light
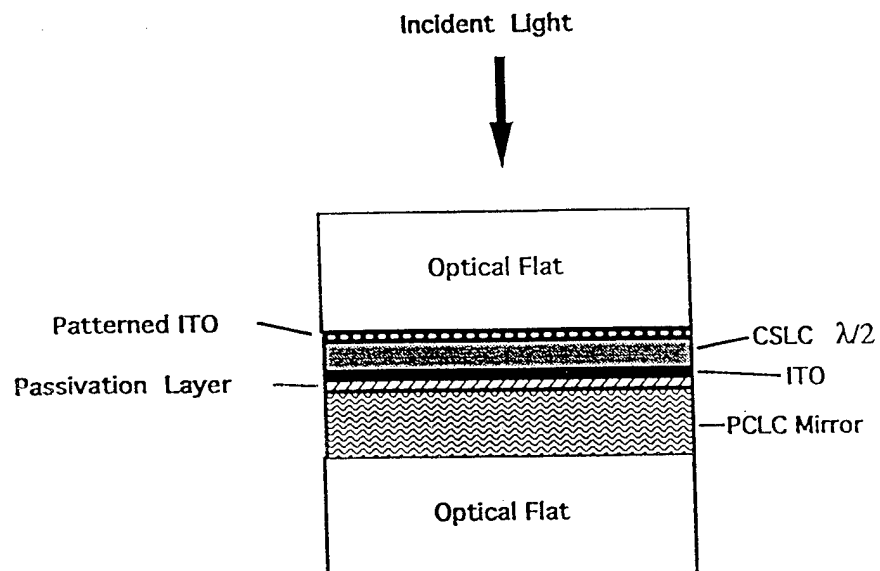
Figure 2. Schematic of the CSLC grating with a polymer cholesteric liquid crystal backplane.

Diffractive Optical Elements for 3-D Displays
Based on the Partial Pixel 3-D Display Architecture

G. P. Nordin, M. W. Jones, R. G. Lindquist, J. H. Kulick, and S. T. Kowel

The University of Alabama in Huntsville
Electrical and Computer Engineering Department
Huntsville, Alabama, 35899

Tel.: (205) 895-6215 x410
Fax: (205) 895-6618

Introduction

Real-time holographic display architectures are currently of significant interest,[1-2] in part due to intense international competition to develop advanced displays for high definition television, three-dimensional (3-D) workstations, and virtual reality systems. We have recently invented an alternate approach to holographic displays for such applications. Our 3-D display architecture (referred to as the "partial pixel architecture") is functionally equivalent to a holographic stereogram, yet lends itself to real-time implementation using flat panel liquid crystal technology in conjunction with diffractive optical elements.[3] A key innovation of the architecture is the encoding of very high space-bandwidth product components typical of holographic displays into a fixed diffractive optical element (DOE), while the lower space-bandwidth product components of actual images are displayed in real-time on a conventional liquid crystal display (LCD). In this paper we discuss diffractive optical element design considerations and implementation issues for real-time 3-D displays based on the partial pixel architecture.

Background

The basic geometry of the partial pixel architecture is illustrated in Fig. 1. A pixelated display is present in the x-y plane, and a viewing region is located a distance d_v from the plane. One can think of the viewing region as a series of adjacent virtual slits that are approximately one pupil diameter wide. As in a holographic stereogram, each eye of an observer sees a different image on the display. When the appropriate set of stereopair images are simultaneously presented on the display (with a single image visible through each virtual viewing slit), the scene appears three-dimensional. In addition, the display exhibits one-dimensional (1-D) motion parallax as an observer moves his or her head from side to side within the viewing region. Since special headgear is not required to view the display, it is also autostereoscopic.

In order to simultaneously display separate images through each virtual viewing slit, each pixel of the display must (1) direct light into each virtual viewing slit and (2) independently

control the amount of light directed to each virtual viewing slit. A pixel fulfilling these requirements could thus appear "on" (i.e., bright) when viewed through virtual viewing slit m, while simultaneously appearing "off" (i.e., dark) when observed through virtual viewing slit $m+1$.

In the partial pixel architecture, these pixel requirements are achieved by subdividing the area of each pixel into smaller regions (i.e., "partial pixels"). Since the display is designed such that the size of each pixel is at the resolution limit of an eye in the viewing region, these partial pixels are not visually distinguishable. Each partial pixel is responsible for directing light into a single virtual viewing slit, as well as controlling how much light is directed towards that slit. Construction of a display that functions like a holographic stereogram is thus reduced to the implementation of partial pixels that provide this basic functionality.

Current Real-time Implementations

We have recently implemented a small real-time monochrome display based on these principles.[4] As illustrated in Fig. 2, it utilizes a conventional liquid crystal display in conjunction with a suitably designed diffractive optical element. Each pixel of the LCD corresponds to one partial pixel and is physically aligned with a single diffraction grating on the DOE as illustrated in Fig. 3. The diffraction grating diffracts light to the appropriate virtual viewing slit, and the LCD pixel acts as an amplitude modulator. The minimum DOE feature size is approximately one micron. Diffraction from the effective partial pixel aperture determines the size of the virtual viewing slit in the plane of the viewing region. The partial pixel apertures are designed such that the virtual viewing slits have a small degree of overlap in this plane.

A top view of the display readout geometry is illustrated in Fig. 4. The viewing region is located 30 cm from the display and consists of 16 virtual viewing slits, each of which is approximately 6 mm wide. Virtual viewing slits –9 to –2 correspond to left-eye images, and slits 2–9 to right eye images. When a set of eight stereo image pairs are simultaneously presented on the display, a 3-D scene with horizontal motion parallax is observable. We have created sequences of such stereo image pairs such that real-time motion in the 3-D scene is achieved at video frame rates. We use a monochrome LCD display from Kopin Corporation, which allows us to drive the display with a standard VGA signal from a notebook PC.

We have recently extended the above display to full-color viewing using a technique that is analogous to rainbow holography. The number of partial pixels per display pixel is increased by a factor of three over the monochrome version, and an incoherent white light source is used to illuminate the display. Each partial pixel is designed to diffract a specific spectral component to

the desired virtual viewing slit. Color filters are not required to implement this particular design, although such filters represent an alternate path to achieving full-color displays.

DOE's

Our work to-date has demonstrated that the partial pixel 3-D architecture does indeed allow the realization of real-time displays that are functionally equivalent to holographic stereograms. However, there are a number of critical issues to be addressed in significantly scaling-up partial pixel architecture displays to useful sizes. Several of these issues are discussed below.

It is clear that future partial pixel architecture displays will require LCD's with very large numbers of pixels. For example, the 3072 × 2048 pixel display currently being developed by Xerox would allow approximately 20 separate 2-D images to be displayed, each with VGA resolution. For higher resolution images with a significant degree of motion parallax, even larger pixel counts are needed.

In addition, significant advances are required for the requisite diffractive optical elements. For example, DOE's are needed with deep submicron feature sizes over large areas (i.e., 11" diagonal or larger displays). The DOE's also need to incorporate an alternate method of defining the physical size of the virtual viewing slits. Currently, each partial pixel architecture display is designed such that diffraction from the aperture of each partial pixel is used to form the virtual viewing slits. A new method is needed to create a significantly taller viewing region in order to greatly enhance the size of the region from which the display can be viewed. We will describe our method of integrating a vertical diffuser function with the individual beam steering gratings for each partial pixel, and analyze the expected performance and potential limitations of such structures when integrated directly with LCD's.

References

1. P. St. Hilaire, S. A. Benton, M. Lucente, M. L. Jepson, J. Kollin, H. Yoshikawa, and J. Underkoffler, "Electronic Display System for Computational Holography", Proc. Soc. Photo-Opt. Inst. Eng. 1212, 174-182, (1990).

2. L. Onural, G. Bozdagi, and A. Atalar, "New High-Resolution Display Device for Holographic Three-Dimensional Video: Principles and Simulations", Opt. Eng., 33(3), 835-844, (1994).

3. J. H. Kulick, G. P. Nordin, A. Parker, S. T. Kowel, R. G. Lindquist, M. Jones, and P. Nasiatka, "Partial pixels: a three-dimensional diffractive display architecture", J. Opt. Soc. Am. A 12(1), 73-83, (1995).

4. M. W. Jones, G. P. Nordin, J. H. Kulick, R. G. Lindquist, and S. T. Kowel, "Real-Time Three-Dimensional Display Based on the Partial Pixel Architecture", Opt. Lett. 20(12), 1418-1420 (1995).
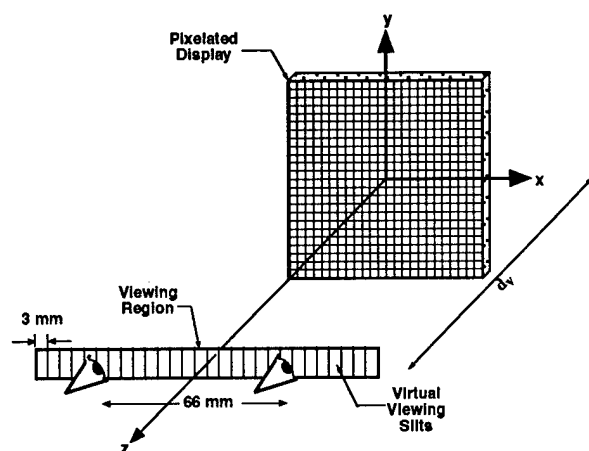
Figure 1. Geometry of the partial pixel architecture.
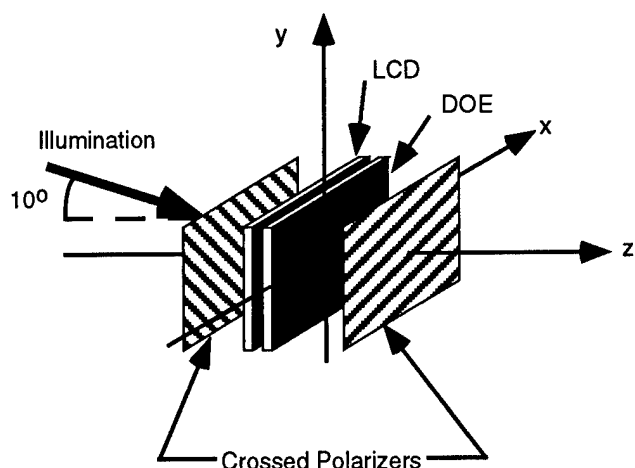
Figure 2. Schematic diagram of a liquid crystal panel-based partial pixel display.
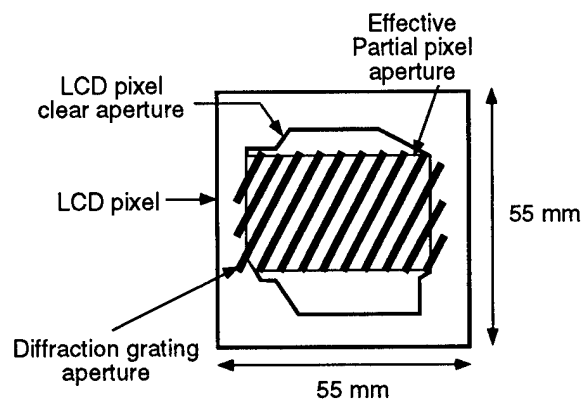
Figure 3. Schematic diagram of a LCD pixel and corresponding diffraction grating.
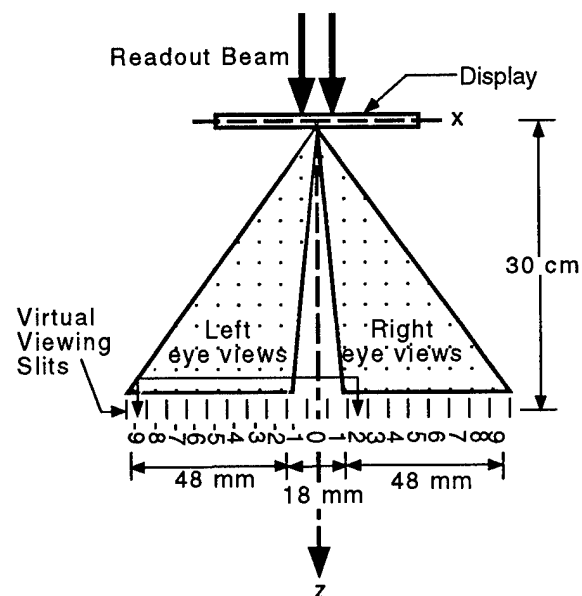
Figure 4. Top view of the readout geometry for the Kopin LCD-based partial pixel architecture display.

# Beam-Pointing Stabilization and Ladar Heterodyne Mixing Efficiency Increase Using a Liquid Crystal Phased Array Device

Mark J. Missey
Vincent Dominic
University of Dayton
Center for Electro-Optics
300 College Park
Dayton, Ohio 45469-3433
513-229-2597
mmissey@engr.udayton.edu

Edward A. Watson
Wright Laboratory
WL/AARI-2 Bldg. 622
3109 P Street
Wright-Patterson Air Force Base, Ohio
45433-7700
513-255-4340

Introduction

Laser radar imaging systems often require the ability to accurately point the transmitted laser beam as well as the ability to mix the return light with a single mode receiver. An addressable liquid crystal phased array provides the precise spatially dependent phase shifts needed to achieve such beam stability and increased ladar heterodyne mixing efficiency. The device consists of a layer of nematic liquid crystals sandwiched between two substrates. One substrate is uniformly grounded, while the other is etched with narrow, closely spaced individual 1-D electrodes. The liquid crystals underneath a given electrode are rotated by applying an appropriate voltage, thus generating a birefringent phase delay. Two of these writable one-dimensional gratings can be cascaded to implement two dimensional phase profiles.

Common Ground
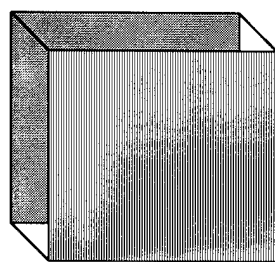
1-D electrodes

Figure 1. Liquid crystal addressable grating

The device used in this work has a 4 cm by 4 cm clear aperture, an 80 μm electrode spacing with a fill factor of unity, and an achievable phase depth of 2π radians for 1.064 μm light.

Beam-Pointing Stabilization

This device was originally intended to demonstrate non-mechanical agile beam steering

through the use of "blazed" phase gratings; active beam stabilization is thus a natural application of the device's capabilities. Ideally, beam steering is achieved by applying a linear phase ramp across the device mimicking the presence of a prism. Unfortunately, the response time of the liquid crystals precludes the use of LC layers thick enough to provide deflections greater than a few millidegrees. In practice, thinner layers are used, and the prism effect is achieved by resetting the phase ramp after every 2π radians of phase delay. The phase grating behaves like a true blazed grating, with the angle of beam deflection determined by:

$$\sin \theta = \frac{\lambda}{\Lambda}$$

where Λ is the phase ramp periodicity. However, unlike etched blazed gratings, the periodicity here may be changed by altering the voltage profile across the device; a beam can then be arbitrarily steered through a range of angles determined by the device electrode spacing. The device used in this experiment has an 80 μm electrode spacing, so a 2π phase ramp spanning four electrodes yields, at 1.064 μm, a steering angle of 0.190°. Clearly, a device with this electrode spacing cannot be used for large angle beam stabilization. However, since the steering angle is entirely determined by the electrode spacing, a beam can be steered to smaller angles with remarkable precision and repeatability. Furthermore, similar devices have been produced with electrode spacings sufficient to yield steering angles of up to five degrees[3].

Since beam deflection with these devices has been previously demonstrated, the question is not if they can be used to actively stabilize a laser beam, but how well. The response time of the liquid crystals and the required degree of beam confinement fundamentally determine the angular disturbance frequencies for which the device can correct. To illustrate this, consider the following diagram where Δ is the maximum angular perturbation, δ is the desired beam confinement, and position 'a' is the center position.
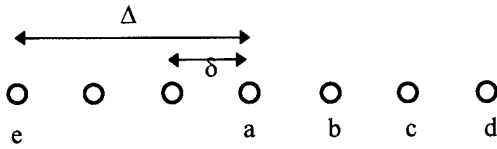
As the angular disturbance deflects the beam to 'b', the liquid crystal device must compensate by applying a phase grating to steer the beam through δ back to the center position. As the beam wanders to 'c', the device must compensate with an additional angle δ, making the entire compensated angle 2δ. Following through the cyclic sequence 'abc...e...a', the maximum cyclic frequency able to be compensated will be:

$$f_{max} = \frac{\delta}{4\Delta\tau_{LC}}$$

where τ_{LC} is the response time of the liquid crystals. Note that LC device cannot continuously compensate because of the 2π grating resets. Although this calculation of f_{max} is approximate, it serves to provide an order-of-magnitude figure for the range of frequencies over which stabilization may be achieved. The measured response time of the grating device of interest is 50 ms; for $\Delta/\delta=10$, this yields $f_{max}=0.5$ Hz. Given this estimate, it is reasonable to expect stabilization of noise bandwidths on the order of 1-10 Hz.

To determine the stabilization performance of the device, the following setup is used.
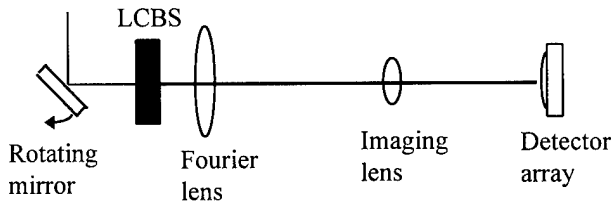
The rotating mirror provides angular disturbances for which the liquid crystal beam steerer (LCBS) compensates. To detect such small angular movements, an imaging lens is used to magnify the Fourier plane of the first lens onto the detector array. The output beam location is continuously recorded on an oscilloscope, and stored for processing.

Initial experiments will provide a user-defined angular disturbance sequence to both the rotating mirror and the liquid crystal beam steerer. Later experiments will provide the beam steerer with corrupted information, simulating motion sensor inaccuracies. Finally, a true closed loop system is constructed where beam position information is provided from the oscilloscope to the beam steerer.

The overall beam confinement and compensation bandwidth of all three systems are measured, and are shown to be inversely related.

Increased Coherent Laser Radar Mixing Efficiency

Coherent laser radar systems are generally designed so that the waist of the transmitted gaussian beam is at the exit aperture of the system; that is, the system is focused at infinity. Such a configuration is ideally suited for far-field target detection, but efficiency decreases for targets in the near field. To demonstrate this behavior, the overall heterodyne-detected signal from a resolved, perfectly diffuse speckle target is investigated. Following previous works[4,5], the average target return power obeys:

$$P_{det} = <\tilde{i}_{det}>^2 R$$

where i_{det} is the intermediate frequency signal current out of the photodetector, and R is the load resistance of the detection circuit, presumably an oscilloscope. The IF signal current obeys the standard target-plane integral:

$$\tilde{i}_{det}(t) = \Re \iint_{A_t} d\bar{\rho}_t \, \underline{\tilde{T}}\left(\bar{\rho}_t, t - \frac{L}{c}\right) \underline{U}_t\left(\bar{\rho}_t, t - \frac{2L}{c}\right) \underline{U}_{LO}^*(\bar{\rho}_t, t)$$

where $\Re$ is the detector responsivity, $\underline{\tilde{T}}$ is the random, complex reflectivity of the target, $\underline{U}_t$ is the transmitted beam at the target, and $\underline{U}_{LO}^*$ is the complex conjugate of the local oscillator field back propagated to the target plane. Assuming the local oscillator and transmit beams are identical gaussians with $1/e^2$ intensity radii of w_{ea} and phase curvature radii R_{ea} at the exit aperture, the average signal power output from the laser radar system as a function of target distance L is:

$$P_{det} = \frac{R\Re^2 P_{LO} P_{trans} \tau \left(\frac{w_{ea}}{L}\right)^2}{1 + \Omega^2}$$

$$\Omega = \frac{\pi w_{ea}^2}{\lambda}\left(\frac{1}{L} + \frac{1}{R_{ea}}\right)$$

where P_{LO} and P_{trans} are the powers of the local oscillator and transmitted beams, and τ is the target reflectivity.

Note that if the radius of phase curvature of the transmitted Gaussian beam at the exit aperture satisfies $R_{ra} = -L$, then $\Omega=0$, and the average power detected is a maximum. Since this condition, $R_{ea} = -L$, corresponds to a geometric-optics focus at a distance L from the exit aperture, the system exhibits the highest efficiency when the transmitted beam is geometrically focused at the target. Because a resolved, perfectly diffuse target has been assumed, the total amount of energy incident on the

target and reflected back to the system is independent of the radius of curvature of the Gaussian beam at the exit aperture, and so the term $E_h=(1+\Omega^2)$ can be thought of as the heterodyne mixing efficiency of the system, which determines the percentage of the light returned from the target that is mixed with the local oscillator to produce a detectable signal.

For an adaptively controlled focus, the mixing efficiency of the system can, in principle, be 100% for any target distance, while a fixed system focused at infinity decreases in the manner shown in Fig. 2.
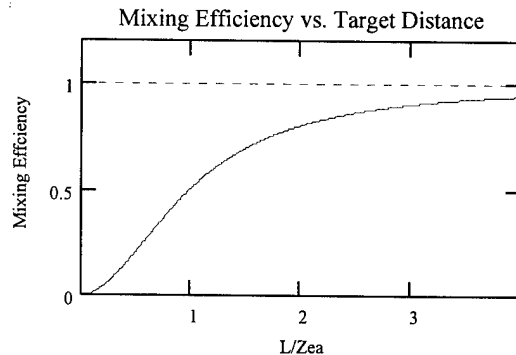
Figure 2. Heterodyne mixing efficiency for adaptively focused system (dashed) and a static system focused at infinity (solid) as a function of normalized target distance L/z^o_{ea}.

Although, the mixing efficiency for a laser radar focused at infinity decreases as the target moves into the near field, the total energy returned to the system increases as $1/L^2$, so that overall the system signal is larger for closer targets, as shown in Fig. 3.
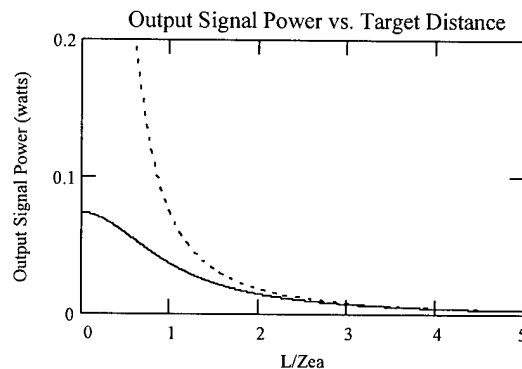
Figure 3. Output signal power of an adaptively focused system (dashed) and a static system focused at infinity (solid) as a function of normalized target distance L/z^o_{ea}. Relevant parameters are: a 1 mJ, 10 ns pulse, $\lambda=1.5$ µm, $w_{ea}=5$ cm, $\tau=0.8$, $\Re=.09$ A/W.

For this reason, few efforts have attempted to adaptively focus the transmitted beam on the target.

If the end goal of a ladar system were simply detection - is a target present or not - then a fixed focus system is sufficient for any target range.

When target characterization and identification are required, then the returned signal will be separated into different spatial bins. Having more bins allows more spatial information to be extracted, but reduces the total energy contained in each bin, eventually power-limiting the system.

Since,

$$\frac{P_{ret}(R_{ea}=-L)}{P_{ret}(R_{ea}=\infty)}=E_h=1+\left(\frac{z^o_{ea}}{L}\right)^2, \quad z^o_{ea}=\frac{\pi w^2_{ea}}{\lambda}$$

the benefit of an adaptive focusing lens is only substantial for target ranges $L \le z^o_{ea}$. For typical ladar systems, $w_{ea}=5$ cm and $\lambda=1.5$ µm, yielding $z^o_{ea}=5.2$ km. Achieving a focus at this distance requires such a slight phase curvature that the phase shift at the $1/e^2$ intensity point is only $\lambda/6$. The addressable liquid crystal device, possessing precise voltage controlled phase shifts, is ideally suited for this task.

Since the paraxial lens equation will be well satisfied for the target distances of interest, 2-D quadratic phase curvatures are used to implement focal lengths from about 7 km to about 5 m; the upper limit is determined by the device uniformity and phase quantization levels while the lower limit is determined by the onset of spatial aliasing and multiple focus spots, which are products of the spatially quantized nature of the device. Furthermore, the response time of the device (~50 ms) allows the system to switch focal lengths in just a fraction of a second.

The laboratory setup shown below is used to confirm the previously discussed theory, and to demonstrate the ability of the liquid crystal device to implement very long focal length lenses.
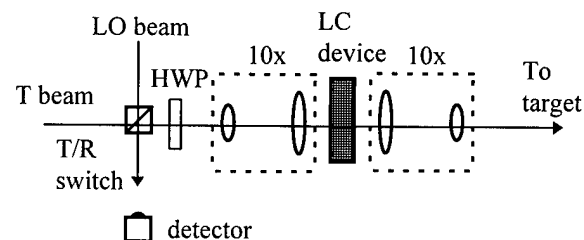

Figure 4. Laser radar system setup consisting of local oscillator (LO) beam, transmitted (T) beam, transmit/receive (T/R) switch, photodetector, half-wave plate, magnifying telescope, liquid crystal phase profile device, and demagnifying telescope.

The second telescope is aligned for demagnification so that the critical z^o_{ea} distance is less than 10 m, allowing demonstration within a closed laboratory environment. The return signal power as a function of target distance for both a static and dynamically focused system is measured and compared to predicted values.

References

1. P. F. McManamon, E. A. Watson, T. A. Dorschner, and L. J. Barnes, "Applications look at the use of liquid crystal writable gratings for steering passive radiation," *Opt. Eng.* **32**(11), 2657-2664 (1993).

2. T.A. Dorschner, R. C. Sharp, D. P. Resler, L. J. Friedman, D. C. Hobbs, R. L. Chandler, and A. Legere, *Basic Laser Beam Agility Techniques (BATS)*, final report by Raytheon Co. prepared for Wright Laboratory WL-TR-93-1020 (1993).

3. P. F. McManamon, T. A. Dorschner, D. C. Corkum, L. J. Friedman, D. S. Hobbs, M. K. O. Holz, S. Liberman, H. Ngyuyen, S. P. Resler, R. C. Sharp, and E. A. Watson, "Optical Phased Array Technology," Manuscript submitted for publication in *Proceedings of the IEEE* (Special Issue on Laser Radar) February 1996.

4. J. H. Shapiro, B. A. Capron, and R. C. Harney, "Imaging and Target Detection with a Heterodyne-Reception Optical Radar," *Appl. Opt.* **20**, 3292-3313 (1981).

5. D. K. Jacob, "Optical Waveguide Mixing for Coherent Ladar Carrier to Noise Ratio Optimization," M.S. Thesis, University of Dayton (1994).

Programmable Wavefront Generation with Two Binary Phase Spatial Light Modulators

Guoguang Yang and Seth Broomfield

Department of Engineering Science, University of Oxford
Oxford, OX1 3PJ, UK

In this paper we propose a programmable wavefront generation system using two binary phase spatial light modulators (BPSLMs). The output of the binary phase hologram has inversion symmetry and is restricted to be space–invariant, if the output of the hologram is viewed in the Fourier plane of a lens. Inversion symmetry may be broken by introducing a fixed binary phase hologram [1,2] but in this case diffraction efficiency η_d is not increased. Alternatively, an asymmetric output may be generated by increasing the number of phase levels [3]. Results obtained in this way increase η_d but the output remains space–invariant.

It has been pointed out by Bartelt [4] and Yang [5,6] that the restriction of space–invariance can be removed by effectively cascading two phase masks in two Fourier–transforming stages. In this paper we consider a similar binary phase scheme [6] except that fixed phase holograms are replaced by binary phase SLMs and the design method to achieve a given wavefront is based on simultaneous, iterative optimization of both SLMs. The system is demonstrated by producing an asymmetric output. Simulation of its performance as a reconfigurable optical interconnect is also presented. Both utilize the space–variant performance of the system.

The two binary phase SLM system and its experimental implementation

The system is shown in Fig 1. The system consists of two cascaded Fourier transforms. It is easy
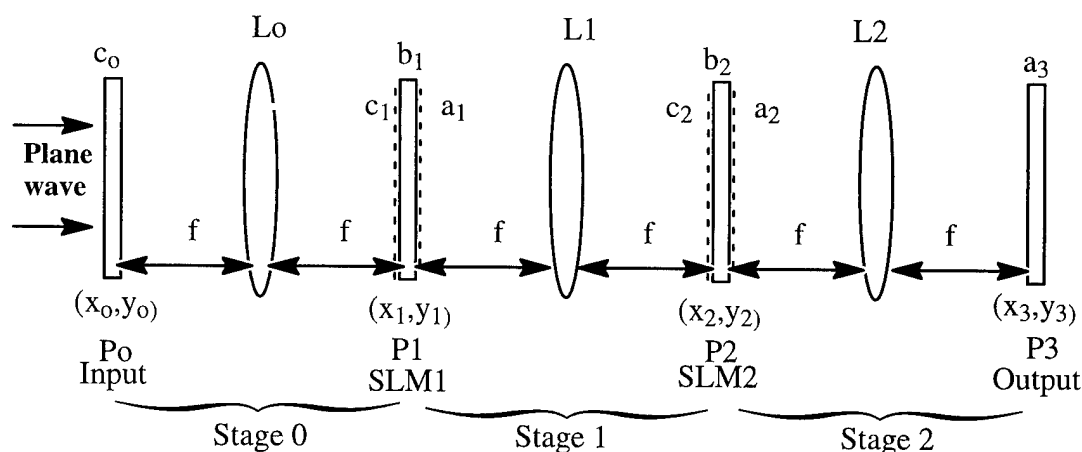
Fig. 1: The two binary–phase SLM system.

to proof that the system is a space–variant system. This is to be contrasted with the impulse response of a single phase SLM system which is a space–invariant system.

Assume the input function is a point at $x_0=y_0=0$, i.e. the complex amplitude of its Fourier transform $c_1(x_1,y_1) = 1$. Two Fourier transforms are performed by the system. The system characteristic can be analyzed according to the Fourier theorem. Schemes for producing outputs with different properties using this system are shown in Table 1. It indicates that *all wavefronts with real symmetric, complex Hermitian, real asymmetric and complex asymmetric properties can be generated with the proposed system using binary phase modulation.*

Scheme	b_1, BPSLM1	c_2, Input of b_2	b_2, BPSLM2	a_2, Input to L2	a_3, Output
1	real and even (symmetric)	real and even (symmetric)	real and even (symmetric)	real and even (symmetric)	real and even (symmetric)
2	real and asymmetric	complex and Hermitian	real and even (symmetric)	complex and hermitian	real and asymmetric
3	real and even (symmetric)	real and even (symmetric)	real and asymmetric	real and asymmetric	complex and Hermitian
4	real and asymmetric	complex and Hermitian	real and asymmetric	complex and asymmetric	complex and asymmetric

Table 1. The configuration schemes of two binary phase SLM systems

In the general two dimensional case, to achieve a space–variant operation from an input wavefront specified by N^2 sampled values to an output wavefront specified by N^2 sampled values, the number of sampling points of the transform matrix which is represented by a hologram with amplitude and phase modulation should equal to N^2xN^2. The complex transmission values of the BPSLMs are only +1 and −1, however. This restricts the wavefront transforms which the system can achieve. In general it is impossible to find the exact solution for large N. An optimisation algorithm has to be used to find the closest approximate solution. Therefore, in the sense of an approximate solution, *general transformations with binary phase SLMs can still be achieved.*

In order to demonstrate the system performance, several patterns shown in Fig.2 are selected as the target functions for the calculation. To provide a comparison, most of the patterns are the asymmetric patterns used in references [1,2]. The direct binary search algorithm is used in the design. Simulation results for the target patterns of Fig.2 are given in Table 2 in which the non–uniformity of the output is defined as $NU = (I_{max}-I_{min})/(I_{max} +I_{min})$. This shows that about 75% efficiency is obtained by using the two BPSLM system with 128x128 pixels for generating the patterns. This is a remarkable increase over the results obtained with a single BPSLM which are shown for comparison in table 2. This comparison shows that not only is the diffraction efficiency higher, but the uniformity is improved with the two BPSLM system.

In the experimental system the binary phase SLM is created by placing a ferro–electric liquid crystal (FLC) SLM between crossed linear polarizers as described in [7]. The calculated designs are loaded to the two SLMs from a computer. The asymmetric pattern shown in Fig. 2.(e) is generated in the experiment. Fig.4 is the experimental output when the optimized binary phase patterns shown in Fig.5 are loaded on the two SLMs. Black and white in Fig.5 correspond to 0 and π phase shift. The measured efficiency is 58% with 6% non–uniformity. The diffraction efficiency

of the experiment is lower than the theoretical prediction. This is due to the aberration of the optical system and not including the diffraction effect in the optimization process.
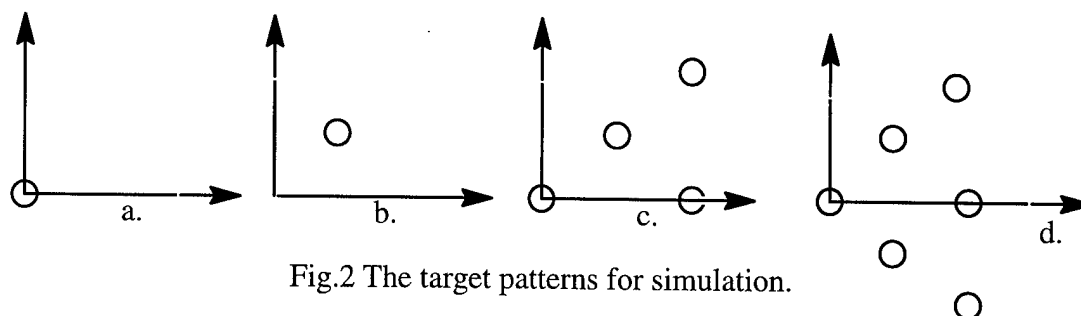

Fig.2 The target patterns for simulation.

Target pattern	calculated η_d (%)	calculated NU(%)	compared η_d (%)	compared NU(%)
a	81.2			
b	81.6			
c	73.8	3.2	41.1 in [3]	7.3 in [3]
d	76.2	0.5	40.4 in [3]	3.0 in [3]
e	75.0	1.0	40.0 in [2]	

Table 2. The simulation results and comparison

The programmable one–to–one optical interconnection system using two BPSLMs

A typical example for which shift variant performance is the programmable optical crossbar one–to–one interconnection system. Most of proposed schemes suffer from the drawback of low efficiency and large spot size. Our system with two BPSLMs can achieve high diffraction efficiency with diffraction–limited spot size. For simplicity, we shall discuss that N 1D light sources are connected to N 1D detectors with one–to–one connectivity. In order to realize the interconnection operation, sampling number of N^2 has to be employed in each SLM. The intensity input C_0 and desired output A_t matrices for N=4 in our simulation are taken to be
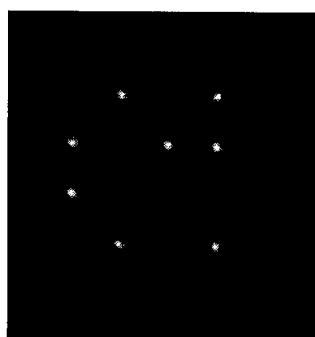
Fig.4 The experimental output pattern created by the cascaded SLM system.
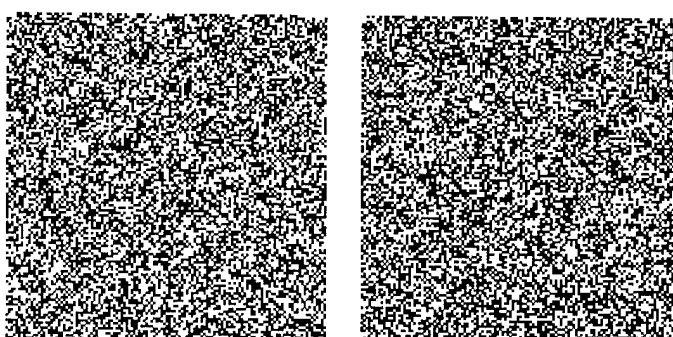
Fig.5 SLM arrays used to create asymmetric output

$$[C_0] = \begin{bmatrix} 1 & 0 & 0 & 0 \\ 0 & 1 & 0 & 0 \\ 0 & 0 & 1 & 0 \\ 0 & 0 & 0 & 1 \end{bmatrix} \qquad [A_t] = \begin{bmatrix} 1 & 0 & 0 & 0 \\ 0 & 0 & 1 & 0 \\ 0 & 0 & 0 & 1 \\ 0 & 1 & 0 & 0 \end{bmatrix} \qquad (1)$$

The system connects the first light source to the first detector, the second to the third, the third to the fourth and the fourth to the second. According to the design procedure discussed above, the optimized actual output for N=4 is

$$[A_t]_{actual} = \begin{bmatrix} \mathbf{\underline{0.816}} & 0.074 & 0.105 & 0.002 \\ 0.080 & 0.016 & \mathbf{\underline{0.758}} & 0.175 \\ 0.005 & 0.036 & 0.245 & \mathbf{\underline{0.767}} \\ 0.055 & \mathbf{\underline{0.750}} & 0.110 & 0.065 \end{bmatrix}, \qquad (2)$$

The results show that high efficiency can also be achieved with the two BPSLM system used for optical interconnection. It is independent of the dimension of the interconnection. As for implementing crossbar switching by using a multiple facet hologram the main drawback of the scheme is that it is not difficult to obtain a small spot size in order to efficiently couple light into a fibre as the full aperture is used for all inputs, instead of using a facet hologram. These make the scheme attractive for interconecting between a large number of nodes with programmable capability.

The crosstalk in the system is still high, about 20%. If the signal to be interconnected is binary, a threshold detector might be used to suppress the cross-talk. However, the required computation time in optimising the system is considerably longer than the time required for a single binary phase hologram. The optimisition of the two SLM system takes several hours run on a Convex machine which is a parallel processing high speed computer.

Conclusions

We conclude that the programmable wavefront generation system with two binary phase SLMs is a high diffraction efficiency and space–variant system. The amplitude and phase of a wavefront can be modulated with the system. It is experimentally implemented by two FLC SLMs. The experimental results are consistent with the theoretical prediction. A programmable optical crossbar interconnection system can also be based on the two BPSLM scheme.

References

1. M.A.A.Neil and E.G.S.Paige, Proc. of 4th Int. Conf. on Holographic Systems, Components and Applications, IEE Conf. Publication 378, 1993, p.85–90
2. M.S.Kim and C.C.Guest. Appl. Opt. 32 (1993) 678
3. S.E.Broomfield, M.A.A.Neil, E.G.S.Paige, Electronics Letters 29 (1993) 1661
4. H.Bartelt, Appl. Opt. 23 (1984) 1499
5. G.G.Yang, D.L.Lian, J.J.Zhang, J.P.Chen and Y.P.Ho, Opt. Lett. 16 (1991) 162
6. G.G.Yang, Proc. of 3nd Int. Conf. on Holographic Systems, Components and Applications, IEE Conf. Publication 342, 1991, p.45–49
7. S.E.Broomfield, M.A.A.Neil, E.G.S.Paige and G.G.Yang, Electronics Letters 28 (1992) 26

Holographic Optical Elements

HTuD 3:30 pm-5:15 pm
Commonwealth Room

Dean Faklis, *Presider*
PSC, Inc.

Modeling Issues for the Design of Volume Holographic and Surface Relief Grating Structures

Raymond K. Kostuk, Charles W. Haggans[+], Eugene Campbell[*], and Tae Jin Kim[++]
Electrical and Computer Engineering Department and
The Optical Sciences Center
University of Arizona
Tucson, Az. 85721

1. Introduction

Diffractive optical components are being used in a greater number of micro optical systems for data storage, optical interconnects, and fiber optic applications. The design of diffractive elements not only requires a detailed understanding of vector diffraction theory, but knowledge of the materials and processing techniques used for fabricating gratings. Models and design programs must be modified to include variations from ideal grating structures. Modeling data must also be collated into a form which points to promising solutions and allows for design optimization.

In this presentation we discuss a number of holographic material processing and fabrication characteristics, and show how they impact grating design and performance optimization. We also show techniques for graphically illustrating theoretical data in a manner which aids in component design.

2. Material and Processing Considerations

When fabricating gratings in volume type holographic recording materials a number of changes can occur to the material between the exposure and reconstruction phase. Although these effects are more pronounced in wet processed emulsions such as dichromated gelatin they also occur in dry processed photopolymers[1] and must be accounted for in the grating design. These factors include emulsion thickness change, fringe plane shear, and non-uniform index modulation with depth. They can be compensated to some degree by changing recording angles, using thicker recording materials, or increasing exposure levels. However other effects such as the variation in the bias index of the recording material and fringe bending with depth can not be readily compensated. In these situations it is often best to redesign the system in which these elements will be used to reduce performance sensitivity on these factors. In this presentation we will show methods for measuring these effects, including them into diffraction analysis programs, and making systems less sensitive to these variations.

3. Design Examples: Polarization Beam Splitters and Retardation Elements

In systems such as optical data storage sensing heads and SEED type switching devices polarization beam splitters and retardation elements are required. Volume gratings can be used to implement both of these components provided that careful consideration of the material properties are taken into account.

Emulsion shrinkage is very critical for polarization beam splitter design

because it introduces a shift in the Bragg angle which in turn changes the diffraction efficiency for s- and p- polarized light. This alters the polarization extinction ratio of the beam splitter and lowers the system signal to noise ratio. One way to offset this effect is to form an unslanted grating which is less sensitive to thickness changes[2]. Experimental efficiency data for a grating of this type is illustrated in Figure 1. The grating shows a very high polarization extinction ratio near the Bragg angle with an alignment tolerance of ± 0.5°.

The form birefringence of sub-wavelength period volume gratings can be used to implement retardation elements[3]. In order to realize phase differences on the order of $\pi/2$ relatively thick emulsions are required because the index modulation varies non-uniformily with depth. Figure 2 shows experimental results for a retardation plate formed in a triple coating of dichromated gelatin film which provides a $\pi/2$ phase shift at 632.8 nm.

4. Data Presentation and Design Optimization

When designing polarization control elements the vector characteristics of the diffraction process must be understood and requires the use of rigorous coupled wave or modal theory for proper description. The data obtained from such analysis can be difficult to evaluate especially if it is desired to simultaneously control several parameters. One approach for dealing with this problem is illustrated in Figure 3. In this case we were interested in selecting values for the polarization angle (α) and the phase retardation (δ) of a surface relief grating. These values are plotted as a set of contours as a function of the grating depth (d) and the azimuthal angle (Φ). This graphical approach allows a more intuitive evaluation of changes in the parameters of interest. Different solutions for desired values of both δ and α can readily be selected, and design regions which are highly sensitive to small changes in grating depth or reconstruction angle can be avoided. This approach to analyzing grating performance will be expanded in our presentation.

+ Currently with 3M Laboratories; * Currently with Lawrence Livermore Laboratory; ++ Currently at NEC Research Laboratory.

5. References

1. A. M. Weber, W. K. Smothers, T. J. Trout, and D. J. Mickish, ``Hologram recording in Du Pont's new photopolymer materials,'' SPIE Vol. 1212, 30-39 (1990).
2. R. K. Kostuk, T.-J. Kim, G. Campbell, and C. W. Han, ``Diffractive-optic polarization-sensing element for magneto-optic storage heads,'' Opt. Lett., Vol. 19, 1257-1259 (1994).
3. T.-J. Kim, G. Campbell, and R. K. Kostuk, ``Volume holographic phase-retardation elements,'' Opt. Lett., Vol. 20, 2030-2032 (1995).
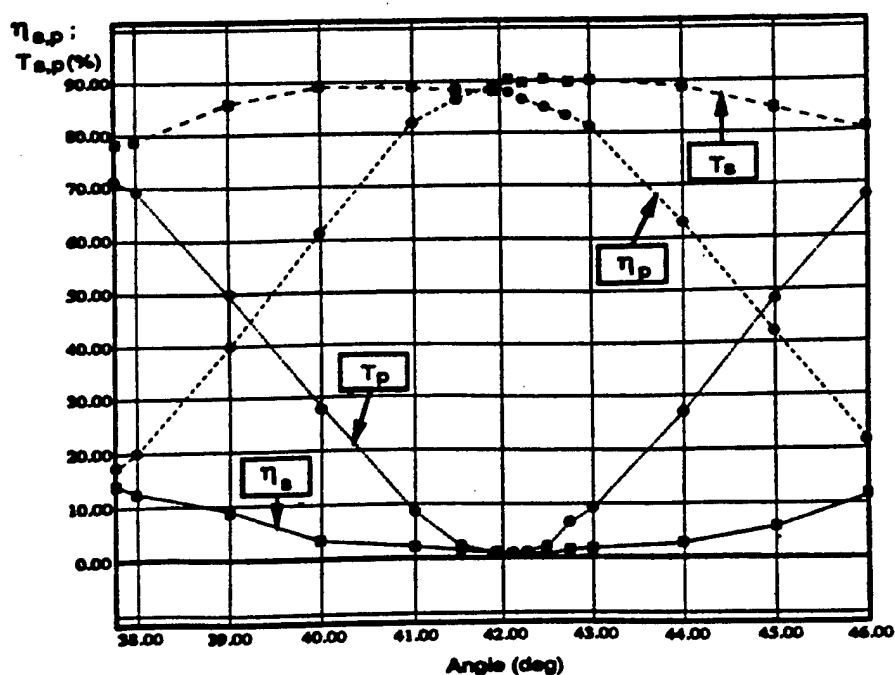
Figure 1. Diffraction efficiency vs. reconstruction angle for an unslanted polarization beam splitter formed in dichromated gelatin.
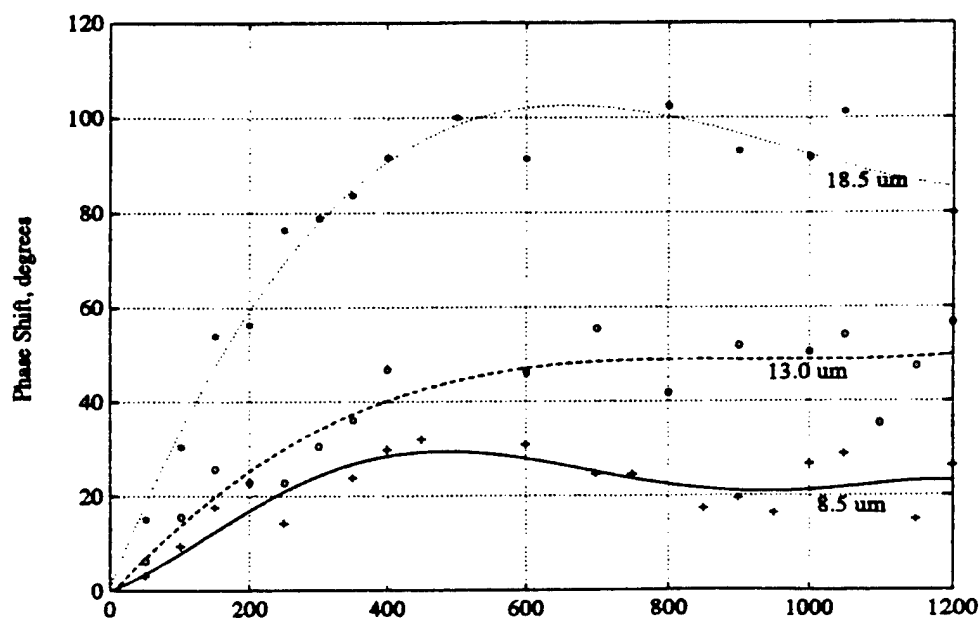

Figure 2. Phase retardation vs exposure (mJ/cm^2) for a grating formed in single (8.5 μm), double (13.0 μm), and triple (18.5 μm) coated dichromated gelatin layers.
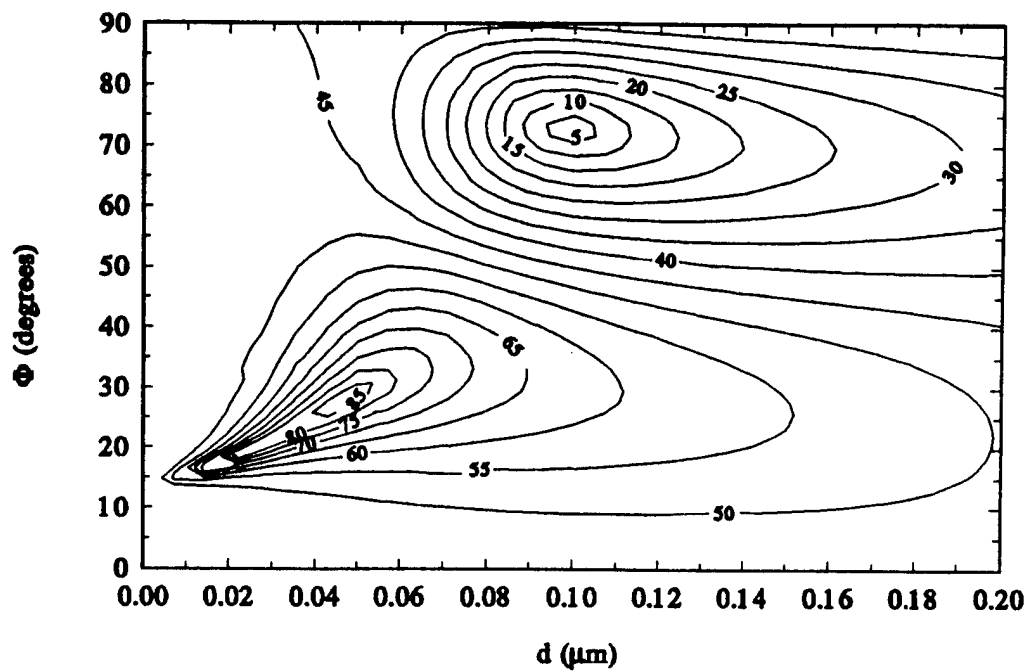
Figure 3a. Contour plot of the polarization angle (α) as a function of grating depth (d) and azimuthal angle (Φ).
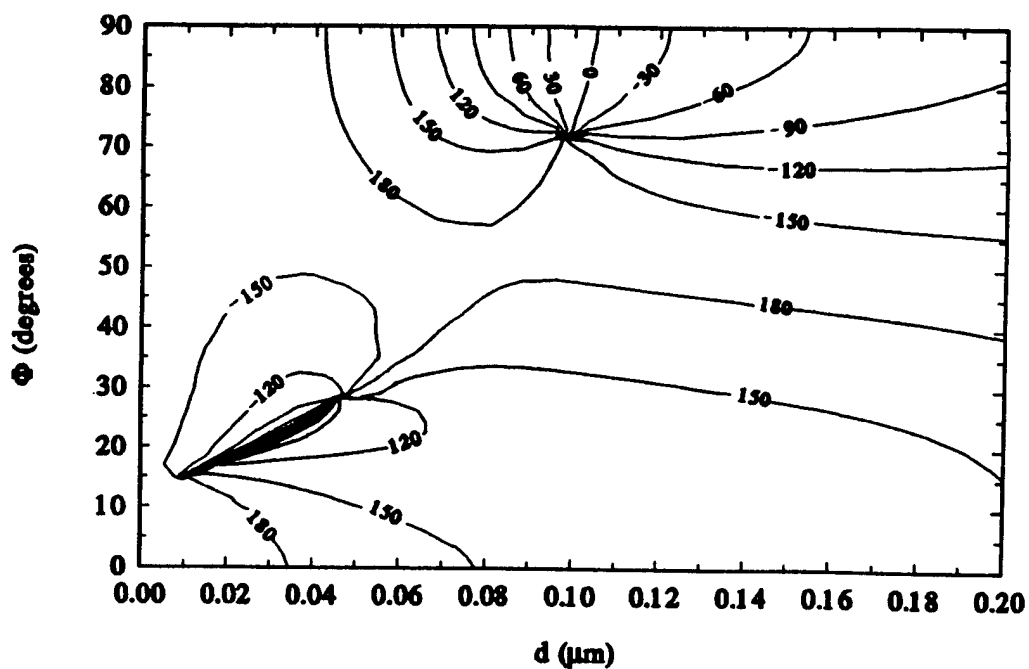

Figure 3b. Contour plot of the phase retardation (δ) as a function of grating depth (d) and azimuthal angle (Φ).

Highly Selective Optical Elements

Nadia Rheinhand
Russian Academy of Sciences

Summary not available.

A Geometrical Derivation of WRITE Beam Criteria for Multiplexed Color Hologram Readout Using Wavevector Triads

Monish R. Chatterjee

Department of Electrical Engineering, Binghamton University, SUNY
Binghamton, New York 13902-6000
Tel: (607) 777-4014
Fax: (607) 777-4464
email: bv0400 @ bingvmb.cc.binghamton.edu

and

Shih-Tun Chen

Department of Electrical Engineering, Binghamton University, SUNY
Binghamton, New York 13902-6000
Tel: (607) 777-4014
Fax: (607) 777-4464
email: ba02340 @ bingvmb.cc.binghamton.edu

The problem of restoring the misaligned output from a grating hologram under READ beam deviations has been investigated recently using a variety of resonant triad models [1-3]. Initially, it was proposed that selective angular and/or wavelength tuning of the READ beam would restore the output beam direction [1]. Subsequently, upon closer examination, it was found that the problem is amenable to different geometrical interpretations depending on whether the grating is untilted or tilted, and whether the READ beam deviation ($\Delta\lambda$ or $\Delta\theta$) is positive or negative [2]. The latter problem has generally been analyzed by assuming a single-deviation model (i.e., with the READ beam having either an angular or a wavelength deviation and not both). It may be shown that the deviation in the desired reconstructed beam direction may be graphically determined from appropriate resonant triads superposed on wavenumber (or β) circles. For the case of an untilted grating with a READ angular mismatch, for instance, an appropriate wavelength tuning will restore the reconstructed beam direction. The amount of tuning necessary will depend on the sign of the angular mismatch (i.e., whether it is greater or less than the Bragg angle). One such scenario is shown in Fig.1.
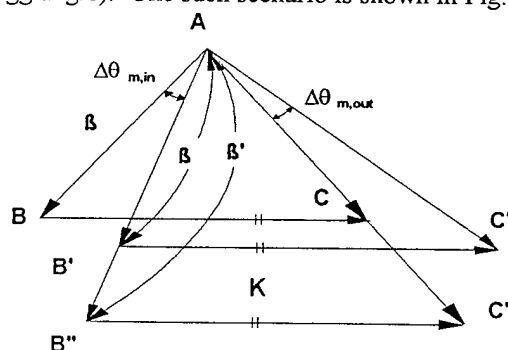
Fig. 1.

In the figure, $\Delta\theta_{m,in}$ is the READ beam angular mismatch (considered positive here), $\Delta\theta_{m,out}$ is the corresponding output deviation, and $(\Delta\lambda / \lambda_{mw})_{tun}$ is the amount of wavelength tuning required for output restoration. Note that the primed and double-primed quantities in the figure refer to the mismatched and corrected wave triads respectively. Also, the quantities R, S and K represent the regular and scattered beams, and the grating vector, respectively. The necessary relationship between the required tuning $(\Delta\lambda / \lambda_{mw})_{tun}$ and the angular mismatch $\Delta\theta_{m,,in}$ is given by [2]:

$$\left(\frac{\Delta\lambda}{\lambda_{mw}}\right)_{tun} = \frac{\sin\left(2\theta_B - \Delta\theta_{m,in}\right)}{\sin 2\theta_B} - 1 \quad , \tag{1}$$

where the subscript "m" refers to the medium containing the hologram, and "in", "out", "w" and "tun" refer to input/incident, output/reconstructed, WRITE and tuning respectively. A similar result may be derived for the required wavelength tuning when the hologram is tilted [2]. A vector triad interaction picture depicting WRITE, mismatched READ and corrected (with angular tuning) wavevectors in the case of READ wavelength mismatch is shown in Fig.2.
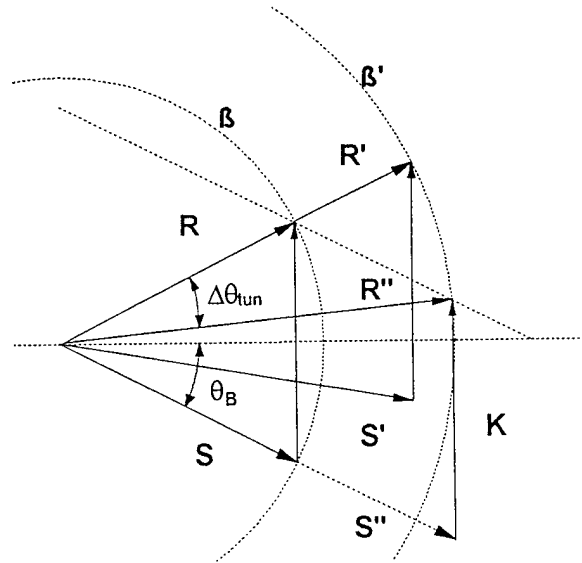
Fig. 2.

In the figure, the primes and double primes once again represent the mismatched and corrected triads, and the dotted circles represent constant wavenumber (β) circles. Note that the quantities R, S and K are as described earlier. The necessary angular tuning for this case is given by [3]:

$$(\Delta\theta)_{tun} = \cos^{-1}\left[\pm\cos^2\theta_B\left(\pm 2(1+\frac{\Delta\lambda}{\lambda_{mw}})\sin\theta_B \tan\theta_B + \sqrt{1-4(1+\frac{\Delta\lambda}{\lambda_{mw}})^2\sin^2\theta_B + \tan^2\theta_B}\right)\right],$$
$$\tag{2}$$

where $\Delta\lambda/\lambda_{mw}$ and θ_B are the fractional wavelength deviation and the Bragg angle respectively.

An important point to be noted about the above resonant triad geometries is that in many cases they support multiple solutions for the tuning problem; in some cases, they also do not permit any solution [2,3]. These conditions are determined by a number of parameters, such as the amount and sign of the mismatch under investigation, and the Bragg angle. In those cases where there are multiple solutions, some of the solutions may be physically meaningless or unrealizable.

The investigations in this paper deal with two extensions of the work described above. The first of these is the case of double- (or mixed) deviations, where the READ beam has a mismatched wavelength *and* a mismatched angle. In this case, restoration may be achieved by wavelength or angular tuning, or a combination of the two. A double-mismatch geometry with angular tuning is shown in Fig.3.
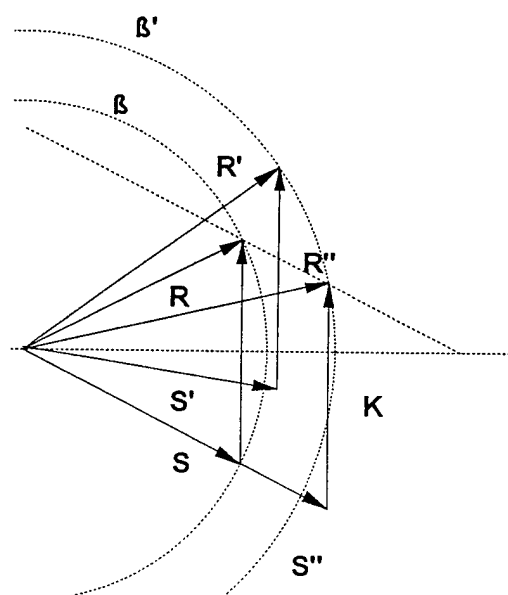

Fig. 3.

The labels on the figure follow the same definitions as in the earlier figures. The second of the extensions is in the context of a conical holographic stereogram with color recording and replay. As pointed out recently by Murillo-Mora *et al* [4], one may record and replay color images by generating three rainbow holograms on each slit hologram component of a holographic stereogram. The slit holograms are recorded around a circle, from which finally a truncated conical holographic stereogram is obtained. As suggested by the authors, the angles of the reference beam (of wavelength λ_0) to record the three rainbow holograms (corresponding to the red, green and blue objects which are stored prior to the recording) should be set at particular values, for which a criterion is given [4]. We show here that this experimental arrangement, and the corresponding WRITE/READ geometries fit adequately within the resonant triad technique described earlier.
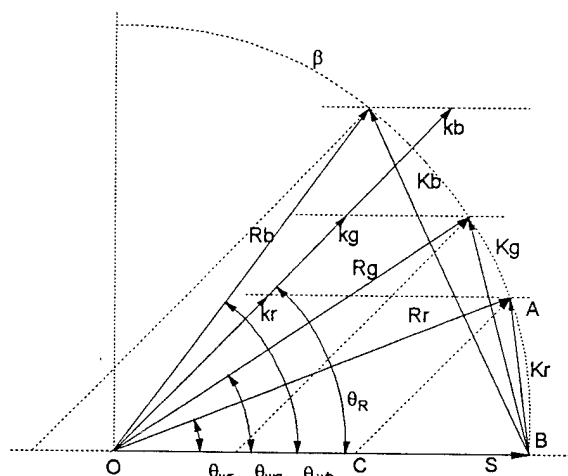
Fig. 4.

In Fig.4 we show a triad configuration in which the vector S represents the common scattered beam direction along which we require all the replayed color images to propagate. Suppose the replay (or READ) beam is incident on the superposed slit hologram at an angle θ_R. We assume that the READ beam is white light (used for reading rainbow holograms); the wavenumbers corresponding to the red, green and blue components of the white light are represented by k_r, k_g, and k_b respectively. The β circle here represents the common wavenumber $(2\pi/\lambda_0)$ corresponding to the reference beam and each of the three object beams (in the S-direction). According to the figure shown, the required reference beam directions are θ_{wp} (p=r, g and b for red, green and blue). Concentrating on the reference direction corresponding to the red object beam, we note that in the triangles AOB and ACB,

OA = OB = $2\pi/\lambda_0$; AB = K_r (the wavenumber of the grating vector for the red object beam); $\angle$AOB = θ_{wr} (the required reference beam angle); $\angle$ACB = θ_R (the READ angle).

From the above triangles, and simple geometrical manipulations, we may show that

$$\sin\theta_{wr} = \left(\frac{\lambda_0}{\lambda_r}\right)\sin\theta_R, \tag{3}$$

which agrees with the suggested criterion [4]. In a similar manner, the required reference angles for the green and blue object beam recordings may be derived. The resonant triad technique may be further applied to predict and analyze WRITE/READ configurations corresponding to monochromatic and color holograms and stereograms, especially when dealing with varying wavelengths and/or angles.

References:

1. M.R.Chatterjee, S.Min and S.-T.Chen, "Holographic Interconnections: An Analytical Investigation of Alignment, Switching and Resolution Issues," EEP-Vol.4-2, Advances in Electronic Packaging, ASME, 1179 (1993).

2. M.R.Chatterjee, S.Min, and S.-T.Chen, "Analysis of the Performance of Untilted and Tilted Interconnection Holograms With Mismatched READ Wavelengths and Incident Angles," submitted to Applied Optics, 1995.

3. M.R.Chatterjee and S.-T.Chen, "A Geometrical and Analytical Interpretation of the Wavelength and Angular Tunabilities of Holographic Gratings for the Restoration of Interconnections Under Mismatched READ Conditions," 1994 OSA Annual Meeting Program, p.125.

4. L.M.Murillo-Mora, K.Okada, T.Honda, and J.Tsujiuchi, "Color Conical Holographic Stereogram," Optical Engineering 34, 814 (1995).

Computer generated holographic photonic band gap structures designed using inverse scattering techniques

S-M. Chang, D.A. Pommet, L. Malley & M.A. Fiddy
Department of Electrical Engineering, University of Massachusetts Lowell,
Lowell, MA 01854, USA
pommet@cemos.uml.edu

Inverse synthesis techniques are important for development of diffractive optical elements. For non-periodic media, approximations can be made which allow estimates of the scattering permittivity distribution to be found. Over the last 15 years [1,2,3] we have moved from trying to *interpret* the most restrictive yet computationally simple of these approximations, the linearizing first Born and Rytov approximations, to the development of techniques which can be applied to both strongly scattering media as well as nonlinear (e.g. χ^3) structures. We have also applied these methods to real experimental data as well as simulated cases, as such work has wide ranging uses in fields as diverse as medical and geophysical imaging, as well as the design of optical components. Emerging from these studies is a clearer understanding as to how the differential cepstral method (see [4]) and distorted wave methods can be integrated in order to synthesize structures which are both strongly scattering and which have prescribed optically controllable scattering patterns.

For imaging from scattering fields, a limitation has been the numerical instability and complexity of the techniques, especially when only limited noisy data samples are available from the experiment. Consequently, this work has gone hand in hand with the development of regularization procedures and data extrapolation techniques incorporating prior knowledge about the structure. For the structure synthesis problem, however, for which one wishes to *specify* the diffracted or scattered field pattern, these difficulties are far less, only ill-conditioning being of concern.

High diffraction efficiencies arise from periodic 3D media (i.e. Bragg diffraction). These structures can be modified to be broadband and wide angle in their behavior and are then referred to as photonic band gap media [5].

It is the study of these scattering phenomena, via the development of new inverse synthesis techniques, that we present here. Based on the efficiency associated with Bragg scattering, we design a scattering distribution which satisfies the Born approximation and which when replicated provides a strongly scattering period structure with photonic band gap-like properties. Designed structures will be created with computer generated holograms (CGHs) based on a new ray-tracing algorithm. It has been shown [6,7] that thin phase holograms can be stacked to increase the overall diffraction efficiency. In this work, we will stack CGHs of the calculated scattering distributions to increase the diffraction efficiency to approach that of a 3D media. Specific attention will be placed on the angular and wavelength dependencies of the CGHs.

Acknowledgment

References

[1]   F. C. Lin and M. A. Fiddy, "Image estimation from scattered field data", International Journal of Imaging Systems and Technology, 2, 76-95, 1990.
[2]   F. C. Lin and M. A. Fiddy, "The Born-Rytov controversy: I. Comparing analytical and approximate expressions for the one-dimensional deterministic case", J. Soc. Opt. Am., A9, 1102-1110, 1992.
[3]   F. C. Lin and M. A. Fiddy, "The Born-Rytov controversy: II. applications to the nonlinear and stochastic scattering problem in one-dimensional half-space media", J. Soc. Opt. Am., A10, 1971-1983, 1993.
[4]   J. B. Morris , R. McGahan, F. C. Lin, D. A. Pommet and M. A. Fiddy, "A Homomorphic Filtering Method for Imaging Strongly Scattering Penetrable Objects", IEEE-AP, 43, 1029-1035, 1995.
[5]   A.A. Maradudin and A.R. McGurn, "Photonic band structure of a truncated two dimensional periodic dielectric medium", J.O.S.A. B, 10, 307-313, 1993.
[6]   B. Ya. Zel'dovich, D. I. Mirovitskii, N. V. Rostovtseva, and O. B. Serov," Characteristics of two-layer phase holograms," Sov. J. Quant. Elect., 14, 364-369, 1984.
[7]   R. V. Johnson and A. R. Tanguay, Jr., " Streatified volume holographic optical elements," Opt. Lett, 13, 1988.

Ray-tracing Approach to Computer-generated Holography with Detour Phase Coding for Precision 3D Beam Patterns

Shih-Ming Chang[+], Drew A. Pommet[+], Michael A. Fiddy, and Freeman C. Lin[+]
Department of Electrical Engineering
University of Massachusetts Lowell
Lowell, MA 01854

[+]also with Wavicle Technologies
175 Cabot Street, 3rd Floor Wannalancit Building
Lowell, MA 01854

A ray-tracing method with a detour phase coding scheme [e.g., 1] is developed to design on-axis and off-axis computer-generated holograms (CGHs). To date, the usual Fourier-transform approach and coding schemes published by others has been restricted to designs for the reconstruction of two-dimensional (2D) light patterns or "objects" (e.g., [1-3]). The ray-tracing method presented here is readily employed to design CGHs for both 2D and 3D reconstructions and these objects can be situated in either Fresnel or Fraunhofer regions. The ray-based approach simply calculates the optical path length from any chosen point in the object domain and computes the phase of the spherical wavefront from a coherent point source at the recording plane. This approach also conveniently permits various incident and reference beam functions to be modeled, as well as quite complex beam shapes, such as snake beams in the reconstruction regime. While sometimes computationally more intensive than a Fourier-based method, we will show how this approach is highly flexible and allows for very precise location of original object points. A further advantage is that transparent and semi-transparent objects can be easily specified [4].

The 3D object is partitioned into cells and the recording plane is divided into pixels. Each pixel on the recording plane is further subdivided into sub-pixels in order to encode both amplitude and phase information about the interference pattern. When illuminated by the original incident beam, each cell on the object can be treated as a reflecting element which broadcasts to a specific pixel in the recording plane. The relative optical paths between object sources and reference beams to the recording plane are specified. The reflection coefficient for each object cell is determined and the amplitudes and phases of the object and reference beams are calculated and coherently summed. The phase differences arise from both the initial phase of the illumination and the different optical path lengths to each pixel on the recording plane.

Two types of detour phase coding schemes are considered. The first coding scheme employes an opaque rectangle having a fixed width w and two adjustable parameters, i.e., height h_{mn} and distance d_{mn} between centers of the rectangle and the (m, n)[th] pixel to store the amplitude and phase of the interference pattern. The second scheme uses two opaque rectangles separated by a distance c_{mn}, each having the same fixed width w and height h. The amplitude and phase in the (m, n)[th] pixel is now stored by two adjustable parameters c_{mn} and d_{mn} the distance between the center of the pixel to the midpoint of these two rectangles. All of these claculated interference patterns are binarized and are hardcopied using a laser printer (with only 300 dots per inch, dpi) resolution. Finally, to fabricate the CGH, this hardcopy is photographed using commercial 35mm black-and-white film with a demagnification factor of 25. With this demagnification factor, we can achieve a resolution on the film of about 7500 dpi or about 150 lines/mm.

The computation time to encode a 3D object into a CGH using our software increases linearly with the increasing number of contributing object points and the number of pixels in the recording plane. We show reconstructions using a converging reconstruction beam and demonstrate that the expected real and virtual images are both successfully recovered. The bright

caused by the converging reconstruction beam in the on-axis case is readily eliminated by introducing a small stop at the focal point of this reconstruction beam. This stop can be sufficiently small that the quality of the reconstructed image is still preserved extremely well. The reconstructed images have sufficiently high resolution that individual pixels on the original image can be resolved. For off-axis CGHs, we can avoid the twin-image problem by adjusting the deflection angle according to the prior knowledge about the maximum spatial frequency content of the object.

Acknowledgement

References

[1] B. R. Brown and A. W. Lohmann, "Complex spatial filtering with binary masks," Appl. Opt., 5, 967-970, 1966.

[2] A. Lee and D. Casasent, "Computer generated hologram recording using a laser printer," Appl. Opt., 26, 136-138, 1987.

[3] T. T. Chia, A. C. Goh, and Y. K. Lai, "Computer generated hologram with a commercial microfilm," Opt. Laser Tech., 19, 263-264, 1987.

[4] S. M. Chang, D. A. Pommet, and M. A. Fiddy, "Computer generated holography by calculating the phase from each image pixel," submitted to Appl. Opt., for review, 1995.

Perry, M. D. — JMC3, JMC4, JTuB10, JTuB16
Pleumeekers, J. — HTuA2
Piper, Eckhard — JMC5
Pommet, Drew A. — JTuB27, HTuD4, HTuD5
Psaltis, Demetri — HMB1

Rheinhand, Nadia — HTuD2
Richling, Keith G. — HMB4
Riza, Nabeel A. — HMA4
Rosen, Joseph — HMA3
Rosenbluth, M. — JMC2
Rushford, Mike — JTuB16

Salaun, S. — HTuA2
Serati, Steven A. — JTuC2
Sharangovich, Sergey N.- HTuA4, HTuA5
Sharp, Gary D. — JTuC2
Shen, X. A. — HMB2,
Shoop, Barry L. — JTuB5
Singer, Wolfgang — JMC5
Singstad, I. — HMC2
Sohn, Yeung Joon — JTuB20
Sonehara, Tomio — JTuB12
Steijn, Kirk W. — HTuA1
Stockley, Jay E. — JTuC2
Sun, Pang-chen — HMC4
Suqing, Tan — JTuB26

Tajahuerce, E. — JTuB7
Teng, Y. Y. — JTuB27

Testorf, Markus — JTuB2
Thomas, Ian — JTuB16
Trout, T. John — HTuA1

Vaudry, C. — HTuA2
Voelz, David G. — HMA2

Wang, Ping — JTuC2
Wang, Y. J. — JTuB27
Wangler, Johannes — JMC5
Watson, Edward A. — JTuC4
Weible, K. J. — JTuB8
Weiner, Andrew M. — HMC3
Wenqi, Gao — JTuB26

Ximing, Deng — JTuB3
Xuegong, Deng — JTuB3

Yang, Guoguang — JTuC5
Yang, Guozhen — JTuB1A, JTuB1B, JTuB11
Yariv, Amnon — HMA3
Yongpin, Li — JTuB3
YUue, Qiu — JTuB3

Zelenskya, T. — HTuA4
Zhang, Guoqing — JTuB1A, JTuB1B, JTuB11
Zheng, Shihai — JTuB1A
Zheng, Yunlong — JTuB17, JTuB18
Zhou, Charles — HTuA3

HOLOGRAPHY
TECHNICAL PROGRAM COMMITTEE

Joseph Marron, *Environmental Research Institute of Michigan, General Chair*

Lambertus Hesselink, *Stanford University, Program Chair*

James Leger, *University of Minnesota, Program Chair*

Daniel Angell, *Ford Motor Company*

Willis Colburn, *Kaiser Optical Systems*

Yeshayahu Fainman, *University of California, San Diego*

Dean Faklis, *Rochester Photonics*

Neal Gallagher, *University of Delaware*

Raymond Kostuk, *University of Arizona*

Demetri Psaltis, *California Institute of Technology*

David Voelz, *U. S. Air Force Phillips Laboratory*

Andrew Weiner, *Purdue University*